Universidade de Aveiro Departamento de Engenharia de Materiais e Cerâmica
2012

Luís Miguel de Almeida Amaral

Desenho Microestrutural de Electrocerâmicos à Base de Titanatos

Microstructure Design of Titanate-Based Electroceramics

Universidade de Aveiro
2012
Departamento de Engenharia de Materiais e Cerâmica

Luís Miguel de Almeida Amaral

Desenho Microestrutural de Electrocerâmicos à Base de Titanatos

Microstructure Design of Titanate-Based Electroceramics

Tese apresentada à Universidade de Aveiro para cumprimento dos requisitos necessários à obtenção do grau de Doutor em Ciência e Engenharia de Materiais, realizada sob a orientação científica da Doutora Ana M. O. R. Senos, Professora Associada do Departamento de Engenharia de Materiais e Cerâmica da Universidade de Aveiro e da Doutora Paula M. L. S. Vilarinho, Professora Associada do Departamento de Engenharia de Materiais e Cerâmica da Universidade de Aveiro.

Thesis presented to the University of Aveiro in fulfilment of the requirements for the awarding of the degree of Doctor in Materials Science and Engineering, under the scientific guidance of Professor Ana M. O. R. Senos, Associate Professor of the Department of Materials and Ceramics Engineering of the University of Aveiro and Professor Paula M. L. S. Vilarinho, Associate Professor of the Department of Materials and Ceramics Engineering of the University of Aveiro.

Apoio financeiro da FCT e do FSE no âmbito do III Quadro Comunitário de Apoio.

o júri

presidente

Prof. Doutor Luís Filipe Pinheiro de Castro
professor catedrático da Universidade de Aveiro

Prof. Doutor Jorge Ribeiro Frade
professor catedrático da Universidade de Aveiro

Prof. Doutor Mário António Caixeiro de Castro Pereira
professor auxiliar da Escola de Ciências da Universidade do Minho

Prof. Doutor Olivier Guillon
professor for "Mechanics of Functional Materials", Friedrich-Schiller-Universität Jena

Prof. Doutora Ana Maria de Oliveira e Rocha Senos
professora associada da Universidade de Aveiro

Prof. Doutora Paula Maria Lousada Silveirinha Vilarinho
professora associada da Universidade de Aveiro

Acknowledgements

First of all, I want to express my deep gratitude to my supervisors, Prof. Dr. Ana Senos and Prof. Dr. Paula Vilarinho, for their demanding and critical but fair supervision and guidance, as well as constant encouragement and discussion along this work.

This thesis is the result of several collaborations. I want to acknowledge the contributions of many persons that were fundamental in the conception and development of this work. I am very grateful to Prof. Dr. Olivier Guillon and Christine Jamin for the collaboration on the constrained sintering studies. This collaboration included a three months stay at the Technische Universität Darmstadt, Germany, in the Ceramics Group lead by Prof. Dr. Jürgen Rödel. I am also very thankful to him and to all the other members of his group for receiving me and making me feel at home during my stay in Germany and later visits.

Many thanks to Prof. Dr. Martin Harmer and Prof. Dr. Jian Luo, for analysis and discussion of the grain growth anomaly of STO; to Dr. Rainer Schmidt, for valuable discussions on the impedance spectroscopy data; to Prof. Dr. Ian Reaney for TEM characterization and discussion; and to Dr. Rosário Soares for XRD texture analysis and discussion.

I want to thank my colleagues of the Electroceramics Group and the department staff for a great work environment (and coffee breaks) and all the help they gave me in several occasions.

I acknowledge FCT, the Portuguese Foundation for Science and Technology, for financial support, under the grant SFRH/BD/40927/2007, and the DAAD/GRICES Bilateral Action n° 0811978.

Estarei eternamente grato aos meus pais, irmão e avós por tudo o que me dão e por terem criado os alicerces de quem eu sou hoje, e aos pais da Ana por tudo o que me dão e por sempre me fazerem sentir em casa.

I will always be grateful to Mia, for being the sweetest thing alive, and to Ana, my love and my better half, who is the beautiful keystone that gives a sense to my life and makes me a better person. I will always treasure her critics, her incentive and her patience for waiting for me and sharing me with this work.

palavras-chave

Electrocerâmicos, $SrTiO_3$, $BaLa_4Ti_4O_{15}$, $Ba_{4.5}Nd_9Ti_{18}O_{54}$, não-estequiometria, fronteiras de grão, deposição electroforética, filmes espessos, sinterização constrangida, anisotropia, propriedades dieléctricas.

resumo

Electrocerâmicos são uma classe de materiais avançados com propriedades eléctricas valiosas para aplicações. Estas propriedades são geralmente muito dependentes da microestrutura dos materiais. Portanto, o objectivo geral deste trabalho é investigar o desenho da resposta dieléctrica de filmes espessos obtidos por Deposição Electroforética (EPD) e cerâmicos monolíticos, através do controlo da evolução da microestrutura durante a sinterização de electrocerâmicos à base de titanatos.

Aplicações sem fios na indústria microelectrónica e de comunicações, em rápido crescimento, tornaram-se um importante mercado para os fabricantes de semicondutores. Devido à constante necessidade de miniaturização, redução de custos e maior funcionalidade e integração, a tecnologia de filmes espessos está a tornar-se uma abordagem de processamento de materiais funcionais cada vez mais importante. Uma técnica adequada neste contexto é EPD. Os filmes espessos resultantes necessitam de um passo subsequente de sinterização que é afectada pelo substrato subjacente, tendo este um forte efeito sobre a evolução da microestrutura.

Relacionado com a miniaturização e a discriminação do sinal, materiais dieléctricos usados como componentes operando a frequências das microondas em aplicações na industria microelectrónica de comunicações devem apresentar baixas perdas dieléctricas e elevadas permitividade dieléctrica e estabilidade com a temperatura. Materiais do sistema $BaO\text{-}Ln_2O_3\text{-}TiO_2$ (BLnT: Ln = La ou Nd), como $BaLa_4Ti_4O_{15}$ (BLT) e $Ba_{4.5}Nd_9Ti_{18}O_{54}$ (BNT), cumprem esses requisitos e são interessantes para aplicações, por exemplo, em estações de base para comunicações móveis ou em ressonadores para telefones móveis, onde a miniaturização dos dispositivos é muito importante. Por sua vez, o titanato de estrôncio ($SrTiO_3$, STO) é um ferroeléctrico incipiente com constante dieléctrica elevada e baixas perdas, que encontra aplicação em, por exemplo, condensadores de camada interna, tirando partido de fronteiras de grão altamente resistivas. A dependência da permitividade dieléctrica do campo eléctrico aplicado torna este material muito interessante para aplicações em dispositivos de microondas sintonizáveis. Materiais à base de STO são também interessantes para aplicações termoeléctricas, que podem contribuir para a redução da actual dependência de combustíveis fósseis por meio da geração de energia a partir de calor desaproveitado. No entanto, as mesmas fronteiras de grão resistivas são um obstáculo relativamente à eficiência do STO para aplicações termoeléctricas.

Para além do efeito do substrato durante a sinterização constrangida, outros factores, como a presença de fase líquida, a não-estequiometria ou a temperatura de sinterização, afectam significativamente não apenas a microestrutura dos materiais funcionais, mas também a sua resposta dieléctrica.

Se adequadamente compreendidos, estes factores podem ser intencionalmente usados para desenhar a microestrutura dos electrocerâmicos e, desta forma, as suas propriedades dieléctricas.

O efeito da não-estequiometria (razão Sr/Ti 0.995-1.02) no crescimento de grão e resposta dieléctrica de cerâmicos de STO foi investigado neste trabalho. A mobilidade das fronteiras de grão aumenta com a diminuição da razão Sr/Ti. A resistividade do interior dos grãos e das fronteiras de grão é sistematicamente diminuída em amostras não-estequiométricas de STO, em comparação com o material estequiométrico. O efeito é muito mais forte para as fronteiras de grão do que para o seu interior. Dependências sistemáticas da não-estequiometria foram também observadas relativamente à dependência da condutividade da temperatura (muito mais afectada no caso da contribuição das fronteiras de grão), à capacitância do interior e fronteiras de grão e à espessura das fronteiras de grão.

Uma anomalia no crescimento de grão em cerâmicos de STO ricos em Ti foi também observada e sistematicamente analisada. Foram detectadas três descontinuidades na dependência do tipo Arrhenius do crescimento de grão relativamente à temperatura com diminuições no tamanho de grão a temperaturas em torno de 1500, 1550 e 1605 ˚C. Além disso, descontinuidades semelhantes foram também observadas na dependência da energia de activação relativamente à condutividade das fronteiras de grão e na espessura das fronteiras de grão, avaliadas por Espectroscopia de Impedância. Estas notáveis coincidências suportam fortemente a formação de diferentes complexos de fronteira de grão com transições entre os regimes de crescimento de grão observados, que podem ser correlacionados com diferentes mobilidades de fronteira de grão e propriedades dieléctricas. Um modelo é sugerido, que se baseia na diminuição da fase líquida localizada nas fronteiras de grão, como o aumento da temperatura de sinterização, um cenário compatível com um fenómeno de solubilidade retrógrada, observado anteriormente em metais e semicondutores, mas não em cerâmicos.

A EPD de filmes espessos de STO em substratos de folha de Pt e a sinterização constrangida dos filmes fabricados foram também preliminarmente tratadas. Filmes espessos de STO foram depositados com êxito por EPD sobre substratos de Pt e, depois de sinterizados, atingiram densidades elevadas. Um aumento da densificação e do tamanho de grão assim como o alargamento da distribuição de tamanho do grão foram observados com a diminuição da razão Sr/Ti, tal como anteriormente observado em amostras cerâmicas. Grãos equiaxiados foram observados para todas as composições, mas um certo grau de anisotropia na orientação dos poros foi detectado: os poros revelaram uma orientação vertical preferencial.

Este trabalho focou-se também na sinterização constrangida do sistema BLnT (Ln = La ou Nd), nomeadamente de filmes espessos de BLT e BNT sobre substratos de folha de platina, e na relação do desenvolvimento de anisotropia microestrutural com as propriedades dieléctricas. As observações durante a sinterização constrangida foram comparadas com cerâmicos monolíticos equivalentes sinterizados livremente. Filmes espessos de BLnT (Ln = La ou Nd) com elevada densidade foram obtidos por EPD e subsequente sinterização constrangida. A anisometria cristalográfica do material em conjunto com um passo de sinterização constrangida resultou em grãos alongados e microestruturas anisotrópicas. O efeito do stress do substrato durante a sinterização constrangida originou graus mais elevados de anisotropia (grãos e poros alongados e orientação preferencial, bem como textura cristalográfica) nos filmes sinterizados relativamente aos cerâmicos equivalentes sinterizados livremente, não obstante o estado equivalente das amostras em verde. A densificação dos filmes de BLnT (Ln = La ou Nd) é retardada em comparação com os cerâmicos, mas depois de longos tempos de sinterização densidades semelhantes são obtidas. No entanto, em oposição a observações na sinterização constrangida de outros sistemas, o crescimento do grão em filmes de BLnT (Ln = La ou Nd) é favorecido pelo constrangimento causado pelo substrato.

Além disso, grãos e poros alongados orientados paralelamente ao substrato foram desenvolvidos durante a sinterização constrangida de filmes espessos. Verificou-se uma forte correlação entre a evolução de grãos e poros, que começou assim que o crescimento do grão se iniciou. Um efeito da tensão do substrato no aumento do crescimento de grão, bem como um forte "*Zener pinning*", origina microestruturas altamente texturizadas, o que também é observado a nível cristalográfico. Efeitos marcantes da anisotropia microestrutural foram também detectados nas propriedades dieléctricas dos filmes de BLnT (Ln = La ou Nd). Juntamente com o aumento da razão de aspecto dos grãos, do factor de orientação e do grau de textura cristalográfica, a permitividade relativa é ligeiramente diminuída e o coeficiente de temperatura da permitividade evolui de negativo para positivo com o aumento do tempo isotérmico de sinterização.

Este trabalho mostra que a não-estequiometria pode ser usada para controlar a mobilidade das fronteiras de grão e, portanto, desenhar a microestrutura e as propriedades dieléctricas de electrocerâmicos à base de STO, com ênfase nas propriedades das fronteiras de grão. O papel da não-estequiometria no STO e dos complexos de fronteira de grão no desenvolvimento microestrutural é discutido e novas oportunidades para desenhar as propriedades de materiais funcionais são abertas.

As observações relativamente à sinterização constrangida apontam para o efeito de tensões mecânicas desenvolvidas devido ao substrato subjacente no desenvolvimento da microestrutura de materiais funcionais. É assim esperado que a escolha adequada de substrato permitia desenhar a microestrutura de filmes espessos funcionais com desempenho optimizado. "*Stress Assisted Grain Growth*" (SAGG) é então proposto como uma técnica potencial para desenhar a microestrutura de materiais funcionais, originando microestruturas anisotrópicas texturizadas com propriedades desejadas.

keywords

Electroceramics, $SrTiO_3$, $BaLa_4Ti_4O_{15}$, $Ba_{4.5}Nd_9Ti_{18}O_{54}$, nonstoichiometry, grain boundaries, electroforetic deposition, thick films, constrained sintering, anisotropy, dielectric properties.

abstract

Electroceramics are a class of advanced materials with electrical properties valuable for applications. These properties are usually very dependent on the microstructure of the materials. Therefore, the general objective of this work is to investigate the tailoring of the dielectric response in thick films obtained by Electrophoretic Deposition (EPD) and bulk ceramics by controlling the microstructure evolution during sintering of titanate-based electroceramics.

Wireless applications in the rapidly growing microelectronics and communications industry became a significant market for semiconductor manufacturers. Driven by the need for constant miniaturization, cost reduction and enhanced functionality and integration, thick film technology is becoming an increasingly important processing approach for functional materials. An adequate technique in this context is EPD. The resulting thick films need a subsequent sintering step and the sintering layer is constrained by the underlying substrate, which has a strong effect on the microstructure evolution.

Related to miniaturization and signal discrimination, dielectric materials to be employed as microwave components in microelectronics and communications applications must exhibit low dielectric loss, high dielectric permittivity and temperature stability. $BaO\text{-}Ln_2O_3\text{-}TiO_2$ (Ln = La or Nd) system materials, such as $BaLa_4Ti_4O_{15}$ (BLT) and $Ba_{4.5}Nd_9Ti_{18}O_{54}$ (BNT), fit those requirements and are interesting for applications, for example, in base stations for mobile communications or in dielectric resonators for mobile phone handsets, where device miniaturization is very important.

By its turn, strontium titanate ($SrTiO_3$, STO) is an incipient ferroelectric with high dielectric permittivity and low losses, which find application in, for example, grain boundary layer capacitors taking advantage of highly resistive grain boundaries. A dependence of the permittivity on the applied field turns this material very interesting for applications in tunable microwave devices. Strontium titanate based materials are also interesting for thermoelectric applications, which may contribute for the reduction of the current dependence on fossil fuels by generating power from waste heat. However, the same resistive grain boundaries are an obstacle to the efficiency of STO for thermoelectric applications.

Besides the effect of the substrate during constrained sintering, others factors like nonstoichiometry, liquid phase and sintering temperature strongly affect not only the microstructure of functional materials but also their dielectric response. If properly understood these factors may be intentionally used to design the microstructure of electroceramics and therefore to tailor their dielectric properties.

The effect of nonstoichiometry (Sr/Ti ratio from 0.995 to 1.02) on the grain growth and dielectric response of STO ceramics was investigated. The grain boundary mobility increases with the decrease of Sr/Ti ratio. The resistivity of bulk and grain boundaries is systematically decreased in nonstoichiometric strontium titanate samples as compared to stoichiometric material. The effect is much stronger for the grain boundaries than for the bulk. Systematic dependences on the nonstoichiometry were also observed for the measurement temperature dependence of the conductivity (much more affected in the case of the grain boundary contribution), bulk and grain boundary capacitance and grain boundary thickness.

A grain growth anomaly in Ti-rich STO ceramics was also observed and systematically analyzed. It is shown that three discontinuities on the Arrhenius-type temperature dependence of grain growth take place with drops in the grain size at temperatures around 1500, 1550 and 1605 ˚C. Moreover, similar discontinuities are also observed in the dependence of the grain boundary activation energy for conductivity and in the grain boundary thickness, assessed by Impedance Spectroscopy. These notable coincidences strongly support the formation of different grain boundary complexions with transitions in between the observed grain growth regimens, which may be correlated to different grain boundary mobility and dielectric properties. A model is suggested, which is based on the decrease of the liquid phase located at the grain boundaries as the sintering temperature increases, a scenario compatible with a retrograde solubility phenomena, reported before for metals and semiconductors but not yet for ceramics.

The EPD of STO thick films on Pt-foil substrates and the constrained sintering of the fabricated thick films were also preliminarily addressed. Thick films were successfully deposited. Increasing densification, grain size and enlargement of the grain size distribution was observed with the decreasing of the Sr/Ti ratio, as previously observed for bulk ceramic samples. Equiaxied grains were observed for all compositions but some degree of anisotropy in the pore orientation was detected: pores showed a preferential vertical orientation.

This work was also focused on the constrained sintering of $BaO\text{-}Ln_2O_3\text{-}TiO_2$ (BLnT, Ln = La or Nd) system, namely $BaLa_4Ti_4O_{15}$ (BLT) and $Ba_{4.5}Nd_9Ti_{18}O_{54}$ (BNT) EPD thick films on Pt foil substrates, and on the relation of the anisotropic microstructure development with the dielectric properties. The observations during constrained sintering are compared with equivalent freely sintered bulk ceramics. High density BLnT (Ln = La or Nd) thick films were obtained by EPD. The crystallographic anisometry of the material together with a constrained sintering step resulted in elongated grains and anisotropic microstructures. The effect of the stress from the substrate during the constrained sintering lead to higher degrees of anisotropy (elongated grain and pore shape and preferential orientation, as well as crystallographic texture) in the constrained sintered films than in the equivalent freely sintered bulk samples, despite the equivalent state of the green samples.

The densification of BLnT (Ln = La or Nd) films is retarded in comparison with their bulk counterparts, but after long sintering times similar densities are obtained. However, in opposition to other constrained systems investigated until now, grain growth is favored by the substrate constraint in the BLnT (Ln = La or Nd) constrained sintered films.

Moreover, elongated grains and pores oriented parallel to the substrate were developed during the constrained sintering of thick films. There is a strong correlation between grain and pore evolution, which started as soon as grain growth takes place. A stress effect triggering grain growth enhancement, as well as a strong Zener pinning effect, leads to highly textured microstructures, which is also observed at the crystallographic level.

Marked effects of the microstructural anisotropy were detected on the dielectric properties of the BLnT (Ln = La or Nd) films. Along with the increase in grain aspect ratio, orientation factor and degree of crystallographic texture, the relative permittivity is slightly decreased and the temperature coefficient of permittivity evolves from negative to positive with the increase of the isothermal sintering time.

This work shows that nonstoichiometry may be used to control the grain boundary mobility and therefore tailor the microstructure and dielectric properties of STO based electroceramics, with emphasis on the grain boundary properties. The role of nonstoichiometry of STO and complexions on the microstructure development is discussed and new opportunities to design properties of functional materials are opened.

These observations regarding constrained sintering point to the effect of mechanical stresses developing due to the underlying substrate on the microstructure development of functional materials. It is then expected that the appropriate choice of substrate will allow designing tailored microstructures of functional thick films with optimized performance. Stress Assisted Grain Growth (SAGG) is then proposed as a potential technique to engineer functional materials microstructures, achieving anisotropic textured microstructures with tailored properties.

Table of Contents

List of Figures

List of Tables

List of Symbols

a, b, c - lattice parameters

A - generic acceptor

C - capacitance

C_B - bulk capacitance

C_{GB} - grain boundary capacitance

D - generic donor

d - interplanar spacing

D_{eq} - average equivalent diameter

$D_{eq,max}$ - largest equivalent diameter

d_s - sample thickness

E - dc bias electric field

e' - conducting electron

E_a - activation energy

$E_{a,GB}$ - activation energy for grain boundary conductivity

$E_{a,B}$ - activation energy for bulk conductivity

f - frequency

f_0 - resonant frequency at ambient temperature

f_{inc} - inclusion volume fraction

G - average grain size

G_a- median grain area

$G_{a,0}$ - initial median grain area

G_0 - initial average grain size

G_A - grain size of an abnormal grain

$h^{\bullet}$ - conducting hole

H - hexagonal setting

i - imaginary operator

I - current

I_C - capacitive current

I_R - ac conduction current

k - number of wavelengths

K_0 - pre-exponential constant

K_B - Boltzmann constant (1.38066×10^{-23} J/K)

k_G - grain growth factor

M - electric modulus

m - grain growth exponent

M* - complex electric modulus

M_{GB} - grain boundary mobility

n - concentration of electrons

p - concentration of holes

pO_2 - oxygen partial pressure

Q - quality factor

Q_{CPE}, n_{CPE} - fitting parameters

Q_g - apparent activation energy for the grain growth process

r - average inclusion or pore size

R - resistance

R_{gc} - gas constant (8.31451 J K^{-1} mol^{-1})

r_A - average ionic radius of A-site cations

r_B - average ionic radius of B-site cations

S - area of electrode

T - temperature

t - time

tanδ – dielectric loss or dissipation factor

t_G - Goldschmidt tolerance factor

U - voltage

V - vacancy

W - bandgap

Z - impedance

Z’ - real part of impedance

Z’’ - imaginary part of impedance

Z''_{max} - maximum of the imaginary part of impedance

α - coefficient of thermal expansion

α_g - geometrical factor

β - constant

γ - surface or grain boundary energy

Δ - variation

δ_{GB} - grain boundary thickness

ε' - real part of the permittivity

ε'' - imaginary part of the permittivity

ε* - complex permittivity

ε_0 - permittivity of free space (8.85×10^{-12} F/m)

ε_r - relative permittivity or dielectric constant

ε_{r0} - dielectric constant at 30 °C

$\dot{\varepsilon}_s$ - strain rate

$\varepsilon_{s,r}$ - radial strain

$\varepsilon_{s,z}$ - axial strain

$\dot{\varepsilon}_s^{free}$ - free sintering strain rate

$\dot{\varepsilon}_s^{constr}$ - constrained sintering strain rate

E^p - uniaxial viscosity

θ - diffraction angle

λ - wavelength

λ_L - figure of merit that represents the tendency for intergranular film formation

ν^p - viscous Poisson's ratio

ρ - relative density

$\dot{\rho}$ - densification rate

ρ_0 - relative density of green compacts

ρ_r - electrical resistivity

σ - electrical conductivity

σ_s - stress

Σ - inverse of the fraction of individual-lattice sites which are common to the two adjoining grains associated with CSL points

τ - relaxation time or time constant

τ_f - temperature coefficient of resonant frequency

ψ - angle (90°- δ)

ω - angular frequency

ω_{max} - frequency of maximum loss

List of Abbreviations

AC - Alternating Current

BLnT - $BaO\text{-}Ln_2O_3\text{-}TiO_2$ (Ln = La or Nd)

BLT – Barium Lanthanum Titanate, $BaLa_4Ti_4O_{15}$

BNT – Barium Neodimium Titanate, $Ba_{4.5}Nd_9Ti_{18}O_{54}$

BSE - Backscattered Electron

BST – Barium Strontium Titanate, $Ba_xSr_{1-x}TiO_3$

ccp - cubic close-packed

CIP - Cold Isostatic Pressing

CPE - Constant Phase Element

CSL - Coincident Site Lattice

DC - Direct Current

DLVO - Derjaguin-Landau-Vervew-Overbeek

DR - dielectric resonator

EDS - Energy Dispersive Spectroscopy

EELS - Electron Energy Loss Spectroscopy

ELS - Electrophoretic Light Scattering

EPD - Electrophoretic Deposition

FIB - Focused Ion Beam

FWHM - Full Width at Half Maximum

GPS - Global Positioning System

hcp - Hexagonal Close-Packed

HIP - Hot Isostatic Pressing

HRTEM – High Resolution Transmission Electron Microscopy

ICPS - Inductively Coupled Plasma Spectroscopy

IGF - Intergranular Glassy Film

IS - Impedance Spectroscopy

ITS - Intelligent Transport System

LAN - Local Area Network

LTCC - Low Temperature Co-fired Ceramic

MIC - Microwave Integrated Circuit

MIM - Metal-Insulator-Metal

MOSFET - Metal Oxide Semiconductor Field Effect Transistor

MW - Microwave

PDF - Powder Diffraction File

PIPS - Precision Ion Polishing System

ppm - Parts Per Million

ppb - Parts Per Billion

PTC - Positive Temperature Coefficient

PTCR - Positive Temperature Coefficient of Resistance

PZT - Lead Zirconate Titanate, $Pb[Zr_xTi_{1-x}]O_3$

RBS - Rutherford Backscattering Spectrometry

RP - Ruddlesden-Popper

SAGG - Stress Assisted Grain Growth

SEM - Scanning Electron Microscopy

SIMS - Secondary Ion Mass Spectrometry

SOFC - Solid Oxide Fuel Cell

STEM - Scanning Transmission Electron Microscopy

ST - $SrTiO_3$ (stoichiometric composition used in this work)

ST 0.995 - $Sr_{0.995}TiO_{2.995}$

ST 0.997 - $Sr_{0.997}TiO_{2.997}$

ST 1.005 - $Sr_{1.005}TiO_{3.005}$

ST 1.01 - $Sr_{1.01}TiO_{3.01}$

ST 1.02 - $Sr_{1.02}TiO_{3.02}$

STO - Strontium Titanate, $SrTiO_3$

TEA – Triethanolamine, $C_6H_{15}NO_3$

TCC - temperature coefficient of capacitance

TCε_r - temperature coefficient of permittivity

TEM - Transmission Electron Microscopy

TGG - Templated Grain Growth

WLAN - Wireless Local Area Network

XRD - X-ray Diffraction

1 Introduction

1.1 Motivation

Electroceramics is a general designation for ceramic materials that exhibit electric properties useful for applications [1-4]. The name electroceramics was given to differentiate ceramics with unique functional electrical, optical and magnetic capabilities from traditional ceramic materials. Electroceramics find application in several fields such as communications, consumer electronics, power conversion and storage and even automation [1-4]. Introduced after the Second World War, these materials had a huge impact on the electronic uprising along with the progress in the quality of life of the developed countries.

Electroceramics have been consolidated in the last decades as one of the most attractive areas in material science because of both the improvement of basic knowledge and its technological impact. Major breakthroughs in the processing of electroceramic materials, in bulk and thin/thick films, as well as improvements in the understanding of the structure-property relation of these materials have been achieved. This has led to many novel concepts, which are nowadays used in many technological applications in a multibillion dollar microelectronic industry [5-8].

For example, wireless applications in microelectronic and communications industry have expanded quickly and became a significant market for semiconductor manufacturers [5; 8]. Applications in this field include multifunctional portable phones, Bluetooth, office voice, video and data transmission through Wireless Local Area Networks (WLAN), Global Positioning Systems (GPS) and automotive safety control, among others [7]. Dielectric materials to be employed as microwave components in these applications must exhibit low dielectric loss, high dielectric permittivity and temperature stability [7].

Driven by the need for miniaturization, cost reduction and enhanced functionality and integration, the field of electroceramics is growing rapidly in many new directions [3]. For example, processing materials in the form of films on top of substrates is an

interesting path for downscaling electronic components previously fabricated in bulk form [3; 9]. To achieve such ambitious goal, the understanding and exploitation of the effects of a constraining substrate on processing and final properties of thick films is of fundamental importance.

Titanate-based electroceramics have received particular attention over the years. This family of materials offer a wide range of technologically useful properties including dielectric, piezoelectric, pyroelectric, ferroelectric, electrooptical and magnetooptical behaviour [1-4]. In addition, their properties may be tailored for the intended application by compositional, stoichiometric, structural or morphological controlled variations.

A good example is lead zirconate titanate ($Pb[Zr_xTi_{1-x}]O_3$) (PZT), one of the most widely exploited and extensively used piezoelectric materials [4]. Applications of this material include sensor and actuator devices, multilayered capacitors, among many others, with an estimated market of tens of billions of dollars worldwide [6]. However, lead is highly toxic and pollutant and due to environmental regulations PZT has to be replaced by lead-free materials [6].

Among the lead-free titanate-based materials, barium and strontium titanates ($BaTiO_3$ and $SrTiO_3$ (hereafter designated by STO), respectively), pure or modified, are of particular importance. $BaTiO_3$ is a classic ferroelectric material with applications as capacitors and positive temperature coefficient (PTC) resistors, among others [1]. $BaTiO_3$-based materials $BaO\text{-}Ln_2O_3\text{-}TiO_2$ (Ln = La or Nd) fit the requirements for applications, for example, in base stations for mobile communications [10] or in dielectric resonators for mobile phone handsets, where miniaturization is very important [11; 12].

On the other hand, STO is an incipient ferroelectric with high and tunable dielectric permittivity and low losses [13]. STO-based materials have been used, for example, as various grain boundary layer capacitors [14] and have potential applications in the field of tunable microwave devices [13] or for thermoelectric energy conversion [15].

Strontium titanate and two compositions from the $BaO\text{-}Ln_2O_3\text{-}TiO_2$ (Ln = La or Nd) system, namely $BaLa_4Ti_4O_{15}$ (BLT) and $Ba_{4.5}Nd_9Ti_{18}O_{54}$ (BNT), are investigated in this work. The first material is a classic example of the cubic perovskite structure and is

tolerant to some extent to stoichiometry variations [16]. In the second case, the materials have perovskite-related structures (hexagonal (BLT) [17] and orthorhombic (BNT) [18]) with anisometry in the lattice parameters. These intrinsic characteristics have a strong influence on the microstructure development during sintering, which may be particularly enhanced when substrate constraint is present [19]. On the other hand, the final properties of electroceramics are usually very dependent on the microstructure [1] which is, therefore, fundamental in establishing the utility and value of the material. A deep knowledge and understanding of the several intrinsic and extrinsic variables interplaying along materials processing is thus essential in order to create value-added materials with optimal properties for intended applications.

Among the most relevant factors in microstructure evolution and final dielectric properties of electroceramics are the characteristics of the grain boundaries. For example, their mobility is determinant in the grain growth behaviour of the material. Additionally, the electrical characteristics of grain boundaries, rather than those of the grain interiors, are the basis of several applications (such as grain boundary layer capacitors [14]).

In summary, there is a multibillion dollar market for electroceramics in microelectronic and communications industry. Dielectric materials with high relative permittivity, low dielectric losses and temperature stability are required for those applications. BaO-Ln_2O_3-TiO_2 (Ln = La or Nd) system materials meet those requirements. STO has potential applications in tunable microwave devices and as thermoelectric material. There is a need for miniaturization and cost reduction and thick film technology is an adequate processing approach. Several factors strongly affect the microstructure evolution during sintering of electroceramics, which is determinant in their dielectric response. If properly understood these factors may be intentionally used to design the microstructure of electroceramics and therefore to tailor their dielectric properties.

1.2 Organization of the thesis

The thesis is organized as follows:

Chapter 2 provides a general review of the state of the art. An overview of sintering theory is presented, including the case in which the sintering body is constrained by a substrate (constrained sintering). Some emphasis is also given to grain boundary related phenomena. Chapter 2 also includes a general description of the materials investigated in this work (strontium titanate and BaO-Ln_2O_3-TiO_2 (Ln = La or Nd)). Special attention is paid to the dielectric properties and applications, as well as to their relation to the materials structure and to microstructure development during sintering. The chapter ends with the statement of the objectives of the work.

Chapter 3 is devoted to the presentation of the experimental techniques and procedures used in the course of this work. A brief description of Electrophoretic Deposition (EPD) and Impedance Spectroscopy (IS) techniques is provided.

Chapter 4 presents the experimental results regarding strontium titanate. The effect of nonstoichiometry on the grain growth and dielectric properties of the material is assessed. A grain growth anomaly and its relation with the dielectric response are also investigated in a Ti-rich STO composition. Finally, the EPD of STO compositions is addressed and some results on the constrained sintering of EPD thick films on Pt-foil substrates are reported and discussed.

Chapter 5 contains the experimental results concerning the constrained sintering of BaO-Ln_2O_3-TiO_2 (Ln = La or Nd)) compositions. Particular attention is given to the effect of the substrate on the anisotropic microstructure development during constrained sintering of EPD thick films. The evolution of pore and grain anisotropy, as well as of the crystallographic texture, along densification under the effect of the substrate are investigated and correlated to the dielectric response of the materials.

Finally, in Chapter 6, the general conclusions are drawn. The present contributions are discussed and new questions are raised, which are proposed as future work.

2 State of the Art

2.1 Free and constrained sintering

2.1.1 Overview of sintering theory

Sintering is the processing step of consolidation of inorganic powder compacts by the use of thermal energy [20-22]. Extensive reference texts on this broad topic are available in the literature [20-23]. During the sintering process, a powder compact is heated to a suitable temperature below the melting point at which the mass transport mechanisms are operative, resulting in densification and coarsening of the microstructure.

During sintering, changes in several properties of the compact, such as mechanical strength, electrical resistance or thermal conductivity, among others, occur. In this sense, the understanding and control of this complex processing step is of vital importance to obtain tailored materials with desired useful properties.

The origin of sintering dates back to the prehistoric era with the firing of pottery. In ancient times, ceramics were important for their function as well as a means of expression and status. Nowadays, its importance is more related to the technological applications and commercial use of sintered materials as components in complex engineering structures. Indeed, sintering encountered a wide range of applications, from bulk ceramic components to complex layered structure for microelectronic components. However, sintering was only fundamentally and scientifically studied after the 1940s and since then remarkable progresses have been made.

From a scientific viewpoint the goal has been to establish the driving force, the mechanism of mass transport and the kinetics of the sintering processes. Theoretical models for ideal arrangements of particles have been developed. In the last few years a more technological approach has been applied. Factors that influence processing times and temperatures have been studied with the aim of decreasing the costs of the possible processing routes. On the other hand, variables that influence the

microstructure and properties of the final product are also important in order to obtain the most suitable material for the desired use.

Sintering occurs over a range of temperatures, but is accelerated as the particles approach their melting range. It takes place faster as the particle size decreases, since diffusion distances are shorter and curvature stresses are larger [23]. The transport mechanisms will depend on the type of material being sintered. Amorphous materials generally sinter by viscous flow [24]. On the other hand, polycrystalline materials sinter by one or more mechanisms occurring singly or in parallel, depending on the materials system and sintering conditions [22]. This makes it difficult to isolate the mechanisms involved and adds to the complexity of the sintering process. In general, bulk transport mechanisms such as volume diffusion, grain boundary diffusion, plastic flow and viscous flow result in shrinkage or densification while surface transport does not [21; 22].

The driving force for sintering is the reduction in the free energy of the system [25] through the reduction of its internal surface areas, leading to a minimal energy state. This occurs via densification and coarsening [25-27], the basic phenomena of sintering [21; 25], whose combined effects determine the microstructural evolution of the compact. By densification in solid state sintering, a gas-solid interface is replaced by a lower energy solid-solid interface (grain boundary), whereas by means of coarsening a reduction in the extent of free surface and of specific grain boundary area is achieved by conversion of many small pores and grains into fewer larger ones.

Sintering processes can generally be divided into three types: solid state sintering, liquid phase sintering and viscous sintering [21; 25]. Solid state sintering occurs when the powder compact is densified wholly in the solid state at the sintering temperature. On the other hand, liquid phase sintering occurs when a liquid phase is present during sintering, but the liquid is not enough to fill the porosity after the rearrangement process. In general, liquid phase sintering allows a reduction in the process cost but usually results in a degradation of some properties, for example, mechanical behaviour [21; 25]. By its turn, viscous sintering occurs when the heat treatment produces enough liquid so that the full densification of the compact can be achieved by a viscous flow of grain–liquid mixture [21; 22].

Solid state sintering has received the greatest amount of attention because it has a strong impact in the production of technical ceramics and it is easier to model than the other types of sintering. Most of the sintering models were developed for solid state sintering and are usually divided into three overlapping stages: initial, intermediate and final [21; 25], as depicted in Figure 2.1-1. The initial stage is characterized by the formation of necks between adjacent particles and its contribution to the compact linear shrinkage is limited to 2-3%.

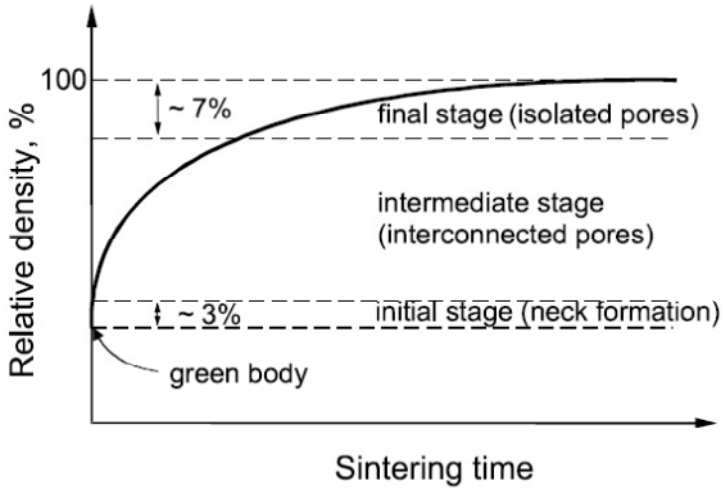

Figure 2.1-1: Typical densification curve of a powder compact showing the three stages of solid state sintering (initial, intermediate and final) [21].

As sintering proceeds, the growing necks merge and the intermediate stage begins. At this stage the porous phase is continuous and intersected by grain boundaries [28]. Figure 2.1-2 (a) shows the channel pore model proposed by Coble [28] for intermediate sintering stage, based on tetrakaidecahedral grains with cylinder-shaped pores along all of the grain edges. Grain boundary migration, or grain growth, becomes more important when the porosity is sufficiently low. Pores coalescence and local redistribution of material from regions of convex curvature to regions of concave curvature take place. Most of the densification occurs in the intermediate stage (up to ≈ 93% of the theoretical density) before the breaking up of the pore channels into

isolated pores, Figure 2.1-2 (b), in the beginning of the final stage that leads the sintering body to the final densification. The pores may remain on grain boundaries, and theoretically disappear after a heat treatment sufficiently long, or alternatively, they can become isolated from the grain boundaries and remain trapped inside the grains. With the reduction of the pore fraction, most of the grain growth occurs in the final stage.

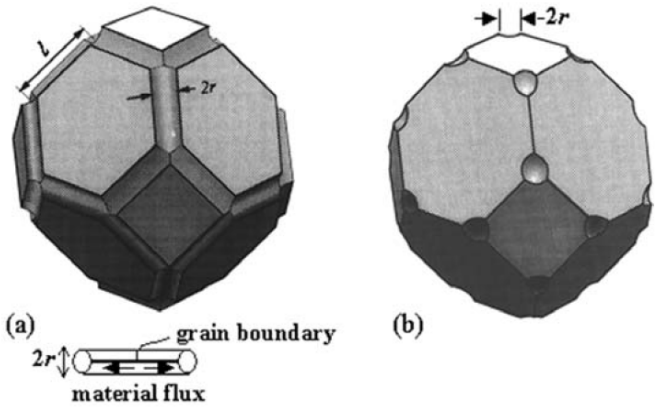

Figure 2.1-2: Coble's geometrical models for (a) intermediate and (b) final stages of sintering [21; 28].

Unlike solid state sintering, liquid phase sintering involves conditions where solid grains coexist with a wetting liquid during the sintering cycle [23]. Several ceramic products such as abrasives, capacitors and magnets have been fabricated in the presence of a liquid phase during sintering [29]. Figure 2.1-3 compares the two types of sintering. Liquid phase sintering was first modelled by Kingery in 1959 [30].

The microstructure change during liquid phase sintering is faster than in solid state sintering because of fast material transport through the liquid. Usually liquid phase sintering involves enhanced densification rates and accelerated grain growth [22; 23]. Three steps that occur in the densification process are shown in Figure 2.1-4: rearrangement, solution-precipitation and coarsening [21; 22; 29].

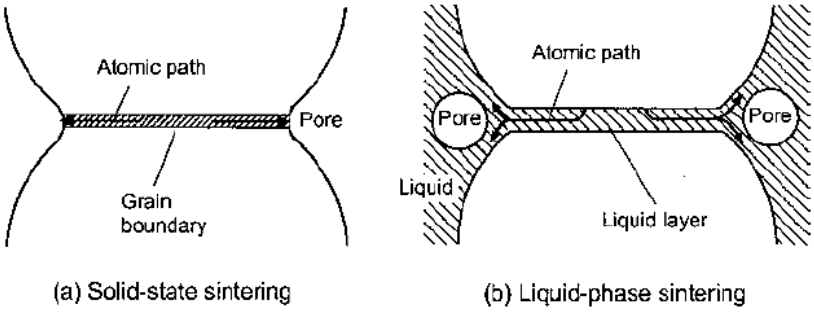

Figure 2.1-3: Schematics of a two-sphere model comparing (a) solid-state sintering and (b) liquid-phase sintering [22], where a liquid layer is present between the grains.

The driving force for densification by rearrangement is the capillary pressure of the liquid phase located between the fine solid particles when the liquid phase wets the solid particles [23]. Each inter-particle space becomes a capillary in which a substantial capillary pressure is developed. The activity at the contact points is increased and this provides a driving force for transferring material in such a way that the particle centres can move together and the density increases.

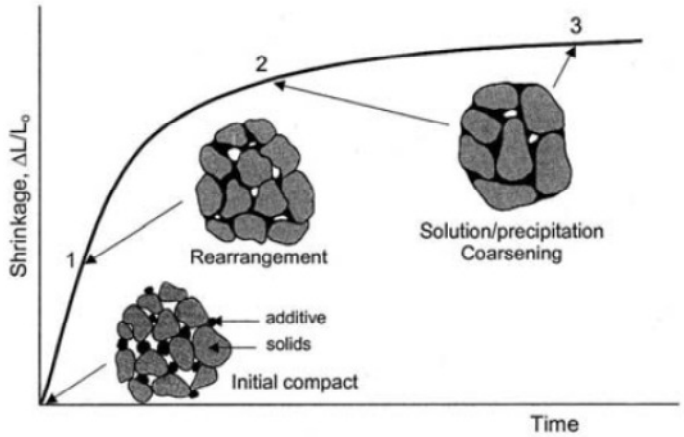

Figure 2.1-4: Schematic evolution of a powder compact during liquid phase sintering illustrating the three processes that take place: rearrangement, solution-precipitation and coarsening [22].

The magnitude of the capillary effect depends on the amount of liquid, particle size and contact angle between liquid and solid [31]. The contact angle is altered by factors that change solubility or surface chemistry. Liquid spreading on the solid replaces solid–vapour interfaces with liquid–solid and liquid–vapour interfaces. The solid–liquid dihedral angle is observed where a grain boundary intercepts the liquid phase, as illustrated in Figure 2.1-5 (a).

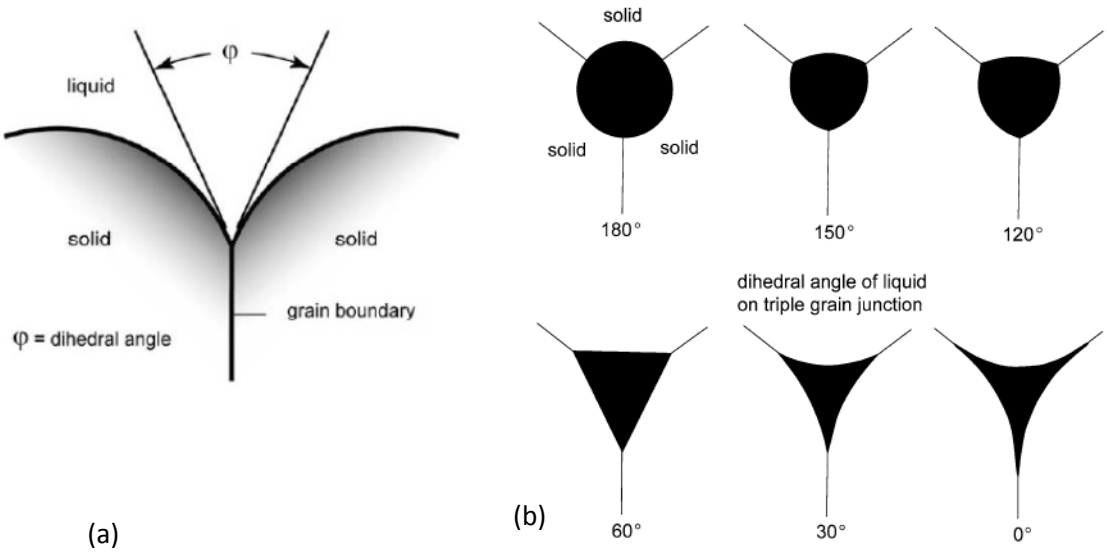

Figure 2.1-5: (a) Dihedral angle for a solid-liquid system and (b) shape dependence on the dihedral angle of the liquid pocket in the triple points [23].

The dihedral angle is a function of the ratio of the liquid interfacial energies. If the ratio of the solid–solid to solid–liquid surface energy is relatively high, then the dihedral angle approaches 0˚ and liquid separates contacting grains, wetting the grain boundaries [21; 23]. At low liquid contents, the liquid forms pockets at the triple points where three grains meet. The shape of that liquid pockets depends on the dihedral angle, as shown in Figure 2.1-5 (b). Low dihedral angles, and therefore increased solid-liquid contact, promote densification in liquid phase sintering [21].

Due to the fact that the grain boundaries are wetted by the liquid present during sintering, liquid phase sintering can be used to design grain boundary properties. The

fraction and distribution of the liquid phase and of the resulting solidified phases produced on cooling after densification is critical to achieve the required properties of the sintered material. Commonly, the amount of liquid formed during sintering is small, typically less than a few volume percent, which can make precise control of the liquid composition difficult.

2.1.2 Grain growth, grain boundary faceting and complexions

On heating, polycrystalline microstructures spontaneously coarsen. Microstructure coarsening, or grain growth, is indeed an important part of the sintering process and has a vital influence on the microstructure development of a sintering body. It increases the diffusion distances for matter transport during sintering and, in this way, reduces the densification rate [22]. Therefore, controlling grain growth is fundamental to achieve high density. Additionally, many technologically interesting properties of materials are very dependent on grain size. Hence, in order to obtain desired properties with optimized performance, a deep understanding of grain growth complex processes is of paramount importance.

Grain growth may be divided into two main types: normal and abnormal. Normal grain growth is characterized by a simple and invariable distribution of relative grain sizes with annealing time, while abnormal grain growth, which occurs by the formation of some exceptionally large grains in a matrix of fine grains, shows a bimodal grain size distribution [21].

Grain growth is intimately related to grain boundary mobility [32] that varies immensely from material to material. Interfaces and the movement of atoms within an interface play a crucial role in determining the processing and properties of materials. Mass transport parallel to grain boundaries during sintering can dominate densification, while transport perpendicular to (across) grain boundaries leads to grain boundary migration and grain growth [26].

Grain boundaries are defective regions that have an excess free energy per unit area. This is evident by the fact that during most thermal and chemical etching processes,

after polishing, material near the grain boundary is preferentially removed, revealing the grain boundary network of the polycrystalline material [33]. The driving force for grain growth is then the reduction of total grain boundary area by transport of material across the grain boundary under pressure gradient provided by the grain boundary curvature [26]. This driving force may be opposed by a drag force on the boundary. This drag or retarding force can have several different components: intrinsic drag from diffusion rate limitations, drag from solutes, which segregate to and interact with the boundary, and drag from pores or precipitates [21; 22]. In this way, the rate of grain boundary motion is sensitive to a large number of thermal, chemical and microstructural variables. Some of them are the crystal structure, the nature of bonding, orientation, stoichiometry, composition or the presence of a liquid phase [34].

The nature of interfaces in solids is highly complex. They may present a vast multiplicity of characteristics, which strongly affect transport kinetics. As examples, grain boundaries can be rough or faceted, clean or with high solute adsorption, have pre-melted films or altered crystallographic symmetry. These features can be used to distinguish one grain boundary from another [35].

Several theories and concepts have been developed for the study of grain boundaries. One of the important concepts to categorize and understand the grain boundaries is grain boundary misorientation, which consists in a rotation about a common axis of one lattice in relation to the other [36]. Low misorientation angles can be accommodated by dislocations [33], as illustrated in Figure 2.1-6. As the lattice misorientation is approximately proportional to the number of dislocations, the grain boundary energy and misorientation are linearly proportional [33].

Particularly at small misorientations, the simplest types of grain boundaries are described as tilt boundaries, in which the misorientation is a slight rotation about an axis lying in the boundary plane, or as twist boundaries, in which the rotation axis is normal to the boundary plane [37]. Tilt boundaries include a single array of edgy dislocations in which the Burgers vector (which represents the magnitude and direction of the lattice distortion associated with a dislocation [38]) is at a large angle to the boundary plane. Twist boundaries on the other hand require at least two sets of

screw dislocations, whose Burger vectors lie in the boundary plane, to accomplish the rotation [37]. However, naturally occurring low angle boundaries are rarely pure tilt or twist boundaries and the rotation may be about more than one axis; the boundary is then referred to as a mixed boundary [36].

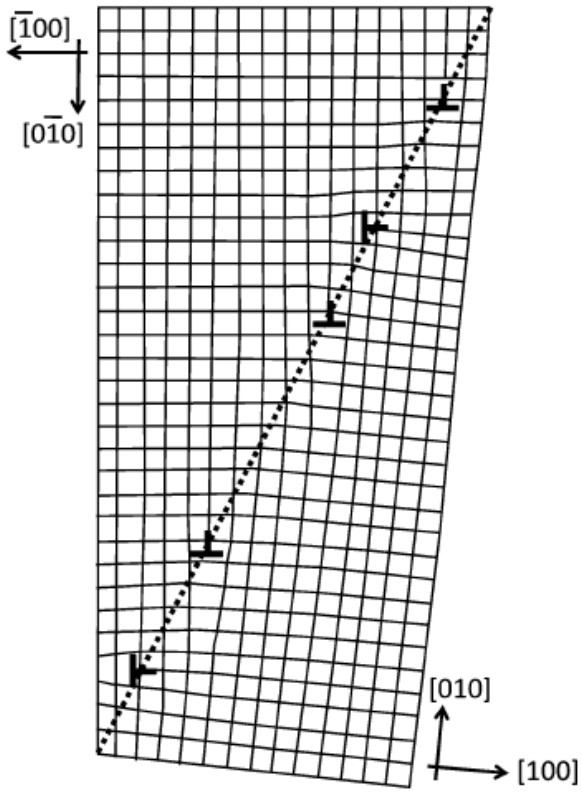

Figure 2.1-6: Schematic of a low angle grain boundary comprised to two types of edge dislocations. The lattice for the crystal to the right of the dashed line (the grain boundary) is rotated with respect to the crystal on the left [33].

For misorientation angles above 15˚ the grain boundaries are called high angle grain boundaries and cannot be described as an array of lattice dislocations since at high misorientation the dislocation cores merge [39]. In comparison to low angle grain boundaries, high angle boundaries are considerably more disordered, consisting of regions of good atomic fit separated by regions of poor atomic fit [37; 40]. In this regime, atomic fit is often significantly better at certain crystal misorientations and positions of

the boundary plane. Some grain boundaries, although high-angle, have a unique set of crystallographic relationships which result in exact coincidence site lattices (CSL) at the boundary plane [37].

CSL are indeed one of the most influential concepts in the study of grain boundaries during the past several decades. CSL misorientations are named by the inverse of the number of coincident sites [33; 37; 39]. A quantity Σ is defined as the inverse of the fraction of individual-lattice sites, which are common to the two adjoining grains associated with CSL points. For example, if one-third of the sites are in coincidence this is known as a Σ3 boundary. Two simple coincidence lattices are illustrated in two dimensions in Figure 2.1-7. Both are formed by a 36.9° rotation, in one case about an axis normal to the boundary (Figure 2.1-7 (a)) and in the other about an axis lying in the boundary (Figure 2.1-7 (b)). In both cases one lattice point in five superimposes (Σ = 5).

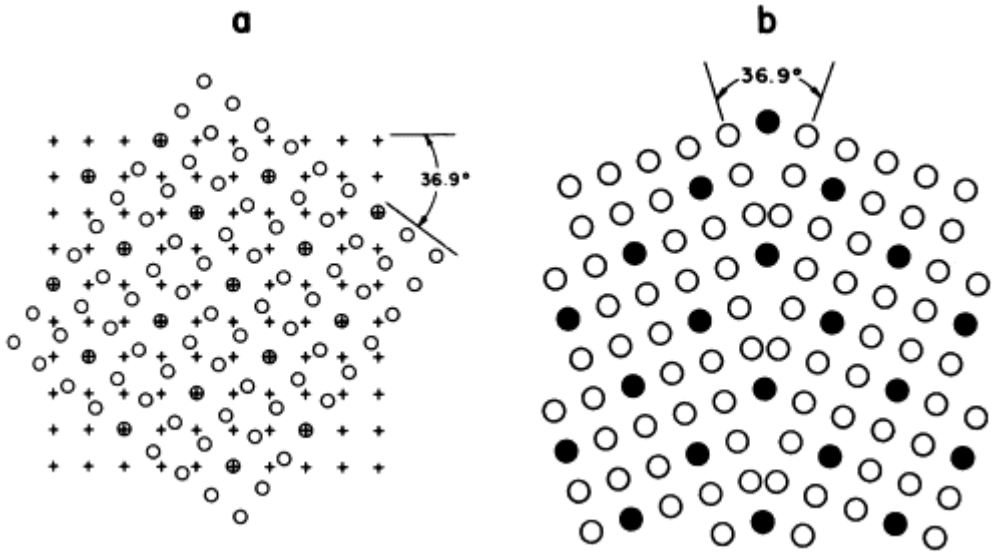

Figure 2.1-7: Schematic illustration of the coincidence lattice formed by a 36.9° rotation of two simple cubic lattices about an axis normal to the plane of the figure. In (a) the boundary lies between the superimposed lattices (twist boundary); in (b), the boundary is normal to the figure and includes the rotation axis (tilt boundary) [37].

Low-angle boundaries, where the distortion is entirely accommodated by dislocations, are Σ1. A boundary with high Σ may be expected to have a higher energy than one with low Σ, in which more lattice sites coincide (good atomic fit) [40; 41]. At CSL misorientations, grain boundaries have a perfect periodic structure. Coincidence grain boundaries also tend to facet [39]. In other words, a curved grain boundary breaks into an array of flat segments. These segments are usually parallel to the densely packed planes in the CSL [39].

The relation of this complex framework of grain boundary characteristics and related atomic transport mechanisms with material properties has interested researchers for a long time. For example, the structure of grain boundaries and its relation to microstructure development and dielectric properties has been a very active field of research [42-50]. Grain boundaries may be atomically ordered (faceted) or atomically disordered (rough) [51; 52], as illustrated in Figure 2.1-8. This structure was reported to be dependent on several factors like stoichiometry, sintering temperature or sintering atmosphere [47; 48; 53].

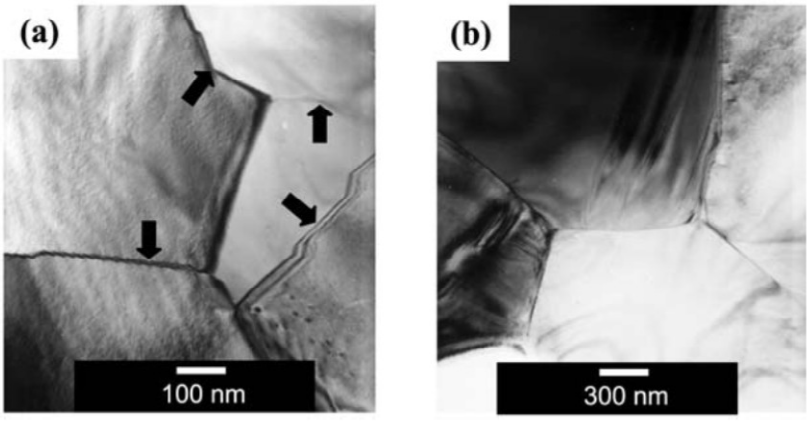

Figure 2.1-8: (a) faceted and (b) rough boundaries observed in 0.1 mol% TiO_2-excess $BaTiO_3$ [53]. Arrows indicate faceted boundaries.

In a material, grain boundary energy is often anisotropic [33]. In this context, faceting appears as a consequence of the crystallographic anisotropy of the grain boundary

energy. The formation of a grain boundary facet is usually due to a low grain boundary energy for the specific facet inclination [43] and the transition to rough grain boundary structures can be achieved for example by increasing anion or cation vacancies in those regions, for instances by the effect of temperature or of a reducing atmosphere [45].

The grain boundary structure is an important factor in determining the grain boundary mobility and consequently the grain growth behaviour of a material [43; 47; 52]. Indeed, large effects of the grain boundary structure on grain growth during sintering have been reported. In correlation with faceting-roughening transitions of the grain boundaries, different regimens from abnormal grain growth to stagnant grain growth were found to occur [45; 47; 51; 53]. Normal grain growth usually occurs in materials with rough boundaries, while abnormal grain growth is often observed in materials with faceted boundaries [47].

Additionally, Lee *et al* [53] suggested that the twin-assisted abnormal growth of $BaTiO_3$ grains can occur only when the grain boundaries are faceted. Yoon and co-workers [44; 54; 55] exploited the relationship between interface structure and grain growth behaviour and suggested that some selective grains can grow abnormally fast by two-dimensional nucleation and growth process when the interfaces are atomically flat. The abnormal grain growth behaviour for faceted boundaries has been explained in terms of the non-linear mobility of a facet with driving force [47; 48; 56].

Along with these effects on the microstructure, a relation of the grain boundary structure, faceted or rough, with the electrical properties has also been observed. Lee *et al.* [49] reported that, after annealing a STO bicrystal in air at 1600 ˚C, a roughening transition occurred at the grain boundary and a semicircle attributed to the grain boundary impedance response, not presented below 1600 ˚C when the grain boundary was faceted, appeared in the impedance spectra. These experimental observations highlight the importance of understanding grain boundary phenomena and the relation with grain growth and dielectric properties of materials.

Further developments in enlightening the grain boundary phenomena and their effect on grain growth processes were made by Harmer and co-workers [35; 50; 57]. Through

intensive grain growth studies in alumina doped with silica [58] or calcia [59], the researchers identified six different types of kinetic behaviour, each of them associated with a grain boundary structure or "phase", which was called complexion [35]. According to the authors, an interface complexion can be considered as a separate phase, which can be made to transform into different complexions with different properties by altering the chemistry and heat treatment. The authors suggested an extension of the Gibbs definition of phase to interfacial features. The difference from traditional bulk phases is that complexions and their associated thermodynamic properties cannot be separated from their adjacent bulk phases. In this sense, two different boundaries having the same complexion will have similar characteristic equilibrium thermodynamic quantities [60], such as a characteristic solute profile, a crystallographic reconstruction, a common disorder parameter or interfacial film width, but not necessarily the same exact atomistic structure.

This new approach was presented as a new unifying concept in materials science, a new framework for kinetic engineering in materials, by utilizing transitions of interface complexions, which produce discontinuous changes in interface transport properties [35; 57; 61]. Figure 2.1-9 shows TEM images of the different complexion types I-VI identified by Dillon *et al.* [35; 58; 59] in alumina and later designated by Dillon-Harmer complexions [62]; Figure 2.1-10 depicts the corresponding schematics. Complexion I is related to sub-monolayer adsorption in the boundary core of dopant cations that results in solute drag. The second one, complexion II, shows no segregation, is a ''clean'' grain boundary of undoped alumina. Complexion III consists in bilayer adsorption that enhances grain boundary mobility relative to undoped alumina. The forth complexion, complexion IV, contains a disordered layer that is associated with multilayer adsorption. The mobility of these grain boundaries are about an order of magnitude faster than clean grain boundaries. The fifth type, complexion V, is associated with a thin equilibrium thickness amorphous intergranular film, often referred as intergranular glassy film (IGF). This interface has typical grain boundary mobilities that are a factor of 50 faster than those for normal grain growth in undoped alumina.

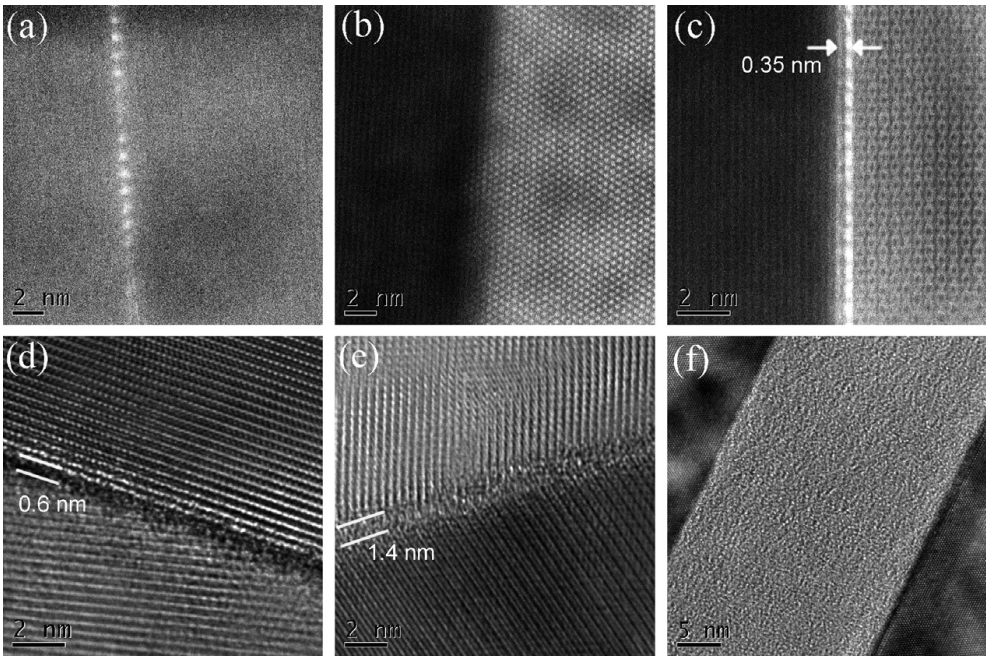

Figure 2.1-9: HRTEM micrographs showing the different types of Dillon-Harmer grain boundary complexions found in alumina (a) complexion I, (b) complexion II, (c) complexion III, (d) complexion IV, (e) complexion V and (f) complexion VI [35].

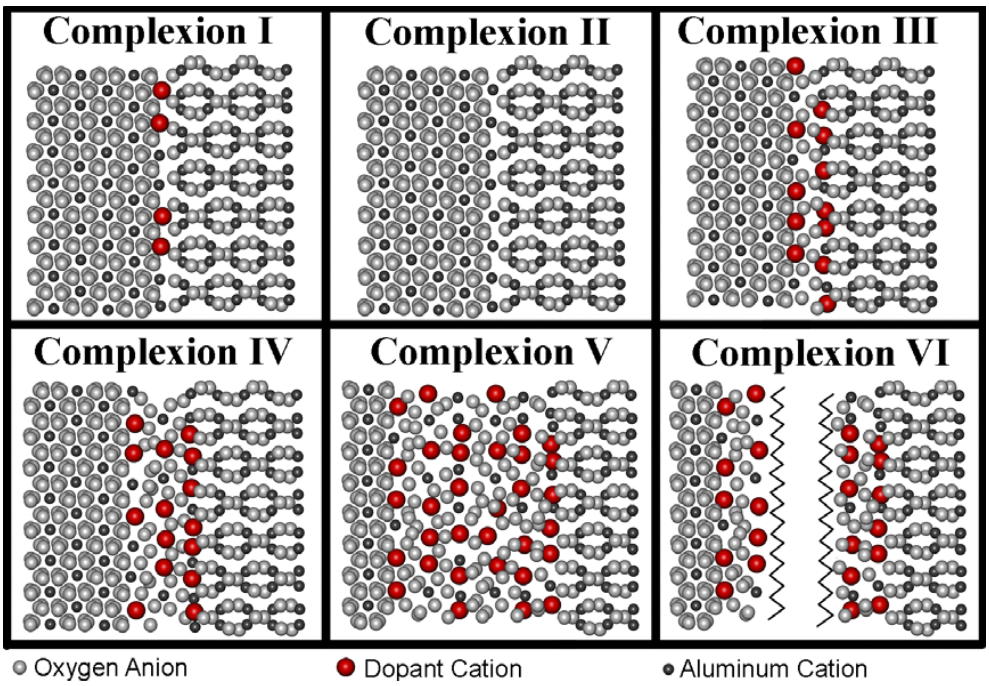

Figure 2.1-10: Schematics of the six different types of Dillon-Harmer complexions found in alumina [35].

Finally, complexion VI, the sixth type of segregation behaviour, is associated with a wetting grain boundary film. This complexion has a mobility that is over two orders of magnitude larger than that of undoped alumina [35; 50; 58; 59].

The grain boundary mobility increases with increasing disorder within the core of the grain boundary, from complexion I to complexion VI [59]. Each grain boundary complexion has a different level of disorder that originates characteristic transport rate and grain boundary mobility. Additionally, Dillon *et al*. reported a general trend towards increasing grain boundary disorder and increasing grain boundary mobility with increasing temperature, originated from transitions between the complexions [59]. The number of complexion transitions that occur increases linearly with grain size (due to grain boundary solute excess concentration) and exponentially with temperature, although the number of transitions occurring in a typical microstructure is usually low [50; 58; 59]. Both the distribution of chemical species in the grain boundaries and the distribution of grain boundary energies, due to anisotropy, are important in predicting which grain boundaries undergo a disordering complexion transition, which is most likely to occur in high-energy grain boundaries [60]. Higher-energy grain boundaries are also preferentially eliminated during grain growth [63].

The coexistence of two or more different complexions at a single temperature, which is possible due to the dependence of grain boundary complexion on chemistry, temperature and crystallography, was proposed as an explanation for the origin of abnormal grain growth [35].

The formation of these complexions was interpreted from the interplay of grain boundary premelting, prewetting and multilayer adsorption [62]. In the original definitions, premelting refers to structural (order–disorder) transitions in unary systems [64] and prewetting refers to adsorption transitions in binary de-mixed liquids [65]. In other words, prewetting refers to a wetting transition occurring when the phase that does the wetting is not yet stable [65; 66]. Premelting, also called “surface melting” [67], is the stabilization of quasi-liquid interfacial layers below the bulk melting temperature in a single phase system [64; 66; 67]. In binary and multicomponent systems, ‘‘premelting-like” films can be stabilized at grain boundaries over wider ranges of

undercoolings, because grain boundary structural disorder can be promoted by solute adsorption [68; 69]. Impurities have also been reported to change equilibrium dihedral angle and increase significantly the penetration length of liquids in polycrystalline materials [70].

As exemplified in Figure 2.1-11, enhanced mass transport related to the formation of these films has been considered the origin of activated sintering below the eutectic temperatures [69; 71]. Luo and co-workers [62; 72-74] have developed a quantitative analytical model to predict the thermodynamic stabilization of IGFs in metal binary alloys as a function of the bulk chemical potentials and temperature. The predictions may be superimposed on a phase diagram as illustrated in Figure 2.1-11 for the case of the W-Co system [72].

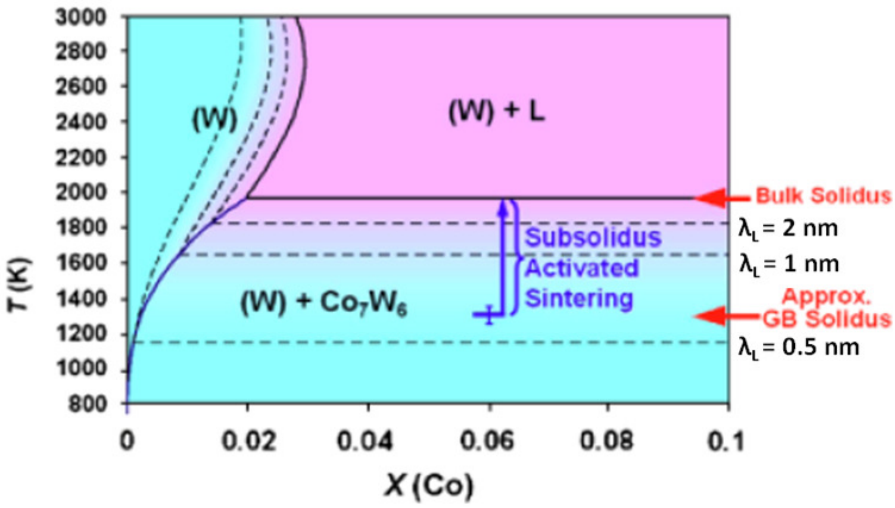

Figure 2.1-11: Computed model predictions of thermodynamic stabilization of IGFs in the tungsten-rich side of the W-Co bulk phase diagram. Subsolidus activated sintering is shown by the dotted lines in the diagram. λ_L is a figure of merit that represents the tendency for the intergranular film formation that scales with the thickness. At a constant temperature, λ_L is constant in the two-phase region and decreases with decreasing dopant concentration in the single-phase region [61; 72].

The results of Dillon *et al*. in alumina [35; 58; 59] show that grain boundaries wetted by an IGF have higher mobility than dry grain boundaries, as just discussed. However, Yoon *et al.* [75] studied the effect of an IGF on grain growth behaviour using $BaTiO_3$ as a model system and claimed that the intrinsic mobility of a dry boundary is higher than that of a wet boundary. According to the authors, the reason for abnormal grain growth previously observed in several systems with wet boundaries is a reduction of the critical driving force for appreciable grain growth in the presence of the films and not the higher mobility of amorphous films compared to dry boundaries [75].

This example shows that a great deal of research still needs to be performed to fully understand interface complexions and their relation with grain growth kinetics and, for instances, dielectric properties of materials. The next scientific challenge is the development of grain boundary complexion or phase diagrams, also containing faceting/defaceting transitions, which could allow the designing of materials through grain boundary or interfacial kinetic engineering [35; 61; 69]. Due to the facts that grain boundary complexion transitions cause abrupt changes in transport kinetics [35; 76] and materials properties and that they can often be retained on cooling [68], quantitative and predictive complexion diagrams are a crucial component for the tailoring of materials. These grain boundary diagrams would allow the use of the most appropriate grain boundary structures to achieve optimal microstructures. Additionally, would be possible to design heat treatment protocols to optimize grain boundary structures for the desired performance properties; finally, grain boundary diagrams would provide information for predicting high-temperature materials properties [69].

The issues addressed so far will be further discussed in following sections of this text, specifically regarding the materials studied in this work.

2.1.3 Constrained sintering

A few decades ago, the interest in structural ceramics and the need to develop improved materials brought new challenges for sintering science. The technological necessity to sinter composite materials arose, in order to produce ceramic matrix

composites with increased fracture toughness [77]. On the other hand, the rapidly growing microelectronic industry required the sintering of functional ceramic materials in complicated miniaturized patterns, such as thin and/or thick films or layered structures [78].

To meet these requirements for continuous miniaturization, one approach is the fabrication of dielectric films directly on metallic foils, which has the potential advantage of allowing device integration with reduced processing costs and space [79]. By depositing and densifying dielectric layers on noble or base metals foils, components can be embedded and integrated into polymer packages, saving space and allowing low cost circuit designs [80]. On the other hand, the ability to process ceramic films conformably on substrates opens up the possibility of innovative structures and designs [81].

These structures can be fabricated by depositing a ceramic powder layer on the top of a substrate using several deposition techniques [82] like tape casting, screen printing or electrophoretic deposition (EPD) [83]. Devices like multilayer co-fired ceramic packages may then be obtained, after a required sintering step [78]. The above cited developments produced added complexity for sintering theory, particularly when parts of a structure densify at different rates and temperatures than other parts (differential densification) or if the sintering is externally constrained (constrained densification) [84].

These situations are illustrated in Figure 2.1-12. In the sintering of composites (Figure 2.1-12 (a)), a porous matrix often densifies around a rigid second phase material, e.g. particles, whiskers, platelets or rods, which is placed under a compressive stress whereas the mean stress in the matrix is tensile [84].

Figure 2.1-12 (b) depicts the case of a ceramic film densifying by sintering on a rigid substrate. The sintering film will be placed in biaxial tension by the substrate, which is under a compensating compression state [84; 85]. In this case the densification can only occur in vertical direction (out of plane) [84; 86], as presented in Figure 2.1-13, which illustrates unconstrained and constrained densification. In layered structures that are co-fired (Figure 2.1-12 (c)), the layers will usually shrink at different rates and temperatures and the layers will constrain each other, again leading to internal

stresses [87]. As illustrated in Figure 2.1-12 (d), even in a single-phase material system internal stress may occur as a result of differential densification originated by inhomogeneous powder packing in the green bodies.

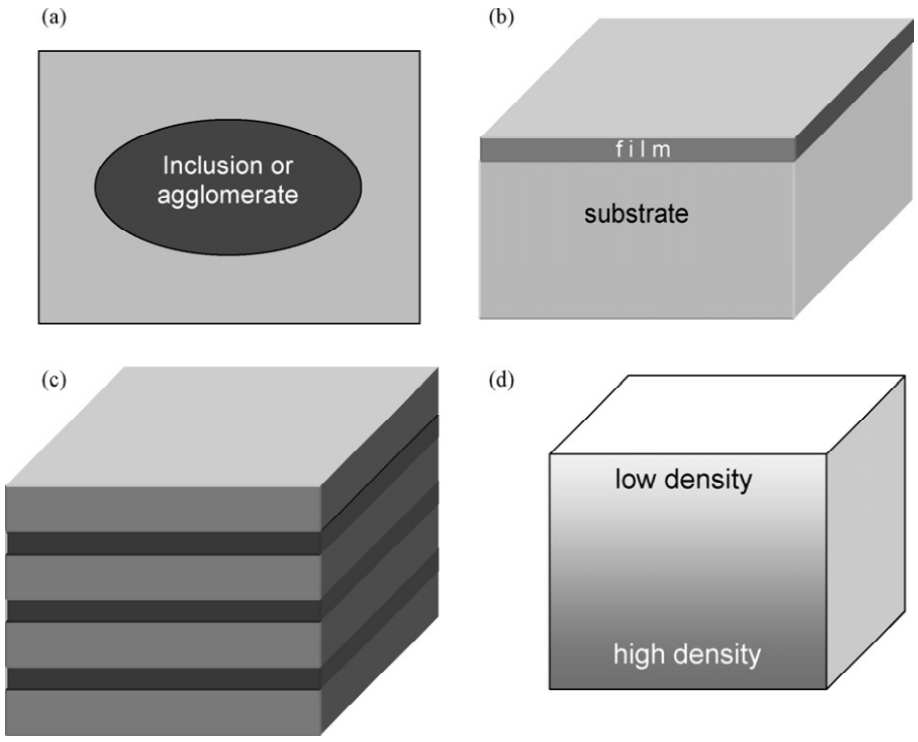

Figure 2.1-12: Schematic illustrations of structures that will undergo differential densification, originating internal stresses: (a) composite materials in which a porous matrix densifies around rigid inclusions, (b) a thin film densifying on a non-densifying substrate, (c) layered structures of two or more types of materials that densify at different rates, (d) a porous material that has density variations [84].

The internal stresses in the situations of Figure 2.1-12 have the potential to hinder densification or lead to defects and distortions in the sintered bodies [84; 88; 89]. Particularly, the stresses exerted by the substrate during constrained sintering of films have been found to retard the densification of powder compacts, leading to lower final densities and different microstructures [84; 90-93].

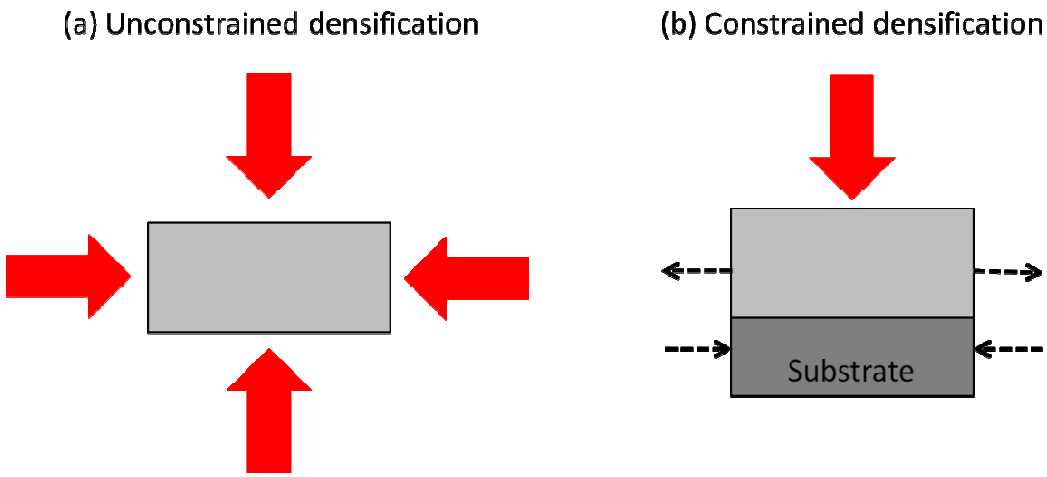

Figure 2.1-13: Schematic illustration of densification during (a) unconstrained (or free) sintering and (b) constrained sintering on a rigid substrate. In a free sintering body (a) densification may occur in all directions. Due to the substrate constraint in (b), densification can only occur in the vertical direction. The dashed arrows indicate the stress state of film (tensile) and substrate (compressive).

The presence of in-plane stresses and differential sintering rates can lead to camber and distortion [85; 89; 94] causing the production of defective components. Commonly observed defects in constrained sintered layers (Figure 2.1-14) also include high porosity, cracking or delamination at the film-substrate interface [84; 88; 89], which may cause obvious problems in manufacturing and degrade the reliability of devices.

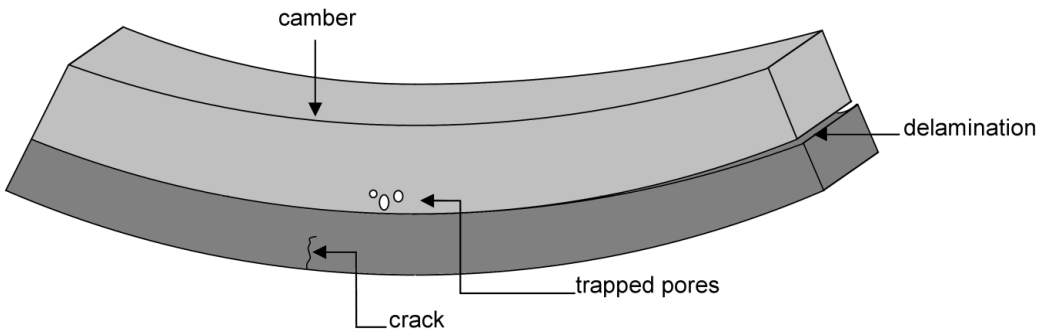

Figure 2.1-14: Schematic of the possible defects during constrained sintering of a film on top of a substrate [95].

The ability to predict and control the microstructural evolution during constrained sintering, as well as the development of ways to avoid or minimize defects, is of evident technological importance. Along with the stated technological demand, constrained sintering has been investigated since the 1980's. In addition to theoretical formulation [96-99] and comparison to experimental observations [86; 91; 100], finite element analyses [101; 102] or discrete element simulations [103] have been applied to the topic.

The focus has been mainly on the development of continuum mechanical models incorporating constitutive laws. These models use a viscous analogy [96-99] to relate strain rates to stresses and enable at least a qualitative description of the effect of mechanical stress or geometrical constraints on the shrinkage behaviour of sintering bodies. The isotropic formulation is well developed and significant progress has been made in using this approach to understand a variety of sintering problems including the densification of constrained films, multilayered systems, composites and pressure assisted densification. The subject was reviewed by Green *et al.* [84].

In the framework of continuum mechanical modelling, a sintering body subjected to an applied load was assumed to show an instantaneous elastic strain and a continuous deformation controlled by viscous flow or creep [104]. However, it was shown that the elastic response has only a negligible effect on the calculated stresses and strains and therefore, sintering bodies are considered as purely viscous [96]. This theory was originally developed for materials that sinter by viscous flow, but has also been applied to materials that densify by solid state diffusion [91; 98]. The continuum mechanical framework is based on the constitutive equations for an isotropic linear elastic solid, as follows.

A porous planar film (infinite in the in-plane dimensions) is considered, which is being sintered on a perfectly rigid substrate (Figure 2.1-15). Assuming a perfect interface (no sliding at the interface), the film can shrink significantly in the normal direction (3) but not in the planar directions (1, 2), due to the constraint from the substrate. This is expected to lead to the development of stresses in the film, specifically in the 1-2 plane in Figure 2.1-15 but not in the 3-direction.

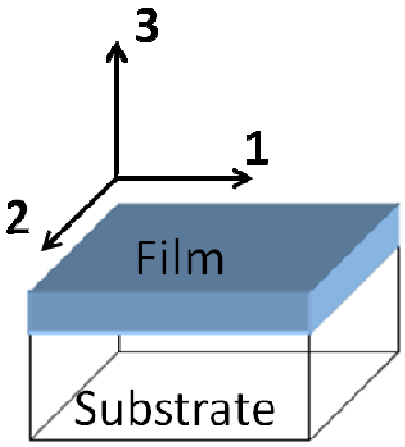

Figure 2.1-15: Schematic of a film on a substrate and coordinate axis.

Therefore, the compatibility and equilibrium conditions are the following, where $\dot{\varepsilon}_{s,i}$ and $\sigma_{s,i}$ are the strain rate and the stress, respectively, in the *i* direction.

$$\dot{\varepsilon}_{s,1} = \dot{\varepsilon}_{s,2} = 0 \qquad (2.1\text{-}1)$$

$$\sigma_{s,1} = \sigma_{s,2} = \sigma_s^{\infty} \qquad (2.1\text{-}2)$$

$$\sigma_{s,3} = 0 \qquad (2.1\text{-}3)$$

Using the viscous analogy [98; 99; 105], for an isotropic, linear viscous material, principal strain rates $(\dot{\varepsilon}_{s,1}, \dot{\varepsilon}_{s,2}, \dot{\varepsilon}_{s,1})$ are related to the principal stresses $(\sigma_{s,1}, \sigma_{s,2}, \sigma_{s,3})$ by constitutive relations of the type

$$\dot{\varepsilon}_{s,1}^{constr} = \dot{\varepsilon}_s^{free} + \left(\frac{1}{E^p}\right)\left[\sigma_{s,1} - \nu^p\left(\sigma_{s,2} + \sigma_{s,3}\right)\right] \qquad (2.1\text{-}4)$$

$$\dot{\varepsilon}_{s,2}^{constr} = \dot{\varepsilon}_s^{free} + \left(\frac{1}{E^p}\right)\left[\sigma_{s,2} - \nu^p\left(\sigma_{s,1} + \sigma_{s,3}\right)\right] \qquad (2.1\text{-}5)$$

$$\dot{\varepsilon}_{s,3}^{constr} = \dot{\varepsilon}_s^{free} + \left(\frac{1}{E^p}\right)\left[\sigma_{s,3} - \nu^p\left(\sigma_{s,1} + \sigma_{s,2}\right)\right] \qquad (2.1\text{-}6)$$

where $\dot{\varepsilon}_s^{free}$ is the intrinsic free sintering strain rate (that is sintering strain rate in the absence of external or internal stresses) and E^p and ν^p are, respectively, the uniaxial viscosity and the viscous Poisson's ratio of the porous sintering body. The sintering

parameters (E^p, ν^p and $\dot{\varepsilon}_s^{free}$) are functions of the microstructure and evolve during sintering. They are specific and characteristic of the porous ceramic body and can be determined, for example, by using discontinuous sinter-forging [106-108]. In this technique, a uniaxial stress is applied on a cylindrical sample during sintering and radial and axial strains are measured as a function of the applied stress.

Equations (2.1-4) to (2.1-6) are analogous to Hooke's Law for linear elastic, isotropic continuum media, with strain rate replacing strain and the addition of the intrinsic free sintering strain rate [84]. It should be noted that there is no identification of the three different stages of sintering as the equations remain the same for the entire process. From equations (2.1-4) to (2.1-6), the tensile in-plane stress and the densification rate of the film can be calculated to be [98]

$$\sigma_s^{\infty} = -\frac{E^p \dot{\varepsilon}_s^{free}}{1-\nu^p} \tag{2.1-7}$$

$$\dot{\varepsilon}_{s,3}^{constr} = \dot{\varepsilon}_s^{free}\left(\frac{1+\nu^p}{1-\nu^p}\right) \tag{2.1-8}$$

The in-plane stress σ_s^{∞} is tensile since $\dot{\varepsilon}_s^{free}$ is negative, E^p is positive and for isotropic bodies $0 \leq \nu^p \leq 0.5$ [96]. This stress develops in the material because of the constraint and is believed to be responsible for the camber that is observed to develop during the co-sintering process [94]. In equation (2.1-8), $\dot{\varepsilon}_{s,3}^{constr}$ is equal to the volumetric densification rate of the constrained film. The volumetric densification rate of the free or unconstrained sintering body is equal to $-3\dot{\varepsilon}_s^{free}$. Therefore, the relation between the two quantities is given by [105]:

$$\left(\frac{\dot{\rho}}{\rho}\right)^{constr} = \frac{(1+\nu^p)}{(1-\nu^p)}\frac{1}{3}\left(\frac{\dot{\rho}}{\rho}\right)^{free} \tag{2.1-9}$$

Assuming a perfect rigid substrate and similar isotropic microstructure for freely sintered and constrained films [109], it may be concluded from equation (2.1-9) that the predicted effect of the constraint is to reduce the densification rate of the constrained film (unless ν^p = 0.5). Moreover, the magnitude of this reduction depends on the viscous Poisson's ratio [110].

The reduction of the densification rate in constrained sintered films is indeed experimentally observed [85; 86; 93; 111; 112] (Figure 2.1-16). However, the effect of the substrate is usually underestimated by the isotropic model predictions. The isotropic assumptions are constantly challenged by discrepancies between experimental and modelled densification curves [86; 108]. As illustrated in Figure 2.1-16, the isotropic model overestimates the densification rate of constrained alumina films on single crystal sapphire substrates by almost a factor of two.

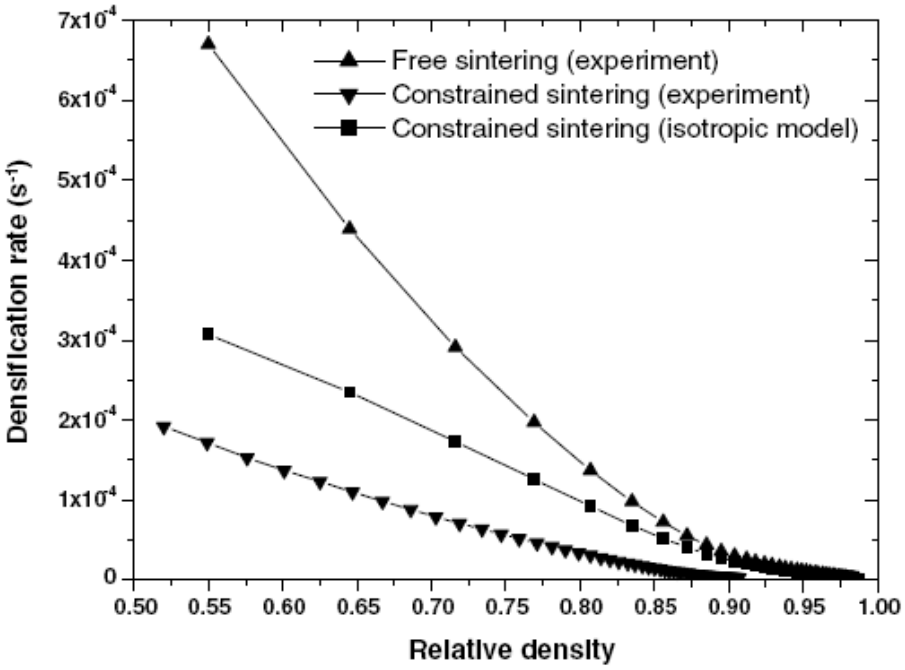

Figure 2.1-16: Comparison between experimental and theoretical densification rates of free and constrained alumina films on single crystal sapphire substrates as a function of density (assuming isotropic constitutive laws) [108]. The isotropic model overestimates the densification rate of the constrained films.

Despite the fact that little difference is usually found in the grain growth behaviour between constrained and free sintering [93; 112; 113], microstructural anisotropy clearly develops with density in constrained films, especially above 90% of relative density [112; 114]. As a result of the geometric constraint imposed by the substrate, densification is only allowed in the vertical direction and the preferred orientation of anisometric

pores or grains [112; 115], particle coordination numbers, neck sizes or pore separations [114] are commonly observed in constrained sintered films.

This anisotropic microstructural development was recently highlighted by quantification made on 2D cross-sections for different materials like alumina [112; 115], zirconia [116] or Low Temperature Co-fired Ceramic (LTCC) glass ceramic composites [85; 111]. Bernard *et al.* [109] used Synchrotron Computed Microtomography to obtain 3D images of glass films on rigid alumina substrates at different stages of sintering (relative densities of 64–98%). The glass films where isotropic in the initial stage and evolved towards anisotropy during sintering to finally become isotropic again at the end of the process. The end of this microstructure evolution was different from what has been observed for alumina layers sintered on alumina substrate [114], where the microstructure was anisotropic until the end of the sintering process. This difference was explained by the difference in the densification mechanism: films made of glass sinter by viscous flow whereas alumina sinters by solid-state diffusion at grain boundaries [109].

The development of anisotropic microstructures depends on the properties of the constraining substrate. It has recently been shown by Ollagnier *et al.* [85; 111] that a degree of geometrical constraint can be defined, depending on the thickness ratio between the sintering layer and the substrate as well as on the mechanical properties of the substrate. If the substrate deforms elastically, by viscous flow or creep mechanisms even at a very limited extent, the degree of constraint might be reduced. One example is the use of a flexible substrate such as platinum foil which can easily deform by creep at the sintering temperature [100].

This results in lower tensile stress acting in the sintering layer when compared with perfect constraining conditions [111; 116]. The microstructure strongly depends on this degree of constraint, as pore size increases when the film is more constrained, as observed for LTCC [85; 111]. When the film is fully constrained, large elongated pores oriented along the thickness direction develop [111; 112; 115], as illustrated in Figure 2.1-17.

Considering four particles, the probability of neck formation at the position 1 and 2 for a film freely sintered is the same, whereas, when the film is constrained, the neck

formation in position 1 is favoured to the neck formation in position 2 as the particles in the direction parallel to the substrate cannot approach each other [95].

Moreover, densification retardation and preferential pore orientation were found to be dependent on the film thickness, with two levels of geometrical constraint: a lower density and finer microstructure were observed close to the substrate, as compared to the centre of the layer [115]. The presence of this interface layer is suggested to result from hindered particle rearrangement [115].

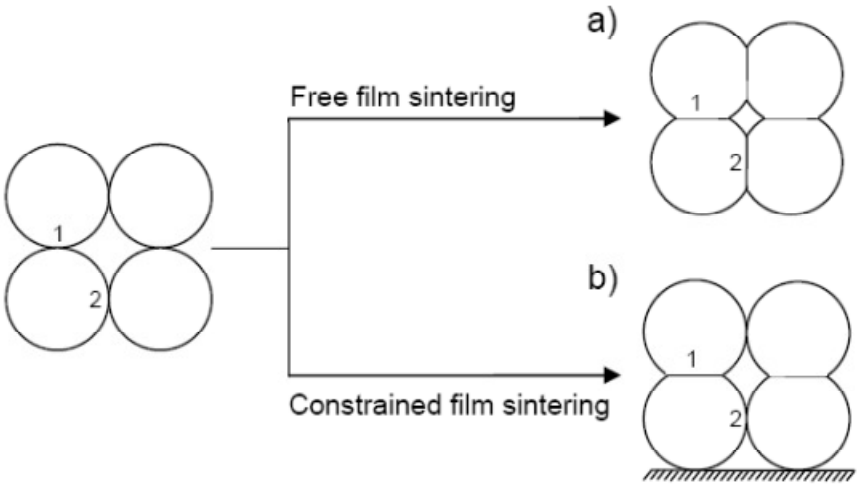

Figure 2.1-17: Schematic diagram of particle morphology of (a) free and (b) constrained polycrystalline films during sintering [95]. The constraint from the substrate leads to microstructural anisotropy development.

Once that the classical isotropic models assume that the microstructure of the constrained film is identical to that of the free film, the microstructural anisotropy developed during constrained sintering is considered to be the reason for divergences between isotropic model predictions of constrained sintering kinetics and experimental observations [86; 108]. Efforts have been made to develop more realistic models incorporating anisotropic constitutive laws. New continuum formulations have been proposed [108; 117] to take into account intrinsic (present from sample

manufacturing) and extrinsic anisotropy (developed due to sintering under external stresses or constrained sintering).

For example, if a transversely isotropic material is considered (plane 1-2 in Figure 2.1-15 is assumed to be isotropic since the in-plane deformation is constrained), the constrained normalized densification rate takes the form [108]:

$$\left(\frac{\dot{\rho}}{\rho}\right)^{constr} = \frac{\nu_{13}^{p}}{1-\nu_{12}^{p}}\left[\left(\frac{\dot{\rho}}{\rho}\right)^{free} + \dot{\varepsilon}_{s,3}^{free}\right] - \dot{\varepsilon}_{s,3}^{free} \qquad (2.1\text{-}10)$$

where the free strain rate $\left(\frac{\dot{\rho}}{\rho}\right)^{free}$ is equal to $-\left(2\dot{\varepsilon}_{s,1}^{free} + \dot{\varepsilon}_{s,3}^{free}\right)$. However, the anisotropic formulation leads to a considerably higher degree of complexity. The development and measurement of appropriate microstructural parameters to quantify anisotropic state of the microstructure are needed. In equation (2.1-10), two values for ν^{p} as well as the global free densification rate and the free strain rate in the thickness direction (direction 3) are required to predict the constrained densification rate.

A better understanding of the sintering behaviour of constrained films, as well as a more realistic and less complex anisotropic model formulation, is therefore necessary in order to optimize the design and manufacturing process of constrained sintered materials. Besides the fundamental scientific interest, this understanding has great technological and economical importance, once that constrained sintering is widely used in the microelectronics industry. Better and more practical prediction and control of the constrained sintering kinetics will then lead to higher production yields, lower costs and more reliable optimized devices.

Additionally, and not less important, the singularities of constrained sintering and its effects on microstructure development, if properly understood, can offer a new tool for microstructure engineering and tailoring of useful technological properties of functional materials. One good example is the work of Fu *et al.* [19], developed in the Electroceramics Group of CICECO at the University of Aveiro, who used the effect of the substrate on the microstructure development to tailor the dielectric properties of $BaNd_2Ti_5O_{14}$.

2.2 $BaO\text{-}Ln_2O_3\text{-}TiO_2$ (Ln = La or Nd)

2.2.1 Dielectric properties and applications of microwave dielectrics

Wireless communications have seen tremendous development in the recent age and became a key factor in modern society. A point was reached where, due to a shortage of the conventional radio frequency region, the usable frequency range has been extended towards millimetre waves [11; 118]. As a consequence, in the present communication systems, microelectronic devices working at such high frequencies are becoming increasingly important. Figure 2.2-1 shows the microwave spectrum and examples of related application fields in this frequency range, from mobile phones to radar or satellite communications.

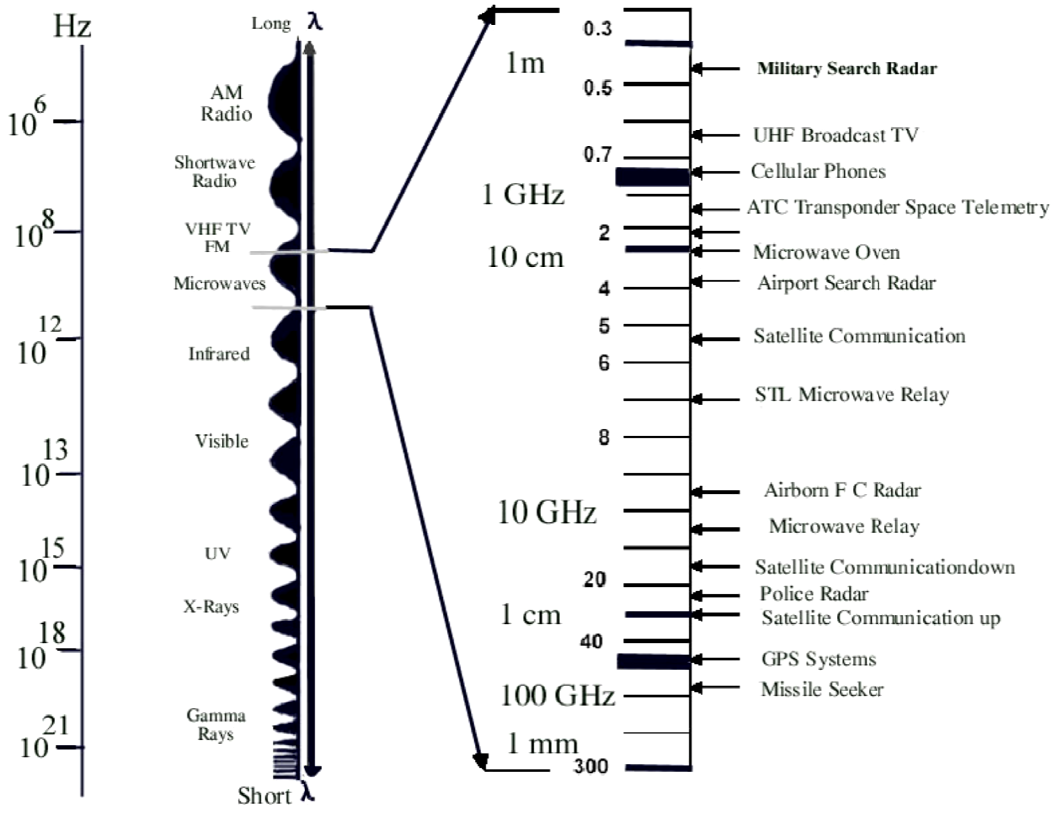

Figure 2.2-1: Microwave spectrum and applications [7].

In these applications, selectivity and stability are necessary to ensure that signals are confined to well defined frequency bands and to prevent the intrusion of unwanted signals which would interfere with the performance of the system. The need for compactness in satellite and hand-held mobile systems is self-evident [1]. In this sense, high relative permittivity (ε_r) ceramics had a very important role in the miniaturization and thus cost reduction of modern wireless communication systems [119] and there remains a great potential for further miniaturization and cost reduction.

Microwave dielectrics with low dielectric losses are of fundamental importance [120]. Low loss dielectric ceramics are in fact the basis of several key components in these systems. Dielectric low loss materials are being used to make a variety of components such as dielectric resonators (DR), filters, oscillators or antennas [11; 12; 119; 121-123].

Applications for these low loss microwave materials components include cellular phones, ultra high speed local area networks, GPS, military radar systems or direct broadcast satellites [1; 11; 12; 120; 121; 123]. Additional applications range from Intelligent Transport System (ITS), to security systems detectors or consumer electronic products [11; 12; 120]. Low loss dielectric ceramics are also used as the substrates for microstrip lines and coplanar waveguides for microwave and millimetre-wave integrated circuits. A microstrip antenna (or patch antenna) for the receivers of GPS, that use a high relative permittivity dielectric substrate has several advantages such as small size, narrow frequency band and good temperature stability [123].

There is a growing body of literature in this very active field of material science and technology research. Particularly, the book of Sebastian [7], published in 2008, offers a comprehensive review of the topic and presents an extensive database of microwave materials, properties and applications. A few examples are presented in the following text for contextualization of the present work.

For a material to be considered as candidate for microwave components, there are three critical requirements [1; 7; 11; 12]. First, the relative permittivity should be as large as possible, since the size of microwave dielectric components is inversely proportional to the square root of the relative permittivity. As an example, miniaturization of mobile hand-held phones is possible due to high permittivity materials, which allows the

decrease of the size of the resonators used in these devices while still maintaining a specific resonant frequency [121].

Second, the dielectric loss tangent (*tanδ*) should be as small as possible to ensure maximum signal discrimination. This is more commonly described in terms of the dielectric quality factor *Q* value (*Q* = 1/*tanδ*), which should be maximized. At microwave frequencies, according to the classical dispersion theory of dielectrics [124], the dielectric constant is unchanged whereas the dielectric loss increases with frequency. Therefore, the product *Q.f* (*f* is the frequency measured in GHz), which is assumed to be constant [1; 123], is often used when comparing microwave materials.

The third requirement has to do with temperature stability of the signal in communications systems. To ensure the essential temperature stability, the microwave dielectric components need to have a near-zero temperature coefficient of resonant frequency (τ_f), so that the signal does not drift during device operation due to temperature fluctuations attributed to the environment or circuit heating. τ_f is defined as follows:

$$\tau_f = \frac{\Delta f}{f_0} \cdot \frac{1}{\Delta T} \qquad (2.2\text{-}1)$$

where f_0 stands for the resonant frequency at ambient temperature, Δf for the frequency variation along the ΔT temperature range. It is self-evident that a material with a significantly non-zero τ_f is useless in microwave circuits as it cannot maintain its resonant frequency as the operating temperature changes.

τ_f is related to the temperature coefficient of relative permittivity $TC\varepsilon_r$ and the coefficient of thermal expansion (α) by the relation [1]:

$$\tau_f = -\left(\frac{TC\varepsilon_r}{2} - \alpha\right) \qquad (2.2\text{-}2)$$

It is also related to the temperature coefficient of capacitance (*TCC*) by the relation [1]:

$$\tau_f = -\frac{TCC - \alpha}{2} \qquad (2.2\text{-}3)$$

However, obtaining optimal values of these three important requirements simultaneously is difficult because high ε_r materials often possess a large τ_f and low Q [10]. Indeed, the trade-off between miniaturization, high permittivity, low losses and near-zero τ_f is a real issue in microwave materials research and development [121].

Microwave materials have been in use for several decades. In the 1960's, some of the earliest works of low loss dielectric materials included, for instance, studies on titania [125] and the pioneering investigations on high relative permittivity tungsten bronze-structured $BaO–Ln_2O_3–TiO_2$ (Ln = Lanthanide, i.e. La, Nd, Sm, etc) [126]. $BaTi_4O_9$ was one of the first microwave ceramics to fulfil the technical requirements for applications [127]. A similar material, $Ba_2Ti_9O_{20}$, was then shown to possess even better properties [128; 129]. These materials, along with $MgTiO_3–CaTiO_3$ [130; 131] and $(Zr,Sn)TiO_4$ [132; 133], among others, formed the first generation of ceramic resonators. At the beginning of the 1990's due to the rapid advancement of mobile telecommunications technology, the requirements for dielectric ceramics used as resonators and filters for base stations and handsets changed. Base stations require higher Q ceramics, 40000 GHz < $Q.f$ < 250000 GHz to prevent heat and interference between signals in high power processing combined with moderate relative permittivity (25 < ε_r < 50). On the other hand, the evolution of microwave ceramics required for handsets was driven by the need for miniaturization with high relative permittivity materials (70 < ε_r < 120) [121]. Along with these issues relating to dielectric loss and temperature stability, the cost of a component has become a prime motivator for companies and researchers.

Figure 2.2-2, in which the quality factor $Q.f$ is plotted as a function of the dielectric constant of dielectric materials, defines three main groups of microwave dielectrics according to their properties envisaging applications. Table 2.2-1 gives examples of representative materials of the three groups and their reported dielectric properties.

The first category includes ceramics with low permittivity and ultra high Q that may be used for devices working at ultra high frequency millimetre-waves and microwave integrated circuit (MIC) substrate applications [11; 12]. For MICs, ceramic substrates should have a low permittivity (to minimize cross-coupling with conductors and to shorten the time for the electronic signal transition). These substrate materials also

need high *Q* dielectric factors in order to maintain overall high *Q* circuits by lowering power dissipation [134].

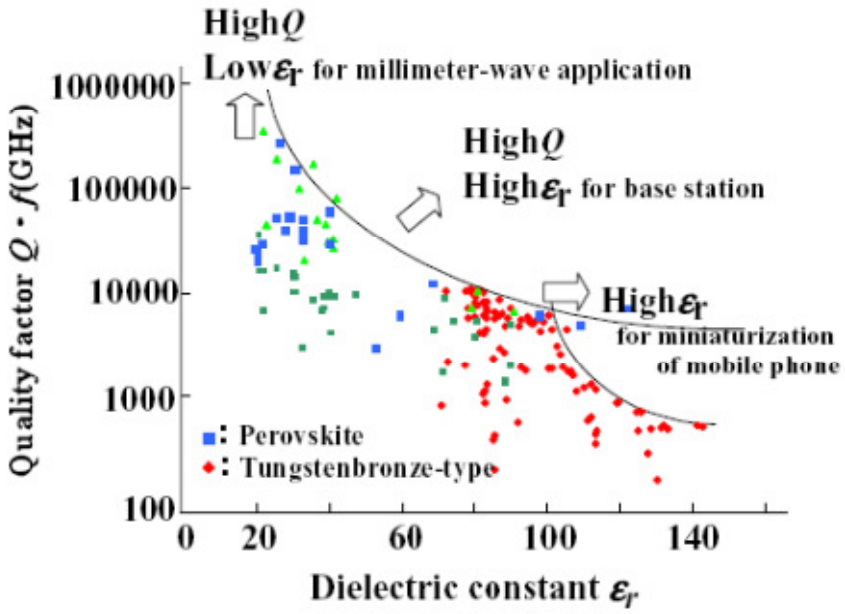

Figure 2.2-2: Quality factor *Q.f* as a function of the dielectric constant of microwave dielectrics [118] defining three groups of materials.

As depicted in Table 2.2-1, materials like forsterite (Mg_2SiO_4) [118], willemite (Zn_2SiO_4) [135] or alumina (Al_2O_3) [136] are examples of materials that fit the requirements for these applications. In the case of alumina, ceramics with high density obtained from high purity and fine grained reagents were reported to have ultra high *Q.f* value of 680000 GHz and a τ_f of -60 parts per million (*ppm)*/°C [118; 137]. Regarding the three materials, by adding TiO_2 (with opposite sign τ_f of +450) near-zero τ_f materials were obtained [134; 135; 138] despite some deterioration of the quality factor.

The second class is related to materials with medium/high permittivity (25-50) and high Q which find application for satellite communication and in cellular phone base stations [10-12]. These materials have the potential of increasing the signal/noise ratio in mobile phone base station applications [12]. Additionally, as the number of base stations

for telecommunications is increasing rapidly, materials with medium-to-high dielectric constant are needed for the resonator miniaturization [10].

Table 2.2-1: Examples of microwave dielectric materials classified in three groups according to their dielectric properties.

Material		ε_r	$Q.f$ (GHz)	τ_f (ppm/°C)	Ref.
Low ε_r and ultra high Q					
Mg_2SiO_4		6.8	270000	-70	118
Zn_2SiO_4		6.6	219000	-61	135
Al_2O_3		9.8	360000	-60	136
Al_2O_3 (high purity)		10.05	680000	-60	118; 137
Medium ε_r and high Q					
$BaO\text{-}TiO_2\text{-}ZnO$		36	42000	--	139
$ZnNb_2O_8\text{-}TiO_2$		37	29000	--	140
$ZnNb_2O_6$		25	83700	--	141
$(Mg,Ca)TiO_3$		20	86000	-3	130
$(Zr,Sn)TiO_4$		34 to 37	50000	0	132; 133
$TiTe3O_8$		50	30600	+133	142
$Ba_nLa_4Ti_{3+n}O_{12+3n}$ (n=0.8-2)		45	30000 to 48000	-21 to -12	143
$Ba(La_{1-y}Al_y)_4Ti_4O_{15}$		44	47000	+1.3	143
$Ba_nLa_4Ti_{3+n}O_{12+3n}$ (n=1)		43 to 49	11583 to 43589	-17 to -2	144-146
$BaO\text{-}TiO_2$ + 0.1 wt% WO_3		35	52000	≈ 0	147
$BaTi_4O_9$		35.6	42600	+12	148
High ε_r and high Q					
$Ba_{6-3x}R_{8+2x}Ti_{18}O_{54}$ (x=2/3)	R = Sm	80	10549	≈ -10	18; 149
	R = Nd	85	10010	≈ +60	
	R = La	105	2024	≈ +470	
$Ba_{6-3x}R_{8+2x}Ti_{18}O_{54}$ (x=0.5)	R = Nd	45 to 84	5600 to 13500	+88 to +77	150-152
$BaNd_2Ti_5O_{14}$		91	Q=1771	-8 to -46	(a)
TiO_2 + 2 wt% CuO		98	14000	+374	153
$Bi_2(Zn_{1/3}Nb_{2/3})_2O_7$		76.1	3260	-79.8	154
$Bi_2(Zn_{1/3}Ta_{2/3})_2O_7$ + 0.5 wt% B_2O_3		63.9	3500	-14.1	155
$Li_{1+x-y}Nb_{1-x-3y}Ti_{x+4y}O_3$		55 to 78	997 to 8896	-62 to +28	156
$Ag(Nb_{0.65}Ta_{0.35})O_3$ – $Ag(Nb_{0.35}Ta_{0.65})O_3$ composite		430	700	< +50	157; 158

(a) Fuji Titanium Industry Co, Lda

Examples of candidate materials for these applications are the systems $BaO\text{-}TiO_2\text{-}ZnO$ [139] or $ZnNb_2O_8\text{-}TiO_2$ [140] (Table 2.2-1). Other materials with properties fitting this category have been reported. Among them are zinc niobate ($ZnNb_2O_6$) [141], $(Mg,Ca)TiO_3$ [130], which is also a very useful dielectric material for high frequency antenna applications, or $(Zr,Sn)TiO_4$, which has been used for resonators since the 1970's [132; 133]. Tellurium-based systems are also interesting because they can be synthesized and sintered at temperatures below 900 °C, as in the case of $TiTe3O_8$ [142].

The $A_nLa_4Ti_{3+n}O_{12+3n}$ (A = Ba, Sr, Ca) [10] homologous compounds are excellent candidates for dielectrics of base stations for mobile communications. In the $BaO\text{-}La_2O_3\text{-}TiO_2$ system, the $Ba_nLa_4Ti_{3+n}O_{12+3n}$ homologous compounds [10; 159] exist on the tie line $BaTiO_3\text{-}La_4Ti_3O_{12}$ [160] nearby the tungsten bronze-type like $Ba_{6-3x}R_{8+2x}Ti_{18}O_{54}$ (R=rare earth: La, Pr, Nd, Sm, etc) solid solutions [149], as shown in Figure 2.2-3.

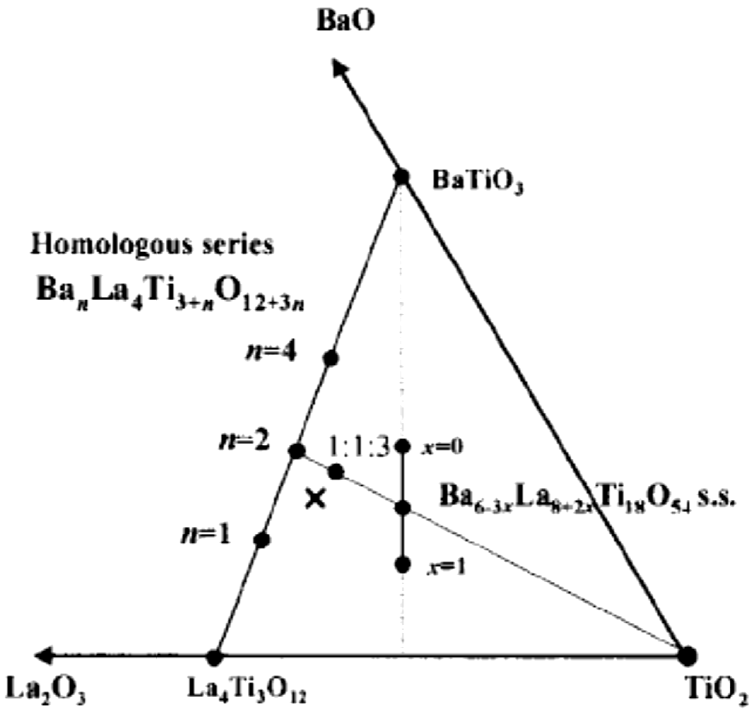

Figure 2.2-3: A part of the $BaO–La_2O_3–TiO_2$ ternary system [143] presenting the $Ba_nLa_4Ti_{3+n}O_{12+3n}$ homologous series.

There are three kinds of homologous compounds: n=1, $BaLa_4Ti_4O_{15}$; n=2, $Ba_2La_4Ti_5O_{18}$; and n=4, $Ba_4La_4Ti_7O_{24}$, which share the same substructure. For n = 2 to 4, the dielectric properties observed for n < 2 (see Table 2.2-1) were reported to be deteriorated due to the formation of the secondary phase $Ba_5La_4Ti_8O_{27}$. Substitution of Al for La in the n = 1 homologue, $BaLa_4Ti_4O_{15}$, originated an improvement of τ_f from negative to +1.3 *ppm*/°C [143]. Several authors reported similar results on the dielectric properties of $BaLa_4Ti_4O_{15}$ [144-146] (Table 2.2-1).

Some compositions of the above mentioned tungsten bronze-type like $Ba_{6-3x}R_{8+2x}Ti_{18}O_{54}$ (R=rare earth: La, Pr, Nd, Sm, etc) solid solutions [149] are good examples of materials of the third category, consisting of high ε_r and high Q dielectrics (Table 2.2-1). These materials have potential applications in mobile phone handsets, namely in resonators, where miniaturization of a device is very important [11; 12; 149].

These solid solutions are well known microwave dielectrics having moderately high relative permittivity between ~70 and ~140, high $Q.f$ (> 2000 GHz) and low τ_f [18; 120; 149]. The compositions in the range x=0.5–0.7 were found to have the best dielectric properties. The distinctive phenomenon is that $Q.f$ values vary non-linearly as a function of composition x in the $Ba_{6-3x}R_{8+2x}Ti_{18}O_{54}$ formula, although ε_r and τ_f vary proportionally to the composition. As shown in Figure 2.2-4, ε_r and τ_f decrease with x whereas $Q.f$ increases with x until reaching a maxima at about x=2/3, decreasing afterwards.

The non-linearity in $Q.f$ was attributed to ordering of the site occupancy of large cations such as Ba and R (rare earth) ions, reducing the internal strain [18; 149]. For x=2/3, higher ordering of R and Ba ions occupying different sites lead to a minimum in the internal strain.

In the $BaO\text{-}Nd_2O_3\text{-}TiO_2$ system, the compositions $BaNd_2Ti_4O_{12}$ and $BaNd_2Ti_5O_{14}$ have been widely studied [161-163]. These compositions are often referred as 1:1:4 (BaO: Nd_2O_3: 4 TiO_2) and 1:1:5 (BaO: Nd_2O_3: 5 TiO_2) compounds, respectively, in correlation with the molar proportion of the oxides. Ceramics of the 1:1:5 composition are currently used in commercial applications (Fuji Titanium Industry Co., Ltd, Japan). As

shown in Figure 2.2-5, the 1:1:4 compound, $BaNd_2Ti_4O_{12}$, belongs to the $Ba_{6-3x}R_{8+2x}Ti_{18}O_{54}$ (R=Nd, x=0.5) solid solutions [163] with the formula $Ba_{4.5}Nd_9Ti_{18}O_{54}$.

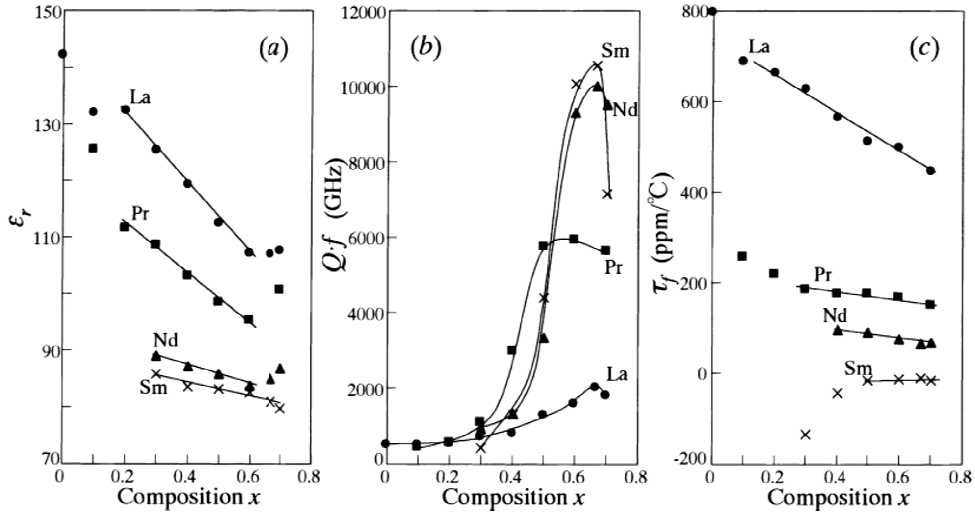

Figure 2.2-4: Microwave dielectric properties of $Ba_{6-3x}R_{8+2x}Ti_{18}O_{54}$ (R = La, Pr, Nd and Sm) as a function of composition. (a) ε_r, (b) *Q.f* and (c) τ_f [149]. *Q.f* values vary non-linearly with the composition although ε_r and τ_f vary proportionally to the composition.

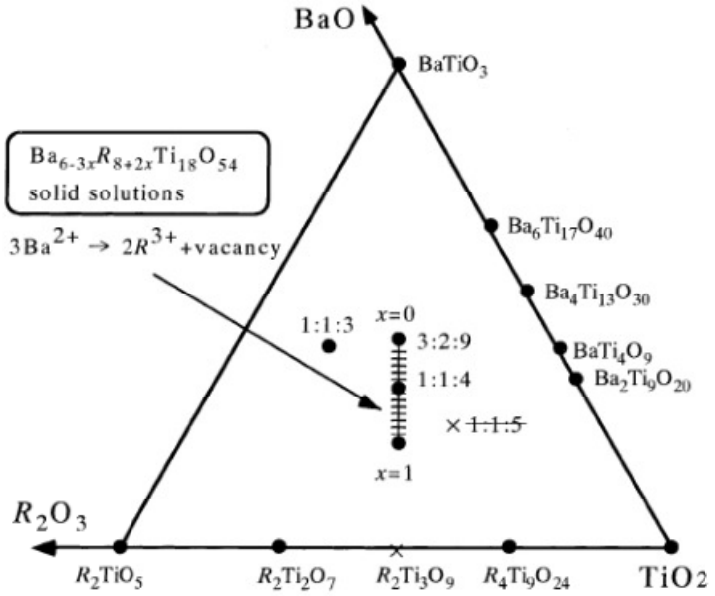

Figure 2.2-5: $BaO\text{-}R_2O_3\text{-}TiO_2$ (R = rare earth) ternary system [149] showing the $Ba_{6-3x}R_{8+2x}Ti_{18}O_{54}$ solid solutions.

Fu *et al.* [164] reported for the first time on the dielectric properties of thick films fabricated by electrophoretic deposition on Pt foils of $BaNd_2Ti_5O_{14}$, the 1:1:5 composition in the BaO-Nd_2O_3-TiO_2 system, in comparison with those of bulk ceramics. The authors reported ε_r and *tanδ* at 1 MHz of 107 and 88 and 0.0006 (Q = 1600) and 0.0003 (Q = 3333) for 52-µm-thick-films and ceramics, respectively. The temperature dependence coefficient of permittivity, $TC\varepsilon_r$ was measured in terms of the parameter

$$TC\varepsilon_r = \frac{\Delta\varepsilon_r}{\varepsilon_{r0}\Delta T} \qquad (2.2\text{-}4)$$

where $\Delta\varepsilon_r$ stands for the change between 30 and 120 ˚C in ε_r relative to the dielectric constant ε_{r0} at 30 °C. The $TC\varepsilon_r$ of 52 µm thick $BaNd_2Ti_5O_{14}$ films was calculated to be lower than +58.5 *ppm*/°C between 30 and 120 °C, indicating a good temperature stability of $BaNd_2Ti_5O_{14}$ thick films. $BaNd_2Ti_5O_{14}$ ceramics showed a $TC\varepsilon_r$ of −36.8 *ppm*/°C [164].

In a related work, Fu *et al.* [19] fabricated 10 to 80 µm thick $BaNd_2Ti_5O_{14}$ films by EPD. This work showed that high Q (low losses of the order of 10^{-4} at 1MHz) $BaNd_2Ti_5O_{14}$ thick films with near-zero $TC\varepsilon_r$ can be fabricated with $45 < \varepsilon_r < 70$ by choosing the right sintering temperature and controlling the anisotropic microstructure development during constrained sintering. However, the constrained sintering was not systematically studied and the origin of such anisotropic microstructure is not completely clear.

Other materials such as TiO_2 [165], BaO-TiO_2 system [147], bismuth-based ceramics, namely Bi_2O_3-ZnO-Nb_2O_5 ternary oxides [166], Li-based materials [156; 167] or $Ag(Nb,Ta)O_3$ [158; 168] (Table 2.2-1) have also received considerable attention for applications of high permittivity ceramics.

The great advances in dielectric materials can be seen in the dramatic decrease in the size and weight of devices such as cell phones in recent years. The importance of miniaturization and cost reduction cannot be overemphasized in any hand-held communication application. This constant need for miniaturization provides a continuing driving force for the discovery and development of increasingly sophisticated materials to perform the same or improved function with decreased size

and weight. From the materials point of view, it is particular important to identify and understand size effects (defects, interfaces, etc). This has been addressed in a systematic way in the case of thin films but not so thoroughly in the case of thick films, in which, for example the need for a sintering step implies a constrained densification. In this way, understanding and controlling the effects of different processing approaches on the properties of these low loss (high *Q*) dielectric ceramic materials has a vital technological importance.

2.2.2 Crystal structure of $BaO\text{-}Ln_2O_3\text{-}TiO_2$ (Ln = La or Nd)

The large majority of microwave dielectric ceramics have the perovskite structure (which will be detailed ahead) or a related one, as is the case of $BaO\text{-}La_2O_3\text{-}TiO_2$ and $BaO\text{-}Nd_2O_3\text{-}TiO_2$ systems, which are referred as BLnT (Ln = La or Nd) for convenience.

In this work, attention is given to two compositions from these groups of materials: $BaLa_4Ti_4O_{15}$ (BLT), the 1:2:4 composition in the $BaO\text{-}La_2O_3\text{-}TiO_2$ system [143], and $Ba_{4.5}Nd_9Ti_{18}O_{54}$ (BNT), the 1:1:4 composition in the $BaO\text{-}Nd_2O_3\text{-}TiO_2$ system [163]. These materials have anisometric crystal structures (hexagonal (BLT) and orthorhombic (BNT)), which is an important aspect regarding microstructural evolution during sintering and may be used to control their dielectric properties.

2.2.2.1 $BaLa_4Ti_4O_{15}$

The structure of $A_nB_{n-1}O_{3n}$ ($n \geq 3$) B-cation deficient perovskite related compounds has received a great deal of attention [10; 17; 169-171]. $BaLa_4Ti_4O_{15}$ (BLT) is the case where A = (Ba, La) and n = 5. The structure of these compounds corresponds to a close packing of AO_3 mixed layers [17] in which the A and O atoms are ordered as shown in Figure 2.2-6 a). Each A atom is surrounded by six oxygen atoms, whereas each oxygen atom has two linearly coordinated A atoms among its six nearest neighbours. Successive layers are shifted from each other, so that the A atom positions in one layer project into the

centre of a triangle formed by the A atoms in the adjacent layers, indicated as position 1 or 2 in Figure 2.2-6 a).

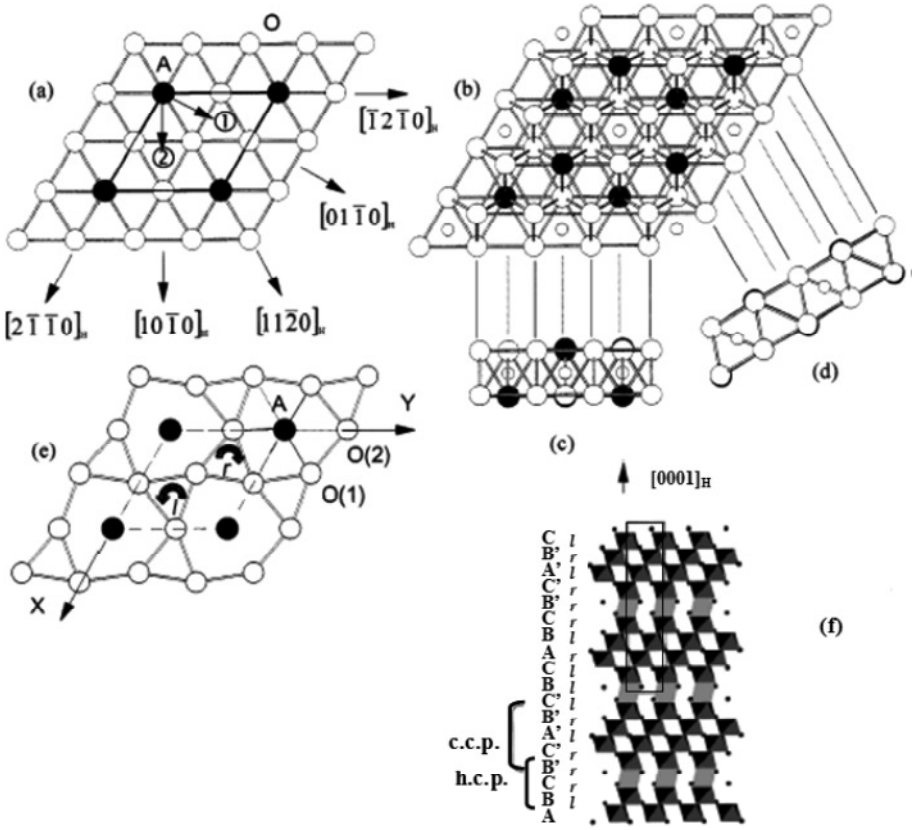

Figure 2.2-6: Schematic views of the AO_3 mixed layers packing in BLT: (a) arrangement of A and O atoms in the AO_3 mixed layers; (b) stacking of two adjacent AO_3 layers, showing the TiO_6 octahedra; (c) view of this stacking along $[10\text{-}10]_H$; (d) view of this stacking along the $[11\text{-}20]_H$ direction; (e) the distorted AO_3 layers in BLT (*r* and *l* visualize the clockwise and counter-clockwise rotations of corner-sharing octahedral respectively); (f) schematic representation of BLT as viewed along $[2\text{-}1\text{-}10]_H$, where the rotations of TiO_6 octahedra around the *c*-axis are represented by *r* (clockwise) and *l* (counter-clockwise). c.c.p and h.c.p stand for cubic close-packed and hexagonal close-packed, respectively [17; 146].

One quarter of the octahedral interstices between two such layers are surrounded exclusively by oxygen atoms and are occupied by Ti atoms, the small open circles in

Figure 2.2-6 (b)–(d). All oxygen octahedra located within the cubic-close-packed (c.c.p) part of the sequence are corner shared and occupied by Ti atoms. In each triplet of face-sharing octahedra, characteristic of the hexagonal close-packed (h.c.p) part of the sequence, the central octahedra are vacant.

The lattice parameter *a* is determined by the hexagonal sublattice of A atoms and remains nearly constant at ~5.6 Å. The *c* parameter depends on the stacking sequence of AO_3 layers (the thickness of each octahedral sheet is ~2.2 Å). In the case of BLT, there are n = 5 AO_3 mixed layers in each perovskite slab. Additionally, a cooperative tilting of TiO_6 octahedra within the perovskite blocks leads to doubling of the *c*-axis. BLT is then ascribed as a trigonal structure with the space group P-3c1 and the lattice parameters are *a* = 5.5720 Å and *c* = 22.500 Å (≈ 10 × 2.2 Å), respectively, in the hexagonal (H) setting [17; 146; 169; 170].

2.2.2.2 $Ba_{4.5}Nd_9Ti_{18}O_{54}$

The crystal structure of $Ba_{6-3x}R_{8+2x}Ti_{18}O_{54}$ (R=rare earth) compounds is presented in Figure 2.2-7. BNT is the case where R=Nd and x=0.5. The structure essentially consists of a three-dimensional framework of corner-sharing perovskite-like octahedra joined together according to a pattern similar to that of the tetragonal tungsten bronzes.

The structure is typified by oxygen octahedra linked at the corners in a complex way to yield three types of channels: the largest ones are the pentagonal sites (A2), the medium ones are the rhombic sites (A1) in 2×2 perovskite blocks and, finally, the trigonal sites (C). The rare earth, for example Nd^{3+} cations, occupy the rhombic channels (diamond sites); Ba^{2+} cations fill the pentagonal channels and the remaining Ba^{2+} ions share the rhombic channels with the Nd^{3+}, according to the structural formula $[R_{8+2x}\,Ba_{2-3x}\,V_x]_{A1}\,[Ba_4]_{A2}\,Ti_{18}O_{54}$ ($0 \le x \le 2/3$; V stands for vacancy). At x = 2/3 Ba and R ions occupy separately A2- and A1-sites, respectively. The triangular sites are empty [18; 149].

The crystallography of $Ba_{6-3x}R_{8+2x}Ti_{18}O_{54}$ (R=rare earth) solid-solutions has been reported by different authors and no general consensus has yet emerged on the space

group of these solid-solutions. Ubic *et al.* [8] reported that the actual space group is almost perfectly described as Pbnm (Nº 62), but is probably more accurately given by Pb21m (Nº 26). The morphology of the crystal is needle-like, elongated along the c-axis [149]. Tang *et al.* investigated the structure of ceramic $Ba_{4.5}Nd_9Ti_{18}O_{54}$, BNT, by synchrotron X-ray powder diffraction from 10 to 295 K. Based on an orthorhombic structure, unit cell parameters of a = 22.3367(5) Å, b = 7.6738(1) Å and c = 12.1842(3) Å were reported [172]. No evidence was found by the authors for any major structural change from 10 to 295 K.

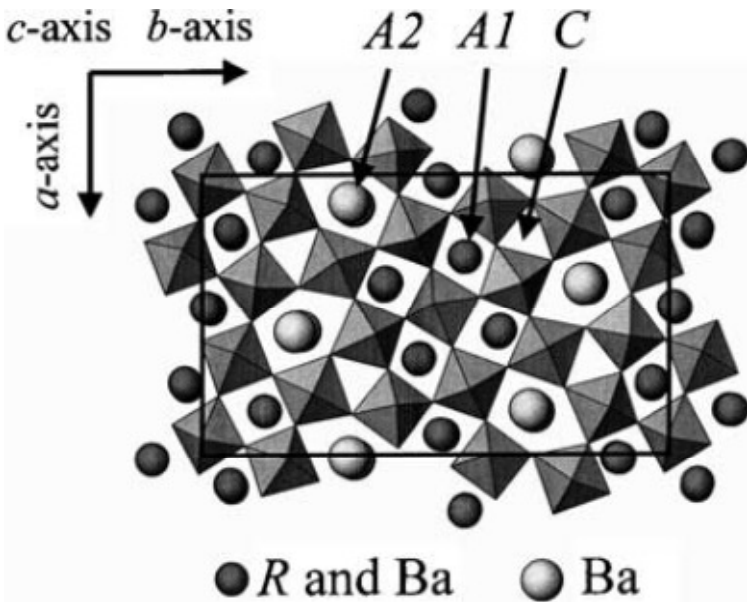

Figure 2.2-7: Tungsten bronze-type like crystal structure of the $Ba_{6-3x}R_{8+2x}Ti_{18}O_{54}$ (R=rare earth) solid solutions. A1 is a rhombic site, A2 is a pentagonal site and C is a trigonal site [18].

2.2.3 Microstructure-dielectric properties relation in $BaO\text{-}Ln_2O_3\text{-}TiO_2$ (Ln = La or Nd)

One of the major research interests in optimizing BLnT (Ln = La or Nd) ceramics for microwave applications have been the tuning of τ_f to zero while retaining a high ε_r and low losses. The use of additives [132], variation of the La or Nd/Ba ratio [173] and a

combination of different rare earth elements [174] have been some of the main approaches reported. These approaches have often been used simultaneously.

Composite structures between two materials with τ_f of opposite sign have also been used as a strategy to obtain temperature stable microwave materials. Zheng *et al.* [175] successfully prepared bulk composites of BLT and BNT by solid state reaction with good properties for thick film-based and antenna core microwave applications. More recently, Vilarinho *et al*. [176] demonstrated an alternative way to combine the tailored performance of composite dielectric thick films with device size scaling that may have a broad technological impact. Using electrophoretic deposition, multilayer composite thick films of BLT and BNT were prepared. The composite thick films exhibit permittivity intermediate between the end members that may be tuned by modifying the ratio between and/or thickness of each layer, thereby tailoring the films for specific applications [176].

Additionally, in microwave materials technology, attention has been given to the development of new low-temperature sintered materials (for example, tellurium or bismuth based compounds, or the CaO–MgO–SiO_2–TiO_2 system) [167; 177] or lowering the sintering temperature of known compositions such as BLnT. Glass addition [178; 179] has been the most used approach though it may often result in the deterioration of the quality factor. Usable properties must however be preserved. Low sintering temperature is very important from different points of views (costs, sustainability and compatibility between materials and technologies). A good example is the case of LTCC technology in which compatibility between the dielectric and the metal electrodes and cost reduction by using non noble metal electrodes are important requirements regarding the multilayer device miniaturization [7; 177; 180].

On the other hand, other intrinsic characteristics of materials may also be explored. The large anisometry in the lattice parameters (a = 5.5720 Å versus c = 22.500 Å, c/a ≈ 4) of BLT is known to promote the growth of lath or plate-like grains which have been reported to align normal to the pressing direction [146]. As observed by Zheng *et al*. [146], this grain orientation originates anisotropic dielectric properties: the relative permittivity measured perpendicular to the pressing direction was 52 whereas in the

parallel direction decreased 20% to 42. Fukami *et al*. [181] also observed anisotropy in the microstructure and dielectric properties of BLT ceramics sintered with plate-like BLT template particles. With increasing amount of template particles, τ_f and ε_r increased whereas *Q.f* remained nearly equal to that of specimens without template particles. These observations clearly show that microstructure anisotropy in BLT may be used for controlling the dielectric properties of the material.

Similarly to the case of BLT, the above described anisometry in the unit cell of BNT results in elongated needle-like grains, as well as in significant anisotropy of the dielectric properties [19; 182]. Recently, the anisotropic microstructure development and its effect of on the dielectric properties of $BaNd_2Ti_5O_{14}$ (the 1:1:5 composition in the BaO-Nd_2O_3-TiO_2 system, BNT 1:1:5) was further investigated in thick films prepared by electrophoretic deposition on Pt foils by Fu *et al.* [19; 164] and compared with counterpart ceramics. Increased grain elongation and texture were observed in the films compared to bulk ceramics. In addition, texture and the aspect ratio of the needle-shaped grains in the thick films were strongly increased with the increase of the sintering temperature.

Very interestingly, along with this anisotropic microstructure development in the thick films, important changes in the dielectric properties were observed: with the increase of grain aspect ratio, the relative permittivity decreased and the temperature coefficient of the permittivity, $TC\varepsilon_r$, changed from -114 to +12 *ppm*/°C [19]. These observations are presented in Figure 2.2-8 and show that near-zero $TC\varepsilon_r$ BNT 1:1:5 thick films can be fabricated by controlling the microstructure development through the selection of the right substrate constraint and sintering conditions. The observed textured microstructure was attributed to the anisometric crystal structure of the material and to the effect of constrained sintering of BNT 1:1:5 thick films [19; 164]. However, the precise factors governing such effects on the microstructure are not understood and a deeper characterization of the microstructural anisotropy development is still needed.

Similar behaviour is expected in other systems with analogous structural anisometry characteristics, as is the case of BLT. Therefore, the observed substrate constraint

effects justify better understanding and may open further technological opportunities by offering a straightforward way to design the microstructure and dielectric properties of these functional materials.

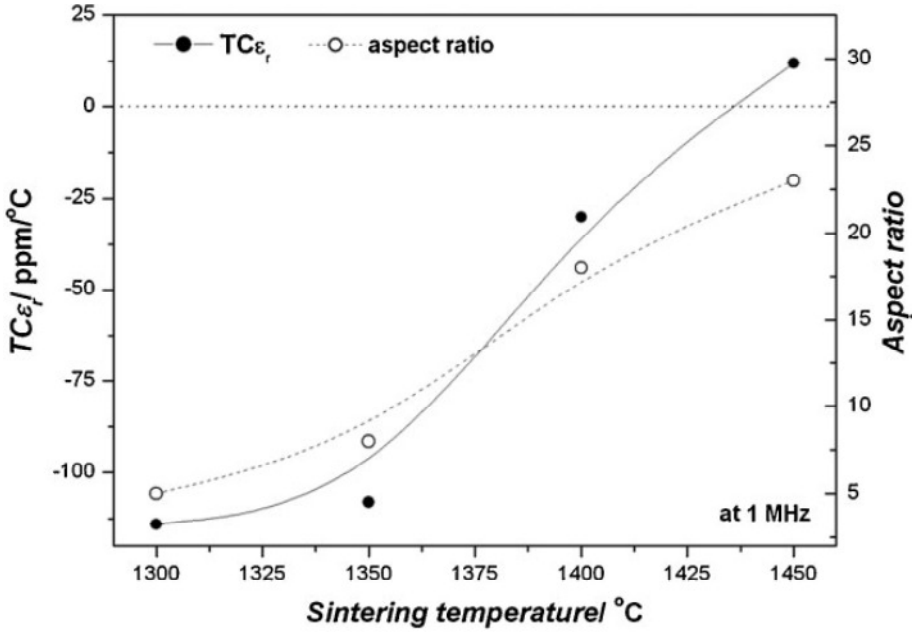

Figure 2.2-8: Dependence of $TC\varepsilon_r$ and aspect ratio of BNT thick films on the sintering temperature [19]. The relation between the two dependences demonstrates that near-zero $TC\varepsilon_r$ BNT 1:1:5 thick films can be fabricated by controlling the microstructure development.

Apart from these studies, very few reports are available on the constrained sintering of thick films on flexible metallic substrates and its effect on the dielectric properties. Considering the interesting dielectric properties of BLnT (Ln = La, Nd) materials and the potential of thick film technology for miniaturization of microwave devices, this lack of understanding ought to be suppressed.

2.3 Strontium titanate

2.3.1 Dielectric properties and applications

Strontium titanate has been attracting a considerable interest from the fundamental point of view for a long time, often being used as model system. STO is a quantum paraelectric [183; 184] in which the dielectric permittivity monotonously increases upon cooling down to near 0 K and no ferroelectric-type anomaly is observed. The paraelectric phase of incipient ferroelectrics is unstable and the ferroelectric state can be induced in STO by the application of a high electric field [185], uniaxial stress [186], oxygen isotope exchange [187] or chemical substitutions in the lattice [188; 189]. Besides quantum paraelectric behaviour, interesting properties of STO include a structural phase transition [190], semiconductivity [191], superconductivity [192], thermoelectricity [193], among others.

On the other hand, STO–based compounds are technologically important materials with a wide range of applications particularly in electronic devices, due to its relatively high dielectric constant (around 300 at room temperature) and low loss tangent [13]. In addition, the dielectric constant of STO reveals a dependence on applied bias electric field, as can be seen in Figure 2.3-1, and therefore may be intentionally electrically tuned [13; 194-196]. This property is called tunability and is strengthened on approaching the paraelectric-ferroelectric phase transition, at which the dielectric constant has a maximum [197]. Tunable microwave devices based on STO are now of particular importance in the microelectronics industry.

Because of these properties as well as good temperature and applied voltage stability, STO has been widely used as various grain boundary layer capacitors [14; 198] and varistors [199; 200]. The electrical properties of grain boundaries in STO, and their differences to the bulk, play a critical role in these devices [201]. For these applications, the material is usually heat-treated in a reducing atmosphere and with a donor addition to built a microstructure of semiconducting grains separated by insulating grain boundaries [14; 198]. Other STO potential application fields range from high-density non-volatile memories [202; 203] to gate dielectric in MOSFET (Metal Oxide Semiconductor

Field Effect Transistor) devices [204], to sensors [205] or Solid Oxide Fuel Cells (SOFC) anodes [206].

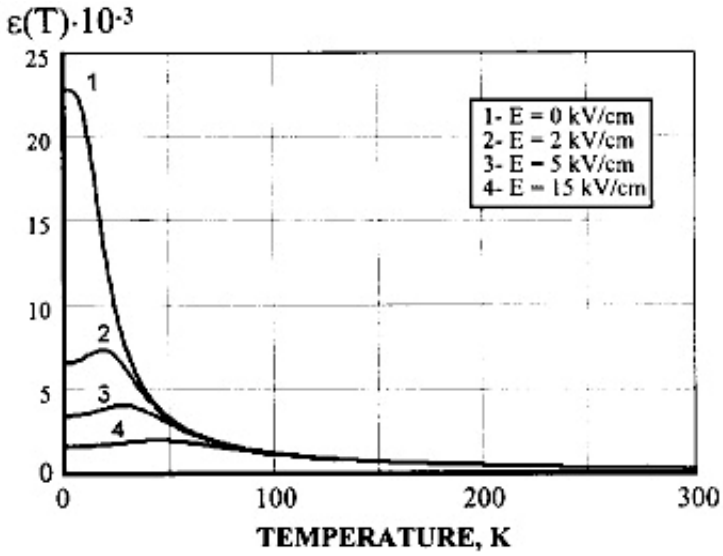

Figure 2.3-1: Dielectric constant of STO single crystal as a function of temperature and biasing field [196]. The dependence of the dielectric constant on applied bias electric field allows for the material to be electrically tuned.

Owing to the extensive use of microwaves in radar and communication applications, very important current applications for STO-based materials are related to microwave microelectronic elements [13; 196; 207]. Examples are dielectric resonators or filters, parallel plate tunable capacitors or varactors, electroded slabs in stack of lens antennas or small low cost microwave phase shifters for use in phased array antennas [13]. However, limiting the material practical application is the fact that substantial tunability is achieved in undoped STO only below ~80 K [208]. Nevertheless, as depicted in Figure 2.3-2, the temperature range of high tunability and high dielectric constant can be shifted towards room temperature by formation of solid solutions between incipient ferroelectric STO and classical ferroelectric barium titanate ($BaTiO_3$) [189; 196]. Such shift corresponds to an induced ferroelectric phase transition in $Ba_xSr_{1-x}TiO_3$ (BST) solid solutions at temperatures in the range of 0-400 K [189].

In a different application field, STO-based materials have recently attracted much attention as thermoelectric materials due to excellent electronic transport properties and stability at high temperatures [15; 193; 209; 210]. For thermoelectric applications, blocking grain boundaries are highly disadvantageous because fast electrical transport inside the electroceramic material is required [15; 211]. The fundamental problem in creating efficient thermoelectric materials is that they need to be good at conducting electricity, but not at conducting thermal energy. Engineering the thermal and electrical properties of the material is therefore essential for these applications.

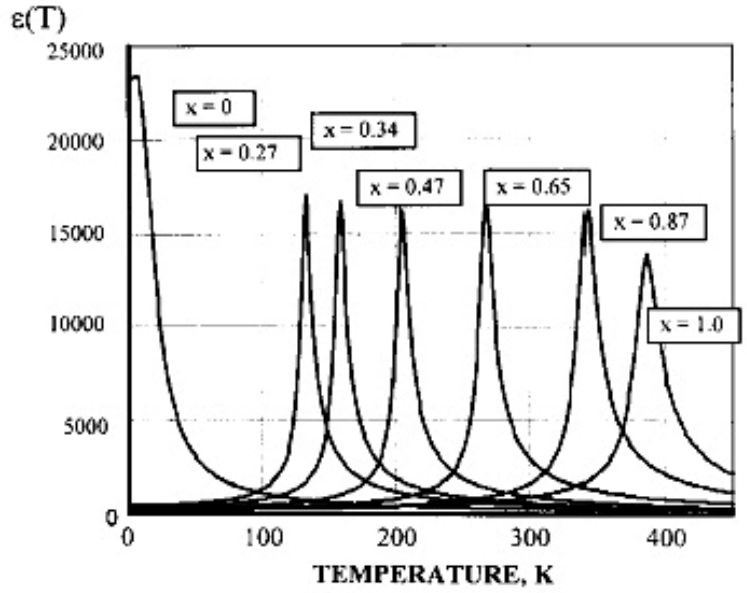

Figure 2.3-2: Dielectric constant of $Ba_xSr_{1-x}TiO_3$ single crystal as a function of temperature for different content of barium (x) [196]. The maximum of the dielectric constant is shifted towards room temperature by the increasing barium content.

This application field can be very important for STO-based materials once that heat-to-electricity conversion is regarded as one of the promising methods to harvest energy from waste heat, from electronic devices to cars and powerplants, as well as from natural heat sources in order to produce usable electricity and thus improve overall efficiency [15; 212]. The demand for alternative energy technologies in order to reduce the

current dependence on fossil fuels constitutes a great motivation for research in the field of thermoelectric materials [212].

2.3.2 Crystal structure

Perovskite is the name of calcium titanate ($CaTiO_3$) but stands for a whole class of ternary oxides that exhibit the same or a related crystallographic structure. This family of oxides is represented by the general formula ABO_3 and has a cubic structure, where A-cations are placed at the cube corners, small B-cations are located at the body centre and oxygen ions (O^{2-}) at the centre of the faces [213], as schematically represented in Figure 2.3-3. The structure can also be regarded as a three-dimensional framework of BO_6 octahedra, arranged in a simple cubic pattern. In the octahedron unit, B-atom is at the centre with the oxygen atoms at the corners shared by different octahedron and A-cations occupying the interstitial positions between the octahedra [213]. A-cations are 12-coordinated and B-cations are 6-coordinated and the ideal perovskite unit cell contains one formula unit, i.e., one A-cation, one B-cation and three oxygen ions.

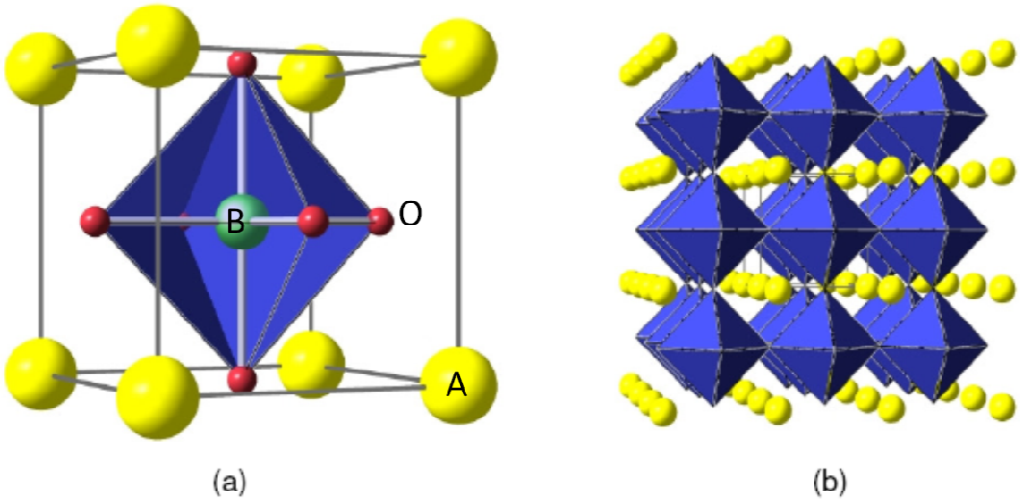

Figure 2.3-3: Two representations of the ideal cubic perovskite structure [213]: (a) the cubic unit cell with octahedral coordination of B-cation and (b) corner sharing array of BO_6 octahedra.

The perovskite structure is very tolerant to cation substitution in both A and B-sites of the lattice and hence may lead to more complex compounds, for example, quaternary solid solutions like BST [214]. The incorporation of a foreign cation into the perovskite lattice depends on the ionic size and electronic structure of both the foreign ion and the substituted one. This affects the stability of the structure and may cause distortions that modify the cubic elementary cell into tetragonal, rhombohedral or orthorhombic structures.

A measure of the perovskite structure stability is the Goldschmidt tolerance factor [183; 215], t_G, that relates the ionic radii of the constituents of the perovskite lattice:

$$t_G = \frac{r_A + r_O}{\sqrt{2}(r_B + r_O)} \qquad (2.3\text{-}1)$$

where r_i (i = A, B, O) denotes the average ionic radii of the constituents of the ABO_3 compound in the respective sites.

The tolerance factor is also a measure of the deviation from the ideal packing that the ionic sizes can move maintaining a stable perovskite structure. The value of t_G is correlated to the structural distortion, force constants of binding, rotation and tilt of the octahedrons, etc. [183]. Several properties, especially related to the dielectric, phase transition behaviour, etc., are directly correlated with this simple tolerance factor approach [216]. For $t_G < 1$, the size of the unit cell is governed by the B-site ion and A-site ions are allowed to fluctuate in their sites. For $t_G > 1$, B-site ions have too much space to vibrate whereas A-site ions are closely packed. For $t_G = 1$, both A and B ions are closely packed.

STO is considered an example of the ideal cubic perovskite structure [190]. In STO, A-sites are occupied by Sr^{2+} ions and B-sites by Ti^{4+} ions. At room temperature, STO has an undistorted cubic perovskite structure of the space group *Pm3m* [217] and its lattice constant is 3.905 Å [183; 218]. The tolerance factor for STO is $t_G \approx 1$ [187], showing the high (ideal) packing of its structure. This does not allow for interstitial site occupation.

From cubic at room temperature, STO presents a phase transition to tetragonal (space group I4/mcm [217]) around 110 K [190; 219]. This phase transition is related with tilting of

the oxygen octahedra around one of the [100] axes [220] and the tetragonal phase is centrosymetric. Therefore, no polarization is induced in STO below 110 K and the transition is a non-ferroelectric structural phase transition with almost no influence on the dielectric response [194].

2.3.3 Phase diagram of the SrO-TiO_2 system

Figure 2.3-4 presents the phase diagram for the SrO-TiO_2 system. The intermediate compound is the stoichiometric STO.

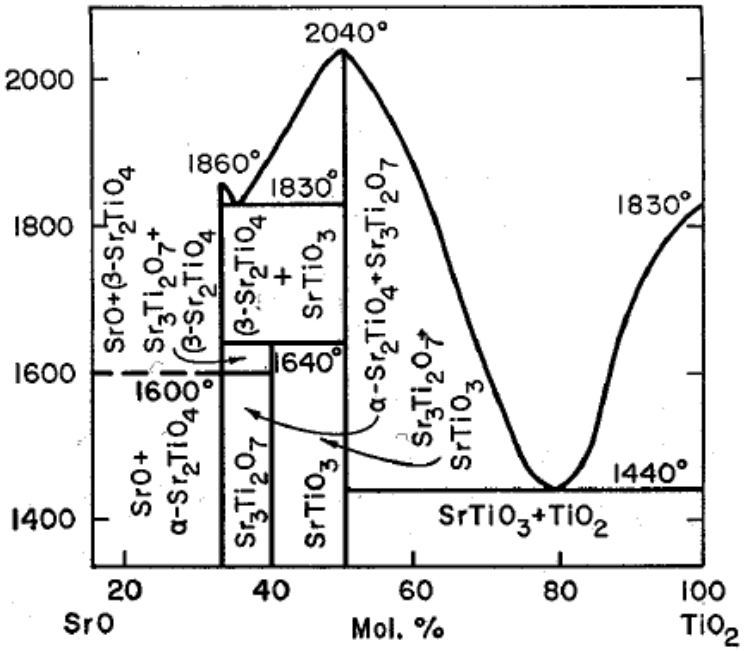

Figure 2.3-4: Phase diagram of the SrO-TiO_2 system [221].

It can be seen that this system has a eutectic point at about 1440 °C for Ti-rich compositions. When a nonstoichiometric powder with Sr/Ti < 1 is sintered above this temperature, a Ti-rich liquid phase forms and affects the densification and grain growth of this material. In the case of the Sr-excess side of the diagram, the eutectic is at 1830 °C, far above the generally used sintering temperatures. Additionally, the

solubility limits for excess SrO or TiO_2 are quite low. Nevertheless, some incorporation is possible as will be reviewed later.

2.3.4 Defect chemistry

Perfect crystals in which all the identical sites are occupied by identical atoms or ions do not exist at temperatures above 0 K [222; 223]. Actually, real crystals show lattice defects, deviations from the ideal crystal lattice, which concentration increases with temperature. Point defects, those that involve only a single atomic species or lattice site, are very important defects in crystalline solids. Intrinsic point defects are electrons and holes, interstitials (Frenkel disorder) [224] and vacancies in the Sr-, Ti- and O-sublattices (Schottky disorder) [224], in the case of STO. These defects occur due of thermodynamical reasons or due to impurity accommodation. Extrinsic point defects are doping elements.

Defects of higher dimension are also present in materials. These defects are one-dimensional defects like dislocations or two-dimensional defects, for instance stacking faults, as in layered structures of the Ruddlesden-Popper (RP) phases [225]. Interfaces, like grain boundaries and surfaces, also need to be considered because they have a significant impact on the characteristics of the material.

Defects affect markedly the final properties of materials. In particular, the electrical properties of STO and other titanates are closely related to the defect structure of the material. The intrinsic generation of electrons and holes by thermal activation over the bandgap and the extrinsic generation of charge carriers due to compensation reactions for lattice defects (impurities or intentional doping) are very important to understand the electrical behaviour and related properties of the material. In addition, the type of defects present in the material and its concentrations influence the matter transport processes during sintering. Therefore, a strong impact on the resulting microstructure and, as a consequence, on the final properties of the material can be expected.

The classical defect notation of Kröger and Vink [226] is often used to describe the defect chemistry of materials and is also used in this work. A general description of the defect

chemistry of titanates is provided. Particular attention is given to strontium titanate, namely to the incorporation of SrO or TiO_2 excess.

2.3.4.1.1 Undoped and acceptor doped titanates

Due to unavoidable acceptor impurities present even in the undoped material [224; 227-229], typically in the hundreds of *ppm*, undoped or acceptor doped titanates have similar defect chemistry [230], which may be assessed by electrical conductivity (σ) measurements. The conductivity behaviour of these materials is usually characterized by an oxygen deficient, *n* type region, with the conductivity decreasing with increasing pO_2, and an oxygen excess, *p* type region, with the conductivity increasing with increasing pO_2. These regions are separated by a conductivity minimum, as exemplified in Figure 2.3-5.

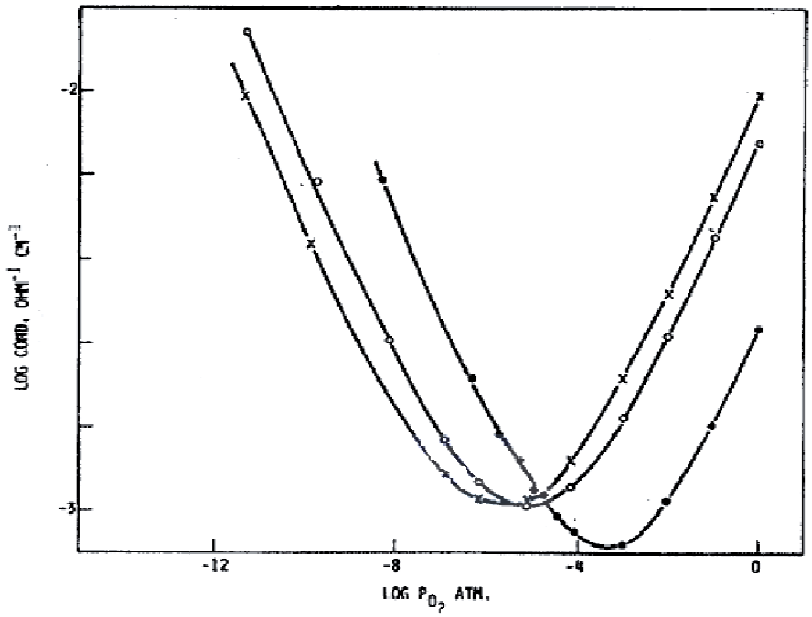

Figure 2.3-5: Equilibrium conductivity profile of undoped and acceptor-doped STO at 1000 °C. • undoped, Sr/Ti=1.0000, ◦ 281 *ppm* Al, Sr/Ti= 0.9950, ˣ 1080 *ppm* Al, Sr/Ti= 0.9950 [230].

At the lowest oxygen activities, the conductivity is consistent with a reduction reaction (equation (2.3-2)) that produces oxygen vacancies, as expected for compounds that have Schottky disorder as their preferred intrinsic ionic disorder [224; 231; 232], and free electrons that go into the conduction band [233]:

$$O_O^x \Leftrightarrow \frac{1}{2}O_2 + V_O^{\bullet\bullet} + 2e^{'} \qquad (2.3\text{-}2)$$

Therefore, in this region, conductivity is dominated by the loss of oxygen and the reduction reaction (2.3-2) is the major source of defects. The transition to this region regarding the oxygen partial pressure depends on the acceptor impurity concentration, i.e., the intrinsic concentration of oxygen vacancies.

Due to their natural abundance, some elements are commonly found as impurities in titanates. These elements, such as Fe^{3+}, Al^{3+}, Mg^{2+} or Na^{+}, show acceptor-type behaviour [224; 227-229]. The incorporation of a generic acceptor oxide, A_2O_3, and the accompanying formation of extrinsic oxygen vacancies during the preparation of acceptor-doped STO from the binary oxides (as usual by the mixed oxide route) can be described by the following simplified reaction in equation (2.3-3) [224]. Here, A_2O_3 virtually replaces $2TiO_2$, with A^{3+} substituting for Ti^{4+}.

$$2SrO + A_2O_3 \rightarrow 2Sr_{Sr} + 2A_{Ti}^{'} + 5O_O^x + V_O^{\bullet\bullet} \qquad (2.3\text{-}3)$$

As a direct consequence of this, any undoped or acceptor-doped STO sample exhibits a specific concentration of oxygen vacancies, which is independent of the reduction reaction (equation (2.3-2)). Only at the lowest oxygen activities, the reduction reaction dominates completely the defect chemistry of these materials. Therefore, in the regions near the conductivity minima, the charge neutrality will be dominated by the oxygen vacancy concentration that is virtually unchanged and fixed by the acceptor concentration.

As pO_2 increases, these extrinsic oxygen vacancies begin to be filled by the oxidation reaction, according to equation (2.3-4), which consumes lattice defects rather than creating them:

$$\frac{1}{2}O_2 + V_O^{\bullet\bullet} \Leftrightarrow O_O^x + 2h^{\bullet} \qquad (2.3\text{-}4)$$

The oxidation and reduction regimens are separated by a conductivity minimum that corresponds to a *n-p* transition and to the perfectly compensated composition, i.e., the oxygen content is chemically equivalent to the total amount of metallic constituents. At this point the only source of electronic carriers is by direct ionization across the band gap [228], according to equation (2.3-5):

$$nil \Leftrightarrow e^{'} + h^{\bullet} \qquad (2.3\text{-}5)$$

where "*nil*" represents the perfect crystal with all electrons in the lowest available energy states. Moving to even higher oxygen partial pressures some of the intrinsic oxygen vacancies can be filled and the oxidation reaction described by equation (2.3-4) becomes effective. As a result, holes develop into the dominating charge carriers. When the material is quenched from a high equilibration temperature down to the vicinity of room temperature, holes can be trapped due to a change of the acceptor's valence state [224; 234] given by the following equation:

$$A^x \Leftrightarrow A^{'} + h^{\bullet} \qquad (2.3\text{-}6)$$

2.3.4.1.2 Donor doped titanates

The situation becomes considerably different when the material is doped by a donor-type element. A donor dopant has a higher oxidation state than that of the host cation it replaces in the solid compound [235]. The impurity centre thus bears an effective positive charge relative to the ideal lattice of the host oxide and requires charge compensation by a species having an effective negative charge, e.g., a cation vacancy, an anion interstitial, an acceptor impurity, or an electron. Typical donor impurities in titanates include large cations with charge >2+ substituted for the alkaline earth ion, e.g. La^{3+}, and small cations with charge >4+ substituted for Ti, e.g. Nb^{5+} or W^{6+}. Thus the impurity oxide has more oxygen per cation than the host oxide it replaces, Nb_2O_5

vs. TiO_2 or La_2O_3 vs. BaO or SrO, and the effect of donor impurities then depends on the loss or the retention of this extra oxygen [235].

Donors have very shallow energy levels (and so, low ionization energies) and are therefore fully ionized down to temperatures of several K [205; 233], according to equation (2.3-7):

$$D \rightarrow D^{\bullet} + e^{'} \qquad (2.3\text{-}7)$$

where *D* stands for a generic donor. Donor-doped titanates may exhibit semiconducting properties with a high conductivity even at room temperature, which is the case when the donors are compensated by electrons. However, the compensation mechanisms in the donor doped titanates are complex [224]. For very low levels of donor doping, the oxygen excess in the donor oxide is lost, even when the material is equilibrated in an oxidizing atmosphere, and compensation is indeed by electrons, according to equation (2.3-8), resulting in a dark colored conducting material:

$$La_2O_3 \rightarrow 2La_{Ba}^{\bullet} + 2O_O^x + \frac{1}{2}O_2 + 2e^{'} \qquad (2.3\text{-}8)$$

As the donor concentration increases, the excess oxygen is retained and the compensation appears to be primarily by cation vacancies, which are, in the case of $BaTiO_3$, Ti vacancies [224; 233; 236], as shown in equation (2.3-9), in spite of the high relative charge of these vacancies. This results in a light colored insulating material.

$$2Nb_2O_5 + 5BaO \rightarrow 4Nb_{Ti}^{\bullet} + 5Ba_{Ba}^x + V_{Ti}^{''''} + 15O_O^x \qquad (2.3\text{-}9)$$

So, as the donor concentration increases, there is an abrupt transition from conducting to insulating material, and, at the same time, a significant change in the microstructure, with the grain size being similar to that of undoped $BaTiO_3$ in the first case and much smaller in the second one [224]. However, despite that the high temperature equilibrium defect in donor doped $BaTiO_3$ is a Ti vacancy mechanism, Ba vacancies can be formed at lower temperature as metastable defects due to very low diffusivity of Ti vacancies [237; 238].

In STO, the cation vacancy compensation was found to occur by strontium vacancies [231-233; 239; 240]. An excess Sr (equal to the compensating strontium vacancy concentration) is fixed by the donor content and may remain in the crystal forming layered Ruddlesden-Popper structures [241], acting as a sink or source for the strontium or, depending on the point of view, its vacancies [233]. In agreement, Meyer *et al.* reported the migration of excess Sr to the surface, under oxidizing conditions, where secondary SrO_x phases grew on top of the surface [231], leaving behind vacant Sr sites, according to equation (2.3-10):

$$Sr_{Sr}^{x} + 2e^{'} + \frac{1}{2}O_2 \Leftrightarrow V_{Sr}^{''} + SrO_{\mathrm{sec}-phase} \qquad (2.3\text{-}10)$$

In the case when Nb_2O_5 is added to STO under an oxidizing atmosphere, for every two Nb ions, one Sr vacancy is formed according to equation (2.3-11) [45]:

$$\begin{aligned} &SrTiO_3 + xNb_2O_5 \rightarrow (1-x)Sr_{Sr}^{x} + (1-2x)Ti_{Ti}^{x} \\ &+ 2xNb_{Ti}^{\bullet} + 3O_O^{x} + xV_{Sr}^{''} + xSrTiO_3 + xTiO_2 \end{aligned} \qquad (2.3\text{-}11)$$

Whether the excess charge of donors is compensated by electrons or by cation vacancies is determined by oxygen partial pressure, annealing temperature and donor concentration [237]. Under highly reducing conditions, the defect chemistry is governed by the reduction reaction (2.3-2). The oxygen vacancies are the predominant ionic defects and electrons are the charge compensating species. At intermediate pO_2 values, the oxygen vacancy concentration becomes small relatively to the extrinsic donor concentration. The compensation of the donors by electrons is dominant.

The concentration of electrons, and thus the dominant n-type conductivity, does not change with the oxygen partial pressure. Because σ has the appearance of a plateau, this regime is also called the “plateau region” or region of electronic compensation. Moreover, a relative independence of the temperature is verified for the conductivity in this regimen [235] indicating that the electron concentration is fixed by the donor concentration and that there is little temperature dependence of the electron mobility. By a further increase of the pO_2 to oxidizing conditions, the compensation for

the donor impurities is attributed to a mechanism of acceptor-like strontium vacancy compensation (as mentioned above).

The conductivity characteristics for STO doped with varying amounts of donors are represented in Figure 2.3-6. As can be seen, the donor-doped samples clearly show the plateau region with insignificant pO_2 dependence of conductivity. With increasing donor concentration, the plateau region becomes more and more pronounced, which is accompanied by an increased conductivity [233].

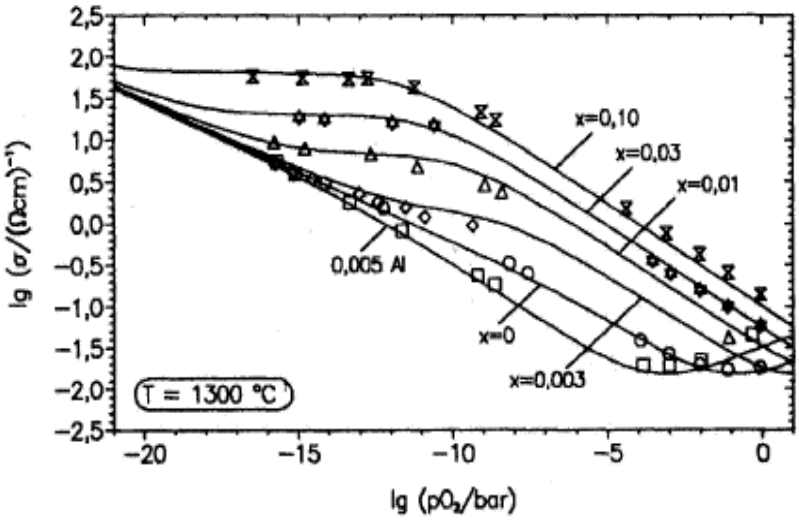

Figure 2.3-6: Equilibrium electrical conductivity of lanthanum donor doped (various concentrations), undoped and aluminum acceptor doped STO ceramics at 1300 °C [233].

2.3.4.2 Grain boundaries

Point defects models discussed above assume that the material is a homogeneous and isotropic system with a diluted concentration of defects. However, grain boundaries are present in polycrystalline ceramics and affect remarkably the overall microstructural evolution and electrical behaviour of the material. Effectively, defects may be directly related to the structure of grain boundaries. For example, Chung *et al.* [45] reported that high ionic vacancy concentration can induce interface roughening in STO.

On the other hand, charge transport in a heterogeneous material may involve bulk pathways and transport across boundaries as well as along boundaries. The behaviour of the material, therefore, turns out to depend significantly on the properties of the grain boundaries, which are markedly affected by its defect chemistry, rather than on the properties of the bulk grains [45; 242; 243]. In fact, as previously mentioned, some electrical properties required for particular applications, such as boundary layer capacitors, low-voltage varistors, or positive temperature coefficient (PTC) thermistors, are a consequence of highly engineered grain boundary electrical barriers [244]. In these cases, grain boundaries are often affected by depletion effects and exhibit highly resistive behaviour [201; 244; 245] acting as barriers to the transport of charge carriers.

The basis for the formation of a charged surface or grain boundary in ionic solids is a difference in the individual defect formation energies [244]. This leads to a preferential enrichment of the interface in the ion of lower vacancy formation energy and the formation of an adjacent space charge enriched in that vacancy. When extrinsic solutes raise defect concentrations above thermally generated concentrations they determine the sign of the grain boundary and the space charge [244].

This grain boundary barrier effect is well known, for example, for *n*-type semiconducting ceramics, being responsible for the varistor effect in donor doped ZnO ceramics as well as for the positive temperature coefficient of resistance (PTCR) effect in donor doped $BaTiO_3$ ceramics [246]. In these cases, a negatively charged grain boundary is compensated by the positively charged donor centres in the bulk adjacent to the grain boundaries forming a depletion space charge layer necessary for electroneutrality.

For undoped and acceptor-doped alkaline earth titanates, positively charged grain boundary interface states seem to be active even at sintering temperatures [244]. A space charge layer model was developed for grain boundaries in acceptor-doped titanate ceramics [238; 244-246]. Due to the existence of positively charged grain boundary states, the regions close to the grain boundaries are depleted of mobile charge carriers with the same charge sign as the grain boundary states (oxygen vacancies and holes are repelled from the vicinity of the grain boundary). At the same time, electrons are

accumulated because the positive grain boundary charge has to be compensated by a negative space charge on both sides of the grain boundary built up by the immobile bulk acceptors.

This redistribution of charges leads to the formation of the space charge layer, as illustrated in Figure 2.3-7. The grain boundary resistivity can be explained by the fact that the major charge carriers have to overcome this positively charged barrier. The width of the grain boundary depletion layer in acceptor-doped STO has been determined to be 30-200 nm, decreasing with increasing acceptor concentration [245].

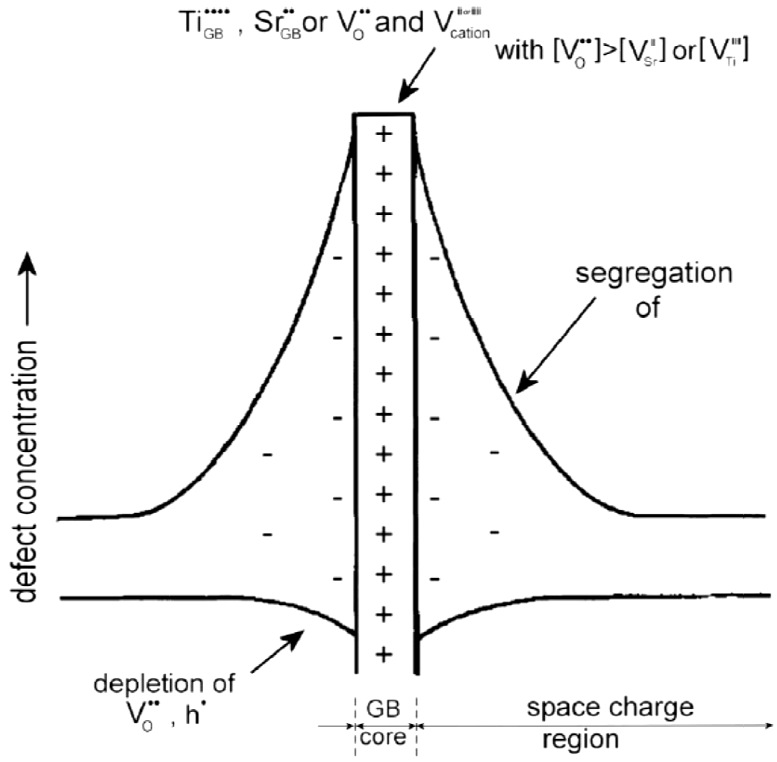

Figure 2.3-7: Possible distribution of charged defects at a nonstoichiometric grain boundary showing a positive grain boundary core and a negative space charge ([247] adapted from reference [244]).

The structural accommodation between two grains occurs approximately over only a few nanometers [243]. The investigations of the grain boundary region in $BaTiO_3$ and STO

by Chiang and Takagi revealed a strong segregation of acceptor impurities to the grain boundary [238; 244]. In contrast, a segregation of donors was not observed. However, another investigation revealed slight donor segregation [243] at the grain boundaries in polycrystalline STO. Chiang and Takagi also found Ti in excess in the grain boundaries and no systematic variation in the excess of Ti with the overall composition, including A site / B site cation stoichiometry [244].

Other investigations confirm the presence of Ti-rich layers at grain boundaries [248-250]. Oxygen deficiency at the interfaces due to unoccupied lattice sites and oxygen vacancy segregation to the boundary were also reported [249]. These vacancies are compensated by electrons resulting from the lowering of the Ti valence, which form a *n*-type layer at the interface [249].

More recently, Bäurer *et al.* [247] using Scanning Transmission Electron Microscopy (STEM) coupled with Energy Dispersive Spectroscopy (EDS) also observed local nonstoichiometry at the grain boundaries of strontium titanate. Ti-rich, neutral and Sr-rich grain boundaries were detected, independently of the bulk composition (Ti or Sr-rich) [247]. This indicates that grain boundaries are additional degrees of freedom in a phase diagram, where compositions not stable as a bulk phase are possible. The possible distribution of defects in the grain boundary region of STO is presented in Figure 2.3-7. Ti rich boundaries showed a retarding effect on GB mobility, probably due to a solute drag mechanism. On the other hand, long (100)-facets, which were neutral or Sr-rich, showed the highest mobility [247]. This was correlated to the high number of Ti and O vacancies in these grain boundaries [42; 251].

It is important to note here that the nonstoichiometry at the grain boundaries must be compensated by defects accommodating the excess of the other species in the bulk. The Ti or Sr-excess accommodation will be reviewed ahead.

2.3.4.3 Surfaces

The surface of titanates strongly influences their macroscopic properties. Usually, the surface region exhibits different behaviour compared to the bulk of the crystal [252; 253].

Consequently, the microstructure evolution of the material may also be affected by surface phenomena. In addition, phenomena related with the surface region are of special relevance for technological applications in which thin layers, such as thin films of STO, are used as dielectrics in microelectronic devices [253]. For reduced thickness, as in the case of films, the influence of the surface may become even more important.

For these reasons, the surface of titanates has received attention in the last few years. It was found that the surface region can be restructured by exposing the sample to extreme atmospheric conditions, elevated temperatures and prolonged annealing times [252-255]. XRD measurements [252] showed that reactions take place in the solid phase in the surface layer of STO, $BaTiO_3$ or $PbTiO_3$ perovskite crystals at temperatures between 500 and 1000 °C, associated with segregation of AO complexes in the direction of the surface. It was reported that the near-surface region of STO, extending several tens of nm into the bulk of the material, develops chemical heterogeneities after thermal treatment in reducing as well as oxidizing conditions [256]. In fact, the surface undergoes a continuous change in time, which leads in the case of oxidizing conditions to a continuous accumulation of SrO on the surface and, in the case of reducing conditions, to the ongoing loss of oxygen from the Ti-enriched surfaces [253; 256].

2.3.4.4 Nonstoichiometry

As previously discussed, the solubility limits for either Sr- or Ti-excess in the STO lattice are quite low and have been discussed for decades [16; 225; 257; 258]. Nevertheless, some incorporation is still possible [259].

It is generally accepted that the interstitial occupation is not likely in STO because of the closely packed perovskite lattice [187; 235]. Additionally, titanium vacancies are generally considered unlikely defects because of its high effective charge that corresponds to a major disruption of the chemical bonding of the crystal. This is in accordance with the notable lack of diffusion of impurities that occupy Ti sites [235]. On the other hand, theoretical calculations within the STO defect models indicate that vacancy disorder is predominant in this material [232]. Accordingly, oxygen vacancies are

known to be easily formed in perovskite compounds [225; 250] and strontium vacancies are often assumed to be the most important defect compensation mechanism in STO [45; 231-233; 260; 261].

After these considerations, the excess oxide, SrO or TiO_2, may be incorporated in the perovskite lattice as shown in Table 2.3-1 and described in the following text. The incorporation of SrO-excess requires the formation of interstitial strontium and oxygen, not likely and therefore neglected, or titanium and oxygen vacancies [16; 225; 259] according to equation (2.3-12). However, considering the high charge of titanium vacancies, the incorporation of Sr-excess would not be very favourable. On the other hand, another way considering cation-site exchange (anti-site defect) may be as presented in (2.3-13) [16; 225]. It was shown that in some perovskite related compounds, some of the Sr^{2+} ions occupy B sites even though it is not necessary from the stoichiometry and so this way of SrO-excess incorporation cannot be excluded [16].

Table 2.3-1: Possible incorporation mechanisms of excess oxide, SrO or TiO_2, in STO.

Incorporation mechanism		Ref.
SrO-excess		
$SrO \rightarrow Sr_{Sr} + V_{Ti}^{''''} + O_O + 2V_O^{\bullet\bullet}$	(2.3-12)	16; 225; 259
$2SrO \rightarrow Sr_{Sr} + Sr_{Ti}^{''} + 2O_O + V_O^{\bullet\bullet}$	(2.3-13)	16; 225
TiO_2-excess		
$TiO_2 \rightarrow V_{Sr}^{''} + Ti_{Ti} + 2O_O + V_O^{\bullet\bullet}$	(2.3-14)	16; 225; 259; 262

According to Witek *et al.* [16], the solubility limit of SrO-excess does not extend beyond Sr/Ti = 1.002. Nevertheless, SrO-excess is known to accommodate in the STO lattice as a three-dimensional mosaic of single-layered rock-salt blocks, forming the so-called Ruddlesden–Popper structures with the formula $SrO.(SrTiO_3)_n$ [225; 241; 259; 262], allowing the accommodation of the excess SrO in the STO lattice.

On the other hand, neglecting interstitial occupation, the incorporation of TiO_2-excess into the lattice requires the formation of strontium and oxygen vacancies [16; 225; 259; 262] according to equation (2.3-14). As mentioned above, the ease of formation of oxygen vacancies in perovskite compounds and the fact that strontium vacancies are assumed to be the most important compensation mechanism in STO [45; 231-233; 260; 261] support this equation as the way of incorporation of TiO_2-excess. It was reported that STO with TiO_2-excess of 0.5 mol% (Sr/Ti = 0.995) shows the presence of TiO_2 as a second phase [16] in the form of rutile [263].

2.3.5 Grain growth and grain boundary phenomena in $SrTiO_3$

Grain growth in titanates is very complex and, as previously mentioned, generally depends on many factors like oxygen partial pressure, dopant species and concentration, nonstoichiometry and sintering temperature, among others, which affect the grain boundary characteristics. All these factors are important to understand the microstructure evolution of titanates during sintering. In this way, if understood and controlled, they may be used to obtain desired final microstructures.

The grain growth of STO has fundamentally and technologically interested researchers for a long time and new revealing results have been published in the last years. Particular attention has been given to grain boundaries and their relation with grain growth of STO. The main observations are summarized in the following text.

Related to high interface anisotropy, faceting of grain boundaries of STO has been related to the origin of abnormal grain growth [264]. Due to a nucleation energy barrier for new atomic layers on a singular surface, some grains may grow abnormally if favoured by the existence of attachment sites [265], such as dislocations [266]. This nucleation-limited growth theory was experimentally validated for STO grains coarsening in a Ti-rich liquid [45; 265].

In agreement with these observations, Chung and Kang [266; 267] showed that dislocations enhance the mobility of faceted flat interfaces in the presence of a thin liquid film between grains in STO. Dislocations did not play any role of grain growth promotion

when the interfaces were curved. Additionally, the effect of dislocations occurred only when the grain boundaries were wetted by an intergranular amorphous phase [267]. From these observations, the authors suggested that an uneven distribution of dislocations might be a cause of abnormal grain growth in polycrystalline STO.

Lee *et al.* [46] used High-Resolution Electron Microscopy to investigate the temperature dependence of faceting of an asymmetric Σ5 boundary between two STO crystals in the temperature range of 1100 to 1600 °C. Changes in faceting behaviour with temperature were observed, as illustrated in Figure 2.3-8. Between 1100 and 1600 °C the boundary was faceted with changes in facet symmetry occurring at 1300 °C. At 1600 °C, faceting disappeared and the grain boundary became defaceted, indicating the occurrence of a grain boundary faceting-defaceting transition [46]. In a related investigation [268], the authors observed that the defaceting transition occurred suddenly between 1570 and 1590 °C.

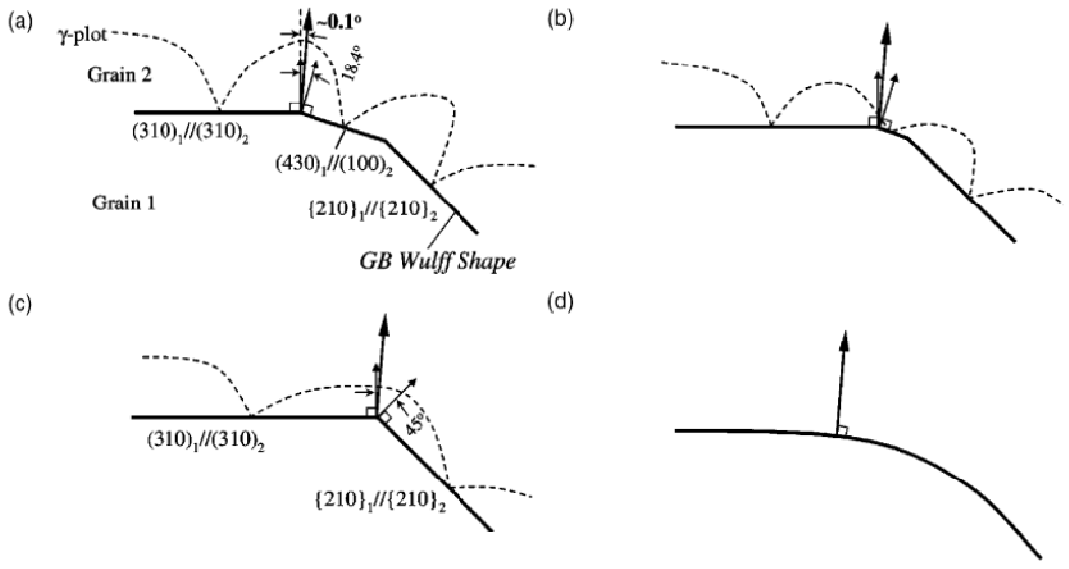

Figure 2.3-8: Schematic diagram for the equilibrium grain shape at the temperatures: (a) and (b) 1100-1300 °C, (c) 1300-1500 °C and (d) 1600 °C. Surface free energy with respect to the surface plane normal orientation (γ-plot) is also illustrated [46]. With increasing temperature, a boundary faceting-defaceting transition is observed.

Further developments were made using a combination of Impedance Spectroscopy, High Resolution TEM (HRTEM) and Electron Energy Loss Spectroscopy (EELS). The rough grain boundary observed at 1600 °C contained more oxygen vacancies than the faceted grain boundaries observed below 1600 °C [49]. Moreover, disordering of grain boundary by the defaceting transition caused an abrupt appearance of grain-boundary impedance at 1600 °C, demonstrating a relation between the change in grain boundary impedance, grain boundary electronic structure and the grain boundary faceting-defaceting transition [49].

Chung *et al*. [45] studied the effect of donor addition and sintering atmosphere on interface morphology and grain growth behaviour in Nb_2O_5-doped STO. The authors reported that ionic vacancies in STO can induce interface roughening and suppress abnormal grain growth. As the concentration of strontium or oxygen vacancies increased with the addition of a donor or reduction in oxygen partial pressure, the shape of the interface changed from faceted to rough and the anisotropy in interface energy disappeared [45]. The grain growth behaviour was reported to be dependent on the interface structure: normal grain growth with a rough interface and abnormal grain growth with a faceted singular interface.

In another investigation, Chung *et al.* [269] studied the effect of sintering atmosphere on grain boundary segregation and grain growth in 2.4 at % Nb-doped STO. The authors found no abnormal grains in samples sintered for 2h at 1360 °C, below the eutectic temperature, in air and in H_2. However, the average grain size in the sample sintered in H_2, where Nb ions were segregated in the boundary regions, was much smaller than in the sample sintered in air. For a sintering temperature of 1460 °C, above the eutectic temperature, the grain growth was also strongly inhibited for the samples sintered in H_2. This suppression of the grain growth was attributed to the grain boundary dragging of segregated Nb and to the reduction in Ti vacancy concentration in H_2 atmosphere.

Other investigations also reported strong suppression of grain growth in STO due to high dopant concentration [260; 261; 270]. The results of You *et al*. [261] for WO_3 doped STO sintered in various atmospheres and temperatures of 1470 °C and 1435 °C showed that the grain size was not dependent on the pO_2 but was very affected by the amount

of dopant: it increased until about 0.3 mol% of dopant concentration, decreasing for higher dopant amounts. Sr-W-rich second phases were observed in specimens with a dopant content of 3 mol%, which were ascribed to the movement of Sr ions from the lattice to the grain boundaries leaving compensating vacancies in the lattice. The formation of Sr vacancies was considered to account for the decrease in the conductivity after 1.2 mol% dopant addition.

Similar results were obtained by Inaculescu *et al.* [260] for Sb-doped STO. Over a critical Sb proportion the average grain size started to decrease and homogeneous microstructures consisting of small grains were observed. The authors correlated this microstructure feature with the change of compensation mechanism of the supplementary charge induced by the Sb^{5+} donor dopant. Below a critical Sb concentration the compensating defects were considered to be the electrons resulted from the Ti^{4+} towards Ti^{3+} reduction. On the other hand, over this concentration value a strontium vacancy compensation mechanism was assumed as the most probable [260], in accordance with the observed coincidence between the grain growth inhibition threshold and loss of semiconductivity in titanates [271; 272].

Peng and Chiang [270] investigated the grain growth of Nb-doped STO and reported exaggerated grain growth at low donor concentrations resulting from the presence of a continuously wetting grain boundary silicate. On the other hand, inhibited growth at higher donor concentrations occurred in microstructures where the silicate phase was non-wetting. This behaviour occurred only in nonstoichiometric compositions with an excess of B-site cations [270].

The presence of IGFs has indeed a significant effect on the grain growth of STO [267; 270]. The distribution of such amorphous phases is important and may considerably change depending on the annealing path and conditions [267]. As an example, a liquid film was reported between grain boundaries of Nb_2O_5-doped STO after annealing in air at 1470 °C, irrespective of a pre-annealing at 1250 °C. On the other hand, with annealing in a reducing atmosphere, two types of grain boundaries, with and without amorphous films were found to be stable. A wetting intergranular phase was found after direct annealing at 1470 °C, whereas the amorphous phase did not penetrate into the grain

boundaries at 1470 °C in samples with a 15 h pre-annealing below the eutectic temperature [267], which lead to the stabilization of dry boundaries before the liquid phase formation. In Ti-excess STO with low donor concentration, a continuous liquid film wets the grain boundaries and faster grain growth occurs [270]. It was reported as well that in the presence of a thin liquid film between grains, dislocations promote grain growth of STO [266; 267]. In another work, 1 mol% TiO_2 was added to the STO powders to create a TiO_2-excess liquid above the eutectic temperature [45]. TEM showed liquid phase in the triple junction of the grains and the interface between the STO grains and the liquid was faceted [45].

Recently, IGFs were also reported for Fe-doped STO [273]. These films were observed even below the STO eutectic temperature of 1440 °C, which was attributed to the possible liquid phase formation at about 1200 °C in the $SrO–Fe_2O_3$ system [274]. Ti-rich and Sr-rich IGFs, both containing Fe segregation, were found coexisting in each sample irrespective of the sintering temperature (below or above the eutectic at 1440 °C). However, with increased dwelling times, some Sr-rich intergranular films turned to Ti-rich, indicating that the former was in a transient state and the equilibrium film had most likely a TiO_2-based composition [273]. These observations are in agreement with those of Bäurer *et al*. [247] that, although no amorphous film was observed between grains, reported a similar trend of Sr-rich grain boundaries to change into Ti-rich ones with extended annealing time in TiO_2-excess STO.

Nonstoichiometry is, in fact, an important aspect influencing grain growth in titanates and particularly in STO. It is often found that TiO_2-excess deteriorates densification while SrO-excess improves it, as observed by Chen *et al*. [275]. A strong influence of nonstoichiometry on densification of STO was observed in dilatometric experiments [259; 263] with higher densification rates measured for Ti-rich compositions [259]. In fact, our previous studies revealed two peaks on the dependence of the densification rate on the temperature for stoichiometric and Ti-rich samples (more pronounced in the later case), whereas a monomodal curve characterized the Sr-rich composition [259]. The position of the peaks varied systematically with the Sr/Ti ratio and was bellow the eutectic temperature; this might be related to the formation of IGFs, leading to subsolidus activated sintering, as previously discussed.

The densification behaviour of stoichiometric compositions is usually closer to that of Ti-rich compositions than to that of Sr-excess ones [259; 263]. Additionally, coarser grain microstructures and higher grain growth rates are observed with the decrease of the Sr/Ti ratio [259; 275-277]. Sr-excess normally leads to normal grain growth whereas abnormal grain growth is often observed for Ti-rich compositions [275; 278].

The changes in the sintering behaviour of STO induced by nonstoichiometry have been correlated with changes in the defect chemistry of the material introduced by the incorporation of the excess oxide [259; 263], as previously discussed. It is also important to recall that the Ti-rich side of the SrO-TiO_2 phase diagram [221] shows an eutectic at 1440 °C. Therefore, liquid phase may form above this temperature for Ti-excess compositions enhancing matter transport. Nevertheless, abnormal grain growth in STO without detected liquid phase has also been reported [247; 279].

Recently, in grain growth studies of STO nonstoichiometric samples sintered in oxygen atmosphere from 1425 to 1600 °C [247], it was reported that Ti-rich Sr/Ti = 0.996 and Sr-rich Sr/Ti = 1.002 compositions showed the same overall growth behaviour, with abnormal grain growth being observed in both cases. On the other hand, in a composition with higher SrO excess, Sr/Ti = 1.005, grains grew normally but with a grain boundary mobility that was similar to the mobility of the abnormal grain growth of the other compositions.

A deeper correlation between grain growth behaviour and grain boundaries in STO was attempted using HRTEM and STEM-EDS. Grain boundaries of normal and abnormal grains were investigated [247]. As presented in Figure 2.3-9, four types of grain boundaries were reported. Type A grain boundaries were atomically flat with a boundary plane parallel to the (100) plane in one of the adjacent grains; type B had the same boundary plane orientation but were atomically disordered or rough; type C were stepped boundaries and type D boundaries were curved. Grain boundaries of types C and D did not show a preferred crystallographic orientation of the grain boundary plane for either of the adjacent grains [247].

The grain boundary chemistry was also evaluated and nonstoichiometry at the grain boundaries was found, weakly correlated to boundary morphology [247]. Ti-rich, neutral

and Sr-rich grain boundaries were detected, independently of the bulk composition. The boundary chemistry showed an important effect on the boundary kinetics, with neutral or Sr-rich (100)-faceted boundaries showing the highest mobility. On the other hand, Ti-rich boundaries showed a retarding effect on grain boundary mobility, which was attributed to a solute drag mechanism [247].

Sr-rich boundaries were only detected in the types A and B whereas no Ti-rich type A boundary was observed. Additionally, type A boundaries were not detected in Sr/Ti = 1.005 that did not show abnormal grain growth. In agreement, abnormal grains in the Sr/Ti = 0.996 sample showed the largest fraction of this type of boundaries and only a small fraction of type D ones. In the Sr/Ti = 1.005 composition, type B boundaries were the largest fraction. On the other hand, the normally grown grains of the Ti-rich composition had more similar fractions of all four kinds of boundaries.

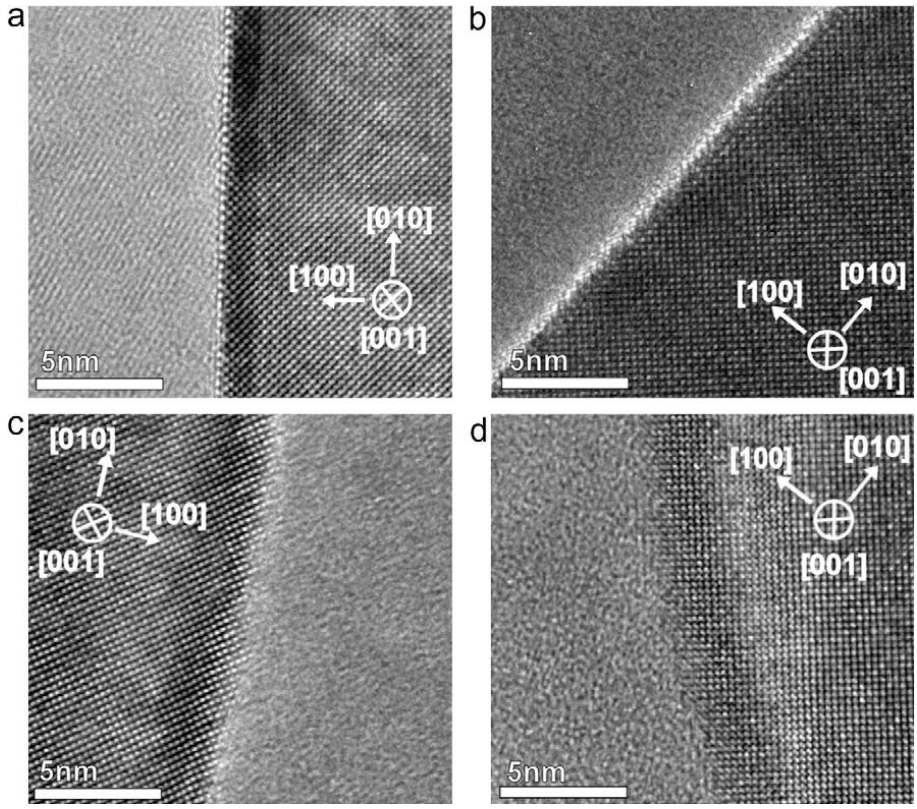

Figure 2.3-9: Grain boundary morphology types observed in STO: (a) type A: ordered flat; (b) type B: disordered flat; (c) type C: stepped; (d) type D: curved [247].

The grain boundary types observed in STO were correlated to the boundary complexions defined in alumina [35; 58; 59] and previously presented in Figure 2.1-9. The low-mobility Ti-excess boundaries were compared to complexion I where the movement is retarded by segregation of a species. The stoichiometric boundaries were found to be of type II whereas high-mobility nonstoichiometric boundaries were associated to complexion III [247].

However, Bäurer *et al.* [247] did not report any amorphous films at the grain boundaries for either normal or abnormal grains, which would be essential for the formation of complexions of types IV to VI observed by Dillon *et al.* [35]. Nevertheless, these complexions should be possible to induce in STO by the stabilization of a liquid film at the grain boundaries, leading to higher grain boundary mobilities [247]. According to Bäurer *et al.* [247], the observation of the different grain boundary types in STO is in agreement with the explanation of abnormal grain growth by the co-existence of two or more grain boundary complexions [35], with the correspondent differences in mobility.

In a related investigation, a grain growth anomaly in strontium titanate was observed [76]. Bäurer *et al.* studied the grain growth behaviour of STO sintered in an oxygen atmosphere in the temperature range of 1200 to 1600 °C. They reported two drops in the grain boundary mobility with increasing temperature independent of the A-site to B-site stoichiometry, as depicted in Figure 2.3-10. The grain growth kinetics did not follow the classical Arrhenius-type temperature dependence, indicating changes in the basic mechanism of grain boundary motion [76].

The unexpected grain growth behaviour observed in STO was related to structural changes of the grain boundaries at high temperatures, such as changes in the faceting behaviour [76; 251]. In samples sintered at 1425 °C, a high preference for grain boundary planes oriented parallel to the 100 direction of one of the adjacent grains was found [247], which did not exist in the low temperature regime (samples sintered at 1300 °C) [251]. This was pointed as a possible explanation for the change in grain growth rate [251].

However, the exact mechanism involved in the mobility drops is still unknown. Additionally, the correlation with grain boundary characteristics addressed in Ref. [247],

namely grain boundary complexions, is unclear and needs further development. Moreover, no link was yet established between the formation of different grain boundary complexions and a particular grain boundary dielectric response.

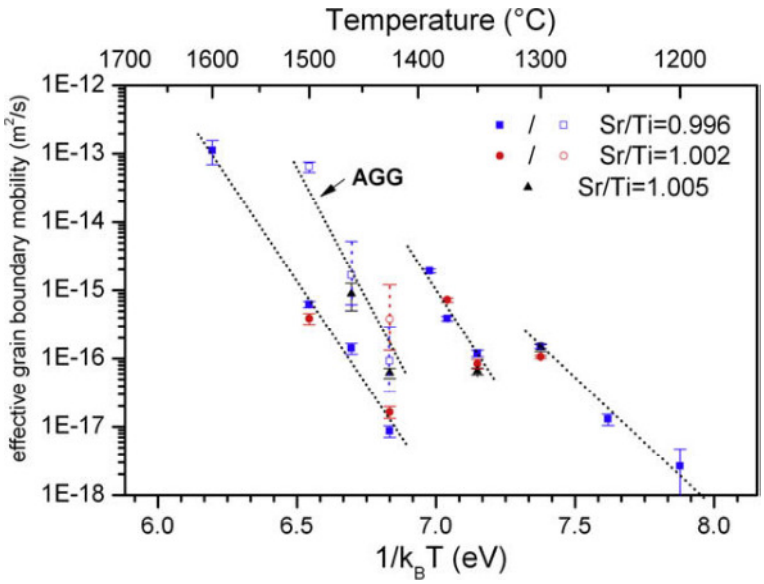

Figure 2.3-10: Arrhenius-type diagram of effective mobility as a function of the thermal activation energy for strontium titanate with various Sr/Ti ratios. Closed symbols represent normal growth, open symbols abnormal growth [76]. Two drops in the grain boundary mobility with increasing temperature may be observed.

The understanding of the grain growth anomaly and the correlation to the grain boundary properties have great scientific and technological importance because it may offer an alternative way of controlling the microstructure and tuning the dielectric response of STO-based compositions without the use of dopants.

2.4 Objectives of the thesis

In the presented context, the objectives of this work consist in the investigation of the tailoring of the dielectric response in EPD thick films and bulk ceramics by controlling the microstructure evolution during sintering of titanate-based electroceramics.

Two important groups of functional materials were chosen: incipient ferroelectric strontium titanate and low loss microwave dielectrics typified by the $BaO\text{-}Ln_2O_3\text{-}TiO_2$ (Ln = La or Nd) family of compounds. The purpose is to use the right combination of intrinsic material characteristics and microstructure determinant processing parameters to study the design of the microstructure and tailoring of the dielectric response of the materials.

The trend of continuous miniaturization and increased integration in microelectronic and communications industry requires the substitution of components previously fabricated from bulk ceramics by, for example, thick films [3; 9]. $BaO\text{-}Ln_2O_3\text{-}TiO_2$ (Ln = La or Nd) low loss dielectrics have anisometric crystal structures and grains tend to grow in the shape of platelets or needles [17; 18]. However, the relation between the microstructure and dielectric properties of these materials is not completely understood. Therefore, the natural trend of elongated grain growth of these materials is exploited in combination with the particular features of constrained sintering, namely the effect of stresses from the substrate [84], to develop anisotropic microstructures with marked effects on the dielectric properties. Relations between processing, microstructure and dielectric response are established.

On the other hand, STO is a well-known insipient ferroelectric. Particular attention has been paid to the semiconduction properties of doped STO for applications like grain boundary layer capacitors [14] (which generally consist of semiconductive grains and insulating grain boundaries [280]) and to the bulk quantum paraelectric properties for tunable microwave applications [13], such as tunable microwave capacitors or microwave phase shifters. This material is also a promising candidate for thermoelectric applications [15; 209; 210; 212]. Heat-to-electricity conversion is regarded as one of the promising methods to harvest energy from, for example, waste heat.

Thermoelectric power-generation applications are currently being investigated by the automotive industry to develop electrical power from waste engine heat from the radiator and exhaust systems for use in next-generation vehicles [212]. In addition, thermoelectric refrigeration technology may be used for electronic component cooling [212]. However, resistive grain boundaries are an obstacle to the thermoelectric efficiency of STO-based materials [211].

Due to the cubic nature of the perovskite structure the effects of constrained sintering are not expected to be as effective in STO as in BLnT (Ln = La or Nd). On the other hand, the fact that the perovskite structure is very tolerant to defects in the lattice may be used to induce changes in the defect chemistry of the material, for example by means of intentional nonstoichiometry [16]. The effect of nonstoichiometry on the microstructure development and dielectric properties of STO is still not clear and requires a systematic approach. Additionally, a discontinuous dependence of the grain boundary properties on the temperature has been reported for this material [76] and, therefore, the appropriate sintering temperature may be used to induce adequate grain boundary properties and control the microstructure evolution leading to resultant tailored dielectric properties.

In summary, this work has two specific objectives: (i) the study of the effect of nonstoichiometry and sintering temperature in ceramics and thick films of STO on microstructure evolution during sintering and on the dielectric response of the material; (ii) the study of microstructural anisotropy development during constrained sintering of BLnT (Ln = La or Nd) and STO thick films and its effect on the dielectric behaviour of the materials.

In the end, both approaches constitute attempts to design the microstructure of the materials and in this way tailor their dielectric responses. Moreover, the results of this work have significant scientific and technological importance in the scope of the investigated materials but also may probably be extended to other systems with generally similar structural and chemical characteristics.

3 Experimental Procedures and Techniques

The present chapter deals with the experimental procedures and techniques used in the course of this work. A description of the experimental aspects from the synthesis of the powders, suspension preparation, electrophoretic deposition of films, pressing of films and bulk samples, free and constrained sintering to the microstructural and dielectric characterization of the samples is presented.

For the study of microstructure development during constrained sintering, thick films were fabricated by Electrophoretic Deposition. A non-exhaustive description of EPD is given and further details can be found in several reviews on the topic (such as references [83; 281-286]).

Impedance Spectroscopy was employed to assess the effect of nonstoichiometry and sintering temperature on the dielectric properties of strontium titanate ceramics, separating bulk and grain boundary contributions. The basic principles are described and for details on IS falling outside the scope of this work references [287-289] are recommended.

3.1 Experimental procedures

The general experimental steps undertaken during the present work are schematically presented in the flowchart in Figure 3.1-1. The first step of the experimental work was related with the preparation of BLnT (Ln: La and Nd) and STO powders. Then, powder suspensions were prepared and EPD was used to fabricate thick films for constrained sintering studies. At the same time, bulk ceramic samples were produced and freely sintered for comparison. The microstructure of both types of samples was then characterized, as well as their dielectric properties. The experimental details of these steps are further explained in the following text and complemented in the corresponding chapter.

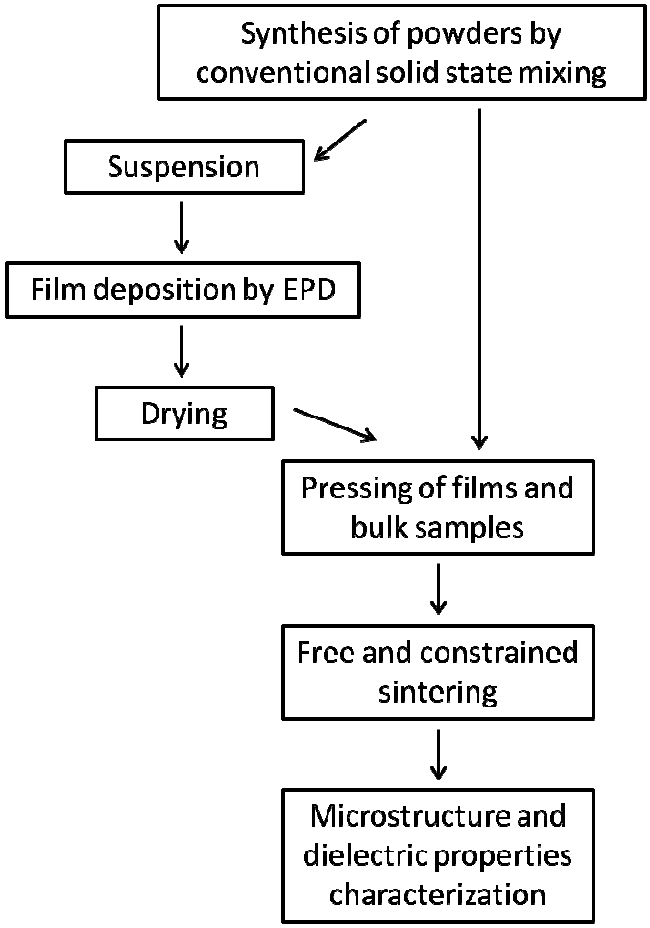

Figure 3.1-1: General flowchart of the experimental procedures used in this work, from powders preparation to sample characterization.

3.1.1 Processing of the samples

3.1.1.1 Powders

The powders of the BLnT (Ln: La and Nd) and STO compositions investigated in this work (Table 3.1-1), in the later case with Sr/Ti ratio variations between 0.995 and 1.02, were prepared by the conventional solid state reaction method from the individual oxides or carbonates. STO powders were prepared from $SrCO_3$ and TiO_2 (99% purity, Merck); in the case of BLT powders, TiO_2 (99.9%), $BaCO_3$ (99.8%) and La_2O_3 (99.9%) (Alfa Aesar) were used; similarly, BNT powders were prepared using TiO_2 (99.9%), $BaCO_3$ (99.8%) (Alfa Aesar) and Nd_2O_3 (99.9%, Aldrich).

Table 3.1-1: STO and BLnT (Ln: La and Nd) compositions used in this work. Milling and calcination conditions are also presented.

Sr / Ti	Designation	Composition	Milling	Calcination
		STO		
0.995	ST 0.995	$Sr_{0.997}TiO_{2.995}$		
0.997	ST 0.997	$Sr_{0.997}TiO_{2.997}$		
1	ST	$SrTiO_3$	5h,	1100 °C,
1.005	ST 1.005	$Sr_{1.005}TiO_{3.005}$	180 rpm	2h
1.01	ST 1.01	$Sr_{1.02}TiO_{3.01}$		
1.02	ST 1.02	$Sr_{1.02}TiO_{3.02}$		
		BLnT (Ln: La and Nd)		
--	BLT	$BaLa_4Ti_4O_{15}$	24h, 180 rpm	1330 °C, 3h
--	BNT	$Ba_{4.5}Nd_9Ti_{18}O_{54}$		1200 ˚C, 3h

The starting precursors were weighed according to the intended stoichiometric proportions and ball milled in ethanol using Teflon pots and ZrO_2 milling balls. The mixtures were subsequently dried at 60 °C for one day and calcined in an alumina crucible. Then, a further milling and drying step followed to break agglomerates and decrease the particle size. The mixing/milling and calcination conditions used regarding the several compositions are also presented in Table 3.1-1.

3.1.2 Electrophoretic Deposition

3.1.2.1 Suspensions

Suspensions for the electrophoretic deposition of BLnT (Ln: La and Nd) and STO films were prepared by slowly adding 1 g of powder to 100 ml of solvent. The mixture was subsequently stirred in an ultrasonic bath for 5 min to promote the dispersion of

powders in the suspension. During stirring, the additives were added to the suspension.

Iodine (I_2) (99,999%, Merck), nitric acid (HNO_3) (65%, PA-ISO; Panreac) and triethanolamine ($C_6H_{15}NO_3$) (> 99%, Merck), abbreviated as TEA, were used as additives for the EPD of STO, BLT and BNT powders, respectively. I_2 [290; 291], HNO_3 [292; 293] and TEA [176] have been reported to be effective additives to disperse diverse ceramic powders in acetone or ethanol based suspensions for the EPD process.

3.1.2.2 Substrates and electrodes

Platinum foils with the dimensions of 11x11x0.025 mm³ (Premion 99.99%, Alfa Aesar) were used as substrates for the deposition of BLnT (Ln: La and Nd) and STO films and also as counter electrodes. In the case of BLT, densified BLT substrates were also used. These 2.5 mm thick BLT substrates were prepared by uniaxial pressing at 100 MPa and then sintered at 1500 ˚C, for 180 min. Their surface was then polished with a coarse grinding paper and coated with a carbon layer.

As previously referred, EPD requires two conducting electrodes (anode and cathode). Therefore, in order to use insulating substrates such as densified BLT, it was necessary to deposit a conducting carbon layer on the substrate surface. This layer acted as a temporary bottom electrode, being burnt out during heating without leaving any residual contaminations.

3.1.2.3 Deposition equipment

The EPD apparatus used in this work is composed of a DC power source (EPS, Stromversorgung Gmbh, Germany), an ultrasonic bath (Branson, USA) and an EPD cell, which was homemade and previously developed in the group [294]. The EPD cell is presented in Figure 3.1-2 and includes three main parts: the base, the mask and the metal pole for conductive connection.

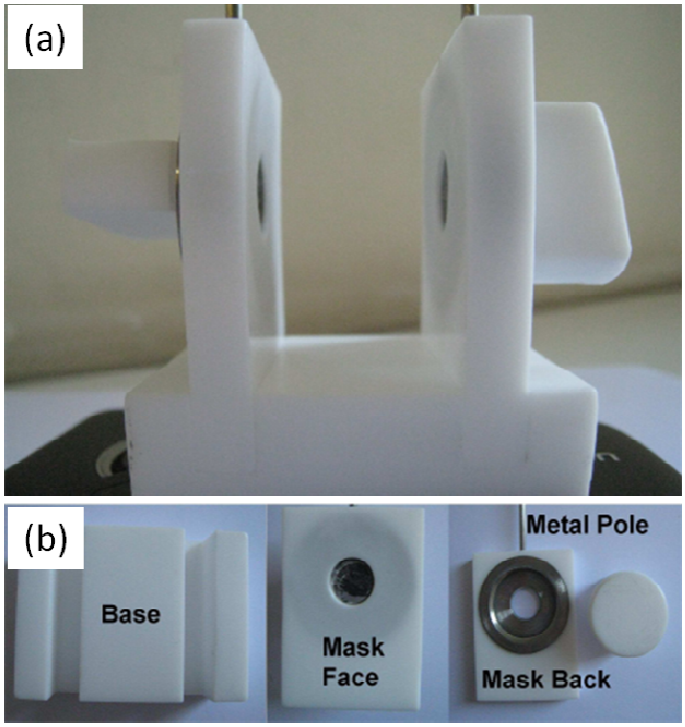

Figure 3.1-2: (a) the EPD cell used in this work and (b) its components [294].

The substrates, Pt foil or carbon coated BLT, were placed in the mask chamber and pressed by the back screw. The two equal masks were mounted on the base and the two steel poles provided the electrical connection to the external power source.

3.1.2.4 Deposition

For the deposition, the EPD cell of Figure 3.1-2 was immersed in the suspension in a 200 ml glass beaker. The platinum foil as working electrode (cathode) was separated 2 cm from the Pt counter electrode (anode) in EPD cell. Prior to each EPD cycle the suspensions were ultrasonically dispersed for 1 min. Constant voltage mode was used in the current work to deposit BLnT (Ln: La and Nd) and STO films by EPD with various deposition times.

3.1.2.5 Post-deposition treatment

3.1.2.5.1 Drying and pressing

The as-deposited films were dried at room temperature for 24 h and then submitted to Cold Isostatic Pressing (CIP) (Stansted Fluid Power Ltd) at 200 MPa, to increase the green density.

3.1.2.5.2 Constrained sintering of thick films

The range of sintering temperature for each material was selected after a dilatometric analysis in a computer assisted vertical dilatometer (Linseis, mod. 4 L70-2000).

The pressed films were heated up with a constant heating rate to the selected sintering temperature and sintered in air. Isothermal sintering times varied from 0 to 720 min.

3.1.2.6 Free sintering of bulk ceramics

Bulk ceramics of BLnT (Ln: La and Nd) and STO were also fabricated for comparison with the equivalent thick films. These bulk specimens (around 1 cm height and diameter) were prepared by uniaxial pressing of the powders at 100 MPa in order to obtain a green density similar to that of the films. They were then sintered using the same heating schedule used for the films.

Bulk samples were also prepared from STO powders with various Sr/Ti ratios for grain growth and impedance spectroscopy studies. In these cases, the powders were uniaxially pressed at 50 MPa and then isostatically pressed at 200 MPa. The samples were heated up to sintering temperatures between 1400 and 1650 ˚C and sintered in air for various isothermal times.

3.1.3 Powders and suspensions characterization

3.1.3.1 Coulter

A laser particle size device (LS230, Beckman Coulter, Inc., USA) was used to determine the particle size and particle size distribution of as-prepared powders.

Based on the effect of light scattering, this method enables the measurement of particles from 0.04 μm to 2000 μm without the risk of missing either the largest or the smallest particles in the sample. The analysis is conducted in suspension with concentrations of 1 g/l, previously ultrasonicated (Branson, USA) for 5 min before each measurement.

3.1.3.2 Zeta potential

The zeta potential of particles in a suspension is measured by applying an electric field across the dispersion. Under the electric field particles within the dispersion will migrate towards the electrode of the opposite charge with a velocity proportional to the magnitude of the zeta potential.

In this work, an Electrophoretic Light Scattering (ELS) spectrophotometer (Delsa- 440 SX, Beckman Coulter, Inc., USA) was used to measure the zeta potential of STO compositions suspended in water. Hydrochloric acid (HCl) and sodium hydroxide (NaOH) were used to vary the pH.

3.1.3.3 Transmittance measurement of UV light

Transmittance is the fraction of incident light at a specified wavelength that passes through a sample and is given as a percentage. Well dispersed suspensions show low percentage of transmittance. In this work, UV Spectrophotometer (UV-2101/3101PC, Shimadzu Scientific Instruments Inc, USA) was employed in the transmittance measurements to assess the dispersion degree of suspensions.

3.1.4 Structure and microstructure characterization

3.1.4.1 X-ray Diffraction

The phase assemblage of calcined powders and sintered samples was examined by powder X-ray Diffraction (XRD) technique.

Because the wavelength of X-rays (from few angstroms to 0.1 angstrom) is comparable to the size of atoms, they are ideally suited for probing the structural arrangement of atoms and molecules in a wide range of materials. A monochromatic X-ray beam with a wavelength λ incident onto a crystalline material at an angle θ leads to diffraction when the distance travelled by the rays reflected from successive planes differs by a complete number k of wavelengths. By varying the angle θ, the Bragg's law conditions are satisfied for different d-spacings in polycrystalline materials [295] according to the equation [296]:

$$2dsin(\theta) = k\lambda \qquad (3.1\text{-}1)$$

In the current work the X-ray diffraction analysis of powders, films and bulk ceramics was carried out with a Rigaku (D/Max-C series) X-ray diffactometer, using Cu-Kα radiation (λ=0.15064 nm). The XRD was typically operated at 50 kV and 30 mA. θ-2θ scans at rate of 1 ˚/min with step 0.02 between 4-80˚ were mainly adopted in the current experiments. The following Powder Diffraction Files (PDF) were considered for phase identification: PDF 01-070-6341 for BLT, PDF 01-070-9069 for BNT and PDF 84-0444 for STO.

The crystallographic texture of BLT films and bulk samples was characterized by means of XRD rocking curves and pole figures (X'Pert MRD diffractometer, Philips, Almelo, The Netherlands). X-ray rocking curves were obtained by tilting the samples through the Bragg angle of the selected plane. In the pole figure measurements the diffracted intensity was collected at a step of 5° in the tilted and rotated angles in the whole hemisphere, at a fixed 2θ angle, that corresponds to the selected reflections of the samples, while the specimen is tilted and azimuthally rotated in relation to the incident beam [297]. Partial pole figures were plotted with PANalytical X'Pert Texture software.

3.1.4.2 Scanning Electron Microscopy

In SEM, an electron beam source emits electrons, which are then collected and focused by lenses to form few nanometers sized probes. Deflection coils are used to operate the electron beam and to scan the sample surface. Simultaneously, another electron beam runs over a TV monitor screen in a synchronized mode. The image magnification is the ratio of the scanned monitor range to the scanned sample range and it is easily controllable by beam deviation elements. Primary electron beam interacts with the specimen surface resulting in different emitted signals (secondary and back scattered electrons, X-ray radiation, etc.), which can be registered with the appropriate detector [298].

In the current work, top view and cross section microstructures of BLnT (Ln: La and Nd) and STO films and fracture surfaces of bulk samples were observed with SEM (XL 30 FEG, Philips Electronic Instruments, Mahwah, NJ; S4100, Hitachi, Tokyo, Japan and SU-70, Hitachi, Tokyo, Japan) coupled with EDS (QUANTAX 400, Bruker, Berlin, Germany). SEM micrographs were recorded and analyzed for microstructure quantitative characterization.

The regions were amorphous phase is located were identified using SEM backscattered electrons (BSE) images obtained from polished but not etched STO samples. The principle of the technique is that larger atoms (with a higher atomic number) have a higher probability of producing elastic collisions between the electrons of the accelerated electron beam and the atoms within the sample because of their greater cross-sectional area. Consequently, the number of backscattered electrons reaching a BSE detector is proportional to the mean atomic number of the sample [298]. Thus, a "brighter" BSE intensity correlates with greater average atomic number in the sample and "dark" areas have lower average atomic number.

3.1.4.2.1 Cross section preparation

The cross sections of green and sintered films were prepared by constructing a sandwich structure (illustrated in Figure 3.1-3) in which the film on flexible Pt substrate

was supported on both sides by rigid alumina slides. This structure was held together by a plastic clamp and then impregnated with resin (CaldoFix, Struers) under vacuum for 1 h.

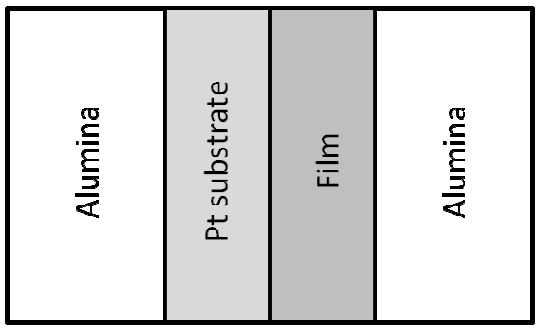

Figure 3.1-3: Schematic representation of the sandwich structure used for cross section polishing. The film on Pt substrate is placed between two rigid alumina slides.

Prior to the impregnation, the resin was heated up at 60 ˚C for 30 min to become more fluid and increase the impregnation quality. After the impregnation, the resin was cured at 80 ˚C for 1h. The resin impregnated samples were then polished with silicon carbide grinding paper, followed by a sequence of fine diamond pastes (15 µm, 6 µm, 3 µm, 1 µm and 0.25 µm). After good quality polishing, the samples were chemically etched using a 0.3 vol% HF- 6 vol% HNO_3 solution for 30 - 45 s or removed from the resin and thermally etched at temperatures 70 - 100 ˚C below the corresponding sintering temperature for several minutes. The etching depth was controlled by the holding time (from 3 to 15 min) and observations with an optical microscope (Nikon, HFX-IIA). Similar etching procedures were followed regarding bulk samples.

3.1.4.2.2 Image analysis

Parameters like films density, pore and grain size and orientation distribution or fraction of liquid phase were then determined through image analysis of SEM micrographs, using the ImageJ freeware (available from http://imagej.nih.gov/). To

perform the image analysis, the SEM micrographs were generally modified in the following way: contrast enhancement, median filtering and thresholding, in order to obtain suitable binary images (Figure 3.1-4 (b) and (c)). The grains sections were manually drawn and every pore section (or liquid phase pocket) was manually evaluated before and after thresholding to avoid errors in pore area. Then an equivalent ellipse (with the same area of the actual section) was calculated for each grain or pore (Figure 3.1-4 (d) and (e)) and its angle with a horizontal line determined.

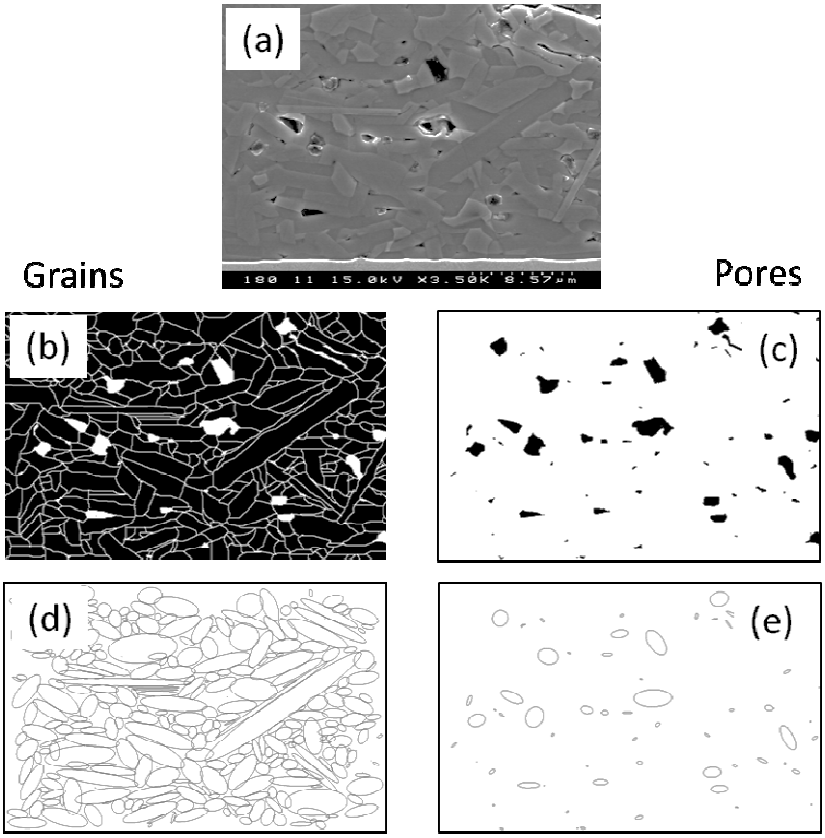

Figure 3.1-4: Image processing for microstructure characterization (grains and pores): (a) raw image, (b) and (c) after manual drawing of grains or pores and binarization, (d) and (e) resulting ellipses.

The elliptical shape was assumed for the quantitative analysis of grain and pore shape and orientation. Concerning this orientation of grains and pores analysis, the direction parallel to the substrate (in-plane direction) corresponds to 0° and the direction

perpendicular to the substrate or in the film thickness (out-of-plane direction) corresponds to 90°, as illustrated in Figure 3.1-5 (a). In the case of the bulk samples, 0° is the radial direction and 90° the axial one (Figure 3.1-5 (b)). An orientation factor was assumed to quantify the degree of shape anisotropy and orientation of grains and pores. This orientation factor is defined as the fraction of weighted cumulative lengths (sum of the length multiplied by the aspect ratio) of grains or pores with orientation in the ranges 0° - 30° and 150° - 180°, as schematically represented in Figure 3.1-5 (c).

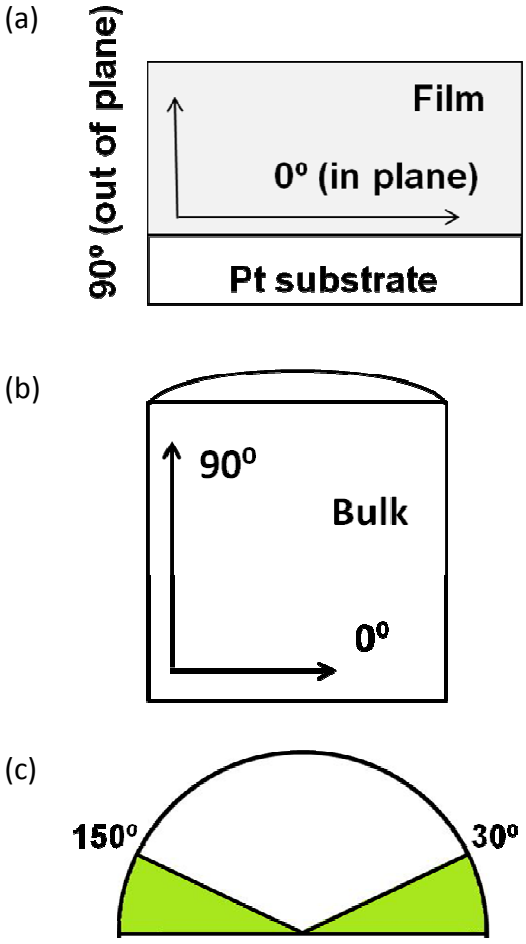

Figure 3.1-5: (a) Illustration of the directions used for orientation quantification in the films and (b) bulk samples. (c) Scheme of the orientation range considered in the orientation factor (0˚ - 30˚ and 150˚ – 180˚).

Around 200 pores and more than 800 grains in more than 3 micrographs were considered for every sample. The quantification of the volumetric percentage of liquid phase was performed similarly to the porosity analysis. At least five images were used in this case, covering around 50000 μm^2 for every sample. The error was determined by the standard deviation of the values obtained from the different images.

The films relative density was estimated from the solid volume fraction obtained from the SEM micrographs. To validate the density values, this method was also applied to bulk samples, whose densities were measured by the Archimedes method and a good agreement within $\pm$1% was found.

The X-ray theoretical density value of 6.195 g/cm^3 was considered for BLT (PDF 01-070-6341), 5.792 g/cm^3 for BNT (PDF 01-070-9069) and 5.117 g/cm^3 for STO (PDF 84-0444).

3.1.4.3 Transmission Electron Microscopy

In a TEM setup, a thin specimen is illuminated with electrons (the primary electrons). Whatever part is transmitted is projected onto a phosphor screen for the user to see. The darker areas of the image represent those areas of the sample, where fewer electrons were transmitted through (they are thicker or denser). The lighter areas of the image represent those areas of the sample that more electrons are transmitted through (they are thinner or less dense). An image in TEM can be formed by using the central spot of unscattered electrons, or by some or all of the scattered electrons. The type of the electrons is chosen by an insertion of aperture into the back focal plane of the objective lens, thus blocking out most of the diffraction pattern except that which is visible through the aperture. If the direct beam is selected, the resultant image is called a bright-field image, and if scattered electrons of any form are selected, a dark-field image is formed. If no aperture is inserted, electron diffraction pattern is observed [299].

For TEM (Hitachi 9000, Tokyo, Japan) observation, the two faces of the bulk samples were polished using a Gatan disc grinder in order to reduce its thickness to ~30 µm. The sample was then glued to a copper ring and ion beam polished using a Precision

Ion Polishing System (PIPS) (Model 691, Gatan, Pleasanton, CA, USA). In the case of the films, a thin layer was directly extracted from the films by means of Focused Ion Beam (FIB), at the Institute of Materials Science, Technische Universität Darmstadt, Darmstadt, Germany.

3.1.4.4 Secondary Ion Mass Spectroscopy

When a solid sample is sputtered by primary ions, a fraction of the particles emitted from the target is ionized. Secondary Ion Mass Spectrometry (SIMS) consists of analyzing these secondary ions with a mass spectrometer. A basic SIMS instrument generally consists of a primary beam source to supply the bombarding species, a target or sample that must be solid and stable in a vacuum, a method of collecting the ejected secondary ions, a mass analyzer to isolate the ion of interest and an ion detection system to record the magnitude of the secondary ion signal [300]. SIMS is recognized as the most sensitive elemental and isotopic surface analysis technique. Most elements may be detected down to concentrations of 1 *ppm* or 1 part per billion (*ppb*). This technique is "destructive" by its nature (sputtering of material). It can be applied to any type of material (insulators, semiconductors, metals) that can stay under vacuum.

SIMS (CAMECA IMS 5f, Paris, France) was used in this work for chemical characterization and to investigate possible interdiffusion between platinum and BLT film, using oxygen ions as SIMS probe. This method allows the analysis of the chemical composition of a volume in the sample with a spatial resolution of ~1µm in the lateral dimension and an accuracy of 1 nm in the height profile. The SIMS measurements were carried out at the Institute of Materials Science, Technische Universität Darmstadt, Darmstadt, Germany.

3.1.5 Dielectric properties characterization

The dielectric properties were measured as a function of temperature and frequency in the capacitive cell illustrated in Figure 3.1-6. For the case of sinusoidal applied voltage U, the current discharge flow *I* of the capacitive cell may be written as:

$$I = \frac{i\omega\varepsilon^* U\varepsilon_0 S}{d_s} = \frac{i\omega(\varepsilon' - i\varepsilon'')U\varepsilon_0 S}{d_s} = I_C + I_R \qquad (3.1\text{-}2)$$

where *i* stands for the imaginary operator, $\omega = 2\pi f$ for the angular frequency, ε_0 for the permittivity of the vacuum (with the value 8.85×10^{-12} F/m), S for the area of the electrodes for a sample capacitor, d_s for the distance between electrodes or sample thickness, ε^* for the complex permittivity, ε' for the real part of the permittivity and ε'' is the imaginary part of the permittivity, related to dielectric loss. Therefore, because the dielectric loss exists in dielectric materials, it can be represented by the circuit analogue of a resistance in parallel with a capacitor and the current *I* has vector components I_C and I_R, as illustrated in Figure 3.1-6 (b) and (c).

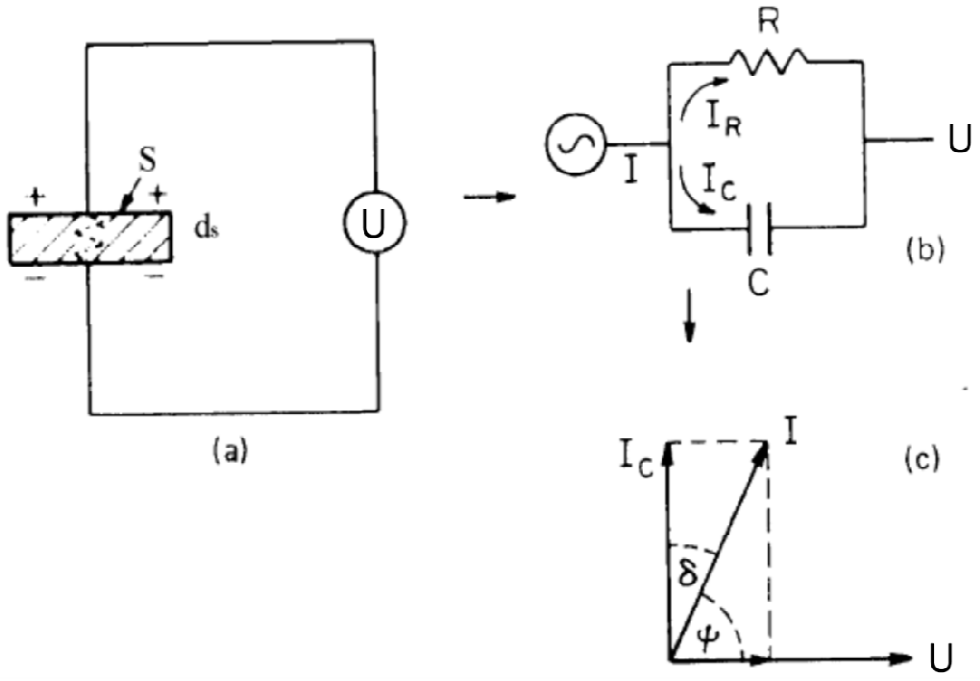

Figure 3.1-6: Equivalent circuit diagrams of capacitive cell (a) of charging and loss current (b) and of loss tangent for a typical dielectric (c) [301].

The current I_C represents a capacitive current proportional to charge stored in the capacitor. It is frequency dependent and leads voltage U by 90°. The current I_R is an AC conduction current in phase with the voltage U, which represents the energy loss or power dissipated in the dielectric. From the ratio of the magnitude of I_R to magnitude of I_C, therefore, one can define a dissipation factor $tan(\delta) = \varepsilon''/\varepsilon'$ [301].

In this work, dual impedance parameter Z-ψ were measured by an impedance bridge (HP 4284A, Agilent, USA) with a metal-insulator-metal (MIM) configuration in the frequency range of 100 Hz - 1 MHz with further recalculation to

$$\varepsilon' = \frac{d_s \sin(\psi)}{\omega Z \varepsilon_0 S} \qquad (3.1\text{-}3)$$

and

$$tan(\delta) = tan(90^\circ - \psi) \qquad (3.1\text{-}4)$$

Au top electrodes were used for the films on Pt (Pt works as the bottom electrode) and the dielectric properties were measured in the direction normal to the substrate plane. These circular Au top electrodes were sputtered using a shadow mask of 0.6 mm diameter. In the case of BLnT (Ln: La and Nd) bulk ceramics, top and bottom Au electrodes with 5 mm diameter were sputtered using a SEM coating unit (E5000, Polaron Equipment Limit) with an argon partial pressure of 2mtorr, an acceleration voltage of 12kV and an emission current of 12mA. The measurement direction was parallel to the pressing direction. To improve the quality of interface between the metal electrodes and the samples, the samples with the sputtered electrodes were annealed at 200 ˚C for 30 min.

For Impedance Spectroscopy, silver paint electrodes were painted on the STO bulk samples bottom and top surfaces and impedance measurements were carried out between 100 Hz and 1 MHz in a selected temperature range of 200 to 700 ˚C. The collected impedance data were normalized by multiplying by the geometric factor S/d_s and analyzed with the software ZView (Scribner Associates Inc., USA).

3.2 Electrophoretic Deposition

The thickness of thick films usually ranges from 1 to 100 µm, but their thickness may go up to millimeters. The deposition methods used for the fabrication of these films lie between thin film processing and machining of bulk ceramics [9; 302]. Thick films are normally fabricated by low-cost processes [82] such as tape casting, screen-printing, ink-jet printing or EPD [83], which are mainly distinguished by the method to deliver the suspension to the substrate. The preparation of ceramic thick films by these methods generally implies the preparation of the precursor powders, preparation of pastes or powder suspensions, printing/depositing of the pastes or suspensions onto a suitable substrate, drying at low temperature and sintering at high temperature to obtain a consolidated layer [281; 303; 304].

Among the above referred techniques, EPD is simple, fast and inexpensive [303]. One of the advantages of EPD over other thick film deposition techniques is the ability to coat complex geometries, which allows easy deposition of the materials onto substrates of various shapes, including long wires or other more intricate shapes [305]. This technique attracted considerable interest not only in academia but also in industry because of the versatility of its use with different materials and substrates and cost-effectiveness. Moreover, its ability to be scaled-up to the fabrication of large product volumes and sizes, as well as the possibility of selective deposition to avoid etching processes, increases the technological competitiveness of EPD [306]. Other advantage of EPD is that, despite being a wet process, it offers easy control over thickness and morphology of the deposited film by controlling simple processing parameters [83].

On the other hand, EPD requires a conducting substrate (or a substrate coated with an electrode), which may act somehow as a limitation for the use of this technique in the production of electronic circuits, for example. A further limitation is the high density of some specific elements as it is very difficult to maintain heavy particles in suspension [303].

The phenomenon of electrophoresis was discovered in 1807 by the Russian physicist F.F. Reuss, who observed movement of clay particles suspended in water when an

electric current was passed through the suspension [307]. However, in ceramic manufacturing industry, EPD of ceramics was first studied by Hamaker just in the late 1930's [308]. It was only in the 1980's that this process received attention for the preparation of advanced ceramics and in more recent years the number of successful applications of this technique has quickly evolved to the level of nanotechnologies [83; 281; 286].

EPD is purely a method of moving (electrophoresis) and arranging (deposition) particles [283]. To produce a dense, mechanically strong layer or object it must be combined with some other process such as sintering to transform the deposited particles into a consolidated microstructure [303; 304].

3.2.1 Basics of Electrophoretic Deposition

EPD is a colloidal forming process in which charged powder particles, dispersed or suspended in a liquid medium are deposited in a conductive substrate under the effect of a DC electric field [83], as schematically represented in Figure 3.2-1.

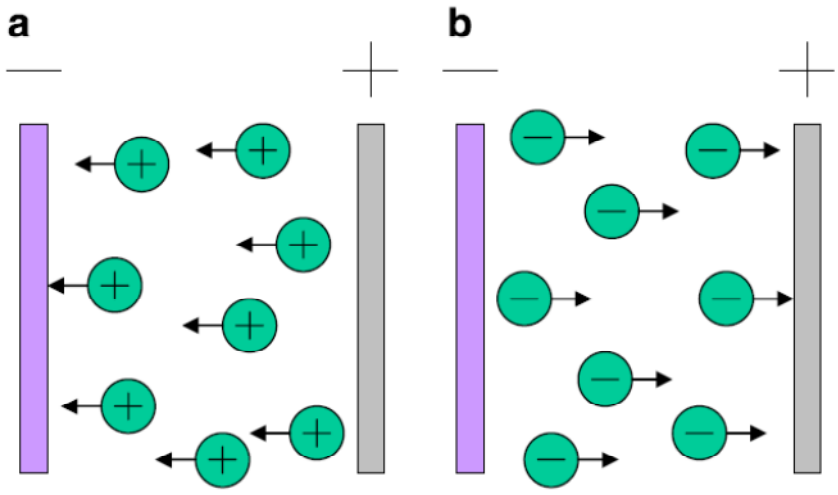

Figure 3.2-1: Schematic illustration of EPD process: (a) cathodic EPD and (b) anodic EPD [83]. The charged particles in the suspension move towards the oppositely charged electrode under the effect of the electric field.

There are three basic steps in EPD process: formation of a stable suspension of the particles, electrophoretic migration of the particles to the deposition electrode and deposition of the particles in the desired arrangement on the electrode surface. In the first step, the objective is to place the particles into a suspension where each of the particles can move independently. The second step consists in the application of a DC electric field to the suspension causing the electrophoretic motion of charged particles toward the oppositely charged electrode. In the final step, the interparticle repulsion that keeps the particles stably suspended is overcome and deposition onto the substrate occurs.

As illustrated in Figure 3.2-1, there are two types of EPD depending on which electrode the deposition occurs. When the particles are positively charged, the deposition is formed on the cathode and the process is called cathodic EPD. On the contrary, anodic EPD refers to the case when the particles deposit on the positive electrode (anode). By suitable modification of the surface charge on the particles, both of the two modes of deposition are possible [285].

The charge of the particles and their electrophoretic mobility are the principal driving force for EPD [83]. Charges on the surface of the particles can be formed by one or more of the following mechanisms [284]: (a) selective adsorption of ions onto the surface of solid particle from the liquid, (b) dissociation of ions from the solid phase into the liquid, (c) adsorption or orientation of dipolar molecules at the particle surface and (d) electron transfer between the solid and liquid phase due to differences in the substances work function. In the case of ceramic or glass particles in water or organic liquids, the last mechanism is not applicable but the first two invariably occur. The sign of the net charge on the particle will depend not only on whether the ions involved are positive or negative, but also on whether mechanism (a) or (b) is dominant. Also, a positively-charged particle may even behave like a negative one, which is attracted to a positive electrode, if an excess of negative ions are attracted to the vicinity of the particle. In water most solid particles acquire a negative charge, but in organic liquids charging may be either positive or negative [309].

The development of a net charge at the particle surface affects the distribution of ions in the surrounding interfacial region, resulting in an increased concentration of counter ions (ions with opposite charge to that of the particle) close to the surface. The liquid layer surrounding the particle consists of two parts: an inner region where the ions are strongly bound (Stern layer) and an outer region (diffuse double layer or lyosphere) where they are more broadly distributed and less firmly associated. Within this diffuse layer is a boundary known as the slipping plane, within which the particle acts as a single entity [310].

A schematic representation of the distribution of charge species and the potential drop across the double layer, in accordance with the Stern model, is represented in Figure 3.2-2. The interaction between charged particles is predominantly governed by the overlap of the diffuse layer and, accordingly, the potential most relevant to the interaction is the one developed at the boundary between the Stern and diffuse layers rather than the potential at the particle surface. This potential difference between Stern plane and the diffuse layer is called the zeta potential [311].

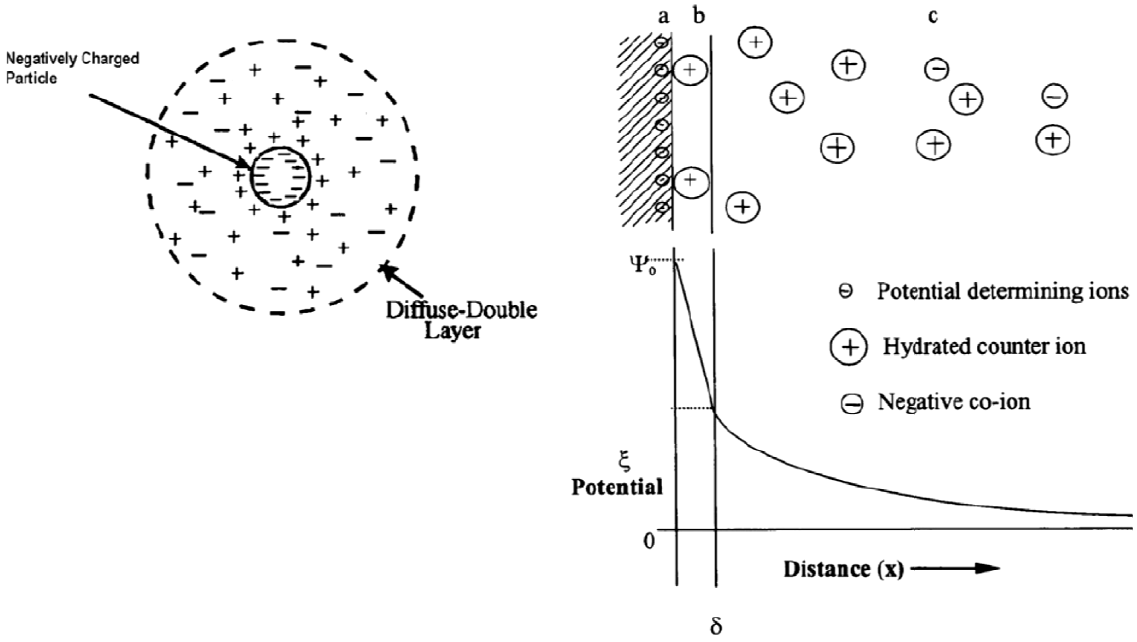

Figure 3.2-2: Schematic representation of the double layer and potential drop across the double layer. a - surface charge, b - Stern layer, c - diffuse layer of counter-ions [312].

The zeta potential is the main parameter determining the electrokinetic behaviour of particles in suspension and as a consequence is a key factor in the EPD process. A high zeta potential and a uniform surface charge density on the surface of suspended particles is very important for a successful EPD. Zeta potential plays a role in the stabilization of the suspension by determining the intensity of repulsive interactions between the particles, in determining the direction and migration velocity of particles during EPD and in determining the quality of the deposit. As zeta potential is closely related to the particles double layer thickness, it provides also information on the agglomeration of the particles in the suspension. In general, the higher the absolute value of the measured zeta potential, the better is the dispersion of the particles in the suspension [311].

The zeta potential is affected by the pH environment and is usually positive for low pH values and negative at high pH. Additionally, the magnitude and sign of the zeta potential depends on many other factors, such as the presence or absence of added electrolytes or the concentration of the suspension itself. Moreover, zeta potential can be controlled by adding to the suspension a variety of charging agents such as acids, bases and specifically adsorbed ions or polyelectrolytes [313]. Consequently, it is possible to use a variety of additives to control the charge magnitude and polarity in the suspensions for EPD.

The process of particle deposition is very dependent on the state of dispersion and stability of the suspension. This has been discussed in the framework of the Derjaguin-Landau-Vervew-Overbeek (DLVO) theory [314; 315], which predicts the stability of colloidal particles suspended in polar liquids. According to this theory, the stability of a colloidal system is determined by the total energy of interaction, determined by sum of the electrical double layer repulsive forces and the Van der Waals attractive forces which the particles experience as they approach one another. This theory has been proved successful in predicting basic features of colloid stability and particle deposition phenomena [83]. Other theories proposed to explain the mechanism of EPD include flocculation by particle accumulation [308; 316], particle charge neutralization [317], electrochemical particle coagulation [318] or electrical double layer distortion and thinning mechanism [283].

However, the interactions between solvent, particles and electric field in EPD are rather complex, as is the deposition process, and there is still no satisfactory and general theory that accounts for the mechanism of EPD. Zeta potential or electrophoretic mobility are usually used as indicators of the ability of a suspension to be deposited but these are not sufficient to determine the success of the deposition. Even though their evident importance regarding the stability of the suspensions, this is somehow an empirical property not closely related to fundamental processing parameters. Nevertheless, research concerning theoretical, modelling and experimental studies is ongoing regarding the technique, which has already been applied successfully for many applications [83; 286; 319-323], despite the incomplete body of knowledge.

3.2.2 Parameters influencing Electrophoretic Deposition

The outcome of EPD depends on several parameters that, as summarized in Table 3.2-1, may be divided in two groups: those related to the suspension and those related to the process [83].

Among the parameters related to the suspension are the physicochemical nature of both suspended particles and liquid medium, surface properties of the powders and type and concentration of the additives (mainly dispersants). Particle size distribution, dielectric constant of the suspension media, conductivity of the suspension, zeta potential and stability of the suspension also have a direct effect on the outcome of EPD.

In EPD, water-based and organic-based media may be used for deposition. However, non aqueous suspensions are generally preferred due to the fact that water-based suspensions cause several problems [324]. In water, electrolysis takes place at low voltages, which results in the formation of gas bubbles leading to poor quality coatings or films. Additionally, the density of the electric current is higher in water suspensions which results in the heating of the suspension and loss of stability. Organic solvents used in EPD are generally polar solvents such as alcohols and ketones. Ethanol,

acetone and methyl-ethyl-ketone are examples of solvents which have been reported as suitable suspension media for electrophoretic deposition [83].

Table 3.2-1: Parameters influencing EPD.

EPD parameters	
Suspension	• Nature of particles and liquid medium • Particle size distribution • Dielectric constant of liquid • Type and concentration of additives • Conductivity of suspension • Viscosity of suspension • Zeta potential • Stability of suspension
Process	• Deposition time • Applied voltage • Conductivity of the substrate

The adequate particle size range for EPD is usually considered to be from 1 to 20 μm but deposition of particles outside this size range may also be feasible [83]. This is exactly the case of nanotechnologies, in which EPD is getting a great deal of attention as a technique for nanoparticle assembly [281; 286]. Regarding large particles, the main problem is that they tend to settle due to gravity and gradients in the deposits may occur.

The effect of the dielectric constant of the suspension media on EPD was studied, for example, by Powers for beta-alumina suspensions in various organic suspension media [325]. The author verified that the conductivity of the suspension increased rapidly with dielectric constant of the suspension media and deposits were only obtained with liquids for which the dielectric constant was in the range of 12–25. Regarding the

conductivity of suspensions, too conductive suspensions usually lead to very low particle motion, whereas if the suspension is too resistive its stability is lost [326]. A suitable window of conductivity exists which is different for different liquid media.

As mentioned previously, the stability of the suspension, which is one of the most essential factors in the conformation process, is closely related to the zeta potential. Colloids with high zeta potential (negative or positive) are stable while colloids with low zeta potentials tend to coagulate or flocculate. Zeta potential plays a major role in the stability of the suspension, in the determination of the direction of the particle migration and on the green density of the compact film [83].

Regarding the EPD process, parameters such as applied voltage, deposition time and conductivity of the substrate are determinant in the final characteristics of the deposited film. During the initial period of EPD, there is generally a linear relationship between deposition mass and time but as the deposition time increases the deposition rate decreases and attains a plateau at very high deposition times. This is due to the fact that the electric field acting on the suspension decreases with deposition time because of the formation of an insulating layer of ceramic particles on the electrode surface [323].

The amount of deposit is usually proportional to the applied potential during EPD process. However, the quality (morphology and density) of the deposit can be deteriorated under high applied fields (>100 V/cm) [320; 327]. A high applied field may cause turbulence in the suspension and particles may move so fast that they may not have enough time to a proper deposition. In addition, the increase of the current density of the suspension media in proportion to the applied voltage may originate unstable suspensions that may influence the morphology quality of the deposit [320].

The uniformity and conductivity of the substrate electrode, particularly for non-metallic electrodes, are critical parameters determining the green quality of deposited of films by EPD. Low substrate conductivity usually leads to a decrease of the deposition rate and to non-uniform green films [328].

All these factors are determinant in the outcome of the EPD process and a proper selection of materials, solvents, additives, substrates and processing parameters is fundamental to the fabrication of high quality thick films. However, after that appropriate selection of solvent, particles and EPD apparatus, the mass of the deposited particles (the thickness of the films) can be readily controlled by the concentration of the suspension, applied potential and deposition time [83].

3.3 Impedance Spectroscopy

IS is a powerful technique for the assessment of the electrical properties of electroceramics by measuring the response of materials to a small applied sinusoidal voltage [288; 289]. Impedance measurements are made over a wide range of frequencies and the different regions of the material are characterized according to their electrical relaxation times or time constants, when an electrical field is applied.

IS became a popular analytical tool in materials research and development because it involves a relatively simple electrical measurement that can readily be automated and whose results may often be correlated with many complex materials variables: from mass transport, rates of chemical reactions, corrosion and dielectric properties, to defects, microstructure, compositional influences on the conductance of solids or even biological systems [287; 289].

Any intrinsic property that influences the conductivity of an electrode-material system, or an external stimulus, can be studied by IS. The parameters derived from an IS spectrum fall generally into two categories [289]: (a) those pertinent only to the material itself, such as conductivity, dielectric constant, mobility of charges, equilibrium concentrations of the charged species and bulk generation-recombination rates; and (b) those pertinent to an electrode-material interface, such as adsorption-reaction rate constants, capacitance of the interface region and diffusion coefficient of neutral species in the electrode itself.

3.3.1 Basics of Impedance Spectroscopy

The general approach of IS is to apply an electrical stimulus (a known voltage or current) to the electrodes and measure the response (the resulting current or voltage) [329]. In general terms, the concept of electrical resistance consists in the ability of a particular circuit element to resist current flow. Quantitatively, the well known Ohm's law defines resistance *R* in terms of voltage *U* and current *I* as [330]:

$$R = \frac{U}{I} \qquad (3.3\text{-}1)$$

In a resistor the alternating current (AC) and voltage are in phase. However, in other circuit elements they may be out of phase. In particular, in capacitors the current leads the voltage by 90˚ and in inductors it lags by 90˚ [331]. Therefore, the concept of resistance must be generalized to that of impedance, which takes phase differences into account [289]. In this way, impedance extends the concept of resistance to AC circuits and possesses both magnitude and phase, unlike resistance which has only magnitude. When a circuit is driven with direct current (DC), there is no distinction between impedance and resistance; the latter can be thought of as impedance with zero phase angle.

IS usually involves the application of an alternating voltage signal to a sample and the measurement of the phase shifted current response [331]. The applied alternating voltage can be expressed as:

$$U(t) = U_0 \cos(\omega t) \qquad (3.3\text{-}2)$$

with $\omega = 2\pi f$ and *f* the frequency in Hz. In a linear system, the response current signal, *I(t)*, is generally shifted in phase by an angle ψ and can be represented by:

$$I(t) = I_0 \cos(\omega t - \psi) \qquad (3.3\text{-}3)$$

The impedance expression is then analogous to Ohm's Law:

$$Z(t) = \frac{U(t)}{I(t)} = \frac{U_0 \cos(\omega t)}{I_0 \cos(\omega t - \psi)} = Z_0 \frac{\cos(\omega t)}{\cos(\omega t - \psi)} \qquad (3.3\text{-}4)$$

To avoid the time-dependency, impedance can be transformed into the frequency domain and represented in the complex plane:

$$Z^*(\omega) = Z_0(\cos(\psi) + i\sin(\psi)) = Z'(\omega) + iZ''(\omega) \qquad (3.3\text{-}5)$$

where $i = \sqrt{-1}$ and *Z'* and *Z''* are the real and imaginary components, respectively. Impedance is by definition a complex quantity and is only real when ψ = 0 and thus *Z* = Z',* which corresponds to purely resistive behaviour [289]. The real part of the impedance is then related to a pure resistance, R. The imaginary part, *Z''*, is for most systems a capacitance, *C*, in the form

$$Z'' = \frac{1}{i\omega C} \qquad (3.3\text{-}6)$$

For a parallel plate capacitor with area *S,* separation d_s between the plates and a medium of permittivity ε' between the plates, the capacitance *C* is given by [288]:

$$C = \varepsilon' \varepsilon_0 \frac{S}{d_s} \qquad (3.3\text{-}7)$$

where ε_0 is the permittivity of free space.

In general, *Z* is frequency-dependent, as defined above. Conventional IS consists of the measurement of *Z* as a function of *ω* over a wide frequency range. It is from the resulting *Z(ω)* vs. *ω* response that one derives information about the electrical properties of the full electrode–material system.

A wide variety of ceramic microstructures occurs in real materials, which under certain assumptions may be modelled by a simple brick-layer model (Figure 3.3-1). The model assumes cubic grains (homogeneous grain size distribution) and laterally homogeneous grain boundaries, assumptions that are often violated in real polycrystalline materials. Nevertheless, under some limits the brick layer model is a useful tool to estimate electrical properties of materials [332; 333]. Different regions of a ceramic sample may then be modelled by an equivalent circuit consisting in a resistance and a capacitance, usually in parallel [288; 331].

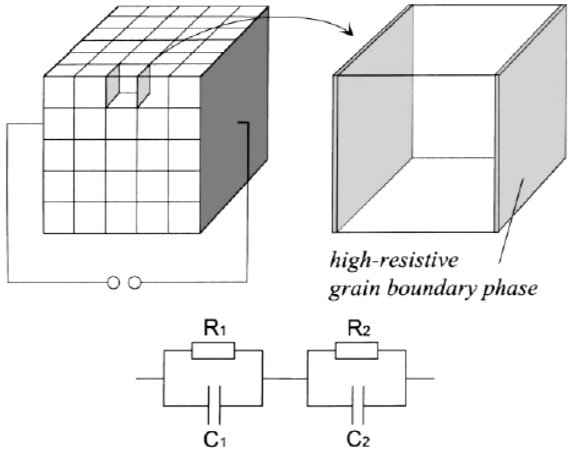

Figure 3.3-1: Brick layer model and resulting equivalent circuit [333].

The product of *R* and *C* gives the characteristic relaxation time or time constant, τ:

$$\tau = RC \qquad (3.3\text{-}8)$$

and at the frequency of maximum loss, ω_{max},

$$\omega_{max} RC = 1 \qquad (3.3\text{-}9)$$

This allows for the separation of different *RC* elements in the impedance spectrum, provided that they show different time constants [288]. In this way, the values of *R* and *C* may be quantified and *RC* elements assigned to different regions of a sample. Indeed, the relaxation time of the grain boundary contribution may be several orders of magnitude larger than that of the bulk contribution and one may thus be able to separate the bulk and grain boundary contributions [332].

In reality, few systems can be represented by ideal resistors and capacitors. Therefore, in order to account for non-ideal behaviour, a well established approach is the replacement of *C* by a phenomenological constant phase element (CPE) [289; 331], which describes a non-ideal capacitor with a frequency independent phase shift with respect to the ideal capacitor. The impedance of a CPE [334] is given by equation (3.3-10) where Q_{CPE} and n_{CPE} are the fitting parameters.

$$Z = (Q_{CPE}(i\omega)^{n_{CPE}})^{-1} \quad (3.3\text{-}10)$$

The related capacitance is given by

$$C = (R^{1-n_{CPE}}Q)^{\frac{1}{n_{CPE}}} \quad (3.3\text{-}11)$$

For n_{CPE} = 1 the CPE equals a pure capacitance and for n_{CPE} = 0 is equivalent to a pure resistance. This way of evaluating capacitance has been used for several systems, such as electrodes for solid oxide fuel cells or protective oxide films on metals [334; 335].

As shown in Figure 3.3-2, impedance spectroscopy data is usually presented in the form of imaginary *Z''* (capacitive) vs. real *Z'* (resistive) impedances, which is known as Nyquist (or Cole-Cole) plot. Each parallel RC element gives rise to a semicircle, from which *R* and *C* may be quantified [288]. After fitting the data, *R* values may be obtained from the intercepts on the *Z'* axis and *C* values by applying equation (3.3-11).

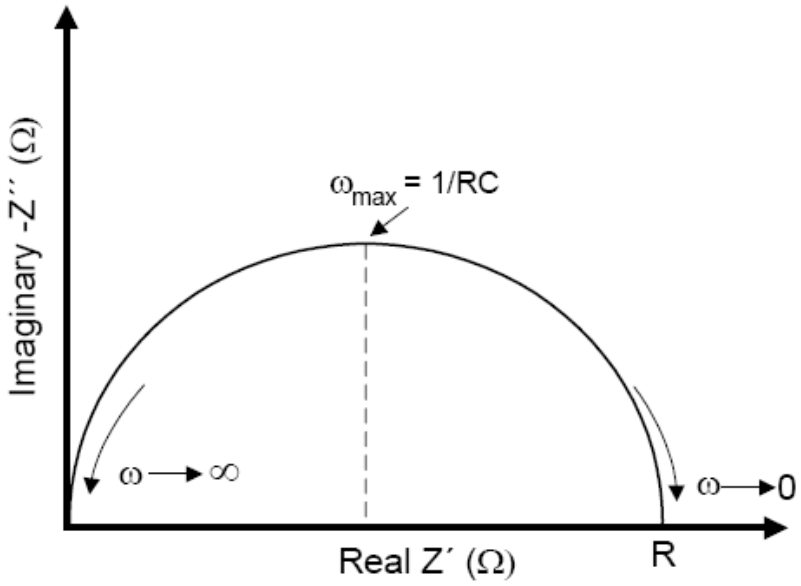

Figure 3.3-2: Schematics of a Nyquist plot showing one time constant.

Having obtained values for these *R* and *C* components, the next stage is to assign them to regions of the sample. It is found that a value around 10^{-12} F is a typical value for the

bulk capacitance of a sample [288]. On the other hand, the grain boundary capacitance usually lies in the range $l0^{-11}$ to $l0^{-8}$ F; the higher capacitances occur in materials that are well-sintered, with narrow intergranular regions. The lower capacitances are often found with poorly sintered samples that contain constriction resistances or narrow contacting 'necks', between grains [288]. The assignment is therefore based on the magnitudes of the normalised capacitances, as shown in Table 3.3-1.

Table 3.3-1: Capacitance values and their possible interpretation [288].

Normalised Capacitance in F/cm	**Origin of the *RC* Element**
10^{-12}	Bulk
10^{-11}	Minor Second Phase
$10^{-11} – 10^{-8}$	Grain Boundary
$10^{-10} – 10^{-9}$	Bulk Ferroelectric
$10^{-9} – 10^{-7}$	Surface Layer
$10^{-7} – 10^{-5}$	Sample – Electrode Interface
10^{-4}	Electrochemical Reaction

A typical impedance spectrum for electroceramics is presented in Figure 3.3-3 for $Ca_{12}Al_{14}O_{33}$ [288]. Two different semicircles are clearly seen, related to grain interiors (bulk) and grain boundaries, according to the determined values for the corresponding capacitances. This complex impedance plane representation, *Z"* vs *Z',* in Figure 3.3-3, is in most cases an appropriate method for presenting the results. However, alternative formalisms of data presentation can yield additional information not easily accessible from the impedance plane alone. One such alternative is the complex electric modulus, *M*,* formalism [288] as follows, where $C_0 = \varepsilon_0 S/d_s$:

$$M^* = i\omega C_0 Z^* \qquad (3.3\text{-}12)$$

Its utility is demonstrated in Figure 3.3-4, regarding donor-doped ferroelectric $BaTiO_3$, electrically inhomogeneous materials in which the grain boundary resistance may dominate the overall impedance.

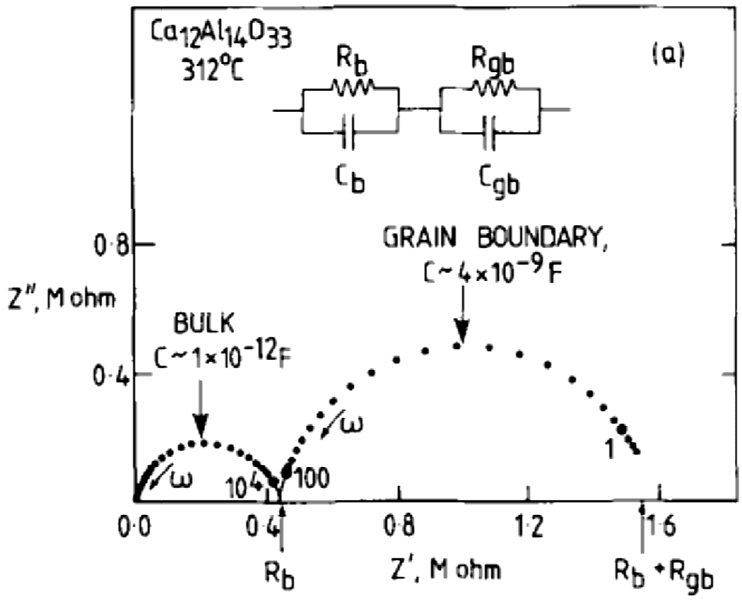

Figure 3.3-3: Impedance data for $Ca_{12}Al_{14}O_{33}$, presented in the complex impedance plane format, *Z''* vs *Z'*. Selected frequency points, in Hz, are marked. The equivalent circuit used to interpret the data is shown, representing a series combination of crystal and grain boundary impedances [288].

Accordingly, a single semicircle is seen in the complex impedance plane (Figure 3.3-4 (a)). On the other hand, the *M* formalism reveals two contributions, as shown in Figure 3.3-4 (b), presenting the spectroscopic plots of the imaginary components *Z''* and *M''*. The higher frequency *M"* peak corresponds to the bulk component of the sample.

In materials that are inhomogeneous and are represented by more than one *RC* element, the resulting *M"* and *Z"* spectra may look very different. *M"* and *Z"* spectroscopic plots highlight different features of the sample by giving different weightings to the data. Impedance plots pick out the most resistive elements in the sample, since the impedance peak height, Z''_{max}, is equal to *R*/2 for that particular

element. On the other hand, modulus plots pick out those elements with the smallest capacitance since the *M"* peak maximum is equal to $\varepsilon_0/2C$ for that particular element [288].

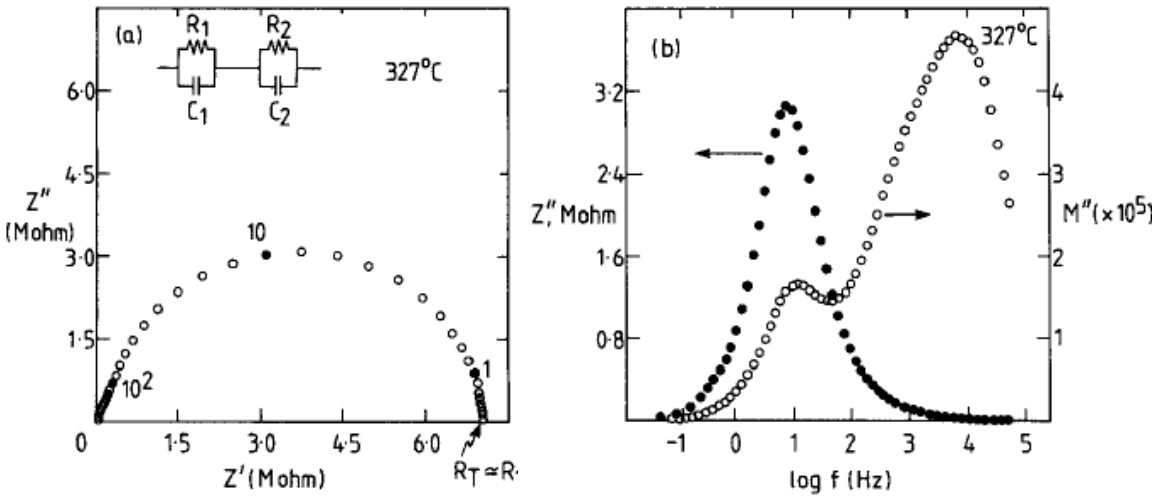

Figure 3.3-4: The same impedance data for doped $BaTiO_3$ are presented (a) in the impedance complex plane and (b) using the electric modulus formalism (spectroscopic plots of *Z"* and *M''*) [288]**.** With the electric modulus formalism in (b) two contributions are visible.

4 Strontium Titanate

4.1 Effect of nonstoichiometry on the grain growth and dielectric response of strontium titanate ceramics

4.1.1 Introduction

As previously discussed, stoichiometry plays an important role in the sintering kinetics of STO, related to defect effects in bulk and grain boundaries [259; 277]. Four different types of grain boundaries were detected in STO by Bäurer *et al.* [247], which were correlated with different grain boundary mobilities. Additionally, sudden drops in the grain boundary mobility with increasing temperature were reported for STO and attributed to changes in the grain boundary faceting behavior at high temperatures [76]. The relation of these grain boundary features with the dielectric properties is, however, neither studied nor understood.

Preliminary results of our group on the dielectric response of nonstoichiometric STO by Tkach *et al.* [277] demonstrated that the variation of the Sr/Ti ratio has only a weak effect on the material intrinsic quantum paraelectric behavior at low temperatures and no dielectric anomaly is observed. However, the relation between nonstoichiometry, microstructure development and grain boundary electrical properties has not been addressed yet. Moreover, no link has been so far established between the formation of different grain boundary complexions and a particular grain boundary dielectric response.

In this chapter, the effect of nonstoichiometry (Sr/Ti ratio from 0.995 to 1.02) on the grain growth and bulk and grain boundary contributions to the dielectric response of STO ceramics is investigated. The grain boundary mobility dependence on the Sr/Ti ratio was assessed by extracting growth factors from grain growth data at 1450 ˚C for Ti-rich, stoichiometric and Sr-rich compositions. The growth factor is used as a

comparable value of the grain boundary mobility. It was observed that the grain boundary mobility increases with the decrease of the Sr/Ti ratio.

Stoichiometric and nonstoichiometric STO ceramics were also analyzed by IS and the dielectric response was correlated to the microstructure. IS is the adequate technique because it allows for the separation of the overall dielectric response of ceramics into the contributions from the intrinsic bulk and extrinsic grain boundaries [288; 336]. Nonstoichiometric STO exhibits lower electrical resistivity than the stoichiometric counterpart. This decrease is systematic for both Ti and Sr-excess and much stronger for the grain boundary resistivity as compared to the bulk.

Moreover, systematic variations with the degree of nonstoichiometry were observed for bulk and grain boundary activation energy for conductivity, capacitance and grain boundary thickness. These changes are correlated to a high defect concentration, namely oxygen vacancies, induced by nonstoichiometry and are consistent with the predominance of different grain boundary complexions dependent on the stoichiometry.

These observations show that nonstoichiometry may be used to control the grain boundary mobility and therefore tailor the microstructure and dielectric properties of strontium titanate based electroceramics, with emphasis on the grain boundary properties.

4.1.2 Experimental details

In the experiments described in this chapter, ceramics of STO compositions with Sr/Ti ratios from 0.995 to 1.02 were prepared and characterized according to the general experimental procedures presented in Chapter 3.

Grain growth studies were performed at 1450 ˚C with isothermal times from 0.1 to 12 h. The samples of the Ti-rich composition ST 0.995 were heated up to the sintering temperature of 1450˚C with a heating rate of 20 ˚C/min. At the end of the isothermal

sintering time, the samples were removed from the hot region of the furnace. After sintering for 0.1 h the ST 0.995 samples showed a relative density of 98 ± 1%.

The samples of the stoichiometric (ST) and Sr-rich (ST 1.02) STO compositions used in the grain growth studies were previously densified at 1350 ˚C for 2 h. The attained relative density was 96 ± 1% in both cases. In order to eliminate the remaining porosity, the samples were then submitted to a step of Hot Isostatic Pressing (HIP) for 1 h at the same temperature of 1350 ˚C and a pressure of 500 bar. The samples then showed relative density values of 99 ± 1%, close to full densification. The dense samples were then introduced in a tubular furnace at the intended temperature of 1450 ˚C and annealed for several isothermal times. The equivalent high density of the samples of the three compositions is important for further comparison of grain growth data because it assures that the samples of the different compositions had similar conditions for coarsening. The average grain size was obtained from the average equivalent diameter by multiplying by the stereological factor 1.22 [337].

For impedance spectroscopy studies, all the samples were sintered at 1500 ˚C for 5 h and attained relative densities above 96%. The technique and further experimental details are described in Chapter 3.

4.1.3 Results and discussion

4.1.3.1 Powders

Figure 4.1-1 presents the XRD spectra of the calcined powders for all the STO compositions under study. In spite of the stoichiometry variations between the compositions, the observed XRD peaks are consistent with the cubic crystallographic structure of STO (PDF # 84-0444) in all cases. No second phases were detected in any of the compositions, within the detection limits of the XRD technique.

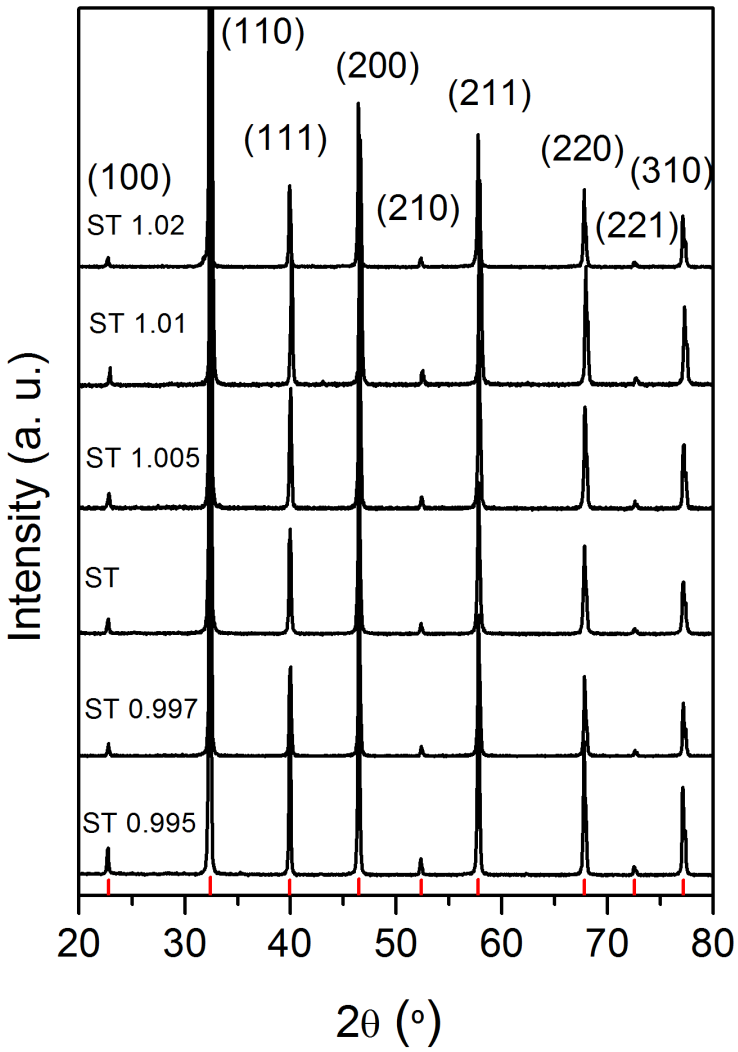

Figure 4.1-1: XRD spectra of stoichiometric and nonstoichiometric STO compositions. Despite the stoichiometry variations, all the peaks in all the compositions correspond to the STO phase. (PDF card #84-0444 is also shown).

Figure 4.1-2 shows the particle size distribution of calcined powders, obtained by laser diffraction (Coulter) for all the compositions. The particle size and size distribution for all the compositions are equivalent, showing a bimodal size distribution with peaks around 0.2 and 2-3 µm. The first peak of the distributions is always below 1 µm whereas the second one corresponds mainly to agglomerates that are destroyed after pressing [259].

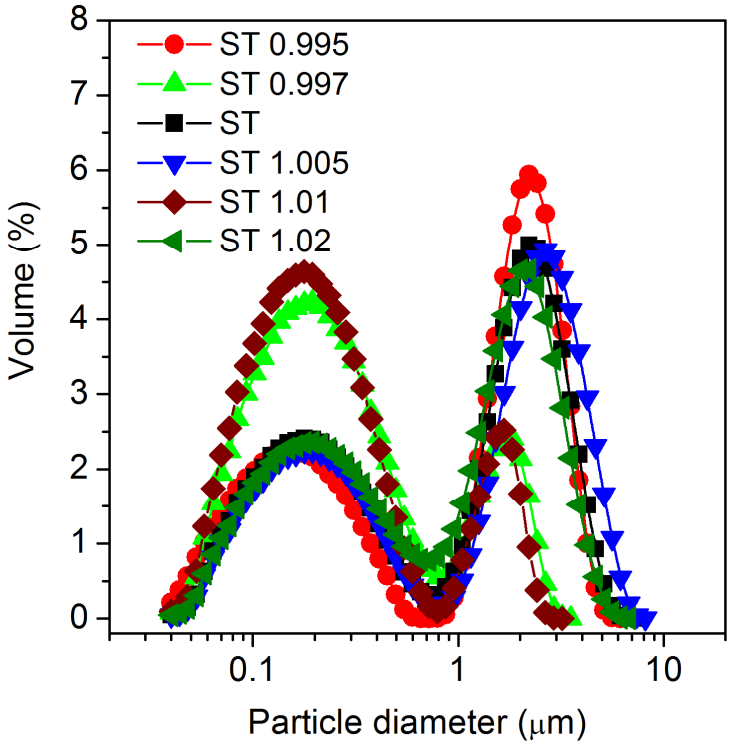

Figure 4.1-2: Particle size distribution determined by Coulter of the STO compositions. Equivalent bimodal size distributions are seen for all compositions.

4.1.3.2 Grain growth and grain boundary mobility

Figure 4.1-3 presents SEM micrographs of samples of the ST 0.995 (Ti-rich), ST (stoichiometric) and ST 1.02 (Sr-rich) compositions after the thermal treatment at 1450 ˚C for several isothermal times.

Coarsening of the microstructure with increasing isothermal time may be observed regarding the three compositions. Moreover, larger grain size is attained for the Ti-rich composition, ST 0.995 (with a lower magnification in Figure 4.1-3, left). Detailing these observations, the evolution with the isothermal time of the equivalent diameter (representing grain size) distribution and the average grain size obtained from these distributions are presented for the three compositions in Figure 4.1-4 and Figure 4.1-5, respectively. In agreement with previously reported results [259; 276], the enlargement of the grain size distribution and the increase of the attained grain size with the decrease of the Sr/Ti ratio are clearly observed.

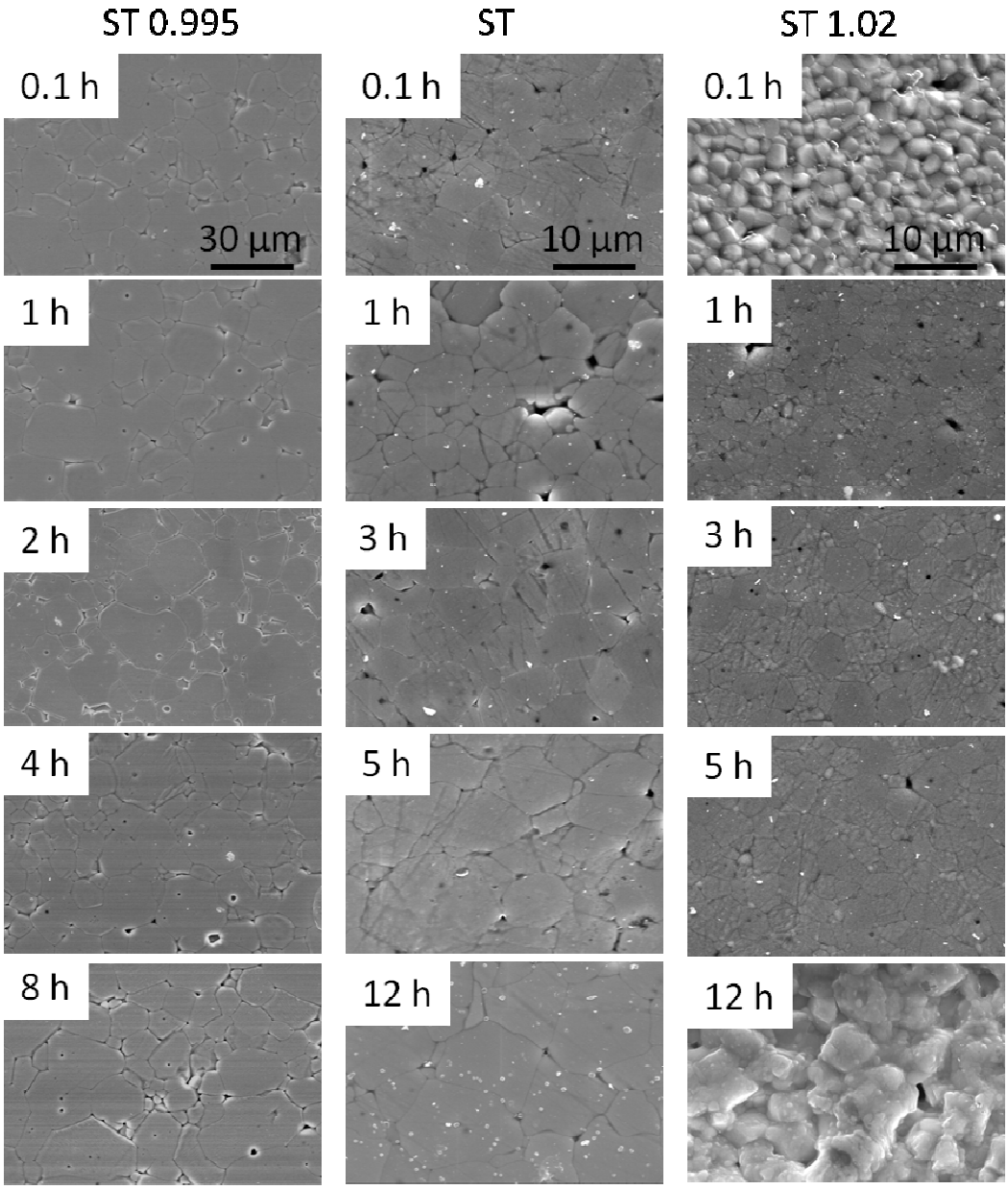

Figure 4.1-3: SEM micrographs of the three compositions: Ti-rich, ST 0.995 (left), stoichiometric, ST (middle) and Sr-rich, ST 1.02 (right) after thermal treatment at 1450 ˚C for several times. Coarsening of the microstructures is visible, as well as the increase of the attained grain size with the decrease of the Sr/Ti ratio.

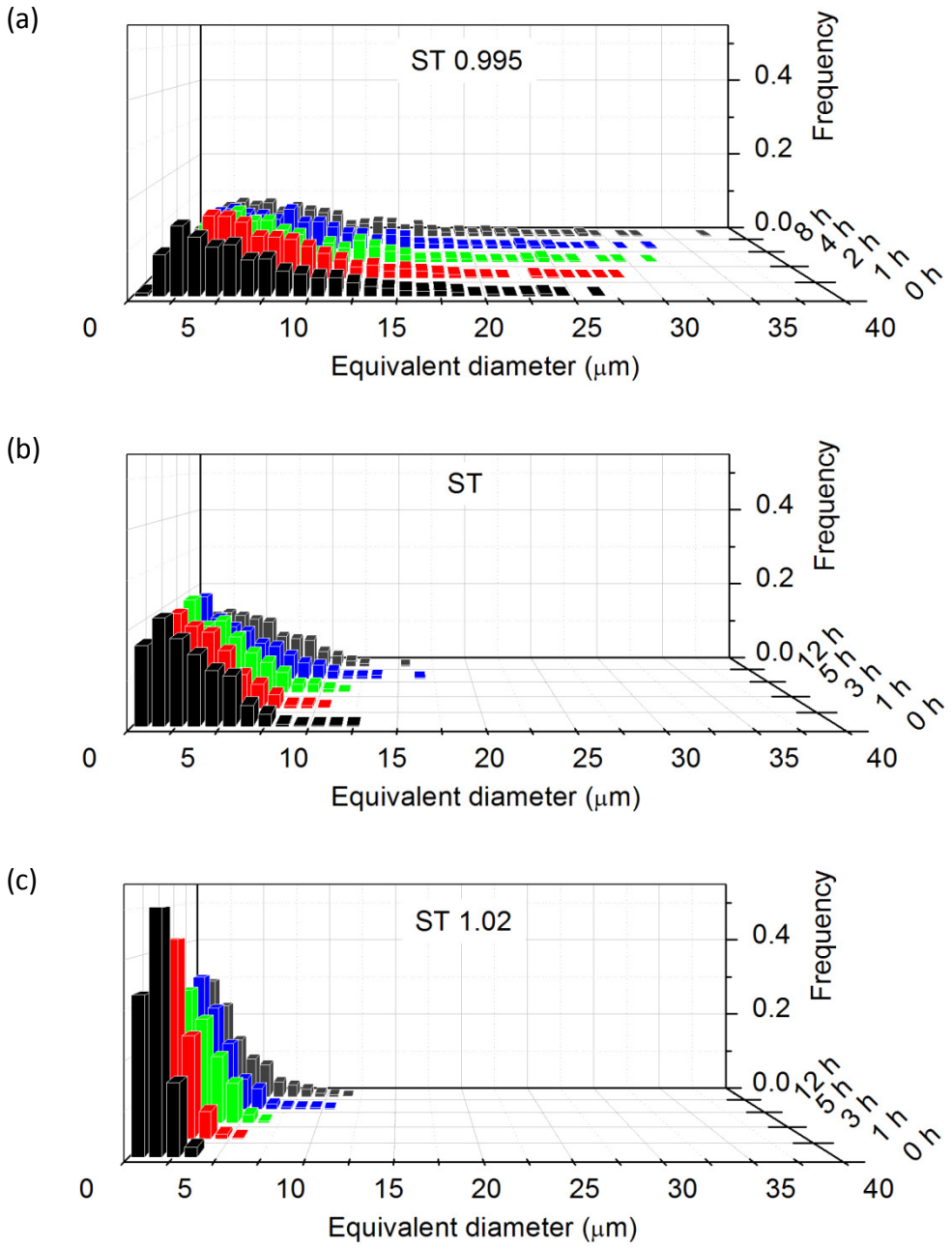

Figure 4.1-4: Equivalent diameter distribution evolution with the isothermal time at 1450 ˚C for the three compositions: (a) Ti-rich ST 0.995, (b) stoichiometric ST and (c) Sr-rich ST 1.02. Larger grain size and enlargement of the grain size distribution are observed with the increase of Ti content.

Despite the effects of the nonstoichiometry in the grain size and grain size distribution, the data regarding the three compositions seem to be consistent with a normal grain growth mode in all the cases.

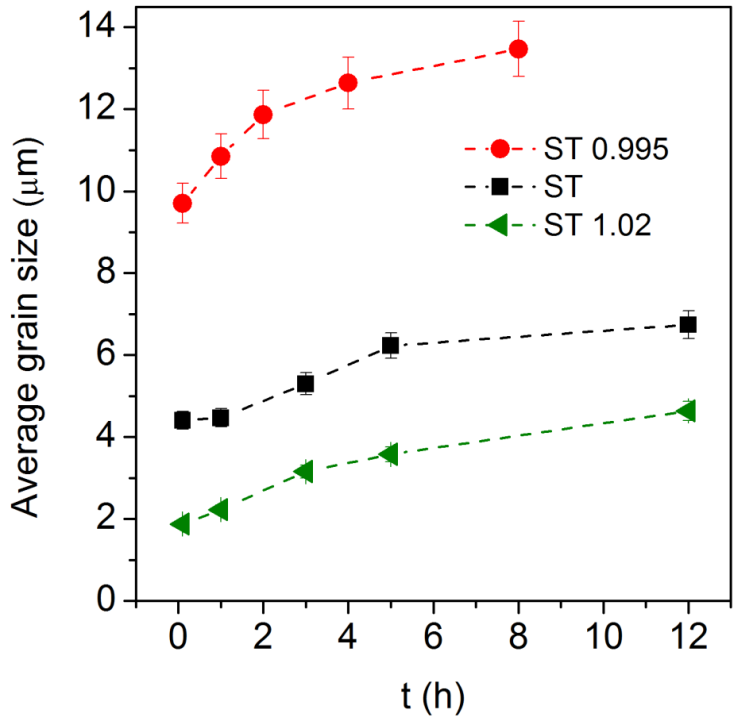

Figure 4.1-5: Average grain size evolution with the isothermal time at 1450 ˚C for the Ti-rich (ST 0.995), stoichiometric (ST) and Sr-rich (ST 1.02) compositions. Along the entire sintering cycle, larger grain size is attained with the decrease of the Sr/Ti ratio.

However, the distinction between normal and abnormal grain growth is sometimes ambiguous [21]. Particularly, the enlarged distributions of Figure 4.1-4 (a) regarding ST 0.995 Ti-rich composition may suggest the occurrence of abnormal grain growth. A criterion for the occurrence of abnormal grain growth was proposed to be [338]:

$$\frac{d}{dt}\left(\frac{G_A}{G}\right) > 0 \qquad (4.1\text{-}1)$$

where G_A is the grain size of an abnormal grain and G the average grain size. This means that the abnormal grain is growing so fast that it drifts away from the normal grain size distribution.

Therefore, to confirm quantitatively whether the grain growth mode is normal or abnormal, a graph of $D_{eq,max}/D_{eq}$ versus time is plotted in Figure 4.1-6, where $D_{eq,max}$ is

the largest equivalent diameter measured for every isothermal time for each composition and D_{eq} the average equivalent diameter.

It can be seen that the slopes regarding the three compositions are very close to zero (from - 0.03 to 0.03), which means that the largest grains remain at least very close to the normal grain size distribution. Additionally, the size of all the largest grains is under ~4 times the average of the respective distribution. Therefore, normal grain growth mode is reasonably assumed for all the compositions (Ti-rich, stoichiometric and Sr-rich).

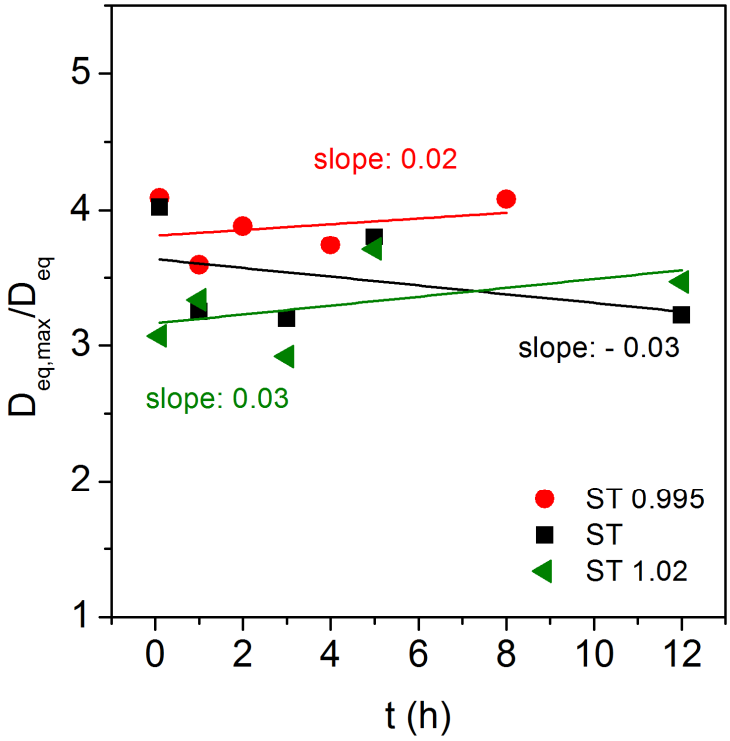

Figure 4.1-6: Maximum equivalent diameter divided by the average equivalent diameter as a function of the isothermal time for the three compositions. Near-zero slopes suggest normal grain growth mode for all the compositions.

The grain growth data in Figure 4.1-5 was used to assess the effect of nonstoichiometry on the grain boundary mobility of STO. As previously mentioned, the

grain boundary mobility, M_{GB}, is the proportionality factor between the driving force for grain growth and the average grain boundary velocity [21; 339].

The normal grain growth rate is typically described by the following equation [35; 339]:

$$G^m - G_0^m = k_G \Delta t \qquad (4.1\text{-}2)$$

with G_0 the initial average grain size at the time t_0, G the average grain size at the time t, m the grain growth exponent and k_G the grain growth factor.

In order to extract grain boundary mobilities from grain growth data, m must be assumed to be 2 (parabolic kinetics), implying a dense system with clean grain boundaries [35]. However, parabolic kinetics do not typically provide the best fit for normal grain growth data, because drag effects [340] normally cause the grain growth constant to be greater than two. In different words, the grain boundary mobility is not constant and decreases with increasing grain size due to decrease of specific surface area and consequent increase of the impurity drag effect [35; 340]. Nevertheless, the decrease in mobility is typically small and the exponent m = 2 was indeed shown to fit adequately normal grain growth data [35; 58; 59; 76; 247]. In these conditions, the growth factor k_G is given by the following equation [339]:

$$k_G = 2\alpha_g \gamma M_{GB} \qquad (4.1\text{-}3)$$

where α_g stands for a geometrical factor of the order of the unit and γ for the grain boundary energy, which is not expected to vary significantly from grain boundary to grain boundary in most ceramics [35] and the possible changes in boundary energy are small compared to the overall changes in k_G [247].

The grain size $(G^2 - G_0^2)$ versus time at 1450 ˚C for the three compositions, assuming parabolic kinetics, is presented in Figure 4.1-7. According to equation (4.1-2), this plot yields a linear relation, as can be effectively observed. This means that parabolic kinetics provides a reasonable fit of the grain growth data. The growth factor k_G may then be extracted from the slope of the lines and can be used as a comparable value for the “effective mobility” of the grain boundaries.

However, for long sintering times, some deviation from the linearity is observed. As previously mentioned, this may be related with increased impurity drag effect due to increasing of the grain size and consequent decrease of the specific surface area [340].

The deviation from the linearity, when long sintering times are considered, is almost negligible for the ST 1.02 composition but significantly increases with increasing Ti content. This is seen when comparing the linear fits with (dashed lines) and without (solid lines) the longest times in Figure 4.1-7. Nevertheless, for short isothermal times, parabolic kinetics revealed to fit the data adequately regarding the three compositions. In these conditions the effect of possible impurities is dilute and the grain boundary mobility can be properly assessed.

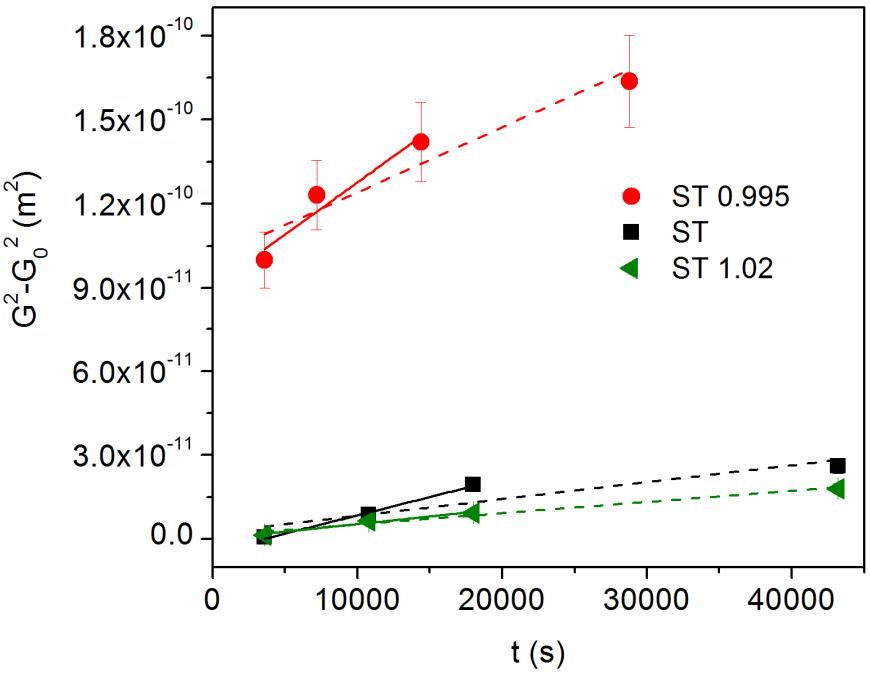

Figure 4.1-7: Grain size versus time at 1450 ˚C for the Ti-rich (ST 0.995), stoichiometric (ST) and Sr-rich (ST 1.02) compositions. Parabolic kinetics provides a good fit to the grain growth data of the three compositions for short sintering times.

Therefore, the growth factor was calculated excluding the data corresponding to the longest isothermal times, as presented in Figure 4.1-7 (solid lines). The results are presented in Figure 4.1-8 plotting the dependence of the growth factor k_G on the Sr/Ti ratio. A marked increase of the growth factor with decreasing Sr/Ti ratio is clearly observed.

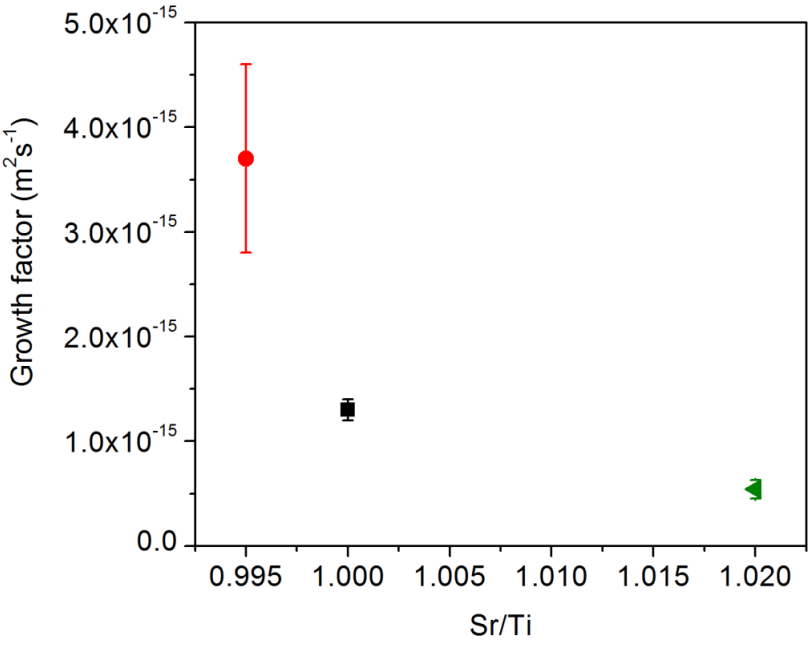

Figure 4.1-8: Growth factor, k_G, at 1450 ˚C for the Ti-rich (ST 0.995), stoichiometric (ST) and Sr-rich (ST 1.02) compositions. The growth factor increases significantly with the increase of the Ti content.

These observations of a strong dependence of the grain boundary mobility on the Sr/Ti ratio are in agreement with our previous results on the effect of the nonstoichiometry on the densification kinetics of STO [259]. In that work, Ti-excess (Sr/Ti = 0.997) enhanced matter transport during sintering whereas Sr- excess (Sr/Ti = 1.02) decreased it.

However, the present findings differ from the results of Bäurer *et al.* [76; 247]. The authors did not observe substantial differences in the effective mobility with the variation of the Sr/Ti ratio from 0.996 (Ti-excess) to 1.005 (Sr-excess). At the same sintering

temperature used in this work, 1450 ˚C, the authors reported growth factors around $4x10^{-17}$ m^2/s for Sr/Ti ratios of 0.996 and 1.002 (normal grain growth) and around $1x10^{-15}$ m^2/s for abnormally grown grains of the previous compositions and normal grain growth of a Sr/Ti=1.005 composition.

The growth factor values obtained in the present work and presented in Figure 4.1-8 are closer to the later value ($1x10^{-15}$ m^2/s). The growth factors found for the Ti-rich and stoichiometric compositions are higher than the referred value by factors of ~4 and 1.3, respectively, whereas the value for ST 1.02 is approximately half of the same value.

Nonetheless, in addition to the differences in the Sr/Ti ratios used in the two works, the samples studied by Bäurer *et al.* were sintered in oxygen atmosphere, which may have a strong impact in the sintering process. In fact, the different behaviour associated to different sintering atmospheres is a strong indication of the role of the defect chemistry alterations induced by the nonstoichiometry on the grain boundary properties. Particularly, the oxygen vacancy concentration, which should be minimized in oxygen atmosphere, may be an important factor in determining the grain boundary mobility in STO.

Regarding another aspect that must be considered, it has been shown that changes at grain boundaries can be induced by impurities [270]. However, the STO compositions under study were prepared from the same reagents with only minor variations of the stoichiometric proportions. Therefore the impurity content should be essentially the same for all compositions.

On the other hand, the effect of the same impurity content may depend on the Sr/Ti ratio, because impurities may have a higher affinity for either the A or the B site of the perovskite lattice. For example, Si impurities occupying the Ti site of the perovskite lattice are expelled from the crystal structure by Ti-excess [270]. Hence, the effect of impurities in changing the grain boundary properties dependently of the Sr/Ti ratio may not be completely excluded.

4.1.3.3 Dielectric characterization by Impedance Spectroscopy

4.1.3.3.1 Microstructural characterization of the samples used for Impedance Spectroscopy

As mentioned above, the presented differences in the grain growth behaviour and grain boundary characteristics induced by the variation of the Sr/Ti ratio may be expected to affect the dielectric response of the material. Particularly, the variation in the grain boundary mobility with the Sr/Ti ratio suggests the formation of different complexions, which may also correspond to different dielectric responses. IS was used to investigate those correlations.

Figure 4.1-9 presents SEM micrographs of Ti-rich (Sr/Ti ratios of 0.995 and 0.997), stoichiometric (Sr/Ti = 1) and Sr-rich (Sr/Ti ratios of 1.005, 1.01 and 1.02) samples used in the IS measurements. The samples were sintered at 1500 ˚C for 5h.

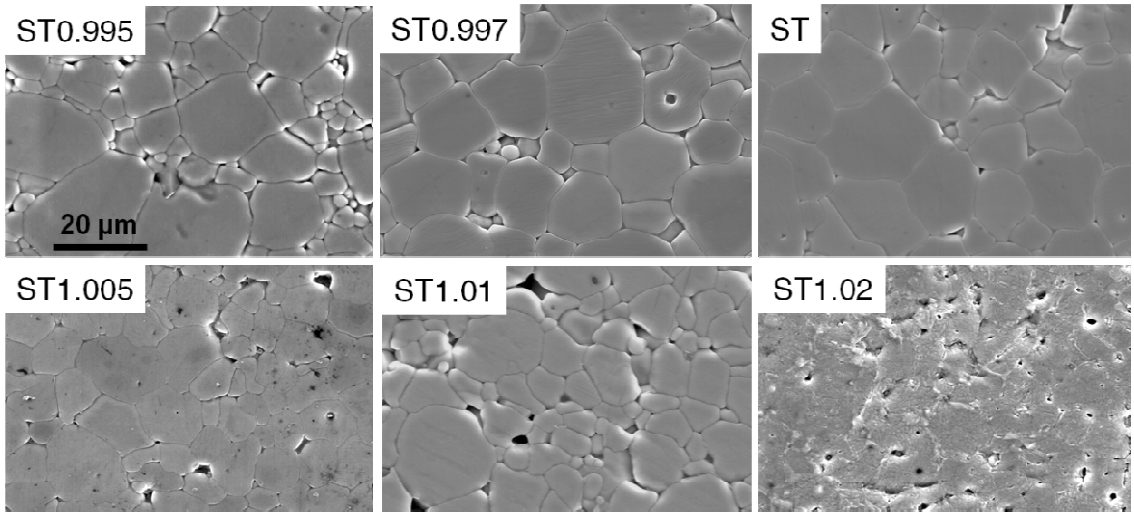

Figure 4.1-9: SEM micrographs of the STO ceramics of the several compositions, with Sr/Ti ratio from 0.995 to 1.02, sintered at 1500 ˚C for 5 h. The attained grain size is dependent on the Sr/Ti ratio.

In agreement with the observations presented above, a dependence on the composition is again clear in the microstructures (Figure 4.1-9), in the grain size

distributions in Figure 4.1-10 as well as in the average grain size presented in Figure 4.1-11. Coarse microstructures with enlarged grain size distribution are observed for Ti-rich compositions, despite the fact that an increase in the number of small grains is found in the sample ST 9.995, corresponding to the larger Ti-excess. By its turn, Sr-rich samples reveal once more finer microstructures and narrowing of the grain size distribution.

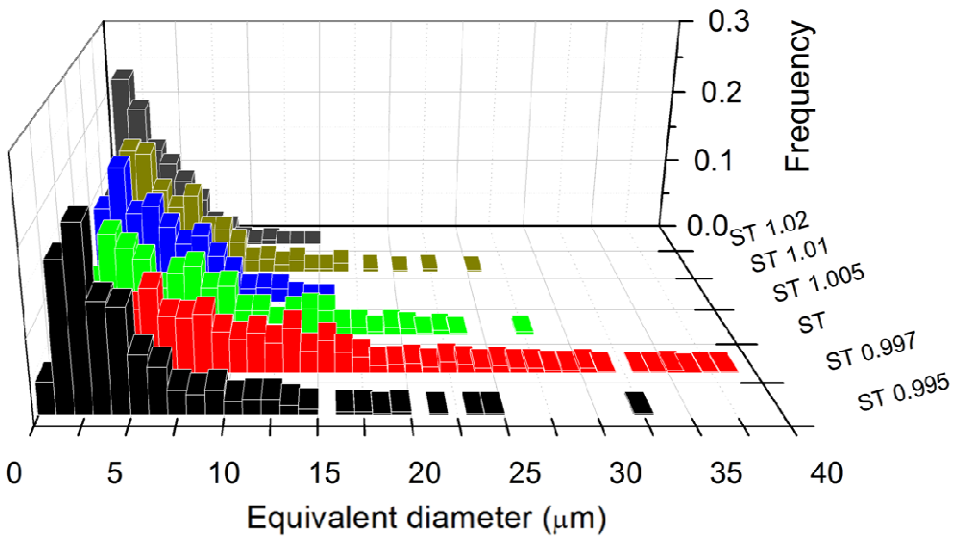

Figure 4.1-10: Equivalent diameter distribution for the several STO samples sintered at 1500 ˚C for 5 h showing again a dependence on the Sr/Ti ratio.

The average grain size variation with the Sr/Ti ratio presented in Figure 4.1-11 summarizes the previous observations for grain growth at 1500 ˚C. Relatively to the stoichiometric sample, 0.3 mol% excess of Ti (ST 0.997) lead to an increase of the average grain size, which was followed by a strong decrease for ST 0.995, with a 0.5 mol% Ti excess. Conversely, the average grain size observed for Sr-rich samples is always smaller than that of the stoichiometric composition. Ti-rich ST 0.995 and Sr-rich ST 1.005 and ST 1.01 samples showed similar average grain size.

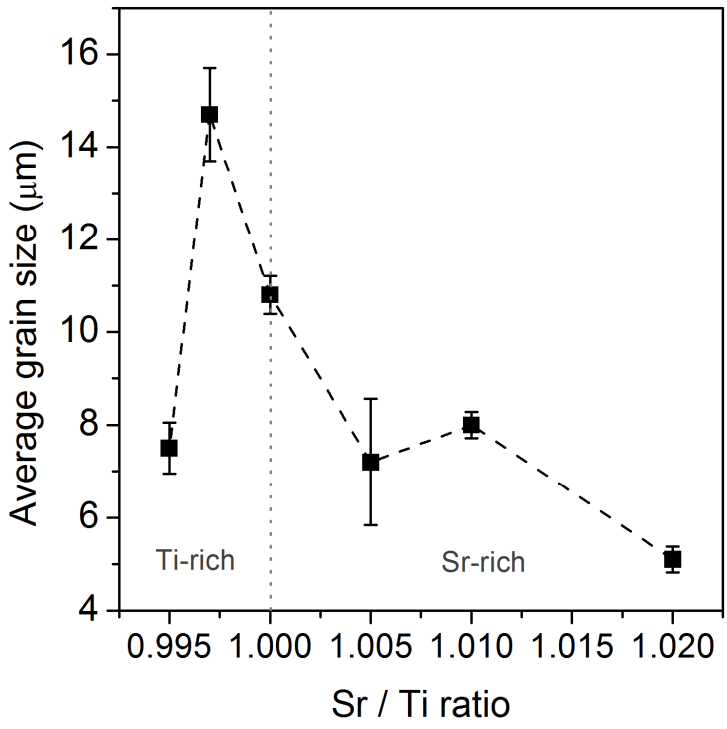

Figure 4.1-11: Average grain size as a function of the Sr/Ti ratio. Nonstoichiometry has a marked effect on the attained grain size.

The dependence of the grain growth behaviour on the nostoichiometry at 1500 ˚C is generally in agreement with the observations at 1450 ˚C. However, it should be noted that the average grain size attained by the Ti-rich composition ST 0.995 after sintering for 5 h at 1500 ˚C (7.5 µm, Figure 4.1-11) is smaller than that observed after sintering for 0.1 h at the lower temperature of 1450 ˚C (9.7 µm, Figure 4.1-5). This unexpected occurrence may be related with the reported grain growth anomaly in strontium titanate [76], which consists in grain boundary mobility drops with increasing temperature. This aspect was systematically investigated and will be discussed in the following chapter.

The variations found in the sintered microstructures may arise from changes in the defect chemistry induced by the several degrees of nonstoichiometry [259] as well as from the presence of traces of liquid phase leading to the predominance of different interface complexions [35; 247] and consequently to different interface kinetics, as observed and discussed above.

TEM micrographs presented in Figure 4.1-12 for ST 0.997, ST and ST 1.02 compositions indeed revealed signs of different grain boundary complexions: rough grain boundaries are observed in all samples, but edges suggesting grain boundary faceting are detected in the Ti-rich and stoichiometric ones.

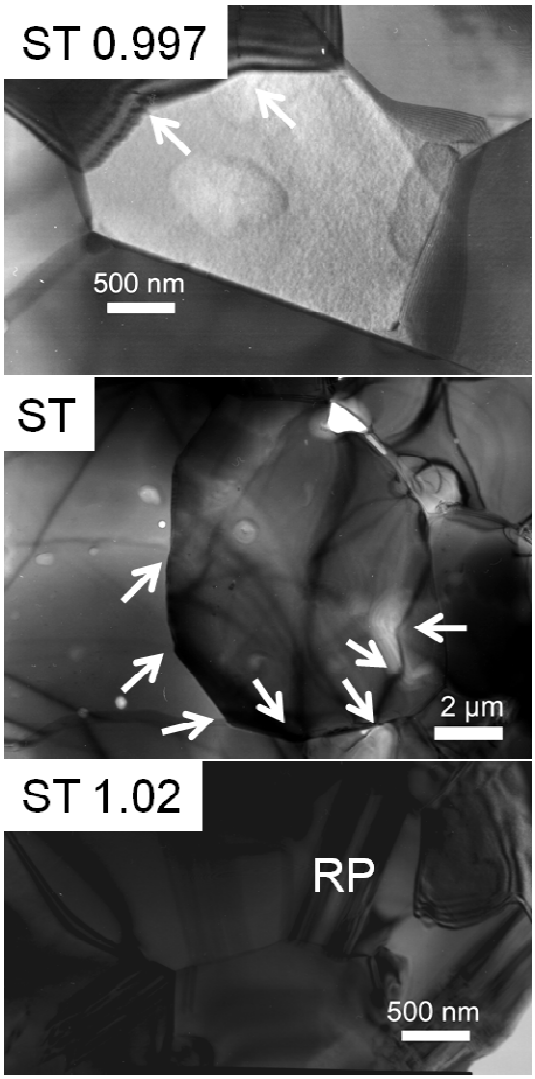

Figure 4.1-12: TEM microstructures of (a) ST 0.997, (b) ST and (c) ST 1.02 ceramics, sintered at 1500 ˚C for 5 h. Arrows indicate sharp edges in the grain boundaries, which are observed for ST and ST 0.995. ST 1.02 samples show RP phases.

Moreover, traces of an amorphous phase could be detected in some triple points of these samples. Furthermore, in Sr-rich sample ST 1.02, a pattern of planar defects inside the grains, characteristic of RP structures [225], is clearly observed.

4.1.3.3.2 Impedance Spectroscopy measurements

Given that the microstructure is an important factor determining the dielectric response of ceramics, the different microstructures characterized above may lead to diverse dielectric responses. Additionally, the effects of the nonstoichiometry on the defect chemistry and on the formation of different interface complexions may by themselves be expected to affect the dielectric response. Furthermore, nonstoichiometry may affect differently bulk and grain boundaries, whose contributions to the overall dielectric properties may be investigated separately by IS, as exposed in the following text.

In Figure 4.1-13, the dependence of the real part of the capacitance on the frequency in the measured temperature range is presented for the sample ST 1.005, as an example. Two main contributions are evident: the high frequency low capacitance (of the order of 10^{-11} F/cm) plateau corresponds to the bulk capacitance; the low frequency high capacitance (of the order of 10^{-9} F/cm) plateau is attributed to the grain boundaries [288]. Additionally, at high temperatures, e.g. 700 ˚C, the curve shows a further upturn at the low frequency end, which represents the onset of the electrode interface relaxation process (capacitance of the order of 10^{-6} F/cm).

Therefore, the samples may be modelled by the equivalent circuit in Figure 4.1-14, which was used to fit the data. The circuit consists in a series of three blocks of a resistor and a CPE in parallel, modelling bulk (R1 and CPE1), grain boundaries (R2 and CPE2) and sample-electrode interface (R3 and CPE3) contributions. However, in the measured temperature and frequency ranges, the electrode-sample interface contribution is generally residual. To fully display the interface contribution, measurements at even higher temperature (or lower frequency) would be necessary.

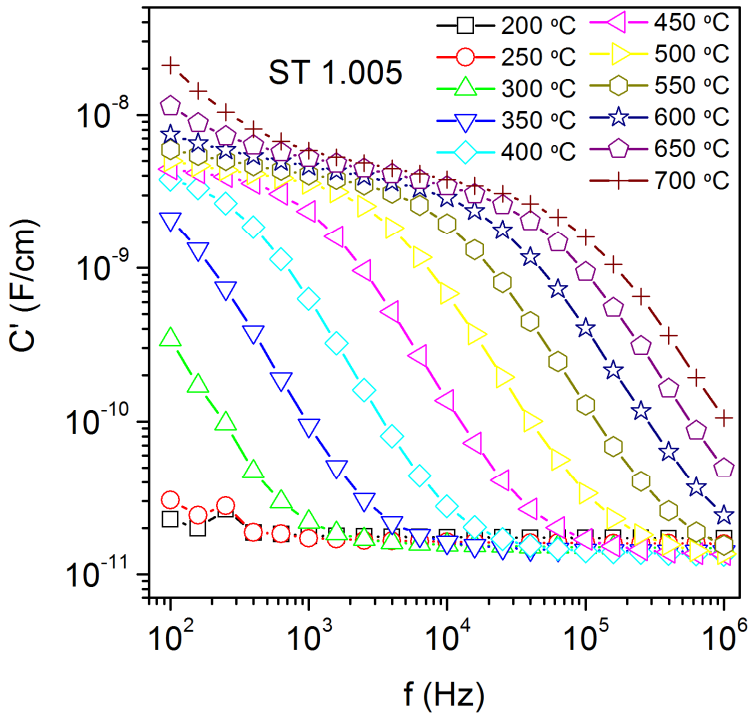

Figure 4.1-13: Real part of the capacitance as a function of the frequency, from 200 to 700 ˚C, regarding the sample ST 1.005, showing three contributions: bulk, grain boundaries and sample-electrode interface.

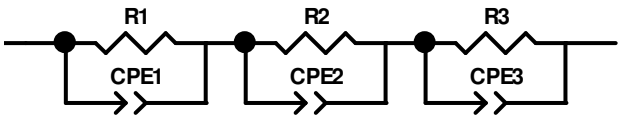

Figure 4.1-14: Equivalent circuit used for data fitting. The circuit consists in a series of three blocks, for bulk (R1 and CPE1), grain boundaries (R2 and CPE2) and sample-electrode interface (R3 and CPE3) contributions.

Well resolved semicircles regarding the two main contributions, bulk and grain boundaries, were clearly observed in the complex impedance spectra. In the used frequency range, well resolved semicircles regarding the bulk relaxation are observed between approximately 200 and 500 ˚C, whereas the semicircles concerning the grain

boundaries are observed roughly between 450 and 700 ˚C. In this way, the contributions of these two entities could be analyzed separately.

As shown in Figure 4.1-15, for all the Sr/Ti ratios, the spectra at 300 ˚C only exhibits the low capacitance (around $1x10^{-11}$ F/cm) high frequency plateau, meaning that the spectra at this temperature is dominated by the bulk contribution, despite the onset of the grain boundary relaxation is already visible. Additionally, the onset of the grain boundary relaxation is shifted to higher frequencies in a systematic way with the increase of the nonstoichiometry (excluding ST 1.02 curve), regarding both Ti and Sr-excess.

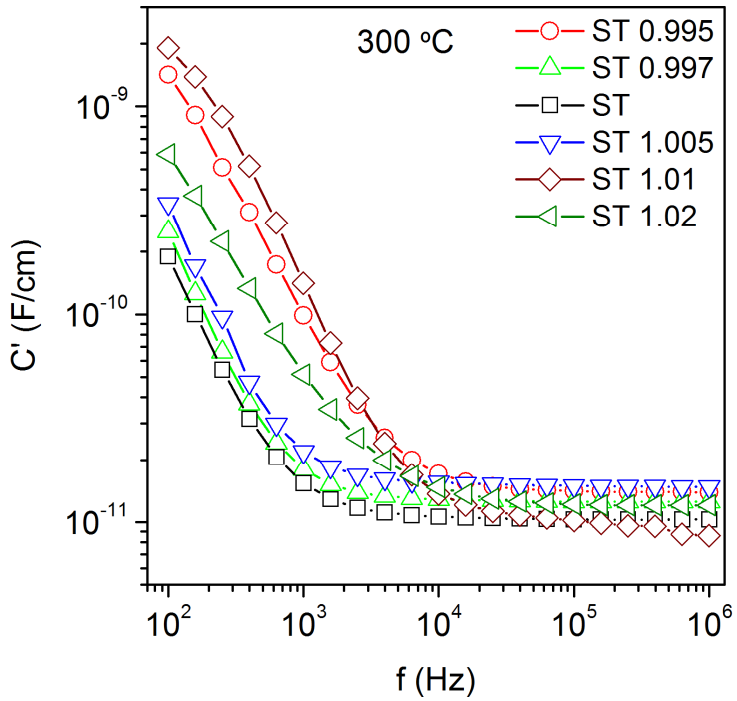

Figure 4.1-15: Real part of the capacitance as a function of the frequency for all samples at 300 ˚C. The plateau corresponds to the bulk contribution; the onset of the grain boundary relaxation is visible.

Figure 4.1-16 shows the Nyquist plots (imaginary *z*'' vs. real part *z*' of the complex specific impedance) at 300 ˚C for all samples. The spectra for all the STO compositions

contain two contributions each, representing the intrinsic bulk and extrinsic grain boundary dielectric relaxations, for high and low frequencies, respectively. However, at this temperature (300 ˚C) and in the used frequency range, the semicircles related to the grain boundary contribution are not completely resolved and only a small low frequency peak appears, in agreement with the capacitance curves on Figure 4.1-15.

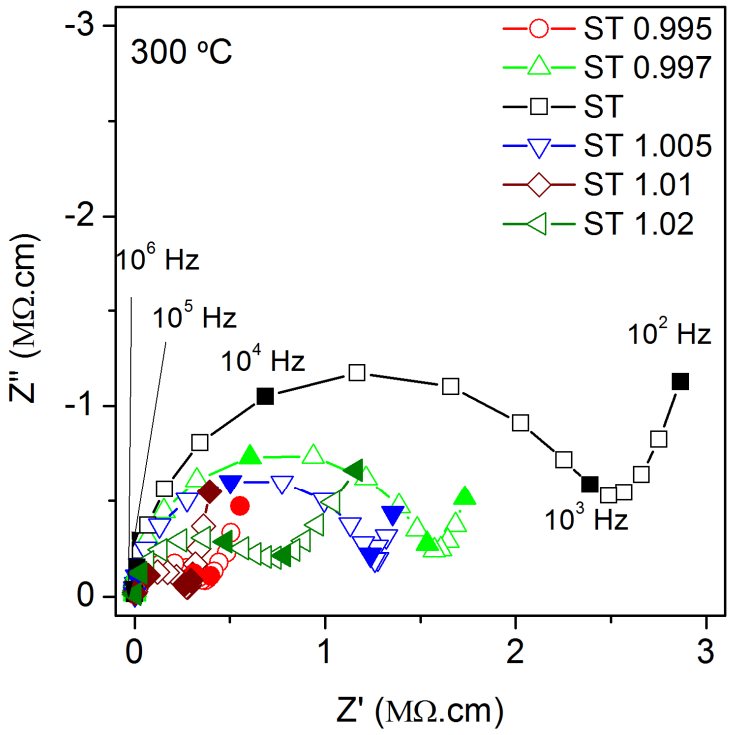

Figure 4.1-16: Specific impedance spectra at 300 ˚C for all samples (the points regarding the frequencies of 10^2, 10^3 … 10^6 Hz are marked with full symbols for all curves). The impedance spectra are strongly affected by nonstoichiometry.

An important observation is that the well resolved bulk semicircles change perceptibly with the very small stoichiometric variations between the samples. A decrease of the bulk resistivity (smaller semicircles) is evident for all the nonstoichiometric samples relatively to the stoichiometric one.

Figure 4.1-17 shows the variation with the frequency of the imaginary parts of specific impedance, Z'', and modulus, M''/ε_0 at 300 ˚C. These plots give different weightings to

the data: Z'' plots show the most resistive elements in the sample ($Z''_{max} = R/2$), whereas modulus plots are more sensitive to the elements with the smallest capacitance ($M''/\varepsilon_0 = 1/2C$) [288]. Both representations in Figure 4.1-17 give similar information and confirm the fact that the impedance spectra at this temperature are dominated by the bulk relaxation. Z'' plots show one well defined peak (related to bulk) and the onset of the grain boundary contribution for low frequencies. Modulus plots clearly show only the peak related to the bulk.

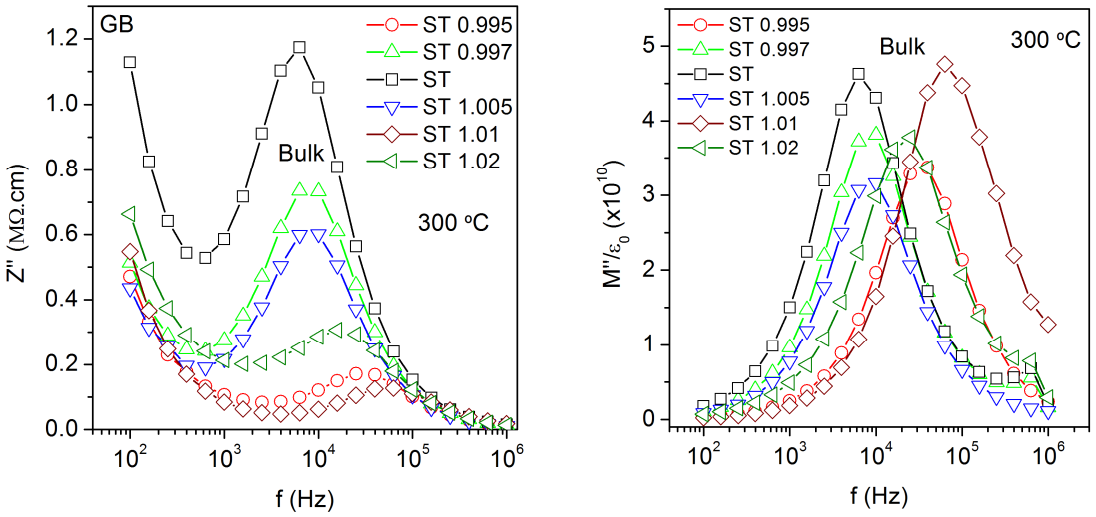

Figure 4.1-17: (a) Z'' and (b) M''/ε_0 spectroscopic plots for all samples at 300 ˚C. Both representations show that the impedance spectra at 300 ˚C are dominated by the bulk contribution, which is affected by the Sr/Ti ratio.

Additionally, excluding the ST 1.02 sample (which has a much larger degree of nonstoichiometry), systematic shifts with the nonstoichiometry in the Z'' and modulus peak positions are evident from Figure 4.1-17, in agreement with previous observations. Moreover, the decrease of the Z'' peak height with the nonstoichiometry is evident (Figure 4.1-17 (a)), in agreement with the decrease of bulk resistivity depicted in the complex impedance plots in Figure 4.1-16.

As a summary of these observations, a quantitative analysis of the variation of the bulk resistivity with the Sr/Ti ratio at 300 ˚C is provided in Figure 4.1-18, which presents the values obtained by fitting the complex impedance spectra in Figure 4.1-16.

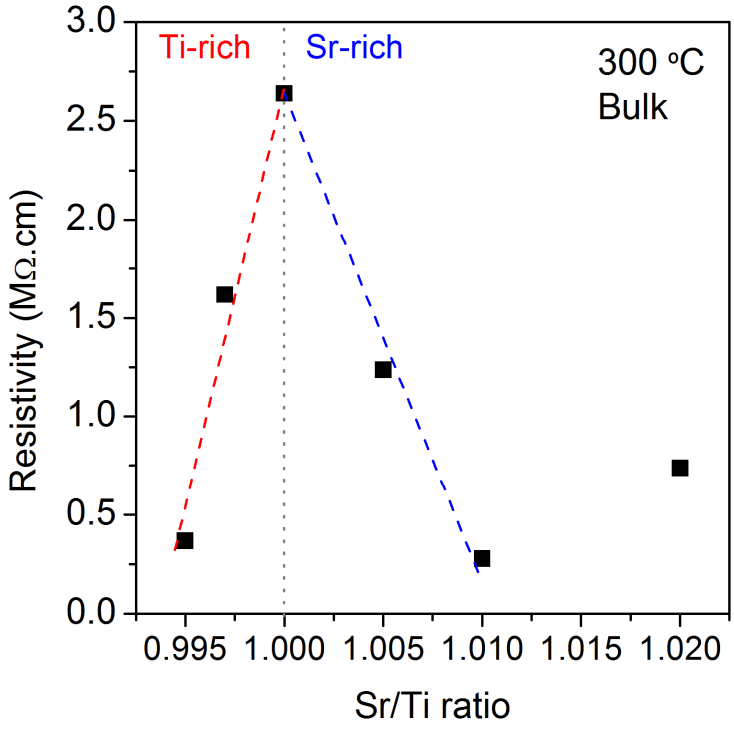

Figure 4.1-18: Bulk resistivity dependence on the Sr/Ti ratio at 300 ˚C. The bulk resistivity decreases systematically with nonstoichiometry.

The decrease in bulk resistivity with the nonstoichiometry is evident. Moreover, between Sr/Ti ratios of 0.995 and 1.01, the decrease is proportional to the degree of nonstoichiometry, regarding both Ti and Sr excesses. The bulk resistivity of the Ti-rich ST 0.995 is 7 times lower than that of the stoichiometric sample, whereas a decrease by a factor of 9 is observed for the Sr-excess ST 1.01 sample (which has a degree of nonstoichiometry twice larger than ST 0.995). On the other hand, the same degree of nonstoichiometry (0.5 mol%) in Ti-rich ST 0.995 and Sr-rich ST 1.005 lead to a more significant decrease of the bulk resistivity in the case of Ti-excess: factors of 7 and 2 were observed, respectively.

Regarding the sample with Sr/Ti ratio of 1.02 (ST 1.02), the bulk resistivity was also considerably decreased (by a factor of 4). However, this decrease is smaller than that of the ST 1.01 sample, which has half the degree of nonstoichiometry. This might be related to the formation of the RP structures, as observed by TEM in Figure 4.1-12. The formation of these structures accommodates the Sr excess and in this way may decrease the amount of defects present in the lattice, leading to a smaller decrease in the bulk resistivity.

As previously mentioned, the grain boundary relaxation is completely visible in the complex impedance spectra at high temperatures (generally between 450 and 700 ˚C). Therefore, a similar analysis to that performed at 300 ˚C is now presented regarding the impedance data at 600 ˚C, revealing important information about the effect of the nonstoichiometry in the grain boundary resistivity.

The fact that impedance spectra at 600 ˚C are dominated by the grain boundary relaxation is evidenced by the spectroscopic plot of the real part of the capacitance at this temperature in Figure 4.1-19. A single plateau is again observed (with the exception of the ST 1.02 sample), this time at low frequencies and for capacitance values of the order of 10^{-9} - 10^{-8} F/cm, assigned to the grain boundaries. Grain boundary capacitances of similar order of magnitude are often found in well sintered ceramics with narrow intergranular regions [288]. An increase in the grain boundary capacitance is observed for all nonstoichiometric samples, relatively to the stoichiometric one.

As was already observed in Figure 4.1-15, the onset of the grain boundary relaxation is systematically shifted for higher frequencies with the increase of the degree of nonstoichiometry. For the samples Ti-rich ST 0.995 and Sr-rich ST 1.01, with high degree of nonstoichiometry, the beginning of the grain boundary relaxation is at the highest frequencies and for lower frequencies the beginning of the sample-electrode interface relaxation is visible.

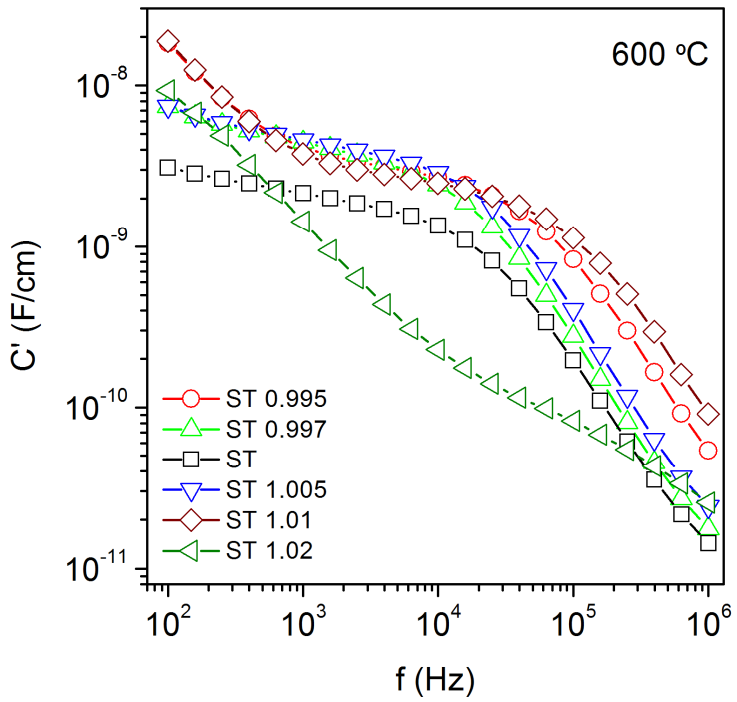

Figure 4.1-19: Real part of the capacitance as a function of the frequency at 600 ˚C for all the samples. The grain boundary response is dominant at 600 ˚C.

The curve related to the sample ST 1.02, with the highest degree of nonstoichiometry that leads to the formation of RP phases, shows however a different behaviour. At this high temperature of 600 ˚C, a new relaxation process seems to be starting at frequencies lower than those of the grain boundary relaxation, with an associated capacitance of the order of 10^{-9} F/cm, similar to that of the grain boundaries of the other samples. In this case, the grain boundary capacitance would be around 10^{-11} F/cm, which is possible since according to Irvine *et al.* [288] the magnitude of grain boundary capacitance usually ranges from 10^{-11} to 10^{-8} F/cm.

A possible explanation is therefore that this new relaxation process is related to the RP phases present in this sample (Figure 4.1-12), or to the interfaces between these layered structures and the main bulk phase. However, this is not clear from the results and needs further clarification. Furthermore, regarding this sample (ST 1.02), for temperatures higher than approximately 550 ˚C, where the grain boundary relaxation becomes less visible and the new one starts to appear, the observed semicircles are

not well resolved and therefore no good data fittings for resistivity quantification were possible, even with the addition of a new R-CPE block to the equivalent circuit.

Regarding the other Sr/Ti ratios (0.995 – 1.01) the grain boundary semicircles are well resolved and dominate the impedance spectra at 600 ˚C, as can be seen in Figure 4.1-20, allowing a good assessment of the grain boundary resistivity variation with the nonstoichiometry. Indeed, at this temperature, the complex impedance spectra show practically only one semicircle, meaning that only the grain boundary relaxation is observable in the frequency range of the measurements.

Additionally, dramatically smaller semicircles for nonstoichiometric samples are evident in Figure 4.1-20 particularly in Figure 4.1-20 (b), which corresponds to the data in (a) zoomed near the origin. Only in this way the semicircles for higher degrees of nonstoichiometry are visible, highlighting the major impact of the small stoichiometric variations on the grain boundary properties. Furthermore, this effect is systematic, with the decrease of the size of the semicircles varying proportionally to the degree of nonstoichiometry for both types of oxide excess. Moreover, the effect of 0.5 mol % excess of Ti has an effect in decreasing the grain boundary resistivity similar to that of the twice as high 1 mol% Sr-excess.

Figure 4.1-21 presents the spectroscopic plots of Z'' and M''/ε_0 for all samples at 600 ˚C. Both figures confirm the previous observations and show that the grain boundary relaxation peak is steadily shifted to higher frequencies by several orders of magnitude with increasing degree of nonstoichiometry. The systematic decrease of grain boundary resistivity for nonstoichiometric samples is again shown by the decrease of the Z'' peak height (Figure 4.1-21 (a)). Regarding the curve of the ST 1.02 sample, the new relaxation process, possibly related to the RP phases, is also visible in Figure 4.1-21 (a), at low frequencies.

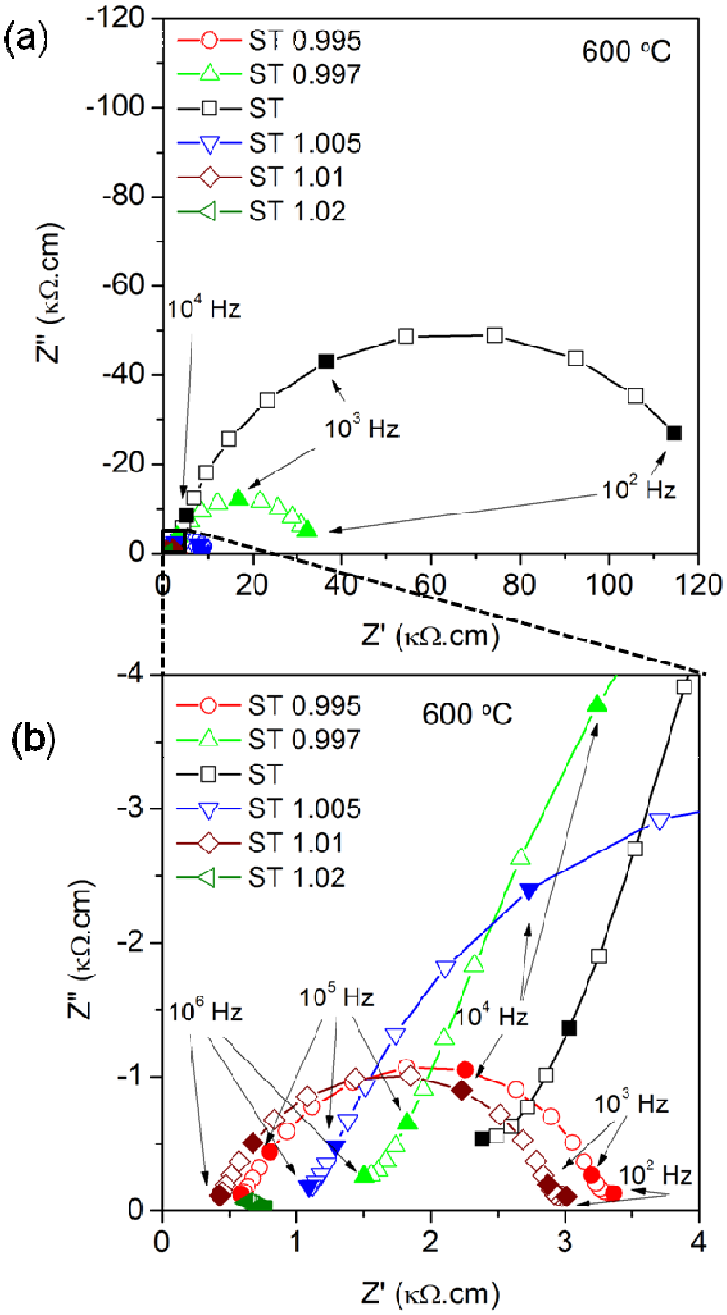

Figure 4.1-20: (a) and (b) Specific impedance spectra at 600 ˚C for all the samples (the points regarding the frequencies of 10^2, 10^3… 10^6 Hz are marked with full symbols for all curves). (b) shows the zooming of (a) near the origin. A marked impact of the nonstoichiometry is observed on the grain boundary contribution.

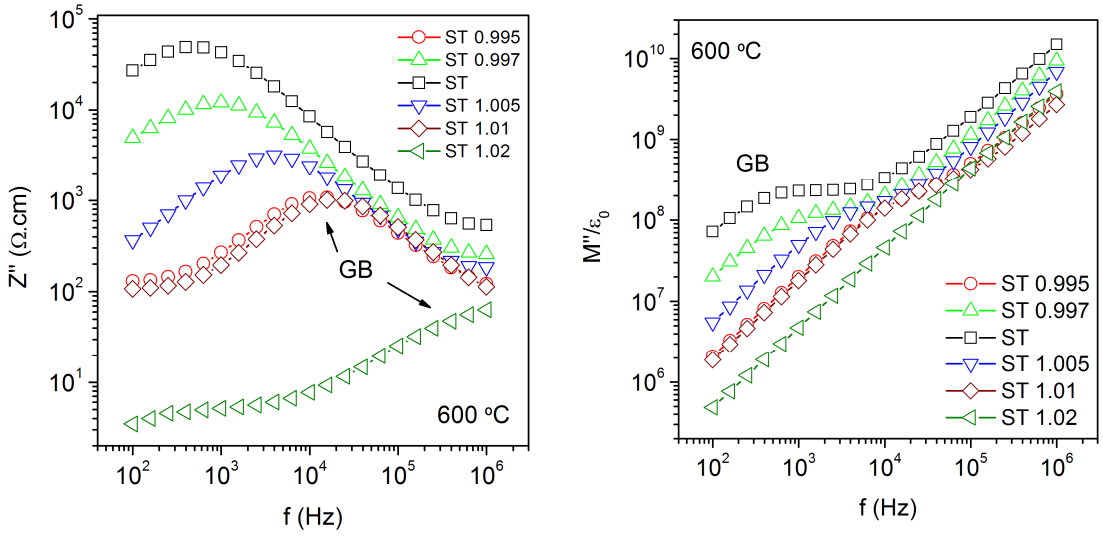

(a) (b)

Figure 4.1-21: (a) Z'' and (b) M''/ε_0 spectroscopic plots at 600 ˚C for all samples. With increasing degree of nonstoichiometry, the grain boundary relaxation peak is shifted to higher frequencies.

The effect the nonstoichiometry (Sr/Ti ratio) on the grain boundary resistivity at 600 ˚C is more clearly demonstrated in Figure 4.1-22. Similarly to the effect on the bulk resistivity, a very significant impact of the small nonstoichiometric variations in the grain boundary resistivity is clearly observed. The magnitude of the decrease of grain boundary resistivity is much higher, however, requiring the use of a log scale to be fully displayed.

Indeed, a decrease by factors of 4 and 17 was found in ST 0.997 and ST 1.005 compositions, correspondingly. A more dramatic change occurred in the grain boundary resistivity of the Ti-rich composition ST 9.995, which was diminished 55 times, related to the stoichiometric sample. Similarly, a factor of 59 was observed in the case of the Sr-rich sample ST 1.01.

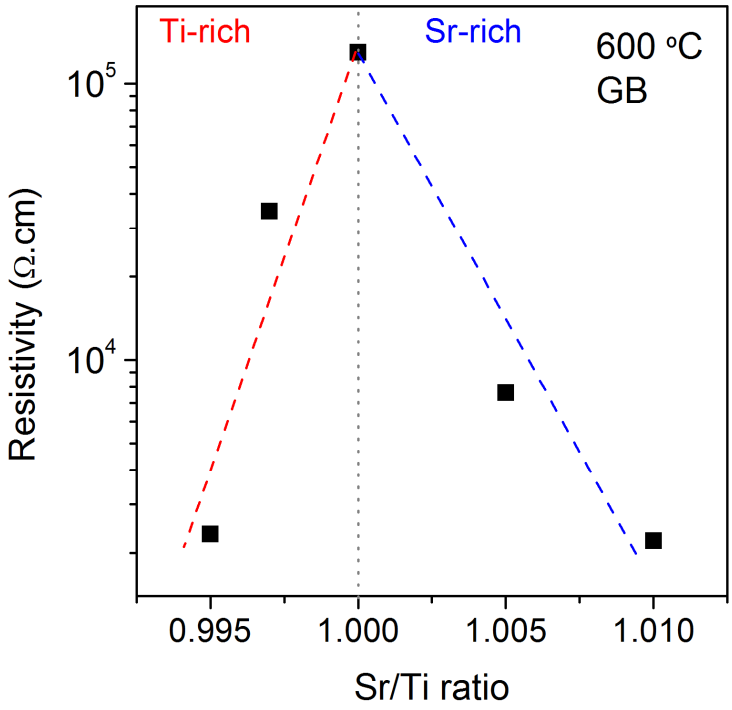

Figure 4.1-22: Grain boundary resistivity dependence on the Sr/Ti ratio at 600 ˚C showing a strong decrease for all nostoichiometric samples.

The stronger effect on the grain boundaries as compared to the bulk may be correlated with previously reported results on the sintering kinetics of STO [76; 247; 259; 277] and may be related to the formation of different grain boundary complexions with consequent variations in mobility, as presented above, and dielectric properties. It should be noted that the grain boundary resistivity is usually expected to increase with the decrease of the grain size due to increased number of boundaries across the sample [341], which does not occur in the present case. All nonstoichiometric samples show a decrease of the grain boundary resistivity, irrespective of the smaller grain size of some samples. This observation confirms the strong impact of nonstoichiometry on the defect chemistry of the material and suggests that other factors may play an important role concerning the dielectric properties of these ceramics. These factors may include the formation of liquid phase during sintering or segregation to grain boundaries, leading to different grain boundary properties. Liquid phase formation may indeed be expected for Ti-rich samples, especially ST 0.995. On the other hand,

the presence of RP structures on Sr-rich compositions, as observed for Sr-rich ST 1.02, may also play a role.

From the values of bulk and grain boundary resistivity, ρ_r, obtained from the complex impedance spectra at several temperatures between 200 and 700 ˚C, the conductivity, σ, is easily calculated ($\sigma=1/\rho_r$). The dependence of the bulk and grain boundary conductivity on the temperature follows a typical Arrhenius law (equation (4.1-4), where E_a stands for the activation energy, K_B for the Boltzmann constant and T for the temperature in K).

$$\ln \sigma = \ln \sigma_0 + \left(\frac{E_a}{k_B T}\right) \qquad (4.1\text{-}4)$$

Then, the following plots in Figure 4.1-23 are obtained for bulk (a) and grain boundaries (b) and activation energy (E_a) values can be determined, as presented in Figure 4.1-24.

The temperature dependence of the bulk and grain boundary conductivity in Figure 4.1-23 shows again the exposed observations at 300 and 600 ˚C and expands the remarks to a wider temperature range. The effects of nonstoichiometry in both bulk and grain boundary behaviour in the studied temperature range are well illustrated. It can be seen that both bulk and grain boundary conductivity increase with nonstoichiometry in a nearly systematic way, in agreement with the decrease of the resistivity previously observed. Additionally, the temperature at which the grain boundary contribution is detected is lowered by the nonstoichiometry.

Furthermore, the lines regarding bulk conductivity of all samples in Figure 4.1-23 (a) are almost parallel, showing similar temperature dependence. On the other hand, strong changes in the temperature dependence of the grain boundary conductivity are observed in Figure 4.1-23 (b). This is clear in Figure 4.1-24, which presents the activation energy for bulk and grain boundary conductivity obtained for all Sr/Ti ratios.

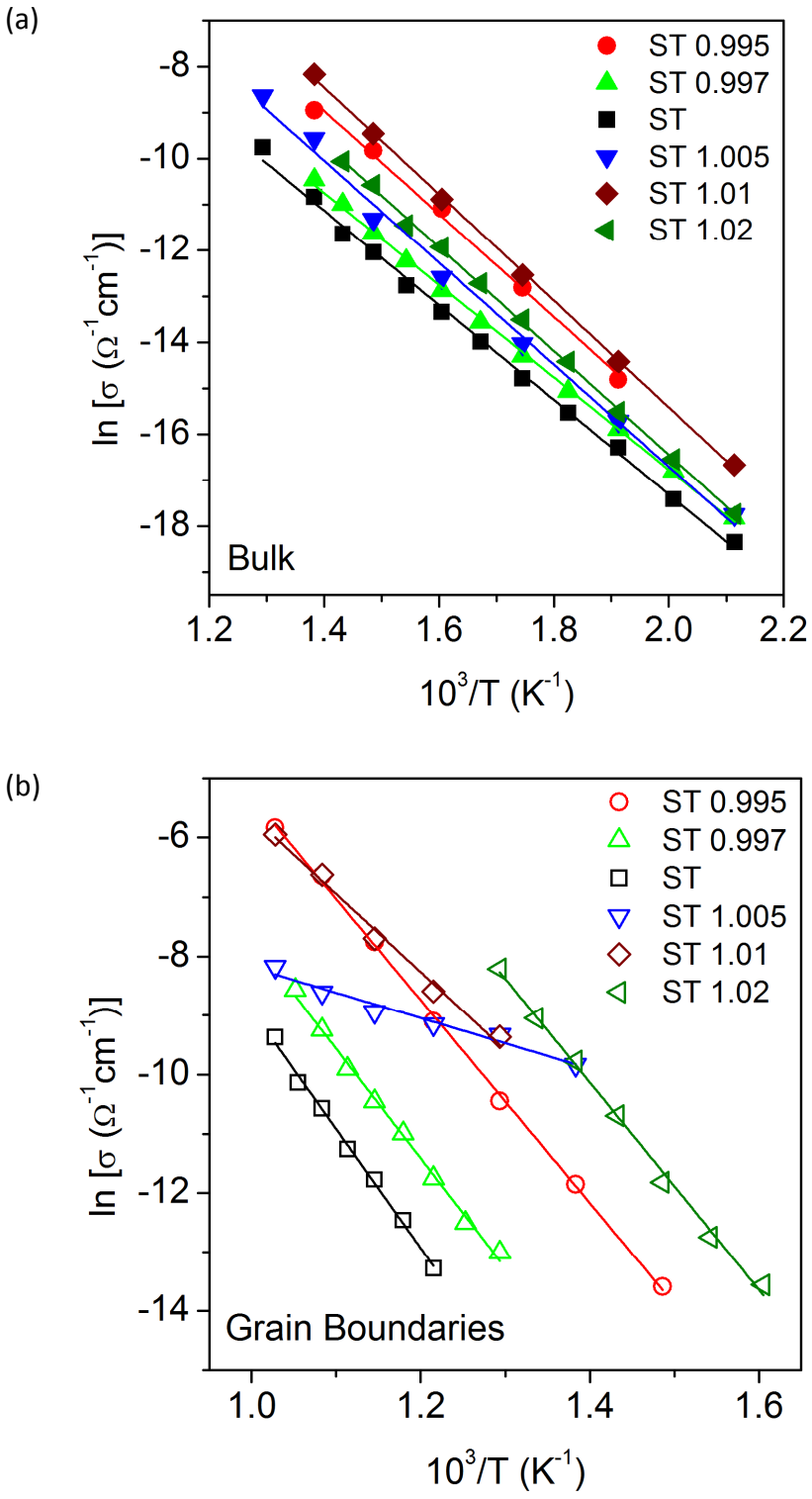

Figure 4.1-23: (a) Bulk and (b) grain boundary conductivity dependence on the temperature. Grain boundaries are more affected than bulk by nonstoichiometry.

Despite the fact that the resistivity of both bulk and grain boundaries was strongly decreased for nonstoichiometric samples, the activation energy of bulk and grain boundaries revealed absolutely different dependences on the composition. The values concerning the bulk conductivity are practically independent of the composition, showing a very slight tendency to increase with the Sr/Ti ratio. All the activation energy values for the bulk conductivity are in the range $0.87 \leq E_{a,B} \leq 1.00$ eV, which is in agreement with previously reported values for the p-type behaviour of undoped and stoichiometric STO [342] and acceptor-doped STO [234; 332; 341; 343; 344] and consistent with ionic charge transport attributed to oxygen vacancies [344; 345].

On the other hand, the activation energy for the grain boundary conductivity shows a remarkable variation with the Sr/Ti ratio and also different behaviour depending on the type of oxide excess. In fact, nonstoichiometry lowers the grain boundary activation energy in every case, when compared to that of the stoichiometric sample (ST, $E_{a,GB}$ = 1.73 eV). However, for Ti-rich compositions the decrease is proportional to the amount of Ti-excess, whereas in the case of Sr-excess, the lowest degree of nonstoichiometry investigated (ST 1.005) induces the largest decrease in the activation energy, which then increases for higher fractions of Sr-excess. Furthermore, the same degree of nonstoichiometry (0.5 mol%) leads to a much stronger decrease of the grain boundary activation energy in the case of Sr-excess (ST 1.005, $E_{a,GB}$ = 0.37 eV) than in the case of the Ti-rich sample (ST 0.995, $E_{a,GB}$ = 1.48 eV).

Typical values of activation energy for the grain boundary contribution are within the range of 1.4 - 1.6 eV, as predicted for acceptor doped STO [344] and confirmed for Fe-doped bicrystals [346] and for ceramic samples of undoped [332] or Fe-doped STO ceramics [347]. The value reported for Ni-doped samples [343; 344] is close to half the bandgap, $W_g/2 \approx 1.6$ eV. This activation energy is associated to a charge transport across the grain boundary assumed to be predominantly electronic, related to an inversion layer at the grain boundary space charge due to accumulation of electrons leading to a "*W*"-shaped conductivity profile [344]. For lower potential barriers, the grain boundary conductivity profile may show a "*V*"-shape, dominating at low temperatures, with an associated activation energy around 1.0 eV, which is combined with the ionization energy of the bulk acceptor [344].

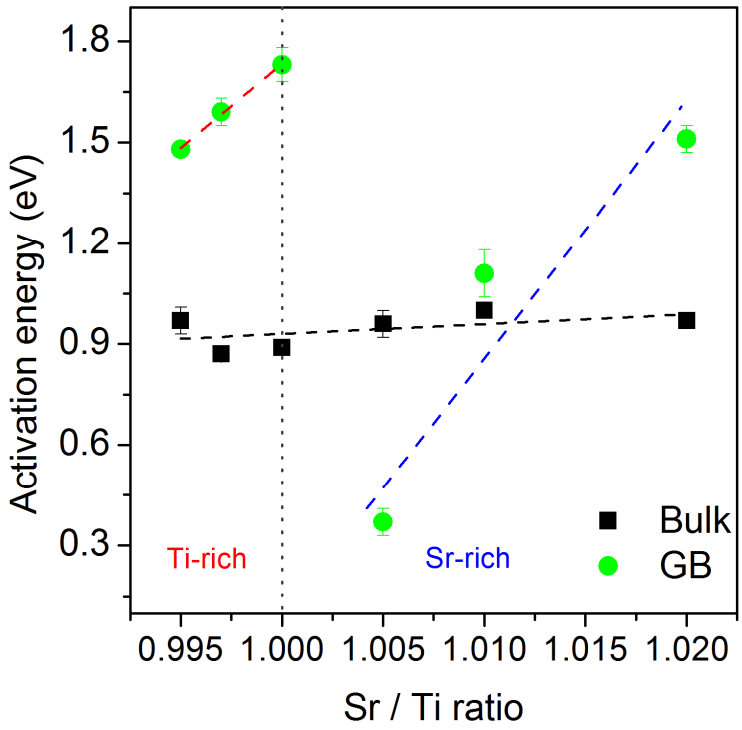

Figure 4.1-24: Activation energy for conductivity for bulk and grain boundaries as a function of the Sr/Ti ratio. Bulk activation energy is nearly independent of the composition; grain boundaries reveal different dependences for Sr and Ti-excess.

In this context, the activation energy for grain boundary conductivity found for Ti-rich ST 0.995 and ST 0.997 (1.59 eV), as well as stoichiometric ST (1.78 eV) and Sr-rich ST 1.02 (1.51 eV), is in agreement with the previously reported values for STO and consistent with a "*W*"-type grain boundary conductivity profile, despite the fact that the activation energy of the stoichiometric composition is slightly higher. On the other hand, the activation energy values for ST 1.005 and ST 1.01 (1.11 eV) are lower, especially that of ST 1.005, which may suggest a "*V*"-shaped profile.

It is important to consider here that some microstructural features, such as a non-uniform grain size distribution, may originate deviations from the ideality of the brick layer model and influence the values for activation energy of grain boundary conductivity obtained from the impedance spectra [332; 348]. Nevertheless, the systematic variation of the activation energy concerning both types of oxide-excess strongly

suggests an effective direct relation between nonstoichiometry and activation energy for grain boundary conductivity.

Figure 4.1-25 presents the variation of the bulk and grain boundary capacitance with the temperature. It can be seen that the values of bulk capacitance are nearly independent of the temperature, as expected for STO materials [332; 343]. Additionally, a small dispersion of values between all the samples is observed, despite the fact nonstoichiometric samples show slightly higher bulk capacitance values. Concerning the grain boundary capacitance, a similar nearly temperature-independent behaviour is observed. However, the variations in the grain boundary capacitance values induced by the nonstoichiometry are again larger than in the bulk. The composition with the largest Sr-excess (ST 1.02) showed capacitance values similar to those of the stoichiometric composition, whereas the highest capacitance was observed in the sample with the lowest Sr-excess, ST 1.005.

The average of the values in Figure 4.1-25 is presented in Figure 4.1-26 for all the samples, illustrating more clearly the dependence of the bulk and grain boundary capacitance on the Sr/Ti ratio.

It is again evident that the grain boundaries are more affected by nonstoichiometry than grain interiors. Systematic variations with the degree of nonstoichiometry regarding bulk and grain boundaries are however obvious in both types of oxide-excess. Regarding Ti-rich compositions, increasing the degree of nonstoichiometry leads to a steady increase of both bulk and grain boundary capacitance, with the later showing a more marked effect.

On the other hand, Sr-excess compositions revealed a different behaviour. Bulk capacitance is higher than that of the Ti-rich and stoichiometric samples and almost independent of the Sr/Ti ratio (with a very slight tendency to decrease with increasing nonstoichiometry). Regarding the grain boundaries, ST 1.005 showed the highest capacitance with further increase of the nonstoichiometry leading to a marked decrease of the capacitance to a value close to that of the stoichiometric composition for ST 1.02.

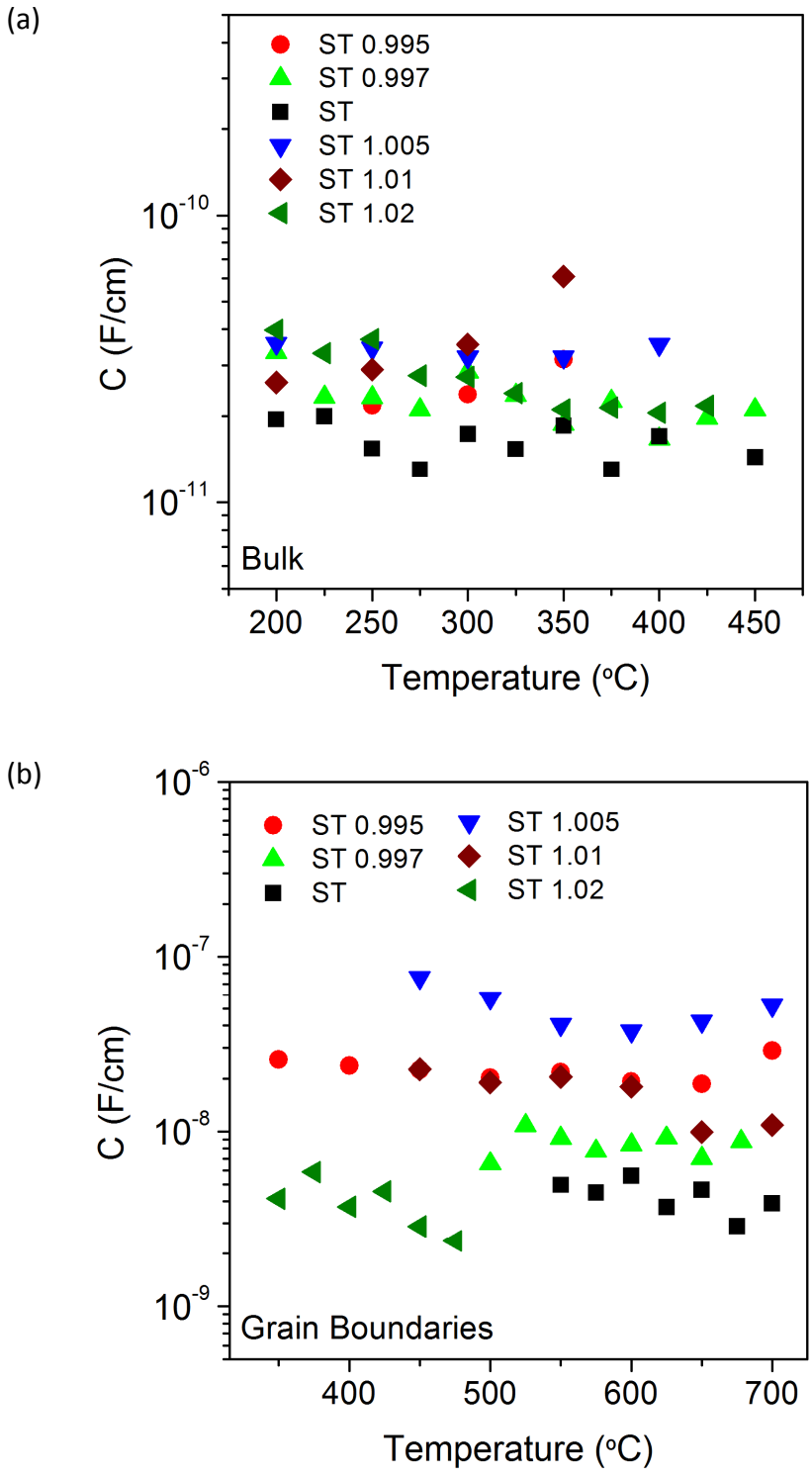

Figure 4.1-25: Measurement temperature dependence of (a) bulk and (b) grain boundaries capacitance. Both contributions are nearly independent of the measurement temperature.

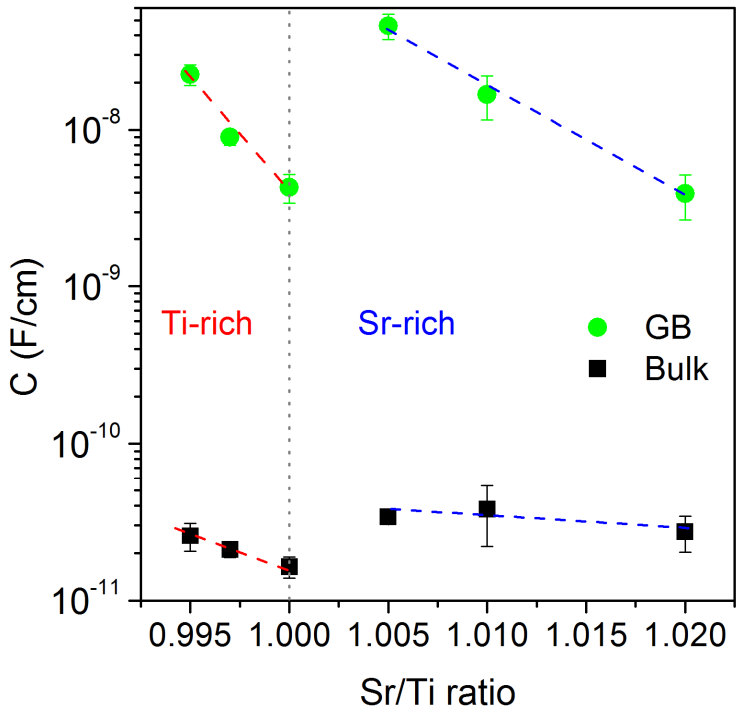

Figure 4.1-26: Bulk and grain boundary capacitance as a function of the Sr/Ti ratio. Grain boundaries are more affected by nonstoichiometry than grain interiors.

From these values of bulk and grain boundary capacitance, the grain boundary thickness may be estimated according to equation (4.1-5) [349-351], where δ_{GB} is the grain boundary thickness, C_B and C_{GB} are the bulk and grain boundary capacitance, respectively, and G the average grain size. An assumption is made that the dielectric constants of bulk and grain boundaries are similar. The result of this estimation is presented in Figure 4.1-27.

$$\delta_{GB} = \frac{C_B}{C_{GB}} G \qquad (4.1\text{-}5)$$

Systematic dependences on the nonstoichiometry are again found for both types of oxide-excess regarding the grain boundary thickness. The variation is however different depending on the type of nonstoichiometry. For Ti-excess, the increase of nonstoichiometry leads to thinning of the grain boundaries from ≈ 41 nm in the stoichiometric composition to ≈ 9 nm in ST 0.995. On the other hand, for Sr-excess, the

increase of the Sr/Ti ratio leads to thickening of the grain boundary from ≈ 5 nm observed for the lower Sr-excess to around 36 nm in ST 1.02.

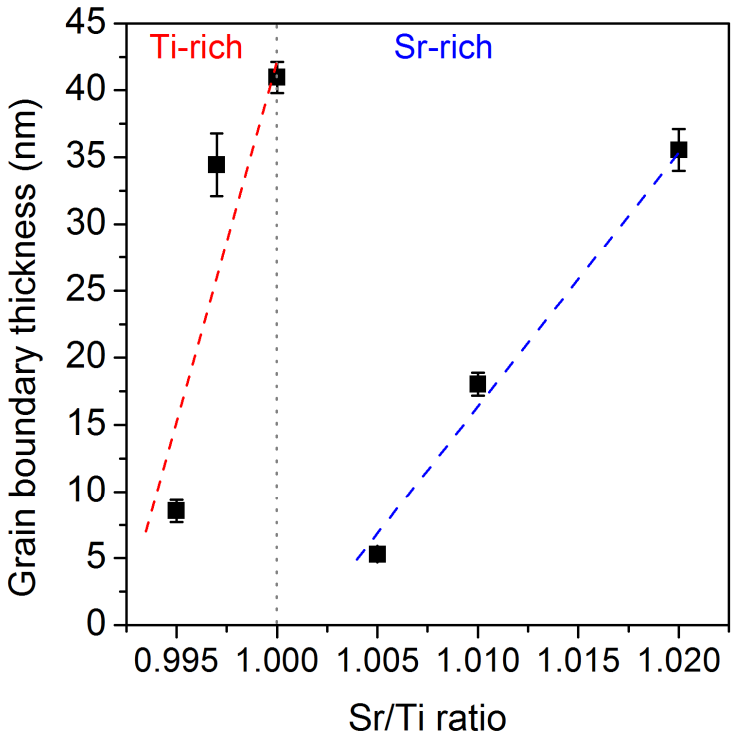

Figure 4.1-27: Grain boundary thickness as a function of the Sr/Ti ratio. Systematic but different dependences are observed for both types of oxide-excess.

Nevertheless, all nonstoichiometric samples revealed a grain boundary thickness lower than that of the stoichiometric composition. The effect of 0.5 mol% oxide excess is similar regarding both types of oxide, as can be seen for Ti-rich ST 0.995 and Sr-rich ST 1.005, which showed the strongest decrease of the grain boundary thickness. This does not exclude the possibility of that for Sr/Ti ratios between 1 and 1.005 the effect may be similar to that of the same degree of Ti-excess.

Based on IS measurements, the width of the grain boundary depletion layer in acceptor-doped STO has been determined to be 30-200 nm, decreasing with increasing acceptor concentration [245; 343]. Grain boundary thickness values between 0.57 and 9.23 nm were also reported for Nb-doped STO [352] and a value of 50 nm was reported for the

boundary thickness of Nb-doped STO bicrystals [353]. Therefore, the grain boundary thickness from around 5 to 41 nm obtained in the present work is in the range of reported values for STO.

The variation of the grain boundary thickness with the Sr/Ti ratio in Figure 4.1-27 shows relatively similar trends to those observed for the activation energy for grain boundary conductivity (Figure 4.1-24) suggesting a direct relation between grain boundary thickness and activation energy for conductivity. Additionally, the decrease of the grain boundary thickness in all nonstoichiometric samples may also be correlated to the fact that nonstoichiometry decreased the grain boundary resistivity in all cases.

Moreover, the systematic dependence of grain boundary thickness on nonstoichiometry, associated to the different microstructures observed by SEM and TEM, to the variations of the grain boundary resistivity, activation energy and grain boundary capacitance, strongly support the predominance of different grain boundary complexions [35; 247] induced by nonstoichiometry. Additionally, these observations show that grain boundary properties may be designed using nonstoichiometry and tailored microstructures and dielectric properties may be obtained.

Particularly regarding grain boundary faceting, a correlation with the grain boundary resistance has recently been reported by Lee *et al* [49]. Annealing a STO bicrystal in air at 1600 ˚C renders the faceted boundary to become defaceted, but in this case a previously absent second grain boundary semicircle then appears in the impedance spectra indicating a strong increase in grain boundary resistance [49]. The rough grain boundary observed by the authors above 1600 ˚C contained more oxygen vacancies than the faceted boundary present bellow that temperature, which were considered to induce a double Schottky barrier and obstruct the charge-carrier transport across the grain boundary.

In the present work, stoichiometric polycrystalline material and with excess of both types of oxides presented bulk and grain boundary impedance responses. Additionally, irrespective of the predominance of different grain boundary structures as observed by TEM analysis in Figure 4.1-12, both types of oxide-excess originated strong decrease

of grain boundary impedance contributions in comparison with the stoichiometric composition.

It is, therefore, suggested that the shape of the grain boundaries (faceted or rough) may not play a crucial role in determining the grain boundary resistivity. Instead, the presence, concentration and distribution of defects induced by nonstoichiometry may be more determining for grain boundary resistivity.

In this context, the possible alterations of the defect chemistry in STO induced by nonstoichiometry must be considered. The incorporation of TiO_2-excess into the STO lattice requires the formation of strontium and oxygen vacancies [16; 225] according to equation (2.3-14). On the other hand, the incorporation of Sr-excess occurs through the formation of the RP structure, but small amounts of Sr-excess can be incorporated by the formation of titanium and oxygen vacancies [16; 225] (equation (2.3-12)), or by a cation site-exchange (anti-site defect) and oxygen vacancies (equation (2.3-13)).

As a result of the alterations on the defect chemistry induced by nonstoichiometry the overall defect concentration is increased, which may be related to the decrease of the bulk and grain boundary resistivity. Moreover, the oxygen vacancy content should be increased in both Ti and Sr-rich compositions, more strongly in the case of Ti-excess. Accordingly, the same amount of oxide-excess (0.5 mol%) showed stronger effects on decreasing the resistivity on both bulk and grain boundaries on the Ti-rich composition. Moreover, such oxygen vacancies may probably segregate to the grain boundaries [49; 249; 354] and the grain boundary resistivity would, therefore, be more strongly affected by the nonstoichiometry than the bulk counterpart, as observed.

Additionally, the unavoidable presence of acceptor impurities should also be taken in consideration. As mentioned before, even undoped STO exhibits a specific concentration of oxygen vacancies due to the presence of acceptor impurities incorporated during processing or already present in the raw materials [224; 227; 228]. However, as already discussed, all the compositions were prepared following the same procedures and from the same raw materials, with only slight variations of the SrO/TiO_2 ratio. Therefore, the effect of impurities should be basically equivalent in all compositions and not sufficient to explain the observed dramatic changes in bulk and,

especially, grain boundary properties. This is also supported by the clear systematic variations with nonstoichiometry in both Ti and Sr-excess cases regarding the several investigated parameters.

Nevertheless, the combined effects of nonstoichiometry (more important) and impurities may therefore originate a high concentration of defects in the material. As previously mentioned, the redistribution of the charged defects is known to lead to the formation of a space charge layer [244; 245; 343]. In STO, the grain boundary core is positively charged whereas the regions close to the grain boundaries are depleted of mobile positive charge carriers such as oxygen vacancies and holes. On the other hand, a negative space charge forms on both sides of the grain boundary due to accumulation of compensating negative charges [244]. Moreover, as observed by Bäurer *et al.* [247], this may result in local nonstoichiometry at the grain boundary region (grain boundary core and space charge) that may be different than the bulk composition (Ti or Sr- rich).

Additionally, it was suggested that an increase in the in Sr/Ti ratio lowers the potential barrier at grain boundary core and hence decreases grain boundary resistance [42]. More generally, the increased concentration of defects induced by the nonstoichiometry may lead to a state of saturation of the grain boundaries, which would decrease the magnitude of the potential barrier beyond the saturation point [244]. According to Klie *et al.* [249], the formation of the grain boundary electrical barriers is probably related to an excess of oxygen vacancies at the grain boundary core relatively to the bulk rather than cation interstitials. In this way, for high defect concentrations, beyond grain boundary saturation a high concentration of defects, namely oxygen vacancies, would also remain in the bulk, which may lead to the reduction of the potential difference and consequently of the grain boundary resistivity.

At the same time, the different defects originated by Ti or Sr-excess may somehow lead to the different behaviours regarding, for example, the variation of the grain boundary thickness for the two kinds of nonstoichiometry. On the other hand, it is important to note that, despite the similar effects on the resistivity, the investigated degrees of oxide excess are higher in the case of Sr than those of Ti-rich compositions.

At the same time, the accommodation of the Sr-excess may be easier due to the formation of the RP structures, which does not occur on the Ti-rich side, where more defects can therefore be expected.

4.1.4 Summary

The effect of nonstoichiometry (Sr/Ti ratio from 0.995 to 1.02) on the grain growth and bulk and grain boundary contributions to the dielectric response of STO ceramics was investigated and discussed in this chapter.

The effect of the Sr/Ti ratio on the grain boundary mobility was assessed by extracting growth factors from grain growth data at 1450 ˚C. The enlargement of the grain size distribution and the increase of the attained grain size with the decrease of the Sr/Ti ratio were observed. It was also found that the grain boundary mobility increases with increasing Ti content.

Impedance spectroscopy is a very sensitive and powerful technique for the study of the effect of small stoichiometric variations. By identifying bulk and grain boundary contributions to the dielectric response, IS revealed that the resistivity of bulk and grain boundaries is systematically decreased in nonstoichiometric STO as compared to stoichiometric material. The effect is much stronger for the grain boundaries as compared to the bulk. Very small variations in the stoichiometry may induce a high defect concentration, e.g. oxygen vacancies, that may segregate to the grain boundaries leading to a stronger reduction of the grain boundary resistivity as for the bulk.

Moreover, systematic dependences on the nonstoichiometry were also observed for the temperature dependence of the conductivity (much more affected in the case of the grain boundary contribution), bulk and grain boundary capacitance and grain boundary thickness. In addition to the effects on grain interiors, these observations are consistent with the predominance of different grain boundary types dependent on the nonstoichiometry, which lead to different microstructure evolution and diverse dielectric response.

This work highlights the importance of considering the effect of commonly observed defects and nonstoichiometry in oxide materials on the dielectric properties. Furthermore, it demonstrates that nonstoichiometry may be used as a tool for microstructure tailoring and grain boundary engineering enabling the design of the dielectric properties of ceramics.

4.2 Grain growth anomaly and related effects on the dielectric properties in Ti-rich strontium titanate ceramics

4.2.1 Introduction

As previously reviewed, a grain growth anomaly in STO was recently reported [76] and related with changes in the faceting behaviour of the grain boundaries at high temperatures [76; 251]. However, the overall scenario behind the grain growth anomaly is not yet known. Additionally, the correlation with grain boundary complexions [35; 247] is unclear and needs further development, namely in the Ti-rich side of the SrO - TiO_2 phase diagram [221] (Figure 2.3-4), where a liquid phase is expected to form above the eutectic temperature of 1440 ˚C. The presence of such a phase and its distribution during sintering are key factors determining grain boundary properties and, consequently, the overall microstructure evolution [22; 23]. Moreover, no relation between the grain growth anomaly in STO and the dielectric properties of the material was yet established.

Therefore, this chapter presents a systematic grain growth study performed over a wide range of temperature using a 0.5 mol% Ti-rich STO composition (ST 0.995). The effect of the amorphous phase in triple points and grain boundaries was investigated. Furthermore, the grain boundary properties evolution with the sintering temperature was assessed by IS. This technique allows to address separately the grain boundary impedance response [288] and therefore to detect changes in the grain boundary dielectric properties. In this way, changes in the grain growth behaviour may be correlated to changes in the grain boundary characteristics that may also be detected from alterations in their dielectric response.

Three discontinuities on the Arrhenius-type temperature dependence of grain growth were observed with drops in grain size at temperatures around 1500, 1550 and 1605 ˚C. These observations were related with the decrease of the liquid phase located at the grain boundaries as the sintering temperature increases. Similar discontinuities are

also observed for the first time by IS in the dependence of the grain boundary activation energy for conductivity and in the grain boundary thickness.

A retrograde solubility phenomenon, reported for metals and semiconductors but not reported before for ceramics, is suggested as a possible reason for the decrease of the grain boundary mobility and related changes on the dielectric properties.

4.2.2 Experimental details

The experimental procedures were generally described in Chapter 3. The samples of the Ti-rich ST 0.995 composition were heated up at 15 ˚C/min to the sintering temperatures, between 1400 and 1650 ˚C, and sintered in air for 2 h, and then cooled at the same rate of 15 ˚C/min. All the samples reached a relative density > 98%, as measured by the Archimedes method. The average grain size, *G*, was determined from the average equivalent diameter, by using a multiplying factor of 1.22 [337]. The error bars were derived from the standard deviation of the values measured in the different images.

The volumetric percentage of liquid phase at each temperature was quantified with ImageJ software using binarized SEM backscattered electron images of polished samples without etching, as previously mentioned. At least five images were used, covering around 50000 μm^2 for every sample. The error bars correspond to the standard deviation of the values measured in the different images. Large error bars may be originated by the difficulty in distinguishing some of the dark regions filled with liquid phase from the residual porosity, which are also darker in the backscattered electron images, although particular attention was taken to it. In fact, a careful comparison between the backscattered and secondary electron images of the same areas was done to identify and eliminate residual porosity. Additionally, and based on the fact that the remaining porosity is mainly intragranular and has a nearly circular shape, whereas the liquid phase is generally observed within pointy areas with edged faces, only dark regions with circularity lower than 0.8 where considered for the liquid phase quantification.

4.2.3 Results and discussion

4.2.3.1 Microstructural characterization

Figure 4.2-1 presents the SEM microstructures of the ST 0.995 samples sintered at temperatures increasing from 1400 ˚C in Figure 4.2-1 (a) to 1650 ˚C in Figure 4.2-1 (h). Similarly to the reported grain growth anomaly [76], it can be seen that grain size does not increase continuously with the increase of the sintering temperature, as would be expected since grain growth transport is a thermally activated process.

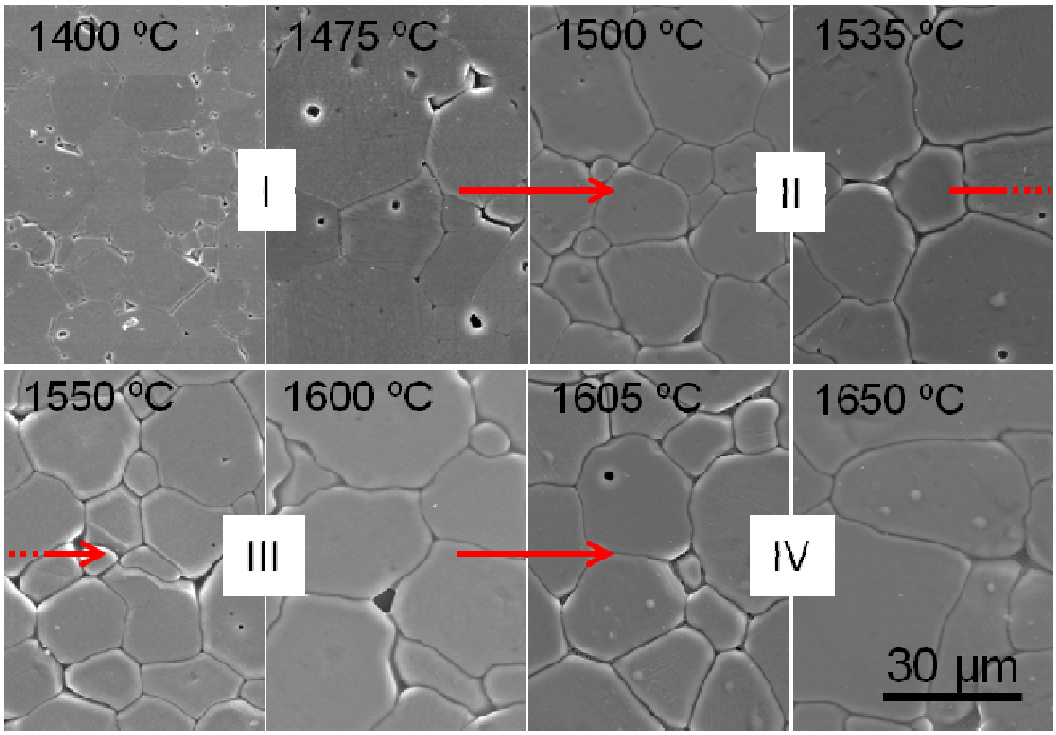

Figure 4.2-1: SEM microstructures of samples sintered at several temperatures (indicated on the images). In spite of the continuous increase of the sintering temperature, the decrease of the grain size is obvious. Arrows signalize the regimen transitions with decreasing of the grain size.

In fact, and differently from the previous report [76], four grain growth regimens can be defined with transitions at temperatures around 1500, 1550 and 1605 ˚C where the grain size decreases. Similar conclusions can be drawn from the dependence of the

average grain size on the temperature depicted in Figure 4.2-2 and from the grains equivalent diameter distribution in Figure 4.2-3. The presented distributions correspond to the temperatures at the beginning and end of the grain growth regimens in Figure 4.2-1. It is indeed clear that there is an increasing of the average grain size and an enlargement of the grain size distribution in every regimen. This is followed by a narrower grain size distribution, with a higher number of small grains, corresponding to a drop in the average grain size and to the beginning of a new regimen.

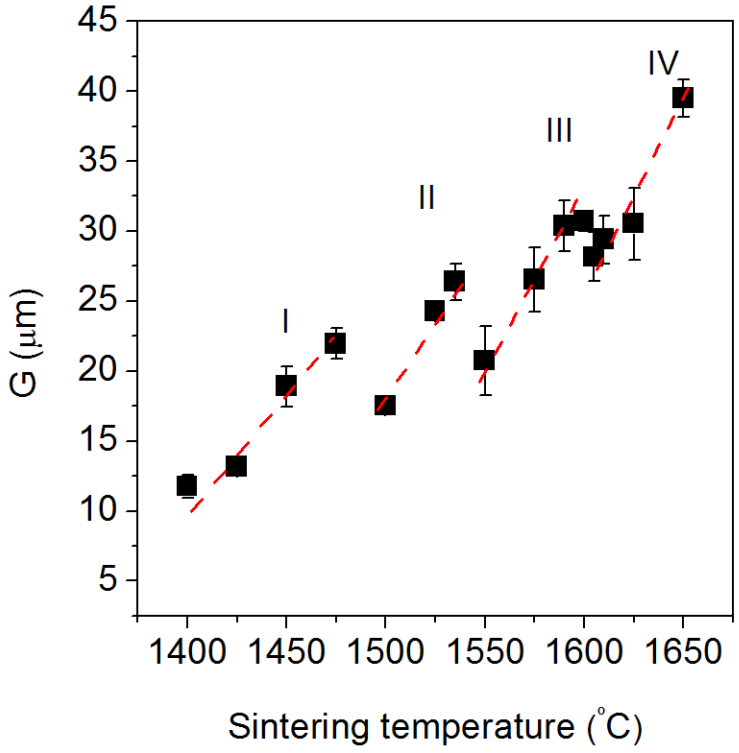

Figure 4.2-2: Average grain size as a function of the sintering temperature defining four grain growth regimens (regimen I, from 1400 to 1500 ˚C, regimen II, from 1500 to 1550 ˚C, regimen III from 1550 to 1605 ˚C and regimen IV from 1605 to 1650 ˚C). Lines are only to guide the eyes.

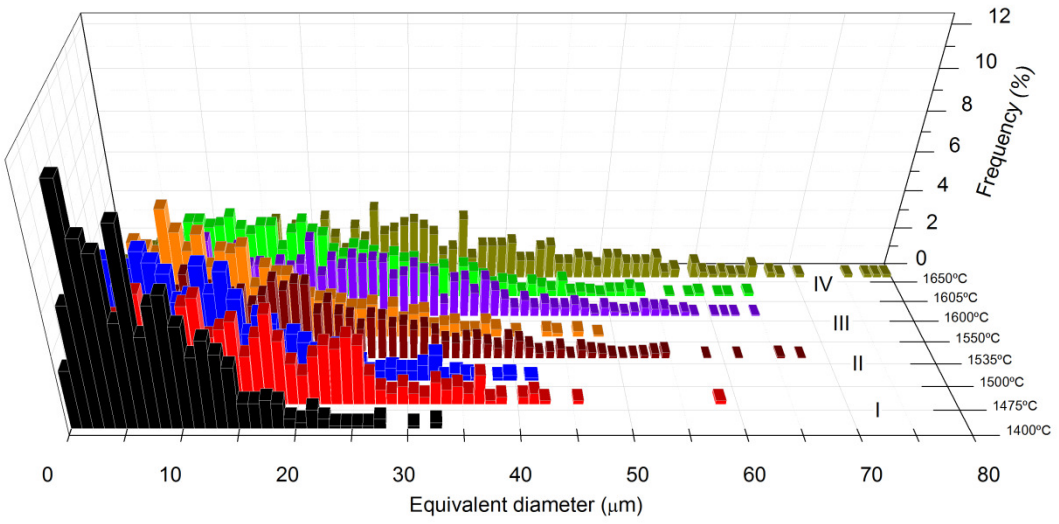

Figure 4.2-3: Distribution of the grain equivalent diameter for sintering temperatures corresponding to the beginning and end of the grain growth regimens indicated as I, II, III and IV.

A careful analysis by SEM of the sintered samples revealed the presence of an amorphous phase. Furthermore, in some triple points, some crystalline material could be observed inside the amorphous phase, as well, probably originated during cooling. Figure 4.2-4 (a) presents a SEM micrograph of a ST 0.995 sample sintered at 1450 ˚C showing in detail a triple pocket with liquid phase and some crystalline material inside. Figure 4.2-4 (b) and (c) show EDS line profiles across the triple point.

It is shown that the amorphous phase is Ti-rich whereas the crystalline material inside is Sr-rich, despite the Ti-excess of the composition under study. Additionally, the Sr-rich crystalline material in the triple pocket may contain Zr-rich impurities, as observed in one of our previous works [259]. These impurities may come from the milling media and are mainly located in those small crystals. Their concentration should be less than 270 *ppm* as previously measured by Inductively Coupled Plasma Spectroscopy (ICPS) [259].

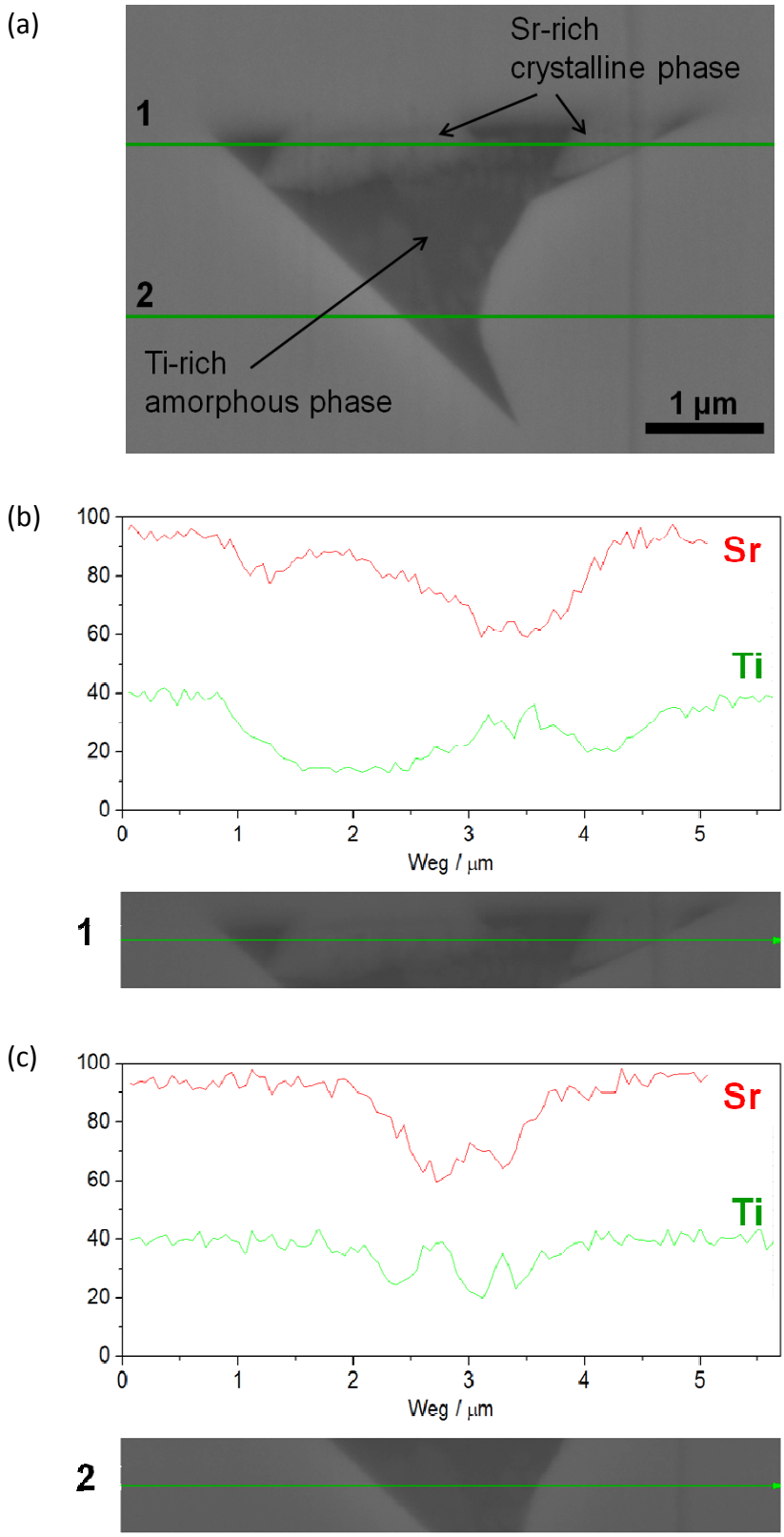

Figure 4.2-4: (a) SEM micrograph of a sample sintered at 1450 ˚C showing a triple point. (b) and (c) EDS line profile along lines 1 and 2 in (a), respectively. A Ti-enriched amorphous phase and Sr-rich crystalline material are seen inside the triple pocket.

From the TEM analysis of selected samples no Ti precipitates could be detected for the samples sintered at 1450 and 1500 ˚C (Figure 4.2-5). However, in the triple points the presence of a liquid phase is evident, confirming the SEM observations. No diffraction contrast emerged as the sample was tilted in the TEM, pointing to the amorphous nature of this phase. Indeed, Ti-rich STO compositions have a eutectic point at 1440 ˚C [221] (Figure 2.3-4), so traces of liquid phase can be expected in these samples.

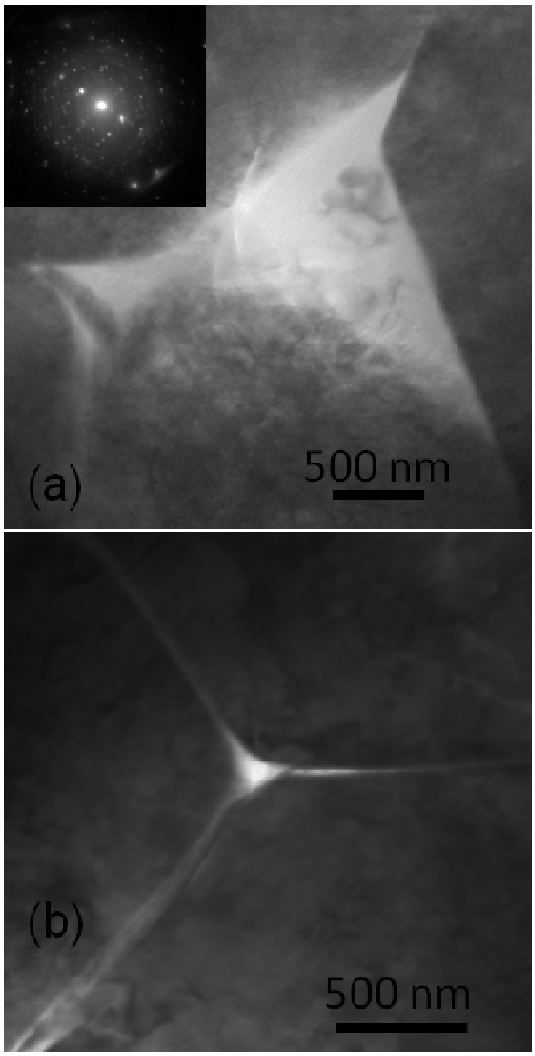

Figure 4.2-5: TEM micrographs of ST 0.995 samples sintered at (a) 1450 and (b) 1500 ˚C. The inset is the electron diffraction pattern from the triple pocket. An amorphous phase was identified in the triple junction and along the grain boundaries.

The presence of the amorphous phase and of crystalline material in the triple pocket is illustrated in the diffraction pattern of the triple point, in the inset of Figure 4.2-5 (a). The diffraction halo is originated by the glassy phase, whereas the small spots are from small crystals inside. Additionally, in Figure 4.2-5 (b) traces of liquid phase can be clearly seen along the boundaries, as lighter regions in the picture.

Due to the observed differences in the composition of the amorphous phase compared to the bulk grains presented in Figure 4.2-4, it is possible to identify the regions where such phase is located using SEM backscattered electrons images. These images are presented in Figure 4.2-6 for sintering temperatures related to the beginning and end of the grain growth regimens. This is possible because larger atoms (with a higher atomic number) have a higher probability of producing elastic collisions between the electrons of the accelerated electron beam and the atoms within the sample because of their greater cross-sectional area. Consequently, the number of backscattered electrons reaching a BSE detector is proportional to the mean atomic number of the sample [298]. Thus, a "brighter" BSE intensity correlates with greater average atomic number in the sample and "dark" areas have lower average atomic number.

The samples in Figure 4.2-6 were polished but not etched. The darker round areas correspond to porosity and the Ti-rich liquid phase is seen in intermediate dark pointy areas, in accordance with the lower atomic number of Ti (22) as compared to Sr (38). The quantification of the fraction of liquid phase present in the samples sintered at the several temperatures is presented in Figure 4.2-7 (b).

Figure 4.2-7 (a) presents the analysis of the grain growth kinetics using the phenomenological kinetic grain growth equation [32; 355; 356]:

$$G^m - G_0^m = K_0 t \exp(-\frac{Q_g}{R_{gc}T}) \qquad (4.2\text{-}1)$$

where G stands for the average grain size at the time t, G_0 for the initial grain size, m for the kinetic grain growth exponent, K_0 for a pre-exponential constant, Q_g for the apparent activation energy for the grain growth process, R_{gc} for the gas constant and T for the absolute temperature.

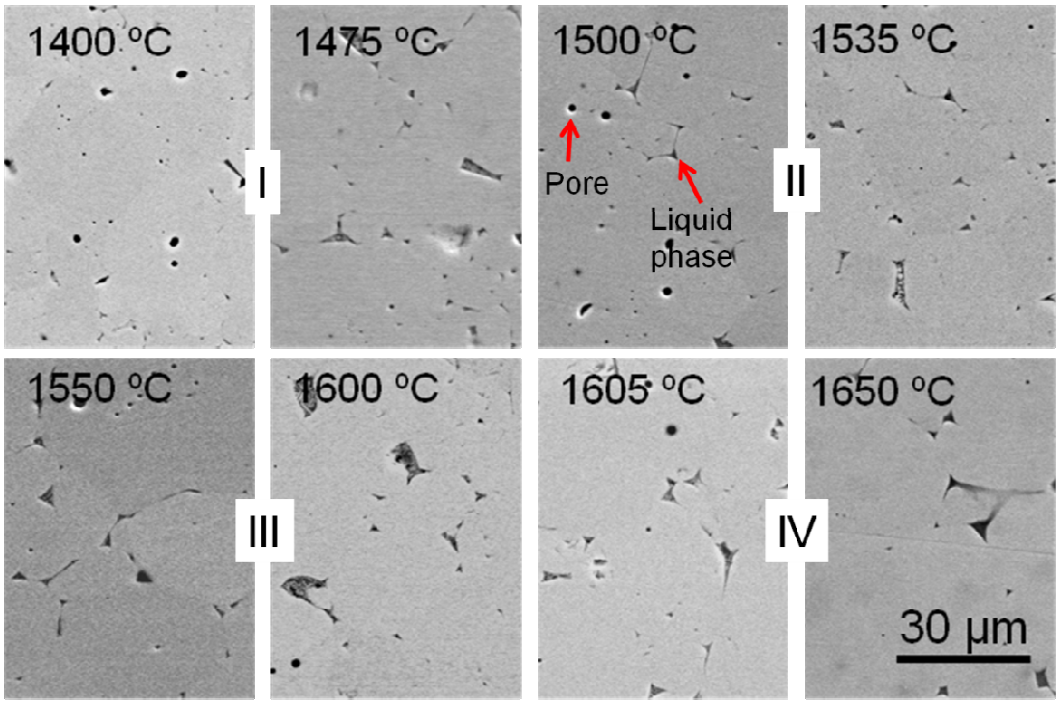

Figure 4.2-6: SEM backscattered electron images of polished samples (without etching) sintered at several temperatures showing the presence of liquid phase. The sintering temperatures correspond to the beginning and end of the grain growth regimens.

Neglecting G_0 that is usually very small compared to G and assuming m = 2, which has been shown to fit well the grain growth kinetics [35; 247] and that the activation energy is constant in certain temperature intervals, equation (4.2-1) can be expressed in the form:

$$\ln(\frac{G^2}{t}) = \ln(K_0) - (\frac{Q_g}{R_{gc}T}) \qquad (4.2\text{-}2)$$

The four grain growth regimens identified in Figure 4.2-1 are again clearly visible in Figure 4.2-7 (a): regimen I, from 1400 to 1500 ˚C, regimen II, from 1500 to 1550 ˚C, regimen III from 1550 to 1605 ˚C and regimen IV above that temperature. For all of them, the average grain size increases with the sintering temperature. However, at temperatures around 1500, 1550 and 1605 ˚C, transitions occur and the average grain size sharply decreases. From Figure 4.2-7 (a), the apparent activation energy for the grain growth process, Q_g, may be estimated. The values for all regimens do not present

significant variation, between 4.5 and 6.6 eV, suggesting that the same mechanism of transport is dominant in the four grain growth regimens.

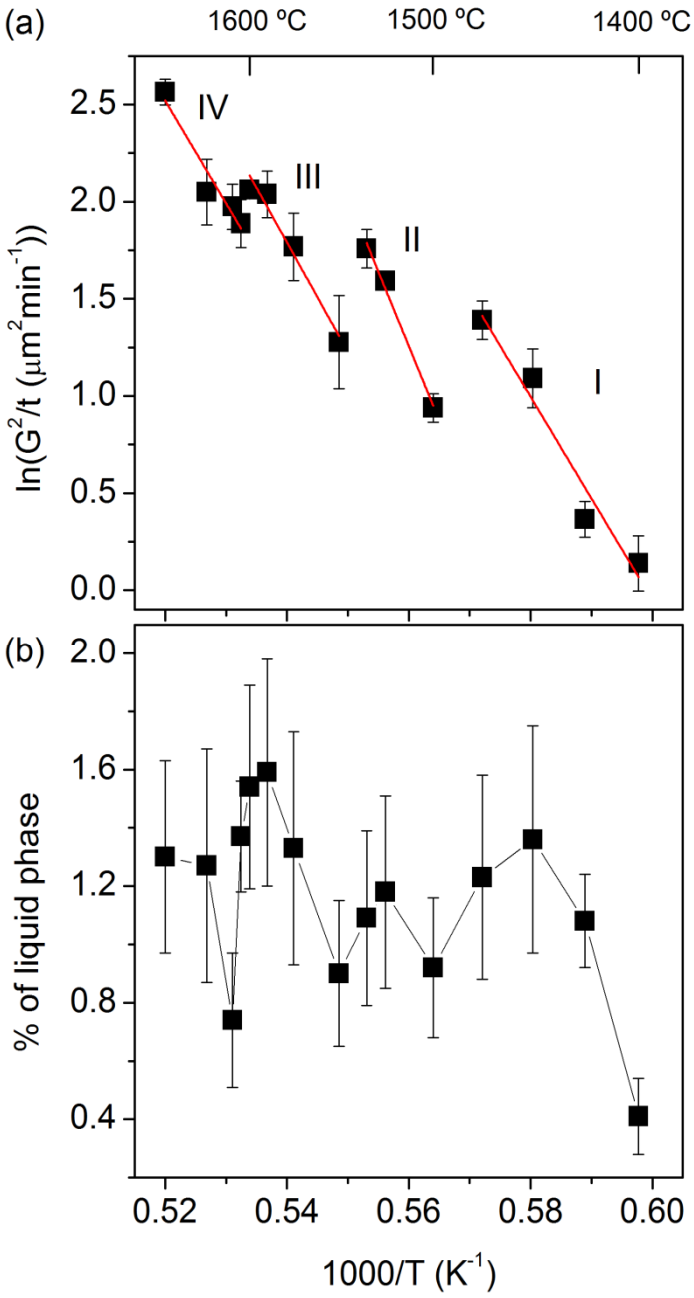

Figure 4.2-7: (a) Arrhenius-type dependence of the average grain size on the sintering temperature defining four grain growth regimens. (b) Volumetric percentage of liquid phase as a function of the sintering temperature. The discontinuous variation of the amount of liquid phase suggests a relation with the observed four grain growth regimens.

The volumetric percentage of liquid phase is shown in Figure 4.2-7 (b). The amount of liquid phase is low at all temperatures, below 2%. However, and in good agreement with the variation of the grain growth regimens (Figure 4.2-7 (a)), its evolution with the increase of the temperature is not monotonous, presenting several maxima in the studied temperature range. At 1400 ˚C, below the eutectic temperature, a small amount of liquid phase is already detected. A possible explanation might be related with the possible presence of impurities, such as Zr, in some triple points. At 1425 ˚C, approaching the eutectic temperature, a strong increase in the percentage of the liquid phase can be seen.

At the beginning of each regimen, the increase of temperature brings an increase of the liquid phase content and, as would be expected, an enhancement of the mass transport is observed, leading to an increase of the grain size. However, when approaching regimen transition temperatures, the amount of liquid phase decreases before the decrease of the grain size. This behaviour may be rationalized considering the interplay of the effects of temperature and liquid phase on the mass transport.

Comparing the present results to those previously reported on the grain growth anomaly in STO [76], some points should be considered. Bäurer *et al.* reported two mobility drops, one between 1300 and 1350 ˚C and other between 1390 and 1425 ˚C. In the present work, the investigated temperature range was 1400 – 1650 ˚C and three drops in the average grain size were observed, at temperatures around 1500, 1550 and 1605 ˚C. The previous investigation [76] was conducted in oxygen atmosphere and the present one in air, which may lead to different microstructural evolution. Furthermore, the investigated compositions are different: 0.4 mol% Ti-excess and 0.2 and 0.5 mol% Sr-excess were used in the previous case, whereas a slightly higher Ti-excess of 0.5 mol% was used on the present work. No formation of liquid phase was reported by Bäurer *et al.* whereas the presence of such phase during sintering seems to play a major role on the present observations.

The solubility limits of SrO and TiO_2 in STO are quite low and have been discussed for more than forty years [16; 225; 257; 258]. According to Witek *et al* [16], the solubility limit of TiO_2 is smaller than 0.1 mol% at 1000 ˚C and the amount held in solution is higher for

faster cooling rates. However, in agreement with the results presented in the previous chapter, there is no second phase detectable by XRD in STO with Sr/Ti of 0.997 [259; 277]. For a slightly higher excess, Sr/Ti=0.995, the composition used in this work, a second-phase detectable by SEM was reported [16]. Bäurer *et al* [263], for Sr/Ti=0.996, observed rutile TiO_2 excess by XRD after sintering at 1400 ˚C, but the detected diffraction pattern peak became less pronounced after quenching the sample from high temperature. Additionally, after sintering at 1500 ˚C, no such phase was evident [247; 263]. These observations indicate that the solubility of excess TiO_2 is higher at high temperatures [263] and is in agreement with a solubility of more than 2 mol% TiO_2 at elevated temperatures reported by Eror and Balachandran [258]. These experimental observations may be consistent with a retrograde solid solubility scenario, as discussed in the following text.

In a general way, there is a maximum solubility at the eutectic temperature and the solubility of specific impurities decreases as the temperature increases [357]. However, as an example, some metal impurities are more soluble in silicon above the eutectic temperature [358]. This behaviour is known as retrograde solubility [359; 360] and has been attributed to a miscibility gap in the free energy of mixing for a large positive enthalpy of mixing, at temperatures higher than the eutectic temperature [359]. Retrograde solid solubility is found in binary systems in which the solid solubility is very small and eutectic temperature is considerably below the melting point of the solvent [361], which fits the present case. This phenomenon has been proved to exist in several binary systems, such as Si-Al [362], Zn-Sb [363] or Cu-Bi [364]. It was also found in the solubility of Zn in GaAs [365] or Fe impurities in Ti [366]. However, to the best of the author's knowledge, up to now this phenomenon was not reported in STO or other oxide systems.

Moreover, thermodynamic modelling and experiments revealed a decrease in the grain boundary diffusivity with increasing temperature as a result of the interplay between the retrograde solubility and formation of a liquidlike grain boundary core [367]. For the case of 0.5 at.% Ni-doped Mo alloy it was shown that the grain boundaries ''solidify'' with increasing temperature, leading to a reduction of grain boundary diffusivity and the authors attributed this phenomenon to the interplay of grain boundary premelting, prewetting and retrograde solubility [367].

Indeed, a similar scenario of interaction of thermal activation, retrograde solubility and impurity stabilized wetting films at the grain boundaries correlated with different complexions and complexion transitions would explain the unusual variation of the amount of liquid phase with the temperature shown in Figure 4.2-7 (b) and the consequent grain growth anomaly observed in STO. The retrograde solubility of the Ti-excess in the lattice would lead to the unusual variation of the amount of liquid phase with the sintering temperature. Consequently, the grain boundary wetting by the liquid phase would also be affected, which could lead to the formation of different grain boundary complexions with different mobilities.

However, the possible presence of impurities may lead to alterations in the phase equilibrium predicted by the phase diagram of the SrO-TiO_2 system. Additionally, as previously discussed, compositions not stable as bulk phases are possible in grain boundaries of STO [247], which are not predicted by the phase diagram. Thermodynamic modelling and a deeper TEM observation of the grain boundaries of samples sintered at several selected temperatures are therefore needed, in order to better characterize and understand the hypothesis of retrograde solubility and the observed relations.

Due to the sensitivity of the electrical properties to the microstructure details of polycrystalline materials, effects on the dielectric properties may also be expected in the present case. A relation between the amount of the liquid phase at the grain boundaries and their electrical response is predictable. The understanding of this relation may even offer a way of tailoring the dielectric response of the material. Accordingly, the resistivity of grains and grain boundaries in Ti-rich STO ceramics was assessed by impedance spectroscopy and new data for the anomaly of the grain growth observed in STO are brought into the discussion.

4.2.3.2 Impedance Spectroscopy

As previously presented, IS provides the ability of analyzing separately bulk and grain boundary contributions to the dielectric response. This ability may be very useful for

the purpose of detecting changes in the grain boundary dielectric response and correlating them with different grain boundary characteristics, as in the present case.

A similar procedure to that explained in the previous chapter was used in this analysis. Complex impedance spectra were collected between room temperature and 700 ˚C (from 100 Hz to 1 MHz) for all the samples under investigation, sintered between 1400 and 1650 ˚C. The equivalent circuit previously considered and shown in Figure 4.1-14 was used to fit the present data and the semicircles were assigned to bulk and grain boundaries according to the previously explained criteria [288].

Complex specific impedance spectra of the several samples sintered between 1400 and 1650 ˚C, collected at 300 and 600 ˚C, are presented in Figure 4.2-8 (a) and (b), respectively. Well resolved semicircles are observed at both temperatures. The assignment of the semicircles to bulk and grain boundary contributions is supported by the magnitude of the capacitance values [288]. As previously observed, at 300 ˚C (Figure 4.2-8 (a)) the spectra are again dominated by the bulk response whereas the grain boundary contribution is dominating at 600 ˚C (Figure 4.2-8 (b)). The capacitance of bulk and grain boundaries is nearly independent of the measurement temperature, in agreement with the previously described observations. The average of the capacitance values from 200 to 500 ˚C for the bulk and from 500 to 700 ˚C for the grain boundary contribution is presented in Figure 4.2-9 for the several sintering temperatures. The error bars represent the standard deviation of the obtained values. It can be seen that the bulk capacitance is approximately $2x10^{-11}$ F/cm, almost independently of the sintering temperature, whereas the grain boundaries show capacitance values of around $4x10^{-8}$ F/cm. As previously discussed, the magnitude of these values is in the expected range for bulk and grain boundary contributions [288]. In the case of grain boundary capacitance, a slight tendency to increase with increasing sintering temperature may be observed.

One important remark regarding the impedance spectra in Figure 4.2-8 is that the sintering temperature has a strong effect on the resistivity of both bulk and grain boundaries. Regarding both contributions, the variation of the size of the semicircles (and consequently of the resistivity) is not systematic with the sintering temperature.

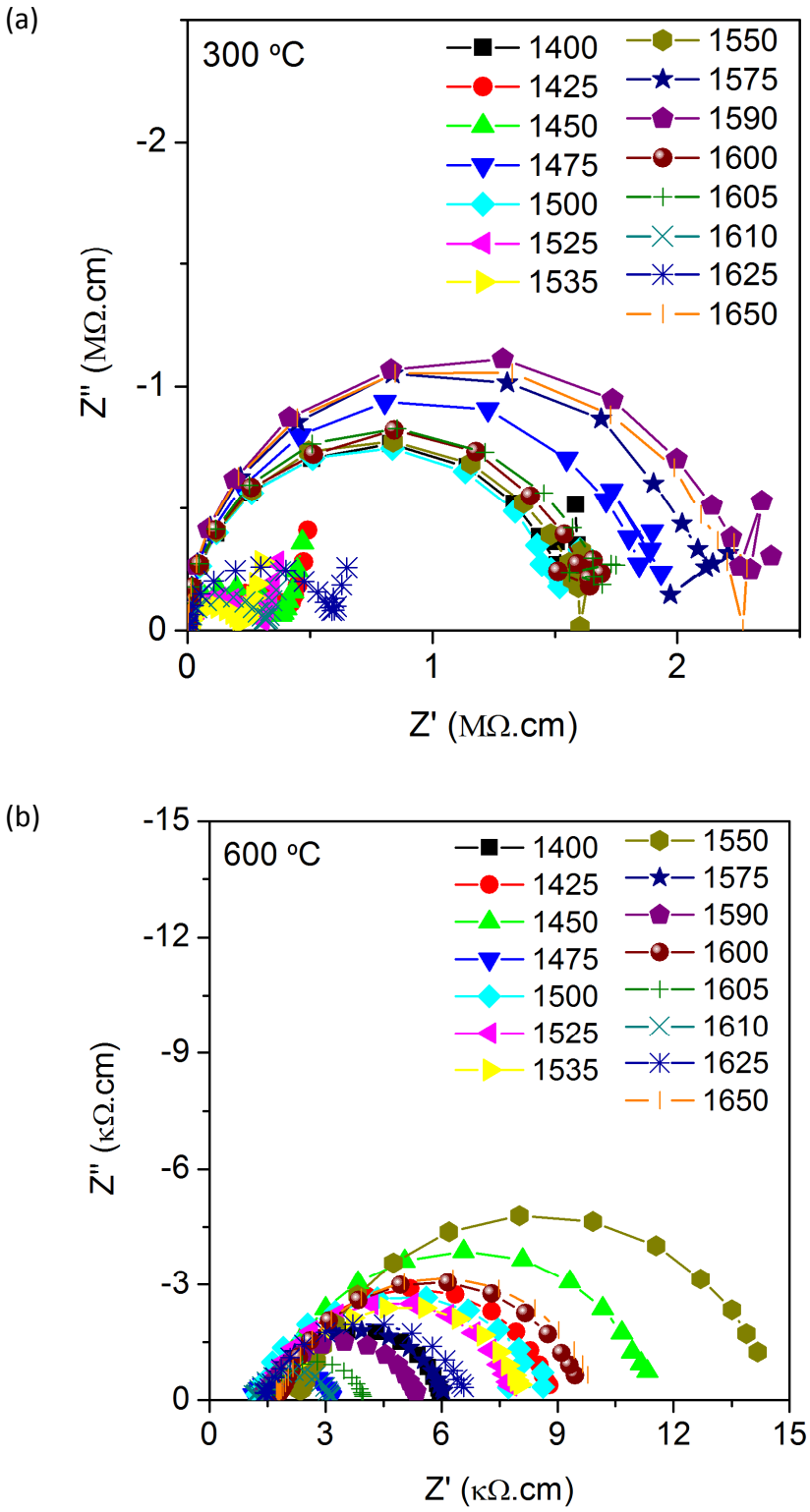

Figure 4.2-8: Complex specific impedance spectra at (a) 300 ˚C and (b) 600 ˚C regarding samples sintered between 1400 and 1650 ˚C. A strong effect of the sintering temperature on the impedance response of bulk and grain boundaries is evident.

The spectra at 300 ˚C in Figure 4.2-8 (a), concerning the bulk contribution, may be roughly divided in three groups. In the first group, samples sintered at 1425, 1450, 1525, 1535, 1610 or 1625 ˚C show bulk resistivity lower than 0.4 MΩ.cm (with the exception of the sample sintered at 1625 ˚C with a slightly higher resistivity). On the other hand, the second group that consists in samples sintered at 1400, 1500, 1550, 1600 and 1605 ˚C exhibit a bulk resistivity around 1.6 MΩ.cm. After that, samples sintered at 1475, 1575, 1590 and 1650 ˚C show a bulk resistivity close to or higher than 2 MΩ.cm.

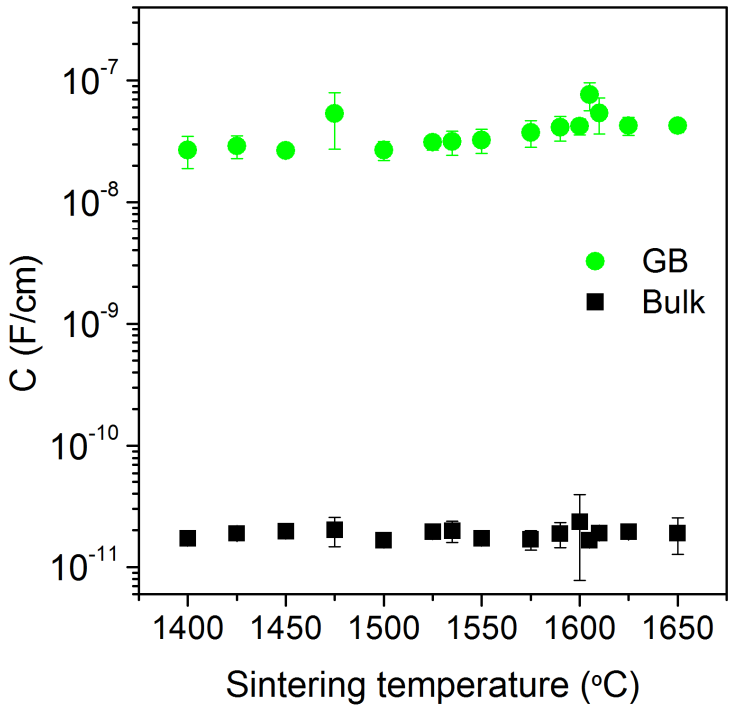

Figure 4.2-9: Average capacitance of bulk and grain boundaries as a function of the sintering temperature. Both contributions are nearly independent of the sintering temperature.

It is interesting to notice that these samples which showed higher bulk resistivity are located near the end of the respective grain growth regimens and that the fraction of liquid phase obtained for these samples is among the highest values (Figure 4.2-7).

Another interesting observation is that, with the exception of the sample sintered at 1600 ˚C, the samples showing intermediate bulk resistivity correspond to the beginning of the grain growth regimens and to low fractions of liquid phase. The samples with the lowest bulk resistivity are located in the middle of the grain growth regimens. An exception is the sample sintered at 1535 ˚C, which corresponds to the end of regimen II.

All samples showed relative densities above 98% and therefore differences in densification cannot explain the changes in the bulk resistivity. The observations of a nonsystematic variation of the bulk resistivity with the sintering temperature and its relation with the grain growth regimens clearly suggest once more a relation with the incorporation of the Ti-excess and its dependence of the sintering temperature. Indeed different levels of solubility of the Ti-excess in the bulk affect the bulk defect concentration and consequently, the bulk resistivity. Therefore, the nonsystematic variation of the bulk resistivity may also be related to the proposed retrograde solubility scenario suggested for the grain growth behaviour and the presence of liquid phase.

Concerning the grain boundaries impedance response at 600 ˚C, in Figure 4.2-8 (b), the dependence on the sintering temperature is also not systematic. One important observation is that the magnitude of the variation of the grain boundary resistivity is much higher than that of the bulk contribution. In fact, the grain boundary resistivity changes dramatically from around 2 kΩ.cm for the samples sintered at 1475 and 1610 ˚C to approximately 12 kΩ.cm for samples sintered at 1550 ˚C.

The Arrhenius dependence of the bulk and grain boundary conductivity on the temperature according to equation (4.1-4) is shown in Figure 4.2-10 for the samples sintered at the several temperatures. Regarding the bulk conductivity (Figure 4.2-10 (a)), all lines are parallel, revealing similar dependence on the measurement temperature. On the other hand, the slopes of the lines concerning the dependence of the grain boundary conductivity on the measurement temperature (Figure 4.2-10 (b)) show a stronger variation with the sintering temperature.

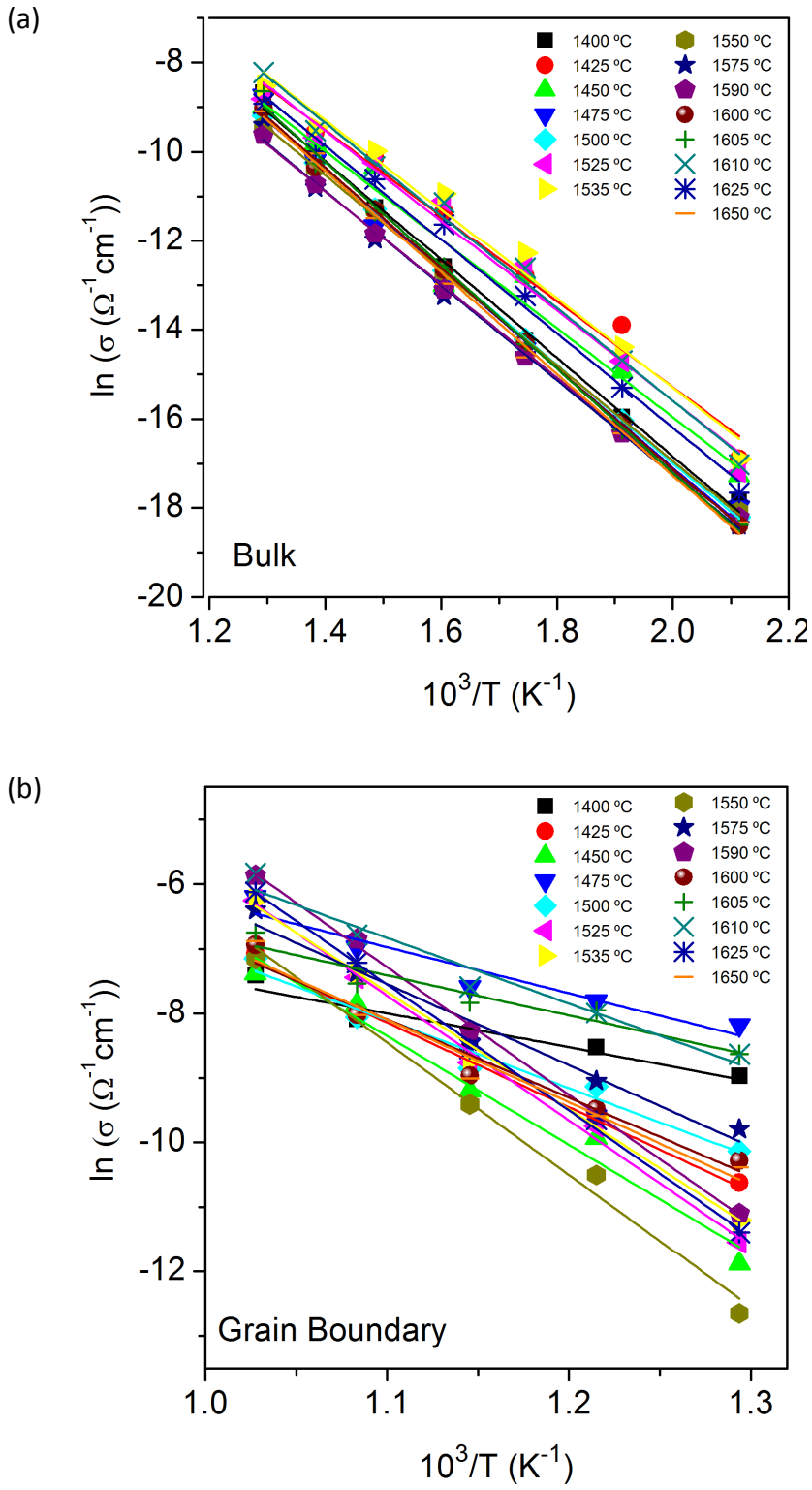

Figure 4.2-10: Arrhenius-type measurement temperature dependence of (a) bulk and (b) grain boundary conductivity. Grain boundaries are much more affected by the sintering temperature than the bulk counterpart.

The dispersion of the grain boundary conductivity values at 500 ˚C is much larger than that of the higher measurement temperature of 700 ˚C. This indicates that the differences in the grain boundary characteristics have a lower effect on the grain boundary conductivity at higher temperatures, where the mobility of the species involved in the conduction process is higher.

These observations are clearly illustrated in Figure 4.2-11 presenting the activation energy for conductivity of bulk and grain boundaries for the several sintering temperatures, obtained from the respective conductivity temperature dependences.

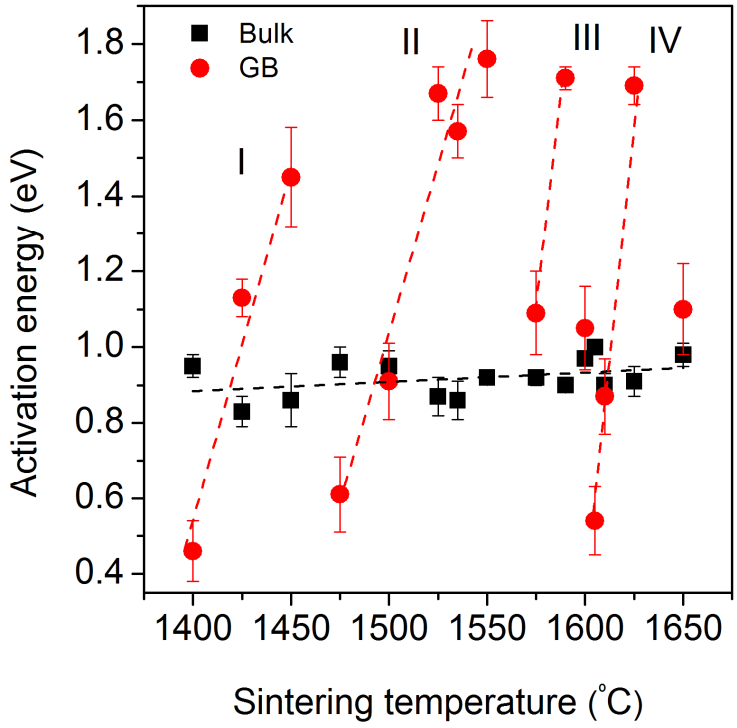

Figure 4.2-11: Activation energy for bulk and grain boundary conductivity as a function of the sintering temperature. A discontinuous variation defining four regimens is also observed for the grain boundary contribution.

Similarly to the observations for the effect of nonstoichiometry on bulk and grain boundaries, the activation energy regarding the bulk contribution is almost independent of the sintering temperature, with values around 0.9 eV, in agreement

with previous reports [332; 341]. Only a small tendency to increase with increasing sintering temperature is detectable. On the other hand, the activation energy for grain boundary conductivity denotes a very strong variation with the sintering temperature, with values oscillating from 0.46 to 1.76 eV. The calculated values of activation energy for the grain boundaries are also in good agreement with the values found for the effect of the nonstoichiometry on STO, as discussed in the previous chapter. On the other hand, typical reported values of activation energy for the grain boundary contribution are within the range of 1.4 - 1.6 eV [341]. For some of the sintering temperatures, much lower values were observed, suggesting in those cases a lower temperature sensitivity of the grain boundary conductivity.

It is again important to consider that microstructural non-ideality, such as a non-uniform grain size distribution, may originate deviations from the ideality of the brick layer model and therefore may affect the determination of the activation energy of grain boundary conductivity from the impedance spectra [332; 348]. Nonetheless, the results clearly show that grain boundaries are much more affected than the bulk by changing the sintering temperature. Also grain size may play a role, once that higher grain boundary resistivity is expected for smaller grain size (or higher grain boundary surface area) [341; 368]. However, the differences in grain size are constant along the whole measurement temperature; therefore, they alone may not explain the different dependences of the grain boundary conductivity on the temperature illustrated by the activation energy values in Figure 4.2-11. Moreover, the strong variation in the activation energy for grain boundary conductivity is not continuous with the increasing sintering temperature. In fact, four regimens, as observed for grain growth and liquid phase, can be defined.

Glassy films wetting the grain boundaries are known to constitute a blocking layer for oxygen ion conduction [368]. For example, Si-rich second phases spreading from the triple points were found to markedly enhance the grain boundary electrical barrier effect on zirconia samples [369; 370]. Additionally, Badwal [368] attributed the inflections or peaks in the grain boundary resistivity of ZrO_2-based electrolytes versus sintering temperature plots to the dynamic nature of the grain boundary phase (composition,

location and wetting properties) and the amount and type of impurities in the starting powders.

In the present case, the amount and type of impurities is obviously the same in all samples because they were prepared from the same powder batch and sintered under the same conditions. Therefore, the strong effect of the sintering temperature observed on the grain boundary conductivity may indeed be related to the discontinuous variation of the liquid phase with the sintering temperature, observed by SEM, and in particular to the location and wetting properties of such phase and the consequent effects on the formation and thickness of intergranular amorphous films.

The coincidence of grain growth behaviour, liquid phase fraction and grain boundary dielectric response strongly suggests the predominance of different grain boundary properties (which could be associated with different complexions) with transitions in between the several regimens. These complexions may have different mobility and dielectric properties and therefore influence the sintering behaviour and the dielectric response of the material. Indeed, the discontinuities in grain size and activation energy for grain boundary conductivity are strong indications of different grain boundary properties, which are observed by two completely different techniques.

Another strong indication of the presence of different grain boundary properties changing with the sintering temperature and the fraction of liquid phase is the grain boundary thickness variation with the sintering temperature, presented in Figure 4.2-12. These values were estimated as previously explained from the bulk and grain boundary capacitance values in Figure 4.2-9 and the average grain size in Figure 4.2-2 applying relation (4.1-5).

It can be seen that discontinuities are also present in the evolution of the grain boundary thickness with the sintering temperature. In fact, Figure 4.2-12 shows a striking similarity to the dependence of activation energy for grain boundary conductivity on the sintering temperature and to the grain growth regimens previously identified. Only the grain boundary thickness of the sample sintered at 1475 ˚C does not fit exactly the observed grain growth regimens: that sample is positioned in the grain growth regimen I whereas the grain boundary thickness is lower than that of the

sample sintered 1450 ˚C. On the other hand, a coincidence is verified in the relative position of that sample regarding the grain boundary thickness and the activation energy for grain boundary conductivity.

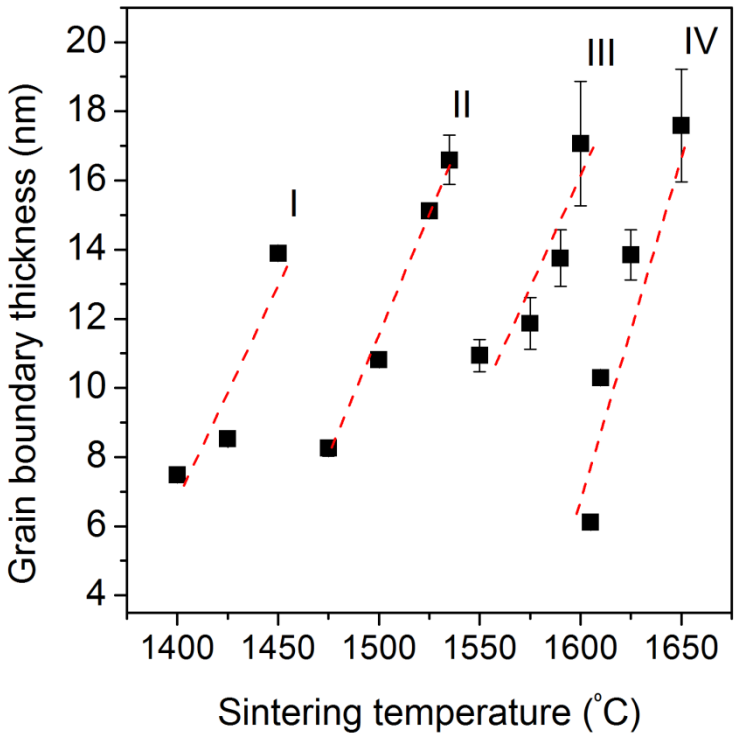

Figure 4.2-12: Grain boundary thickness dependence on the sintering temperature assessed by impedance spectroscopy. A discontinuous variation with four regimens is again observed.

The grain boundary thickness values in Figure 4.2-12 are in good agreement with previously reported values [245; 343; 352; 353] and with those found in the previous chapter, particularly for the sample with the same degree of nonstoichiometry (ST 0.995).

At this point, one important aspect must be highlighted. As illustrated in Figure 4.2-13, there is a remarkable coincidence in the behaviour of the several parameters investigated and described in this chapter. A scheme with the major trends of the variation with the sintering temperature observed for the average grain size, percentage of liquid phase, grain boundary activation energy for conductivity and grain

boundary thickness is drawn in the same figure to highlight the similarities in the respective dependences on the sintering temperature.

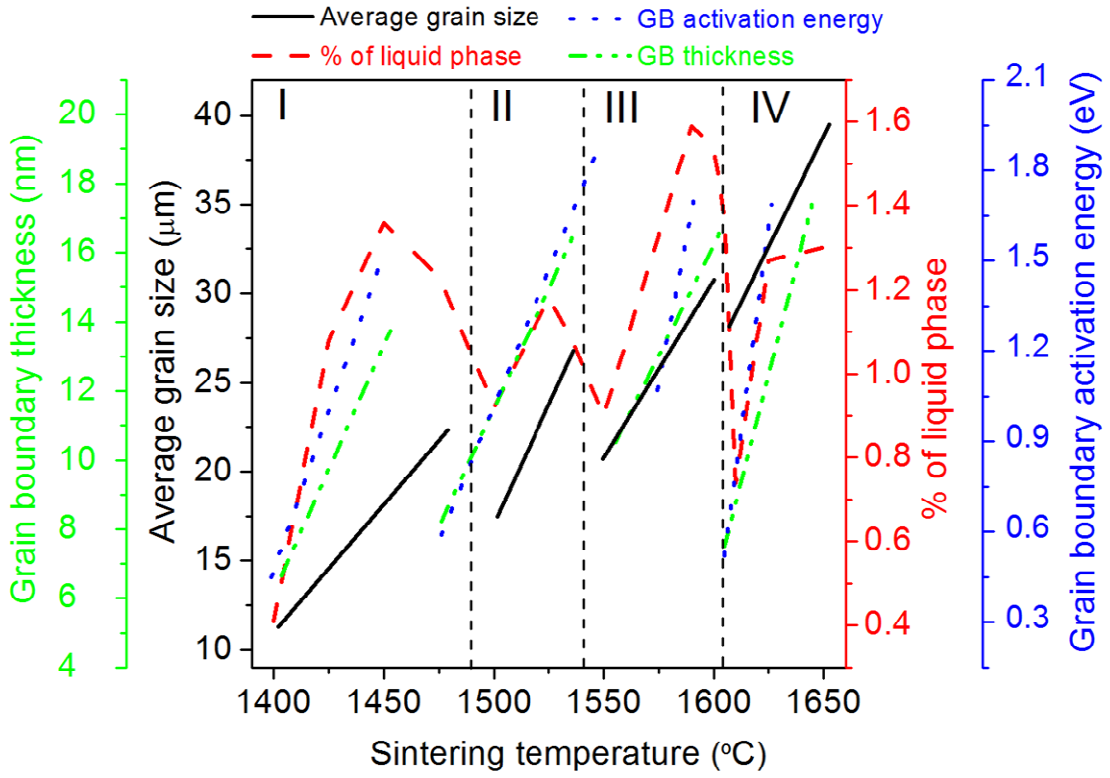

Figure 4.2-13: Illustration of the dependence of the average grain size, percentage of liquid phase, grain boundary activation energy for conductivity and grain boundary thickness on the sintering temperature. There is a clear relation between all these parameters, defining unambiguously four regimens.

In fact, all parameters seem to be related and to define four regimens separated by sudden variations. This suggests the occurrence of changes at the grain boundaries at determined temperatures, namely transitions between grain boundary complexions, leading to the discontinuous behaviour of the investigated parameters.

4.2.4 Summary

Discontinuities on the evolution of grain growth with the sintering temperature of a 0.5 mol% Ti-rich STO composition (ST 0.995) were observed, defining four grain growth regimens with transitions at temperatures around 1500, 1550 and 1605 ˚C. These transitions correspond to grain size decreases, despite the increasing sintering temperature. This anomalous behaviour is directly related to the presence of liquid phase, which amount varies discontinuously with the temperature, suggesting a scenario of retrograde solubility.

Effects on the dielectric properties were also verified by IS. The correlation between discontinuities in grain growth behaviour and grain boundary dielectric response was observed for the first time. Grain boundaries dielectric response was much more affected by the sintering temperature than that of the bulk counterpart. Furthermore, changes were detected in the activation energy for grain boundary conductivity and grain boundary thickness, which may be well correlated to the formation of an amorphous phase and to the grain growth regimens detected by SEM.

These new results have great scientific and technological relevance in tailoring the microstructure and dielectric response of STO based materials and using grain boundary complexion behaviour for materials design.

4.3 Electrophoretic deposition and constrained sintering of strontium titanate thick films

4.3.1 Introduction

For device miniaturization, in addition to the need for optimized properties, materials must be processed in ways that allow easy integration of small, lightweight and cost-effective components [79]. Hence, the ability to mass-produce dielectric functional films with repeatable performance at low costs is nowadays of major technological importance. As already discussed, this can be achieved using thick-film deposition technologies [9], such as EPD [83], followed by a constrained sintering step.

However, particularly regarding thick films of functional materials on metallic substrates, systematic studies of constrained sintering were rarely reported. Additionally, if properly understood, the constraint from the substrate may be intentionally used as a tool for microstructure and properties design [19].

In this chapter, the role of the suspension media and the EPD process parameters were systematically addressed and optimized. Thick films were successfully deposited by electrophoretic deposition on Pt-foil substrates using acetone with addition of iodine. A preliminary investigation of the constrained sintering on Pt-foil substrates of STO thick films with several Sr/Ti ratios was then performed. Increasing densification, grain size and enlargement of the grain size distribution was observed with the decreasing of the Sr/Ti ratio, as previously observed for bulk ceramic samples. Equiaxied grains were observed for all the compositions but some degree of anisotropy in the pore orientation was detected: pores showed a preferential vertical orientation.

4.3.2 Experimental details

Three compositions were used in this work: Ti-rich ST 0.997, stoichiometric ST and Sr-rich ST 1.02. The general experimental procedures previously described in Chapter 3

were followed for the preparation and characterization of powders, suspensions and sintered samples.

Several solvents for EPD suspensions were tested: de-ionized water, acetone, ethanol and ethylene glycol. Iodine (I_2) was used as additive. The EPD process parameters were systematically studied by performing depositions varying the concentration of the suspensions, the amount of additive, the deposition voltage and the deposition time. The EPD performance was evaluated by means of the deposit weight: the substrates were weighted before and after the deposition, being the difference the weight of the deposited material. Homogeneity and surface roughness were considered as indicators of the film quality after visual inspection.

The STO thick films were heated up to 1500 ˚C, at 5˚C/min, in air. The grain size measurements were performed through image analysis of SEM top view micrographs, considering more than 600 grains for every sample. A stereological factor of 1.22 [337] was used to obtain the average grain size from the equivalent diameter, considering circular areas.

4.3.3 Results and discussion

One of the most important parameters for a successful EPD deposition is the charge of the particles in suspension. Zeta potential, a measure of the particles surface charge [284], is a straightforward indication of the stability of suspensions. Figure 4.3-1 presents the variation of the zeta potential with the pH for the three compositions in water. The particles have a high surface charge for low and high pH values, with the isoelectric point being attained for pH values lower than 7, around 6 for the Ti-rich composition, and for values slightly lower than 4 for the stoichiometric and Sr-rich compositions. For high pH values, a decrease in the zeta potential of the ST 0.997 and ST compositions was recorded, indicating that the suspensions are more stable at low pH. In a general way, the dependence of the zeta potential on the pH is similar in the three cases, which indicates that an equivalent behaviour of the particles in suspension can be

expected for all the three compositions. Low pH values seem to be the most favourable conditions for EPD of these STO compositions.

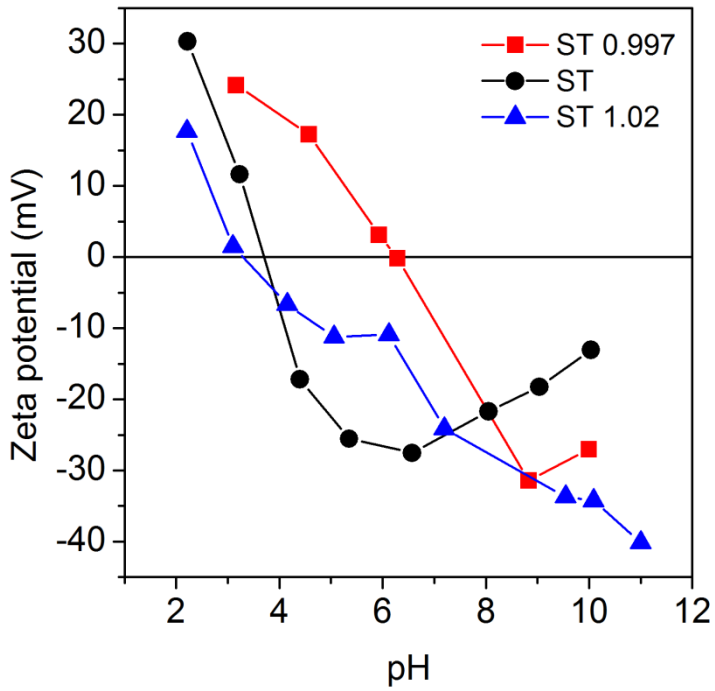

Figure 4.3-1: Similar zeta potential dependence on the pH for ST 0.997, ST and ST 1.02 compositions measured in water.

The effect of the suspension media and addition of I_2 on the particle size distribution (Coulter) for the stoichiometric composition is illustrated in Figure 4.3-2. Bimodal distributions for all solvents can be observed, with a constant position of the first peak, around 0.2 µm. The second peak is more dependent on the solvent and addition of iodine. When iodine is added to ethanol or acetone suspensions, a decrease of the second peak and an increase of the first one are observed.

This confirms that the second peak is, at least to some extent, related with agglomerates that are reduced by the iodine addition, which contributes to a better dispersion and stability of the suspensions. Iodine (I_2) dissolves rapidly in the organic solvent where it reacts producing positively (H^+) and negatively charged (I^-) ions [371; 372].

Vilarinho *et al.* [372] suggested that the generated protons are adsorbed on the surface of the suspended particles, making them positively charged and enhancing the electrostatic repulsion force. Consequently, the dispersion and stability of the suspensions are improved.

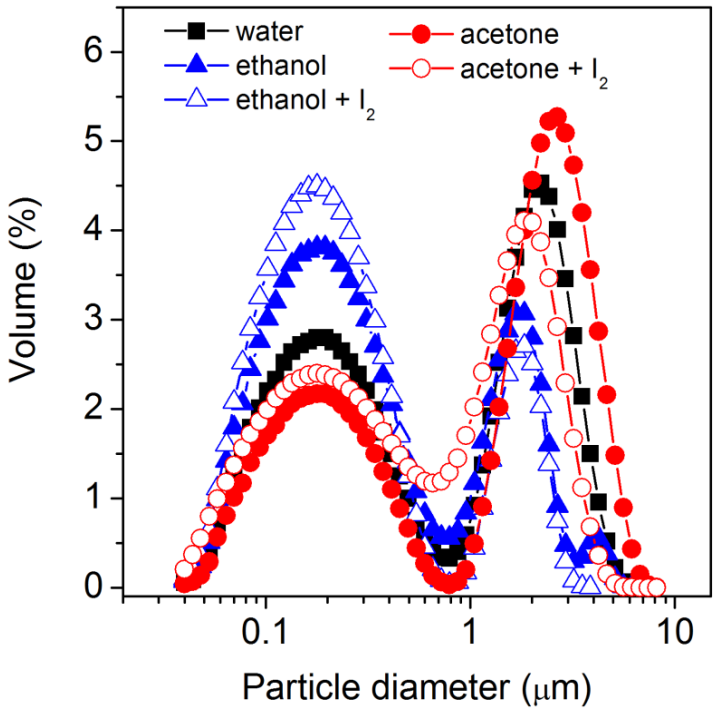

Figure 4.3-2: Particle size distribution of the powders of the stoichiometric composition in different solvents. Particularly in acetone, the addition of I_2 reduces the second peak, which is mainly related with agglomerates, leading to a better dispersion of the powders.

A good assessment of the stability of a suspension can be obtained by measuring the UV light transmittance and by its variation with time [372]. Low transmittance values and small variations with time are indicators of a stable suspension. The variation with time of the transmittance of the several suspensions in study is presented in Figure 4.3-3. For the water suspension, although stable with time, a high transmittance can be observed, which means that the major part of the particles was not able to be kept in

suspension. Additionally, no effect of the iodine addition was found. Similar behaviour was observed for the case of ethylene glycol, despite the lower transmittance values.

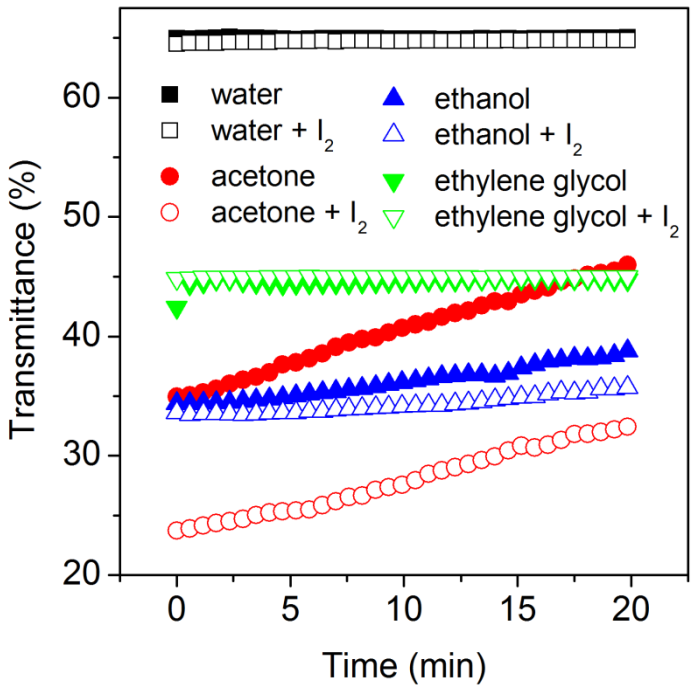

Figure 4.3-3: Variation with time of the transmittance of the suspensions of the stoichiometric powder in several solvents. Suspensions in acetone with I_2 addition show the lowest transmission values, in accordance with the effect of I_2 on the particle size distribution.

On the other hand, ethanol and acetone suspensions revealed lower transmittance values, even though some variations happened with time. The iodine addition has a strong effect in these suspensions, more in the case of acetone, reducing the transmittance values. This is a clear indication of the enhancement of the dispersion of the suspension by the additive, in agreement with the previously discussed effect of iodine in the particle size distribution in Figure 4.3-2. For short times, acetone and iodine present the lower transmittance values. These short times fit well the timing for EPD, as the deposition is performed a few seconds after stopping the stirring.

After the characterization of the several suspensions, their EPD performance was evaluated, by attempting to deposit films. First, the solvents were tested without the iodine addition. No deposition occurred with any of the solvents. On the other hand, with the addition of iodine, successful depositions occurred with ethanol and acetone. Figure 4.3-4 presents optical micrographs of good quality as-deposited films obtained with these suspensions. These results confirm the indications of increased suspension stability with the iodine addition from zeta potential (Figure 4.3-1), particle size distribution (Figure 4.3-2) and UV transmittance (Figure 4.3-3). The successful depositions occurred for standard pH meter readings of 1 – 2 for ethanol plus iodine and 2 – 3 for the case of acetone plus iodine, as expected from the analysis of zeta potential in Figure 4.3-1.

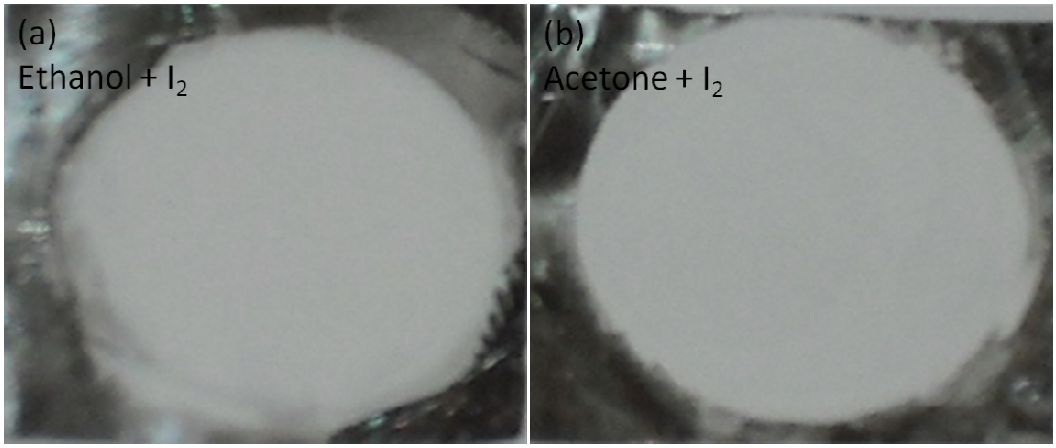

Figure 4.3-4: Optical micrographs of as-deposited ST films from (a) ethanol and (b) acetone suspensions, with I_2 addition. Both suspensions originate good quality films.

As the films obtained with acetone and iodine showed higher quality, this suspension was selected for further studies. Figure 4.3-5 illustrates the dependence of the deposit weight on the concentration of the suspension, the amount of iodine added, the deposition voltage and the deposition time.

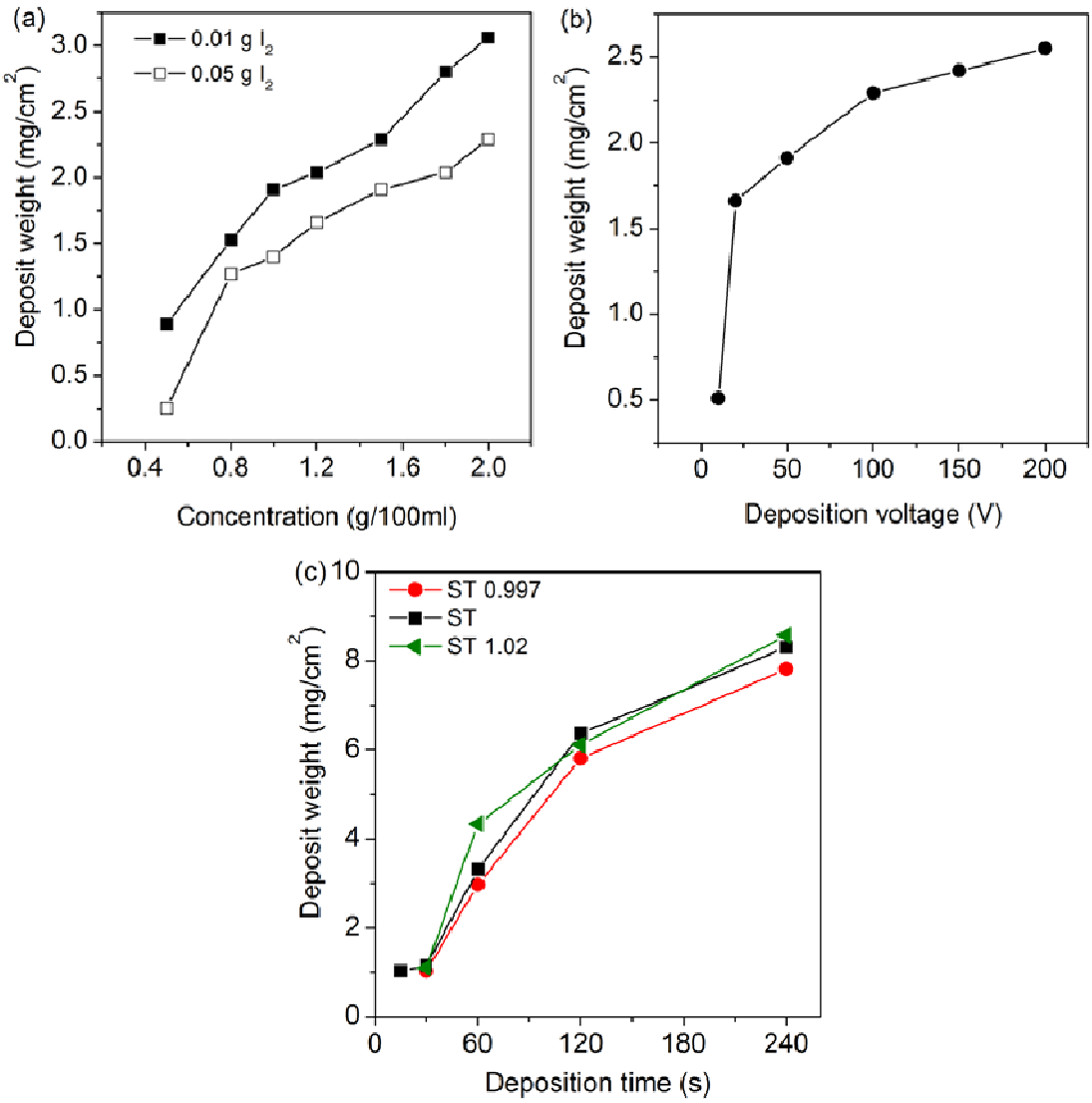

Figure 4.3-5: EPD deposit weight dependence on (a) concentration of the suspension for ST, 100 V and 1 min of deposition time, (b) deposition voltage for ST, 1 g/100 ml and 1 min deposition time and (c) deposition time for ST 0.997, ST and ST 1.02, at 100 V, 1 g/ 100 ml. The deposit weight increases with the concentration of the suspension and with the deposition voltage and time.

For the stoichiometric composition, deposition voltage of 100 V and 1 min of deposition time, it can be seen in Figure 4.3-5 (a) that the deposit weight is very sensitive to the amount of iodine added: without iodine no deposition occurred, but if too much iodine was added the amount of particles deposited decreased, probably due to the increase of the suspension conductivity [373]. On the other hand, the

deposited weight clearly increases with the concentration of the suspension. However, for high concentrations, it is difficult to maintain the stability of the suspension and the films become less homogeneous.

Regarding the deposition voltage, Figure 4.3-5 (b), for the stoichiometric composition, it can be concluded that the deposit weight increases with increasing applied voltage. However, this dependence seems to present an asymptotic behaviour. After a substantial increase of the deposit weight with the applied voltage for low voltages, smaller increases are observed when high voltages are applied. This can be explained by the fact that high voltages may originate turbulence in the suspension [83], with particles strongly interacting with each other and with the substrate, which makes the deposition less effective.

Figure 4.3-5 (c) presents the evolution of the deposit weight with the deposition time. The three compositions present equivalent behaviour, as expected from similarities observed in the powders particle size characterization (Chapter 4.1) and zeta potential results (Figure 4.3-1). Resembling the observations regarding the deposition voltage, for long deposition times smaller increases in the deposit weight occur. One reason is that, as the deposition occurs, the particle concentration in the suspension decreases, which lowers the deposition rate [290]. Another explanation is a voltage drop across the electrodes as the insulating deposited layer forms on the deposition electrode, resulting on a decrease of the deposition rate [283]. Additionally, for long deposition times, and also for high deposition voltages, the quality of the obtained films clearly deteriorates. Films become inhomogeneous, with evident roughness on the surface.

The observed dependence of the deposit weight on the studied parameters offers simple ways to control the thickness of the films and to obtain thick deposits in short periods of time. Considering all these observations, the following deposition parameters were selected: 1 g of powder per 100 ml of acetone, with approx. 0.01 g of iodine addition, 100 V and 1 min of deposition time. Using the selected parameters, good quality, reproducible thick films of the three compositions were deposited. The SEM top-view microstructures of the obtained as pressed green films, after CIP at 200 MPa, are depicted in Figure 4.3-6.

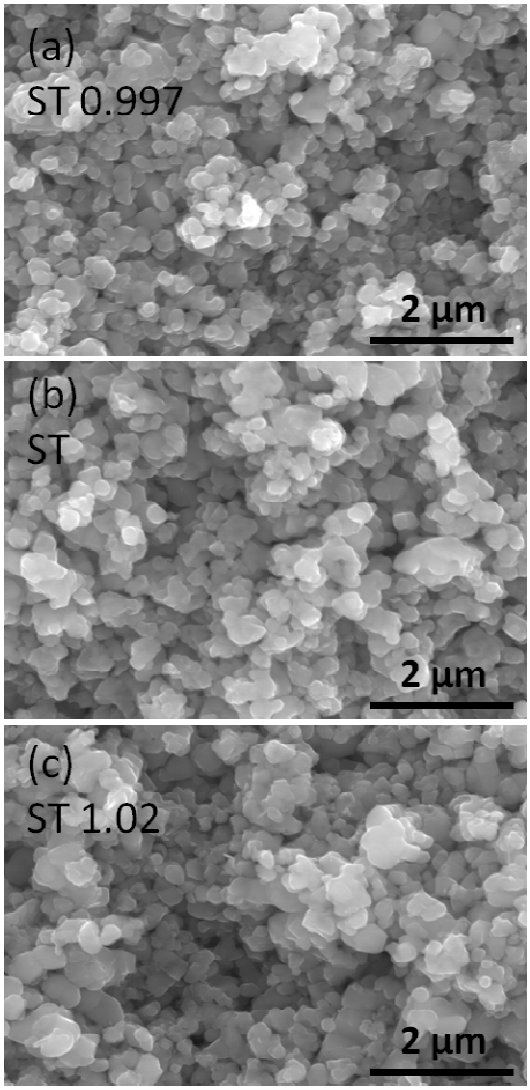

Figure 4.3-6: SEM top view microstructures of the as-pressed thick films: (a) ST 0.997, (b) ST and (c) ST 1.02. Green samples have similar microstructures.

The films present similar particle size and packing characteristics with clearly submicron particles. After CIP, the green films of the three compositions showed similar green densities of 47 ± 1 %.

Figure 4.3-7 presents the SEM top-view microstructures of the films after sintering. All the films were heated up to 1500 ˚C, at 5 ˚C/min. Figure 4.3-7 (a) and (b) illustrate the effect of the CIP step on the final microstructure of ST 0.997 films: without CIP (Figure

4.3-7 (a)) the resulting films are very porous and with smaller grains; after CIP, a step that increased the green density, the films present higher density and a coarser microstructure (Figure 4.3-7 (b)).

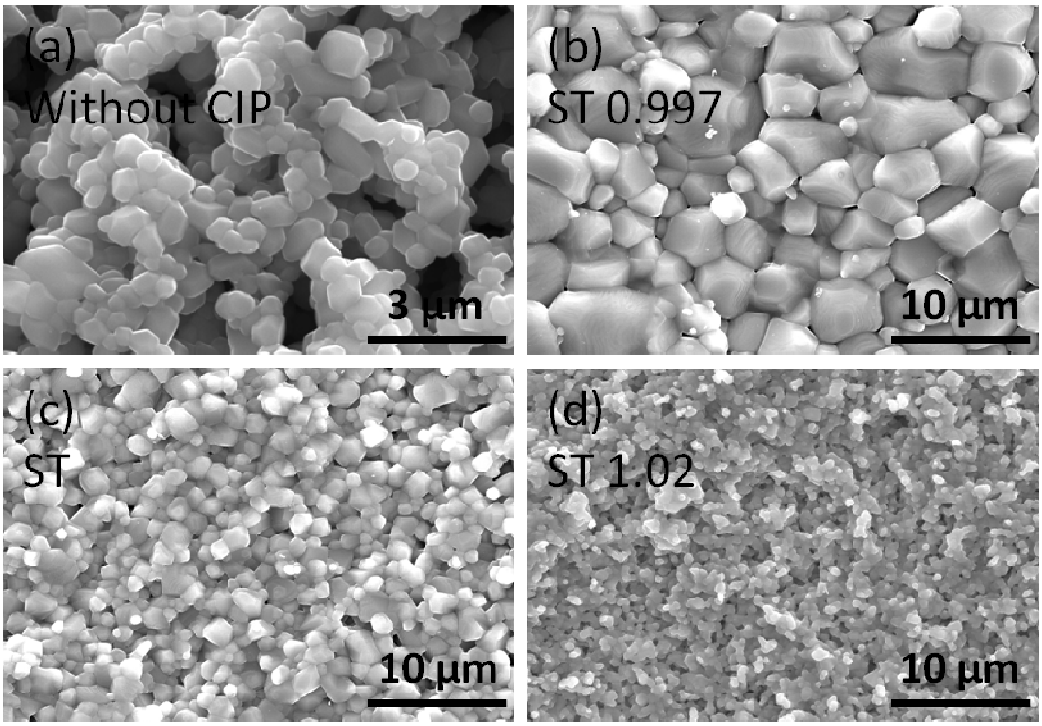

Figure 4.3-7: SEM top view microstructures of films heated up to 1500 ˚C at 5 ˚C/min: (a) ST 0.997 without CIP; (b) ST 0.997, (c) ST and (d) ST 1.02, with CIP. CIP increases the final density of the films. Grain size decreases with the increase of the Sr/Ti ratio.

Another important and obvious observation is the decrease of the grain size with the increase of the Sr/Ti ratio, from Figure 4.3-7 (b), for the Ti-rich composition, to (c) for the stoichiometric one and to (d) regarding the Sr-rich composition.

Figure 4.3-8 portrays the equivalent diameter distribution for the films. The average grain size is shown in Table 4.3-1. A narrow equivalent diameter distribution can be noticed for the Sr-rich composition, along with the small average grain size of 0.5 µm. Only residual grain growth occurred for this composition. The stoichiometric composition, ST, revealed a slightly larger distribution, with an average grain size

nearly three times larger than ST 1.02. By its turn, the Ti-excess originated a large distribution and a coarse microstructure, attaining an average grain size larger than twice that of the stoichiometric composition.

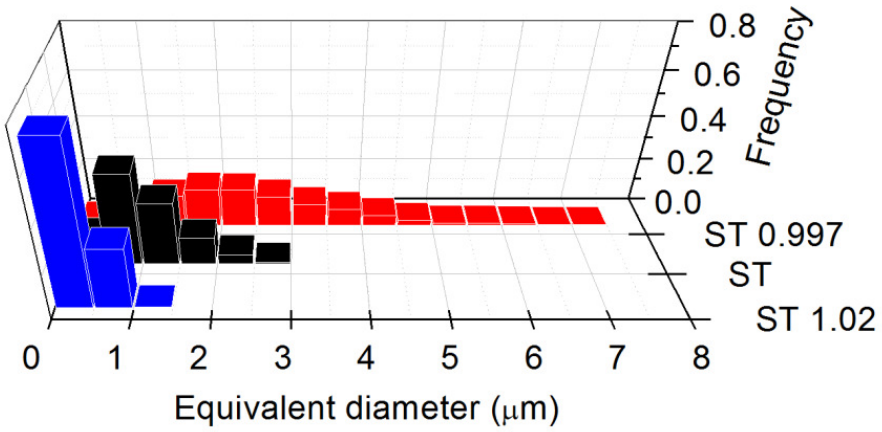

Figure 4.3-8: Equivalent diameter distribution for the sintered films of the three compositions. Enlargement of the distribution is seen with the increase in Ti content.

The cross-section microstructures of the films are shown in Figure 4.3-9. The thickness of the ST 0.997 and ST films is around 12 µm. The film of the ST 1.02 composition is thinner (≈ 5 µm), probably due to removal of material by the rubber tube during the pressing step. The thick films revealed good adhesion to the Pt substrate (the separation of the ST film from the substrate visible in Figure 4.3-9 (b), occurred during cutting or polishing, as no delamination was observed in any other circumstances). The films are homogeneous through the thickness of the layers, with equiaxied grains as usually observed for STO ceramics [259; 277], related with the cubic structure of the material.

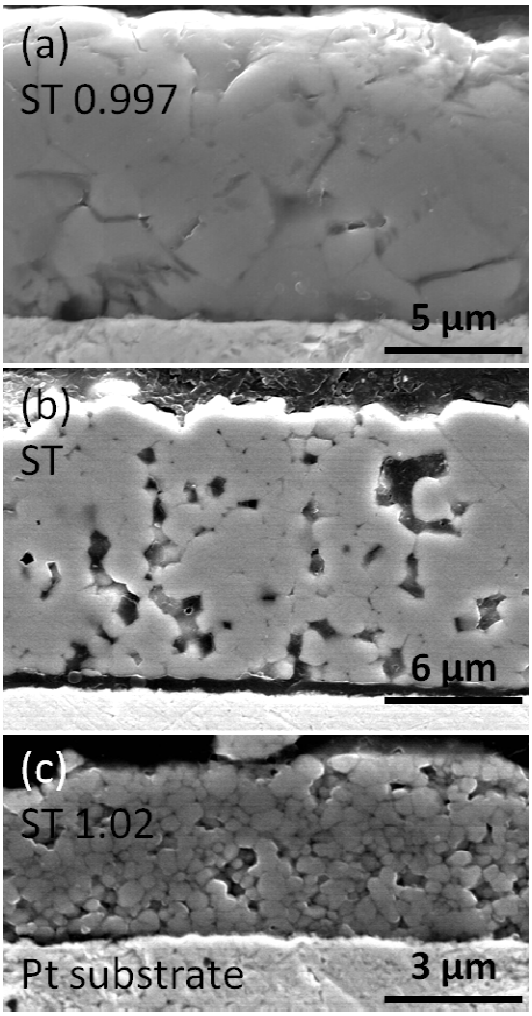

Figure 4.3-9: SEM cross-section microstructures of films heated up to 1500 ˚C at 5˚C/min: (a) ST 0.997, (b) ST and (c) ST 1.02. Along with larger grain size, the Ti-rich film is denser than the stoichiometric and Sr-rich ones.

The effect of the nonstoichiometry on the microstructure is again clearly visible. The relative density attained in the constrained sintered films of the three compositions is presented in Table 4.3-1. It is noticeable that the film of the Ti-rich composition, Figure 4.3-9 (a), is denser than the others. While this film reached almost full densification, a higher fraction of porosity is still visible in the films of the stoichiometric and Sr-rich compositions, Figure 4.3-9 (b) and (c), respectively.

Table 4.3-1: Relative density and average grain size attained in STO thick films after heating up to 1500 ˚C at 5 ˚C/min.

	Relative density	**G (µm)**
ST 0.997	0.98 ± 0.01	3.3 ± 0.4
ST	0.94 ± 0.02	1.4 ± 0.1
ST 1.02	0.93 ± 0.02	0.5 ± 0.1

The observations regarding densification and grain growth in STO thick films are in agreement with our previous results on the effect of nonstoichiometry on the sintering kinetics of STO ceramics. Accordingly, an increase of the densification rate and enlargement of the grain size distribution with the decrease of the Sr/Ti ratio were reported for STO ceramics [259].

As previously discussed, the constrained sintering [84] of ceramic layers on top of substrates is known to deviate from the classic sintering models. The substrate exerts an effect on the sintering processes, as the sintering layer is not allowed to shrink in the substrate direction [84]. Therefore, due to the constraining effect of the substrate, densification is often retarded in films [86]. In this way, the high densification verified in the STO films (particularly for the ST 0.997 composition) may be related with a reduction of the degree of substrate constraint due to the flexibility of the Pt-foil substrate [100].

Another common effect of the constraint from the substrate is the development of microstructural anisotropy as, for example, elongation and vertical (out of plane) preferential orientation of pores [84]. Figure 4.3-10 illustrates the pore orientation distribution measured in the cross section micrographs (Figure 4.3-9) of the films of the stoichiometric composition, ST, which show well defined pores. A preferential vertical pore orientation is in fact found. Around 42% of the pores are oriented in directions near the perpendicular to the substrate.

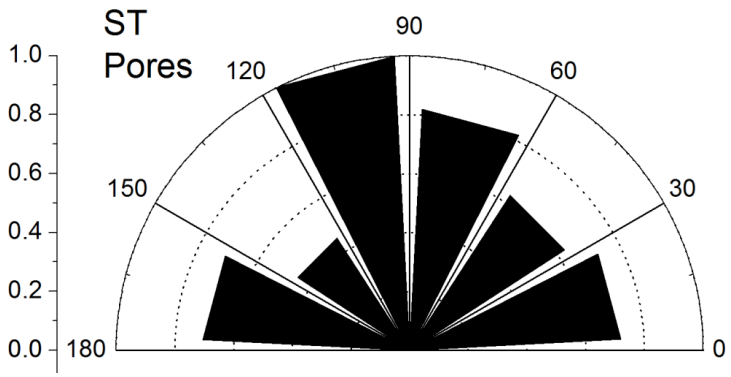

Figure 4.3-10: Pore orientation distribution for the films of the stoichiometric composition (ST) showing a preferential out-of-plane pore orientation.

However, despite the anisotropic orientation of pores, significant anisotropy in the orientation of grains is not expected due to the reduced grain growth and to the cubic nature of the STO crystallographic structure and the consequent equaxied grains observed in the SEM cross section (Figure 4.3-9) and top view (Figure 4.3-7) micrographs regarding the films of the three compositions.

4.3.4 Summary

Thick films of stoichiometric and nonstoichiometric STO compositions were successfully deposited by EPD on Pt-foil substrates. Acetone and ethanol were found to be suitable suspension media for the EPD of STO powders. The best EPD performance was obtained using acetone with the addition of iodine.

The deposit weight is dependent on the concentration of the suspension, on the amount of iodine added and on the deposition time and voltage. These dependences can be used to control the thickness and quality of the films. CIP of the green films enhanced markedly the final density of the films.

The effect of the nonstoichiometry on the microstructure of the constrained sintered thick films revealed to be similar to the case of bulk ceramics: increased densification and grain size and enlargement of the distribution with decreasing Sr/Ti ratio. Grains

shape is equiaxied independently of the stoichiometry and substrate constraint. In agreement with previous results of constrained sintering, a preferential vertical pore orientation was observed. However, the influence of the constrained sintering and of the nonstoichiometry on more developed microstructures as well as their combined effects on the dielectric properties of STO thick films still need to be addressed in order to achieve thick films with tailored and optimized properties.

Nevertheless, this preliminary investigation of the constrained sintering of STO EPD thick films raises several technologically important questions. Among them is the role of the flexible Pt substrate on densification and grain growth or the anisotropic microstructural development under the substrate constraint. Moreover, as previously referred, because these microstructural features are expected to affect the dielectric response of functional materials [19], the understanding of the constrained sintering of ceramic layers on top of metal-foil substrates may constitute a way to achieve tailored and optimized functionality.

5 $BaO\text{-}Ln_2O_3\text{-}TiO_2$ (Ln: La or Nd)

5.1 Constrained sintering and dielectric properties of $BaLa_4Ti_4O_{15}$ thick films

5.1.1 Introduction

Besides the scientific interest, the investigation of constrained sintering in functional systems represents a matter of fundamental importance for the related processing technology. However, very few studies have been carried out on the constrained sintering of thick films on flexible metallic substrates. In particular, in the functional oxides of $BaO–La_2O_3–TiO_2$ system such studies have not been reported.

As previously presented, BLT has a layered perovskite-type structure with a hexagonal symmetry. In opposition to the previous case of STO, the large anisotropy in the BLT lattice parameters ($c/a\approx4$) has been reported to promote the growth of plate-like particles in bulk ceramics [146]. This usually leads to the development of microstructural anisotropy, which may be enhanced in thick films by the effect of the substrate [19].

In a recent work carried out in the Electroceramics Group of CICECO at the University of Aveiro [19] a relation between the anisotropic microstructure development in $BaNd_2Ti_5O_{14}$ (BNT 1:1:5) thick films prepared by EPD on Pt foils and the dielectric properties was reported. By controlling the sintering temperature, near-zero $TC\varepsilon_r$, high Q thick films could be fabricated. The observed textured microstructure was attributed to the anisotropic crystal structure of BNT materials and to constrained sintering effects. However, the observed substrate constraint effects are not completely understood.

Therefore, this chapter focuses on the constrained sintering of $BaLa_4Ti_4O_{15}$ (BLT) thick films deposited by EPD on Pt foils and BLT rigid substrates. In particular, the effect of a compliant substrate such as Pt on the constrained densification and grain growth

behaviour of BLT is systematically addressed. Due to its flexibility and inertness, platinum acts at the same time as electrode (during the EPD process as well as for the ready-to-use capacitor) and physical support.

Besides densification retardation and enhanced grain growth in BLT constrained sintered films, anisotropic microstructure development was also observed when compared with bulk samples having similar green packing and sintered under the same conditions. The evolution of the microstructural parameters (grain and pore shape and orientation, texture) during densification and their correlation were investigated in films and compared with the morphological evolution in bulk samples. The effect of microstructure anisotropy on the dielectric properties was also assessed.

The observations of this chapter point to the effect of mechanical stress developing during constrained sintering on the microstructure development. It is then expected that the appropriate choice of substrate will allow designing tailored microstructures of functional thick films with optimized performance.

5.1.2 Experimental details

The general experimental procedures described in Chapter 3 were adopted in this work. Some details specific of this chapter are presented in the following text.

The EPD parameters optimized in the previous chapter were adjusted and employed to fabricate BLT thick films. The deposition of BLT powders was performed on platinum foils and on dense BLT substrates. EPD was carried out at constant voltage (100 V) for 4 min of deposition time. The films were submitted to two cycles of CIP: the first one at 50 MPa, to increase the adhesion of the film to the substrate, and the second one at 200 MPa, to increase the green density. The resulting film thickness measured by SEM was 35 ± 6 µm.

Films were sintered at 1500 °C with a heating rate of 25 °C/min until 1400 °C and approximately 7 °C/min between 1400 and 1500 °C. Isothermal sintering times varied from 0 to 720 min. The shrinkage of BLT bulk samples during free sintering was

obtained by means of a laser dilatometer, measuring strains in axial and radial directions [374]. The sintered bulk samples were then cut along the diameter, polished and thermally etched at 1430 °C for 10 min for SEM analysis. Laser dilatometry [86] couldn't be applied to continuously record the films shrinkage, due to the experimental difficulties arising from the flexibility of Pt substrate.

5.1.3 Results and discussion

5.1.3.1 BLT powders

As shown in Figure 5.1-1, after 3h of calcination at 1330 °C, the BLT powders were monophasic within the XRD detection limit.

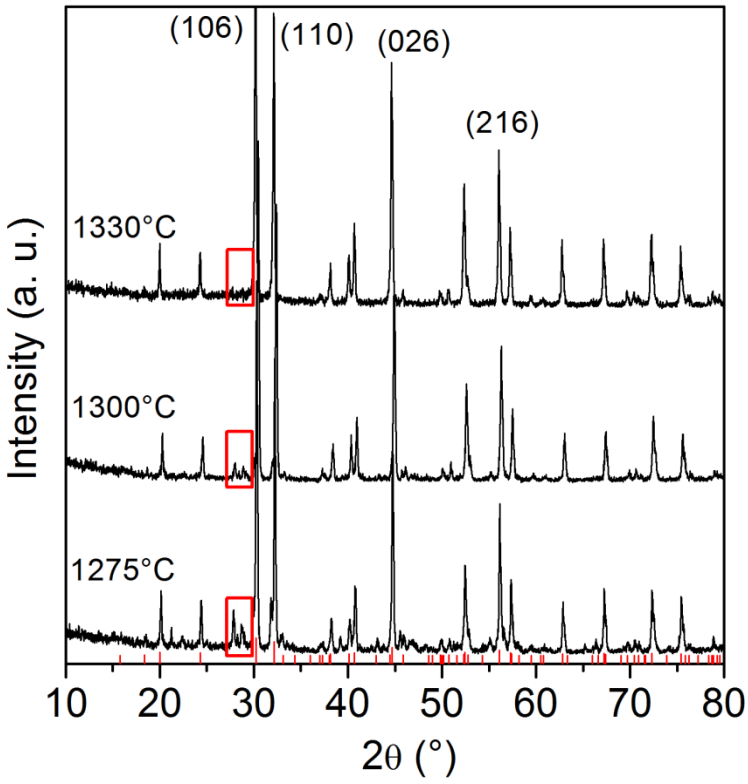

Figure 5.1-1: X-ray diffraction patterns of BLT powders calcined at 1275, 1300 and 1330 °C for 3h. The boxes indicate the peaks belonging to $BaLa_2O_3$ second phase, which is no longer present at 1330 °C. PDF card #01-070-6341 is also shown.

For all the studied calcination temperatures the dominant phase is BLT but for 1275 and 1300 °C $BaLa_2O_3$ second phase was detected, as highlighted by the boxes of Figure 5.1-1.

After ball milling, the powders show a bimodal particle size distribution, Figure 5.1-2, with particle diameter below 4 μm. The particle size was also analyzed by SEM and a median particle size of 0.22 μm was obtained, in agreement with the Coulter results in Figure 5.1-2.

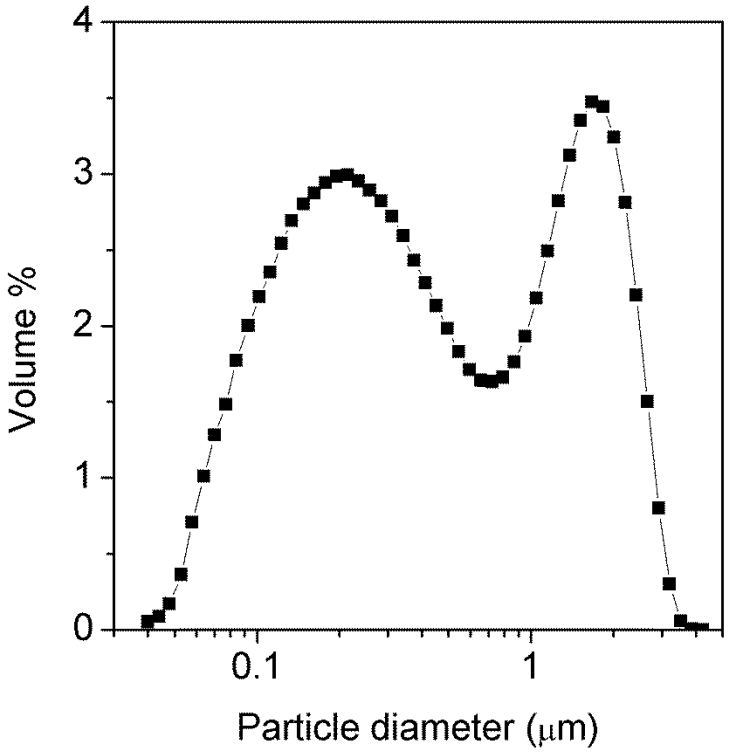

Figure 5.1-2: Particle diameter distribution of BLT powders. A bimodal distribution is observed, with particle diameter below 4 μm and median of 0.22 μm.

5.1.3.2 Effect of the substrate

The densification behaviour of BLT is presented in Figure 5.1-4 (a). The evolution of the relative density during isothermal time of freely sintered bulk is compared to that obtained for constrained thick films sintered on flexible platinum foils and rigid BLT

substrates. The samples were sintered at 1500 °C, with isothermal times ranging from 0 to 180 minutes. The green relative density of the bulk was 53 ± 2% and of films 49 ± 2%. This difference in the green density is not large and it is assumed to have a minimal effect on the densification behaviour of the material.

The relative density of the bulk samples was calculated using the formula (5.1-1) (adapted from Ref. [106]) from the radial ($\varepsilon_{s,r}$) and axial ($\varepsilon_{s,z}$) strain curves on Figure 5.1-3.

$$\rho_i = \rho_f \frac{exp\left(2\varepsilon_{s,rf} + \varepsilon_{s,zf}\right)}{exp\left(2\varepsilon_{s,ri} + \varepsilon_{s,zi}\right)} \qquad (5.1\text{-}1)$$

where the index *i* stands for the instant of the measurement and the index *f* for the end of the isothermal time. It is assumed that no further densification takes place during rapid cooling. Thus, parameter ρ_f was taken as the measured Archimedes density, assuming that it was equal to the density at the end of the isothermal time.

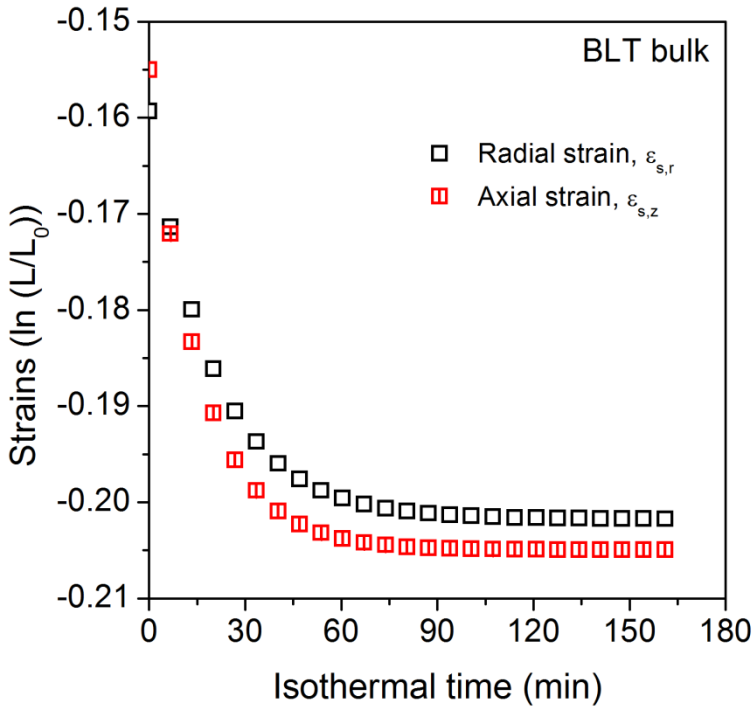

Figure 5.1-3: Radial and axial true strains as a function of the isothermal time measured with a laser dilatometer for cylindrical BLT bulk samples.

The relative density of the freely sintered bulk sample was 82% at the beginning of the isothermal time and reached 97% after sintering for 180 min, as measured by the Archimedes method, with most of the densification occurring during the heating ramp and the first 30 min of isothermal time. Regarding the experimental values obtained for films on Pt, a lower density of 65% is reached at the beginning of the isothermal time (0 min), in opposition to the 82% for the bulk. Following the same trend, after 60 min, the bulk density was 95%, close to the final densification of 97%, whereas the film densification was much delayed, reaching only 88% of relative density.

On the other hand, in spite of the initial densification retardation, it is interesting to observe that the film final densification on Pt reached 96% after 180 min at 1500 ˚C, a value equivalent to the final density reached for free sintering. For films sintered on rigid BLT substrates it is remarkable that the final density is also similar to the one obtained with platinum substrate highlighting the fact that, despite a higher rigidity and degree of constraint, high density can be reached after a certain time, if the temperature is high enough.

This is an interesting behaviour and quite different from those previously reported for other materials like alumina [86; 115], zirconia [116], zinc oxide [91], gold [93], or even LTCC glass-ceramic composite [85] sintered on rigid substrates at moderate temperatures, where the maximal final density was always lower than the one of freely sintered bodies. Nevertheless, as observed in the previous chapter regarding STO thick films, if temperature is sufficiently high, final densities can be closer to the theoretical ones, or at least close to the density achieved under free sintering conditions. For example, alumina films sintered at 1350 °C achieved a density of ~97% after 240 min, whereas a free sintered sample was densified to 99% after 8 min [86]. Similarly, yttria doped zirconia solid electrolytes for fuel cells need to be gas tight (i.e., the density should be above 95%). This was reached by Wang and Atkinson [375] by increasing the sintering temperature from 1250 °C to 1350 °C and holding time from 1 h to 48 h. A jump in density from ~85% to ~97% was consequently observed.

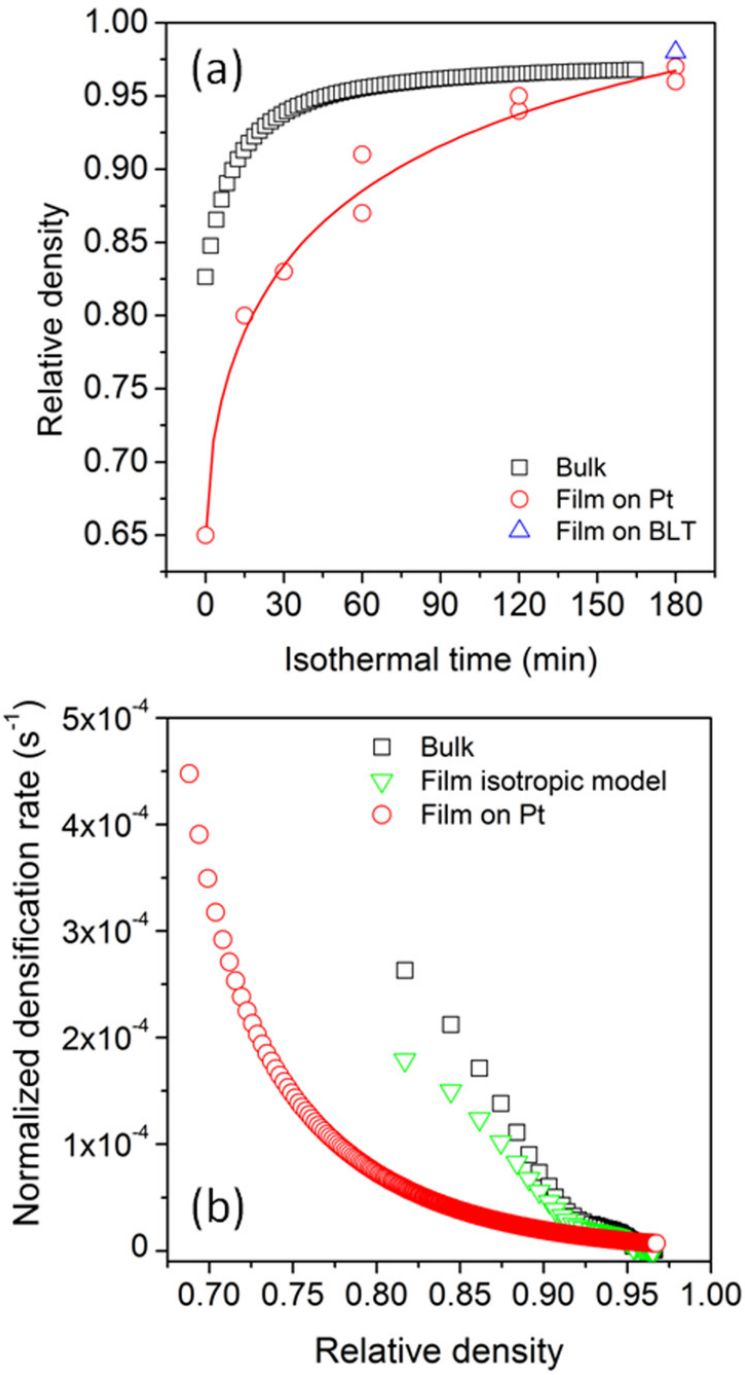

Figure 5.1-4: (a) Relative density as a function of the isothermal time; (b) normalized densification rate as a function of the relative density. The densification of the constrained films is initially delayed but the final density is similar to that of freely sintered bulk samples. The isotropic model prediction of the constrained densification rate lies closer to the free densification rate than to the experimental constrained curve.

A prediction of the normalized densification rate of the constrained films can be obtained applying the isotropic continuum mechanical model, according to the expression (2.1-9) [105], from the free sintering behaviour and the viscous Poisson's ratio (ν^p). ν^p was calculated after Venkatachari and Raj [110], as a function of the density, according to the relation:

$$\nu^p = \frac{21[ln(1-\rho) + 0.5\rho(\rho+2)] + 4\rho^2}{42[ln(1-\rho) + 0.5\rho(\rho+2)] - 4\rho^2} \qquad (5.1\text{-}2)$$

The normalized densification rate of the freely sintered bulk sample is equal to $-3\dot{\varepsilon}_S^{free}$. Assuming a perfectly rigid substrate and similar microstructure for bulk and film, a lower densification rate is predicted by the isotropic model for the constrained film, as compared to the body sintered without any constraint.

In Figure 5.1-4 (b) the normalized densification rate dependence on the relative density for bulk and films on platinum is presented. At 83% of relative density, the normalized densification rate of the freely sintered bulk sample is higher than the one experimentally observed for the film by a factor of ~5, whereas the modelled normalized densification rate is 3.5 times higher than the experimental one. On the other hand, when 95% of relative density is attained, absolute values and the difference between densification curves are reduced: the free densification rate is only 1.2 times higher than the experimental constrained one, which, in turn, is very close to that of the model prediction, as the viscous Poisson's ratio tends towards 0.5. A comparison with the modelled density is not possible, because constrained normalized densification rate is only known above 82% of density (see Figure 5.1-4 (b)) and extrapolation of this curve at lower densities (65%) may be prone to large errors.

The fact that the isotropic modelled curve lies closer to the free densification rate than to the experimental constrained curve was already observed for alumina films sintered on alumina substrates [86] and attributed to the development of anisotropy in the microstructure due to the geometrical constraint.

To complement this analysis, top view SEM microstructures of BLT films sintered on Pt at 1500 °C for several isothermal times are presented in Figure 5.1-5. The evolution of

densification and grain size can be followed in these images. Grains present a platelet shape with a high aspect ratio.

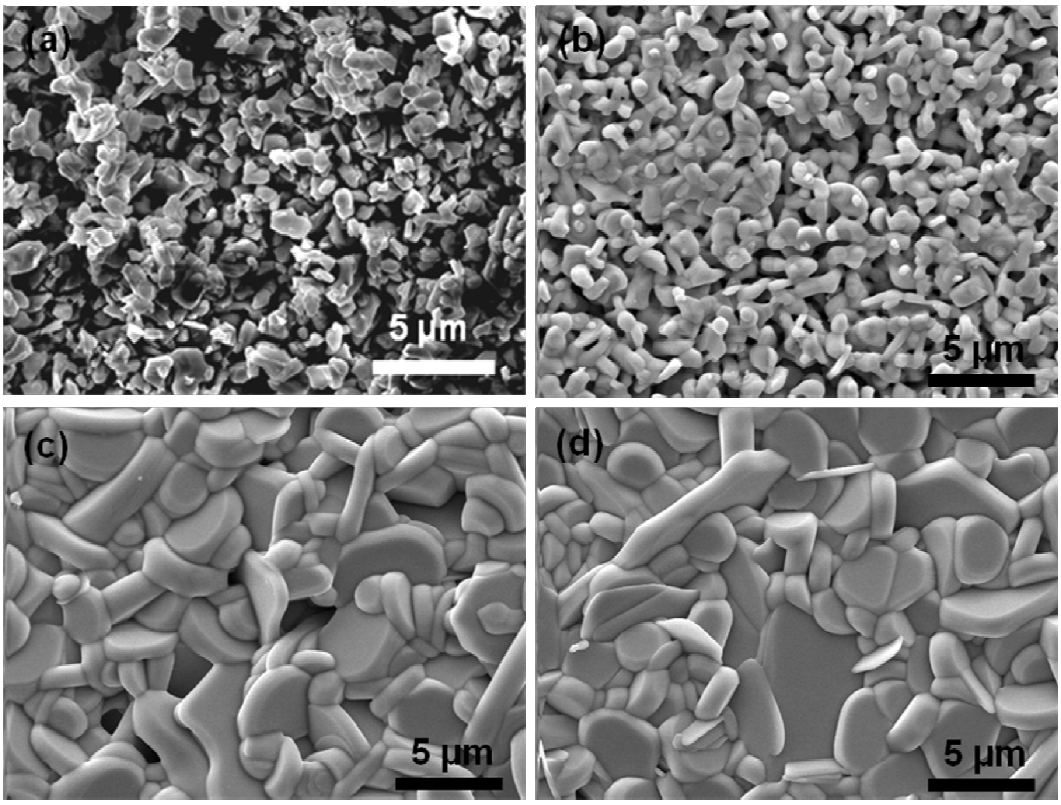

Figure 5.1-5: SEM top view microstructures of BLT films on Pt substrate: (a) green film and films sintered at 1500 °C for (b) 0, (c) 60 and (d) 120 min. Typical BLT grains with platelet shape and high aspect ratio are observed.

In Figure 5.1-6, SEM microstructures of films on Pt, films on BLT and bulk sintered at 1500 °C for 180 min, are presented. After 180 min, large grain coarsening can be noticed. Additionally, grain size is larger in the films than in the bulk, the largest grains being observed for films sintered on rigid BLT substrates.

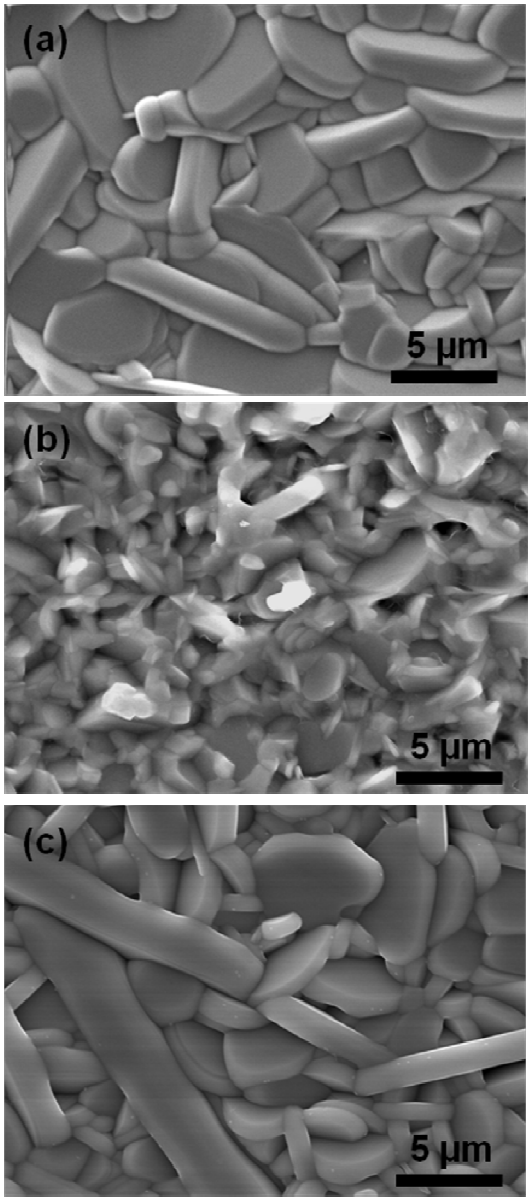

Figure 5.1-6: SEM micrographs of BLT samples sintered at 1500 °C for 180 min: (a) film on Pt (top view); (b) bulk (as sintered surface); and (c) film on BLT (top view). Grain size is larger in the films than in the bulk specimen.

The evolution of the grain area distribution, measured in etched cross-sections (shown ahead in section 5.1.3.3) of the films sintered on Pt at 1500 °C, from 0 to 180 min, is presented in Figure 5.1-7 (a). The results are compared with the grain area observed for the bulk sintered under the same conditions for 180 min and for films on BLT substrates in Figure 5.1-7 (b). Because sections of the grains have an elongated shape,

the grain area was chosen as a more representative parameter for the quantification of the grain size than others (like for instance the equivalent diameter or Ferret's maximal diameter). For the films sintered on Pt foils, considerable grain growth occurred in the first 15 min of sintering time (corresponding density: 80%) with some grains reaching areas close to 3.5 µm².

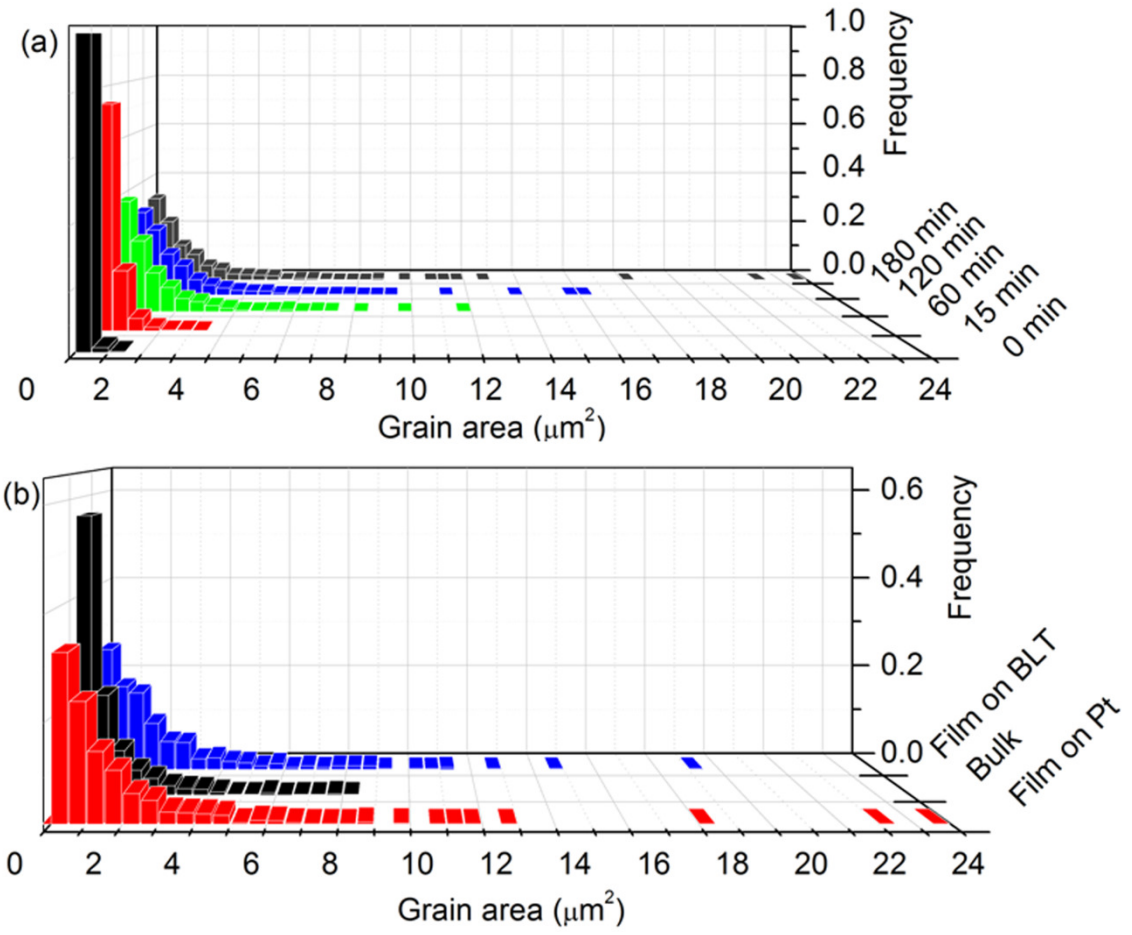

Figure 5.1-7: Evolution of the grain area distribution at 1500 °C (a) with the isothermal time for films on Pt and (b) for film on Pt, bulk and film on BLT, sintered for 180 min. A steady enlargement of the distribution with the isothermal time is visible for the films, which is narrower in the bulk sample.

In agreement with the SEM top views, a progressive enlargement of the distribution with the isothermal time is visible, giving rise to heterogeneous and broad grain area

distribution in dense films, after 60 min. Two populations can be distinguished: one of grains with areas roughly below 4 µm² and another one composed of large elongated grains reaching 25 µm² after 180 min of isothermal time. The frequency of such large grains is however low, as 93% of the grains are smaller than 4 µm². Similar observations can be made for the films sintered on BLT substrates. Oppositely, the bulk sample sintered under the same conditions showed more uniform grain growth with a narrower grain area distribution below 9 µm².

The variation of the median grain area with the isothermal time for constrained films and free bulk is depicted in Figure 5.1-8. Although starting with the same initial particle size and similar green packing, films and bulk followed different sintering trajectories: lower or equivalent density (Figure 5.1-4 (a)) and higher grain size (Figure 5.1-8) are observed for the films when compared with bulk samples submitted to the same thermal cycle.

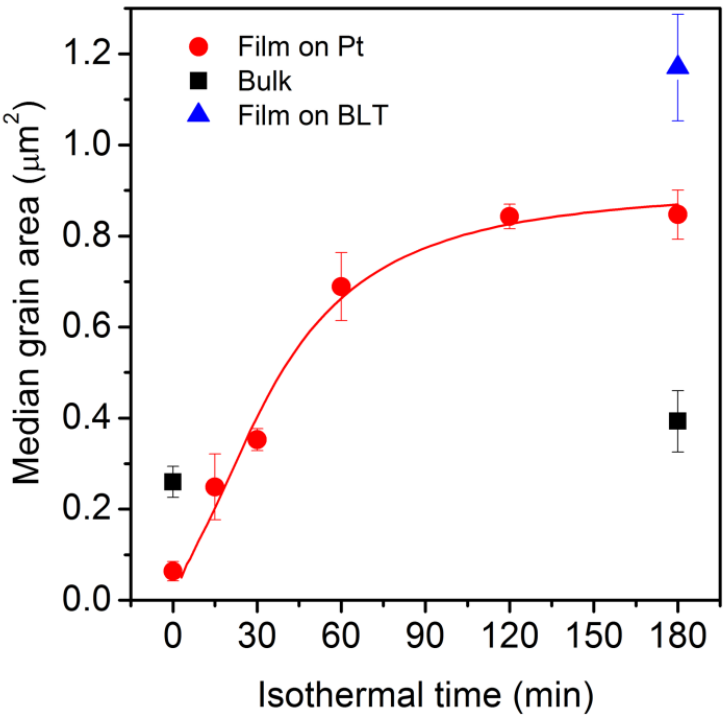

Figure 5.1-8: Median grain area as a function of the isothermal time for films and bulk. Median grain area increases with the substrate constraint.

This contrasts with precedent results showing for gold layers on silicon [93] and alumina films on alumina [112] that the sintering trajectory was hardly affected by the constraining conditions. Related to a narrower grain area distribution, the bulk sample shows a significantly smaller median grain area at the end of the sintering cycle. In fact, the median grain area of the constrained film on Pt is 2.2 times larger than the grain area of the freely sintered bulk sample at a density of 96%. The final median grain area for the films on Pt is 22 times larger than the initial value. The grain size for films sintered on rigid BLT substrates, after 180 min at 1500 °C, is even larger than for the films sintered on platinum foils, as it reaches around 1.2 µm² (1.4 times more than on platinum).

Figure 5.1-9 shows that there is a good adhesion between the film and the substrate, without delamination. This has to be contrasted with the poor adhesion of alumina layers sintered at 1200 °C, which could be easily detached from similar platinum foils [100]. Moreover, no residual porosity is left near the substrate, in contrast to what was observed for alumina layers sintered on alumina substrates [115]. Grains present a needle shape, with a high aspect ratio, and small pores are located between the elongated grains.

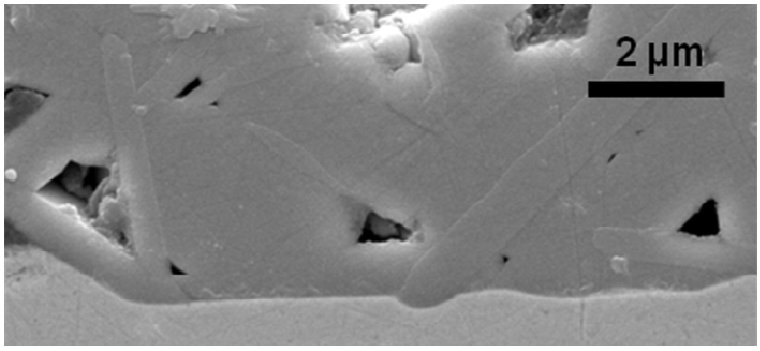

Figure 5.1-9: SEM cross-section micrograph of a film sintered for 120 min showing the interface between the film and the Pt substrate and the deformation of the platinum.

The substrate is locally deformed confirming that it cannot be considered as perfectly rigid, as in the simple model given by equation (2.1-9). Nevertheless, no macroscopic

curvature after sintering could be measured, even if the geometry of the bi-layer is obviously asymmetrical, thus potentially leading to camber. As a comparison, 50 µm thick alumina/Pt bi-layers showed extreme curvature values already at 1200 °C, due to the important creep deformation in the metal layer [100]. Several explanations can be given to rationalize this effect. First, the difference in thermal expansion coefficient is minimal between platinum and BLT, which explains that during heating and cooling no warping was observed. From room temperature to 1500 °C, the average coefficient of linear thermal expansion for platinum is 11.3×10^{-6} K^{-1} [376] whereas for BLT it is 12.3×10^{-6} K^{-1} (obtained from strain curves of dense bulk specimens during cooling). Second, under isothermal conditions at 1500 °C, platinum is very soft, with creep strain rates of 2.2×10^{-6} s^{-1} under 1 MPa and 6.3×10^{-4} s^{-1} under 5 MPa [100]. Such stress levels are expected in constrained systems (even though the unbiased measurement of compatibility stresses is very difficult to carry out) [100]. These levels of strain rate correspond to the shrinkage rate observed for the films, which means that platinum can accommodate the deformation of the sintering layer attached to it.

The interaction between Pt substrate and BLT films was further analyzed by SIMS. The profile of elemental composition is depicted in Figure 5.1-10. The SIMS height profiles for a BLT sample sintered at 1500 °C for 180 min with an average thickness of roughly 13 µm is presented.

The element count for ^{47}Ti and ^{18}O ions originating from the BLT film as well as ^{194}Pt ions from the substrate are plotted as a function of the distance from the film surface. Element counts for Ba and La isotopes follow the same trend as for Ti. The curves can be divided into 3 regions: the first does not contain any platinum from the substrate and starts at the film top and ends roughly 5 µm below the surface. From 5 µm to 13 µm, both film and substrate materials are detected, with platinum content continuously increasing. More than 13 µm below the surface, the platinum count reaches a plateau, whereas the ^{47}Ti and ^{18}O counts decrease steeply but do not go completely to zero, as expected. No platinum has diffused into the uppermost 5 µm of the film. The intermediate region does show a nonzero platinum concentration despite the fact that the substrate lies further below. This effect is caused by the interface roughness and the bending of the substrate as shown in Figure 5.1-10 (b). As the

analyzed area is very broad (150 µm), large fluctuations in the film height and substrate roughness are taken into account during the measurement.

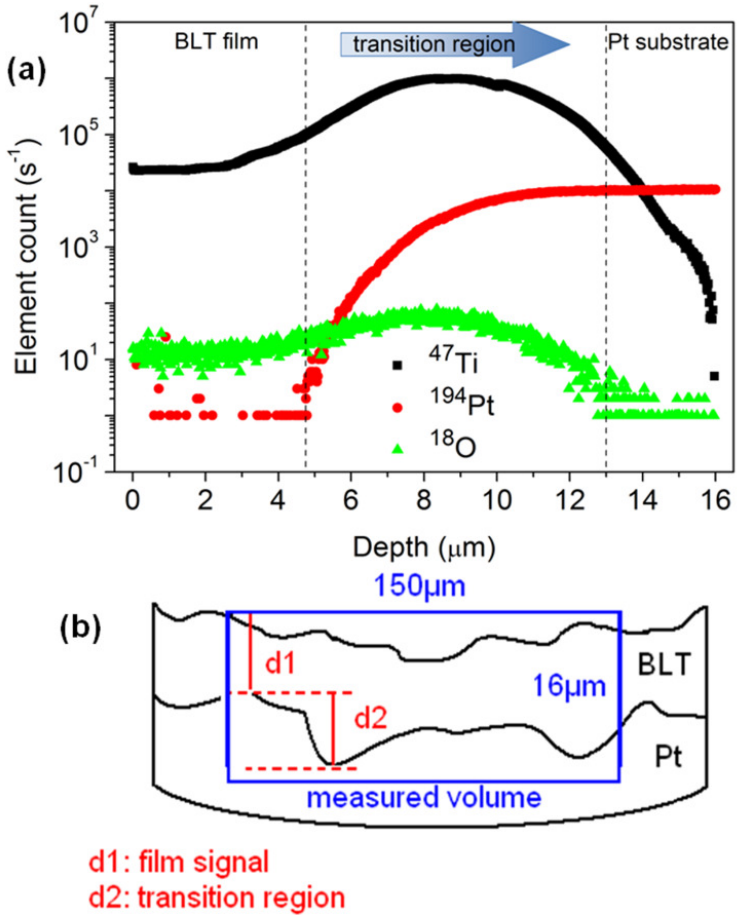

Figure 5.1-10: SIMS profile: (a) element counts dependence on the depth and (b) schematic representation of the measured sample. No platinum has diffused into the uppermost 5 µm of the film. The intermediate region does show a nonzero platinum concentration, which is caused by the interface roughness and the bending of the substrate.

As no gradient in the microstructure (grain size, density) could be observed on polished cross-sections at any time, it is assumed that the presence of platinum is minimal everywhere in the ceramic layer or at least that it does not affect its sintering behaviour. By using a rigid BLT dense substrate, we ruled out the possibility of

platinum contamination and aimed at increasing the tensile stress at the same time, which resulted in larger grain growth rate (Figure 5.1-6 to Figure 5.1-8).

Furthermore, the BLT films on Pt were also analysed by Rutherford Backscattering Spectrometry (RBS) [377]. This technique is a widely used nuclear method for the near surface layer analysis of solids. A target is bombarded with ions and the energy of the backscattered projectiles is recorded with an energy sensitive detector. RBS allows the quantitative determination of the composition of a material and depth profiling of individual elements. RBS is quantitative with a good depth resolution of the order of several nm and a very good sensitivity for heavy elements of the order of *ppm*.

However, the large BLT film thickness (beyond the optimal conditions for the RBS technique, which is more appropriate for thin films) does not allow the determination of the Pt profile by RBS: the Pt substrate is beyond the analysed depth. Nevertheless, in the analysed thin surface layer no Pt contamination was detected, which strongly supports the conclusions drawn from the SIMS measurements.

5.1.3.2.1 Discussion

It is known that during constrained sintering the densification is generally retarded and lower densities are obtained at the final stage [84]. In addition, in the case of solid state diffusion, anisotropy of the neck size with larger necks parallel to the substrate and, as a consequence, anisotropy of the interparticle pores, elongated perpendicularly to the substrate, were also observed [112; 116; 375]. In this work, films of BLT sintered on Pt foils present a retarded densification as expected, when compared with the BLT bulk sample and that is clearly depicted in the variation of the relative density as a function of the isothermal time (Figure 5.1-4 (a)) and on the normalized densification rate as a function of the relative density (Figure 5.1-4 (b)). Films and bulk, starting from similar initial green states, have different densification rates for the same relative density during almost all the process. However, in the final stage of sintering at 1500 °C the densification rate and the final density are almost the same as the bulk samples. Due to its ability to deform by creep, the use of platinum foil decreases the tensile stress to

only a few percent of the theoretical stress with an infinitely rigid substrate. The compliance of the substrate can therefore contribute to the diminution of the constraint during sintering by deformation as observed in Figure 5.1-9. Nevertheless, even a stiffer dense BLT substrate enables full densification after 180 min. Although the high temperature mechanical behaviour of BLT has not been evaluated, this shows that if sintering temperature is high enough, full densification of constrained films is possible.

The microstructure of these films exhibits a clear grain growth, with increasing grain elongation (Figure 5.1-5 and Figure 5.1-6), and width of grain size distribution (Figure 5.1-7). For long sintering times, cross-sections revealed a median grain area larger for the films when compared to the bulk samples sintered under the same conditions, (Figure 5.1-8). In addition, the comparison of the top view of the films with the as-sintered surface of the bulk, Figure 5.1-6, leads to the same conclusion. Therefore, the larger grain size in the films is observed in the samples surface as well as in their interior, showing that this phenomenon is not an effect of the increased surface area of the films.

The observed anisometry of the grains, related to the crystallographic structure and hexagonal symmetry of BLT, is increased during constrained sintering. Indeed, elongated grains can be observed in the bulk samples, as well, although with a lower degree of elongation (Figure 5.1-13 and Figure 5.1-16).

However, the larger grain area observed in the films is different from what has been reported for constrained sintering of alumina [112] and zirconia [116] films, for which, despite retarded densification, no favoured grain growth was observed when compared with the bulk counterparts. Both films and bulk followed the same trajectories, with a final grain size not larger than 4 times the initial particle size. In the present work, a clear enhancement of the grain growth during sintering is highlighted. The driving force for grain growth is the reduction of the total grain boundary area, leading to a decrease in the total free energy in the system (as atoms present in these disordered regions have a higher energy than those located in the crystalline bulk) [22]. On the other hand, abnormal grain growth is characterized by the rapid growth of a

few grains at the expense of smaller ones. This leads to the fact that the grain size distribution does not evolve homothetically with time. Exaggerated grain growth is possible in high purity materials, when anisotropy of the grain boundary energy or mobility is high [21]. It was for example observed by Jung *et al.* [48] on barium titanate that the sintering atmosphere plays a significant role on the nature of the grain boundaries, a faceted one leading to a more pronounced abnormal grain growth compared to a rough one. In addition, dislocations and liquid phase may promote abnormal grain growth [21; 22]. In the present case, exaggerated grain growth may have two origins: (i) a possible chemical reaction between the ceramic layer and the metal, leading to a modification of the sintering and grain growth behaviours or (ii) a mechanical effect related to the tensile stress acting on the grain boundaries and leading to a different microstructure evolution.

Considering chemical effects, abnormal grain growth is favoured by the presence of liquid phase, small grains or anisotropy in grain boundary energy [21]. The presence of impurities controlling the structure of the grain boundary may also play a role [21; 35]. It has been reported in the literature that metal can diffuse from the electrode into the oxide layer. For example, silver contaminates LTCC glass ceramic materials above 900 °C [378]. Platinum may also be found in adjacent BST when produced by sol-gel method [379]. However, SEM pictures (Figure 5.1-9) complemented by SIMS analysis (Figure 5.1-10) ruled out the possible reaction between BLT and the Pt foil, as no indication of reaction/diffusion was found. Furthermore, in the case of the BLT film on the rigid BLT substrate, only mechanical effects related to contact roughness and interdiffusion can be at the origin of enlarged grain growth.

Additionally, a closer look at the grain boundaries of BLT bulk and film was enabled by TEM. No traces of a liquid phase could be found in both types of samples, as shown in Figure 5.1-11. Both samples present clean grain boundaries and triple points, with no evidence of a wetting liquid phase and residual liquid pockets. In this way, the presence of a liquid phase as the origin of the enhanced grain growth observed for the films can also be eliminated.

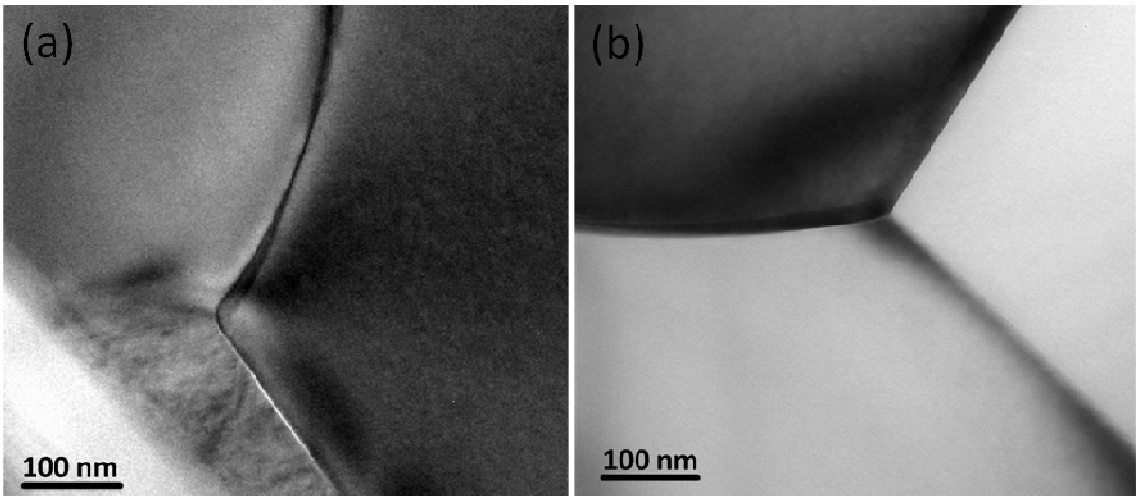

Figure 5.1-11: TEM micrographs of (a) film on Pt and (b) bulk sample sintered for 180 min at 1500 ˚C. Film and bulk samples present clean grain boundaries and triple points, with no evidence of a wetting liquid phase or residual liquid pockets.

Concerning the mechanical stress argument, one has to recall that only grain boundary curvature is involved in classical descriptions of grain growth mechanisms and mechanical stress does not play a role in this process. Nevertheless, this assumption has to be examined in more detail and is in some cases contradicted by experiments and theory. The fact that tensile stresses may affect grain growth behaviour by accelerating grain boundary movement has to our knowledge not been reported for ceramic layered systems. But if this hypothesis is correct, the tensile stresses should be increased by increasing the rigidity of the substrate, which should lead to a higher effect on microstructure evolution. This is indeed what is observed in the present study when comparing the microstructure development of BLT films on Pt foils and BLT films on BLT rigid substrates. Films sintered on rigid BLT substrates, for similar final density (97% after 180 min at 1500 ˚C, Figure 5.1-4 (a)) achieve a higher median grain area (Figure 5.1-8) than the films sintered on Pt foils under similar conditions. This indicates that the mobility of the grain boundaries, or the driving force for atomic transport responsible for the anisotropic grain growth, is higher in the case of higher tensile stresses caused by a stiffer substrate.

Several research groups have been focusing their efforts on the consequences of applied stress on the grain boundary motion of metals and, not as often, ceramics. In particular, Winning *et al.* [380; 381] could show on planar and curved grain boundaries in aluminium bi-crystals that a stress acting on a grain boundary affects its mobility. A flat grain boundary without loading remains immobile, while it begins to move under a stress as low as 10^{-1}-10^{-3} MPa and at temperatures between 200 and 650 °C. In the case of pure metals, a grain boundary can be assimilated as an arrangement of dislocations. Under a mechanical shear stress these dislocations will move by means of glide/climb mechanism, causing the whole boundary to move. The misorientation angle of the dislocations does not seem to play a major role. In the case of nanocrystalline aluminium thin film, it was even possible to trigger significant grain growth at room temperature, under a tensile stress of several hundreds of MPa [382]. Phase field model, taking into account microelasticity describing the interactions between neighbouring grains with different crystalline orientations and elastic response, also describes the effect of stress on grain growth of copper [383]. Softer grains grow at the expense of harder ones, leading to the conclusion that texture could be controlled by an external load.

For ceramics, very few works report on the dynamic grain growth for dense materials under large strain levels [384; 385]. Reference work on the topic was provided by Besson and Abouaf [386; 387]. They observed for 99.98% pure polycrystalline alumina and consolidated by HIP that stress could favour exaggerated grain growth. The final grain size was proportional to the applied stress (up to 200 MPa). They also showed that pressure has no effect on already dense specimens and proposed that damage introduced during densification in the form of point defects or dislocations is healed by grain growth. One has to recall that, usually, pressure-assisted sintering of ceramics including alumina (like sinter-forging [106] or hot-pressing [388]) leads to a reduced grain size when compared to free sintering, as densifying mechanisms are enhanced under pressure while coarsening ones are not modified. Their model relies on the concept of power density produced by viscoplastic deformation and can be applied to porous materials. According to the authors, the damage in material induced by HIP is recovered by grain growth.

Measurement or prediction of the stress developing in the layer is definitively required in order to validate this approach. The difficulty here is that the tensile stress is not constant [389]. Figure 5.1-8 indicates that grain size saturates after long dwell time: in the case of constrained films, this can be rationalized by the fact that the tensile stress is expected to decrease in the final stage of sintering, as it is proportional to the sintering rate. In the case of hot pressing, this was explained by the exhaustion of damage induced by stress and released by grain boundary motion.

From a more general point of view, the grain boundary mobility and the dependence of the mobility on the stress state will depend on the sintering material (chemical and structural nature) and on the characteristics of the grain boundaries (structure, impurities, liquid phases). This may be the reason why in the case of BLT films an effective grain growth when compared with the bulk is observed, while in the case of other materials such as alumina [112] or gold [93] this effect was not observed. In order to consolidate our understanding, systematic investigation of the effect of stress during sintering should be undertaken, including macroscopic shrinkage and microstructural characterization. The investigation of the large microstructure anisotropy developed during constrained sintering of BLT films is presented in the following text.

5.1.3.3 Pore and grain anisotropy

SEM cross-section microstructures of BLT films on PT in the green state and sintered at 1500 °C for several isothermal times (0, 60, 120 and 180 min) are presented in Figure 5.1-12 and Figure 5.1-13 (a). In the micrographs of the sintered films, Figure 5.1-12 (b) to (d) and Figure 5.1-13 (a), the platinum substrate is visible at the bottom. The evolution of densification and grain coarsening can be followed in these images.

The SEM cross-section micrograph of the green film (Figure 5.1-12 (a)) shows a homogenous and well packed film with green density, ρ_0=49%. The maximum dimension of the initial particles is near 2 µm and agglomerates constituted of finer grains are observed, as illustrated in the inset in Figure 5.1-12 (a). A median major axis of 0.31 µm and median aspect ratio of 1.82 µm were determined for grains, revealing

some anisometry already in the powder state. Regarding the sintered films, the attained relative density, ρ, ranged from 65% at the beginning of the isothermal time (0 min, in Figure 5.1-12 (b)) up to 96% at the end of the 180 minutes sintering cycle (Figure 5.1-13 (a)).

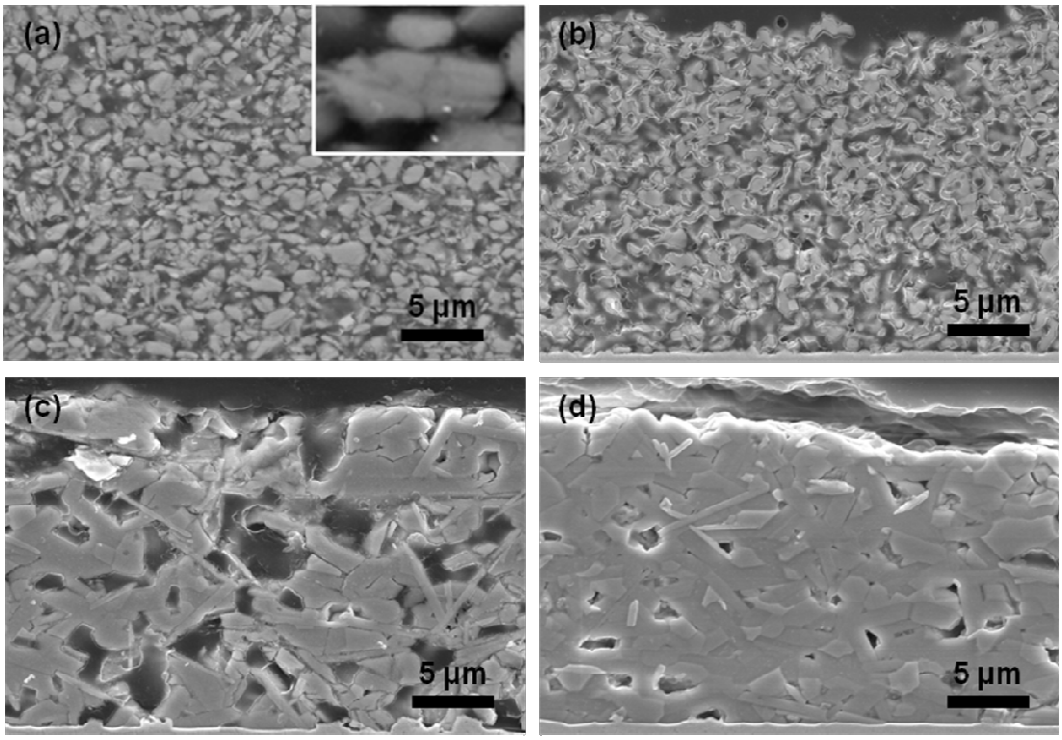

Figure 5.1-12: SEM cross-section micrographs of BLT films: (a) homogenous and well packed green film, ρ_0=49% (inset shows particles constituted by agglomerates of finer grains); films sintered at 1500 °C for (b) 0 min, ρ=65%, (c) 60 min, ρ=83% and (d) 120 min, ρ=91% (the platinum substrate is visible in the bottom of the pictures). The evolution of densification and grain coarsening can be followed.

The sintered films were well adherent to the Pt substrate. No evident porous layer was detected near the substrate, in contrast with previous observations in constrained alumina films or LTCC [85; 87] where a porous layer close to the substrate could be identified; in our case, the pores seem to be uniformly distributed through the thickness of the films.

Grains present a needle shape (in the cross-section, due to the section of the platelet shaped grains) with high aspect ratio and this grain elongation tends to increase with sintering time. Figure 5.1-13 presents the cross-sections of BLT film deposited on Pt substrate (Figure 5.1-13 (a)), a bulk sample (Figure 5.1-13 (b)) and BLT film on dense BLT substrate (Figure 5.1-13 (c)) all sintered in the same conditions of temperature and time (1500 °C, 180 min).

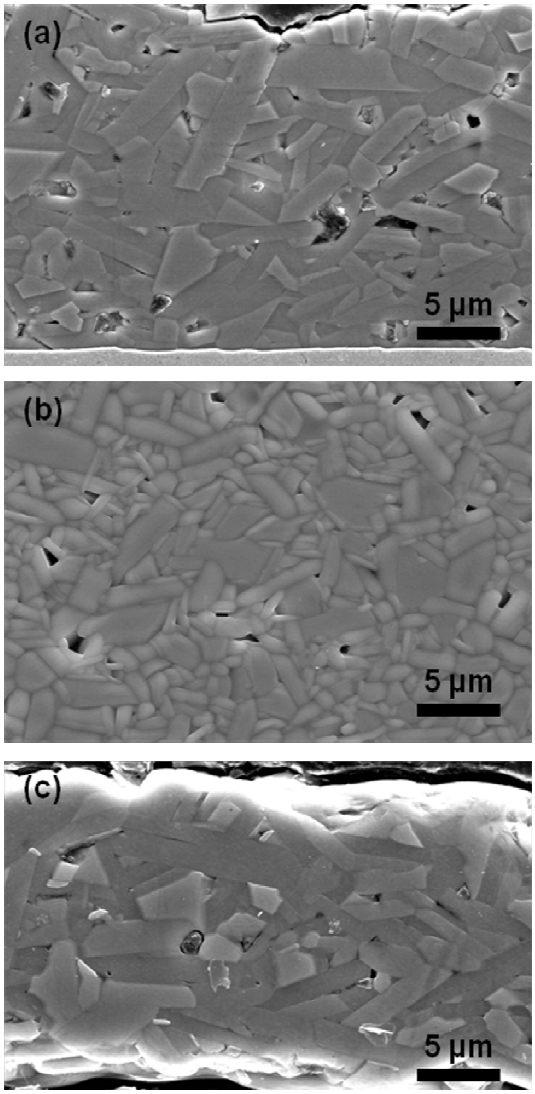

Figure 5.1-13: SEM cross-section micrographs of BLT samples sintered at 1500 °C for 180 min (ρ=97±1%): (a) film on Pt; (b) bulk and (c) film on BLT. Grain size and elongation increase with the degree of constraint.

Equivalent relative density of ρ=97±1 % was obtained for all the samples but different microstructures are observed: grain size and elongation seem to increase with the degree of constraint. A quantitative analysis of the microstructure is presented and discussed in the following sections.

The variation of the median grain area with the relative density (sintering trajectory) for constrained films and free bulk is depicted in Figure 5.1-14. Because sections of the grains have an elongated shape, the grain area was chosen as a more representative parameter for the quantification of the grain size. Although starting with the same initial particle size and similar green packing, films and bulk followed different sintering trajectories. In fact, at final density, the median grain area of the freely sintered bulk sample is 10 times larger than the initial grain area, whereas a ratio of 22 and 30 is found for the constrained films on platinum and BLT, respectively.

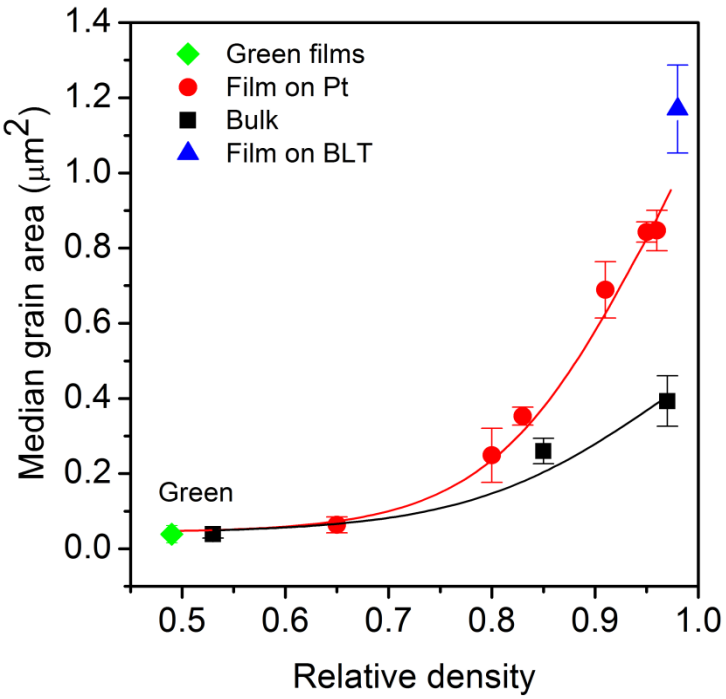

Figure 5.1-14: Median grain area as a function of the relative density for films and bulk. Despite the similar green state, films and bulk followed different sintering trajectories. Median grain area increases with the substrate constraint and even more for the rigid BLT substrate.

It can be seen in Figure 5.1-15 that the density of pores and median pore area in BLT/Pt samples decrease regularly when varying the density from 80 up to 96% (for densities lower than 80% the pore analysis was not performed because pores form a continuous network). The density of pores and median pore area determined in the bulk and in the BLT film on BLT substrate are also represented. The points regarding these samples lie close to the extrapolated lines defined by the BLT/Pt samples.

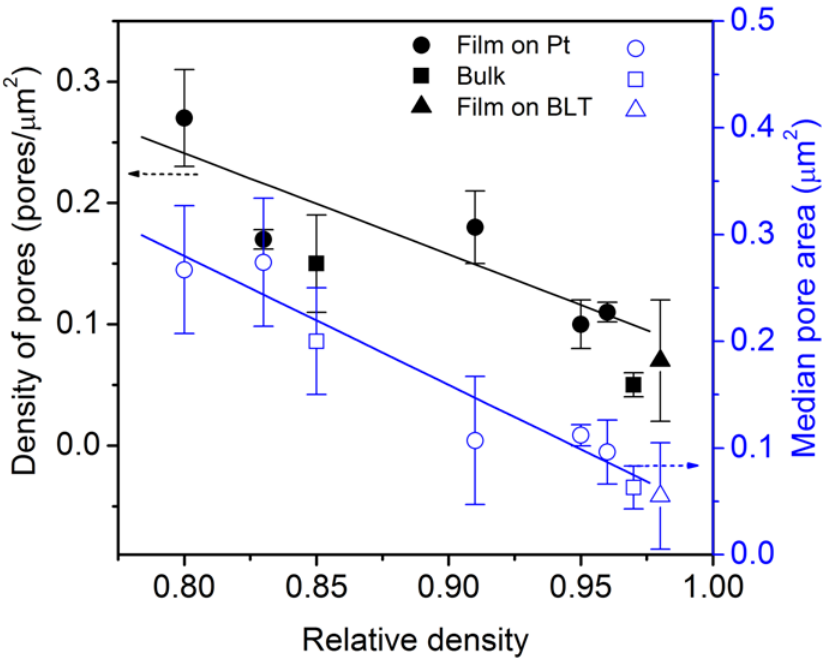

Figure 5.1-15: Density of pores and median pore area as a function of the relative density for films and bulk (trend lines for the film on the Pt substrate are drawn). The density of pores and median pore area in BLT/Pt samples decrease regularly with increasing density.

The variation of the grains and pores median aspect ratio with the relative density is presented in Figure 5.1-16. The more rigid the substrate is, the more elongated the grains and pores are. A similar observation has been reported for $BaNd_2Ti_5O_{14}$ [164], where needle shaped grains with high aspect ratio were present in films but not in free sintered bulk. The grain size, Figure 5.1-14, and grain aspect ratio, Figure 5.1-16, in 97% dense bulk BLT have values equivalent to those met in the films on platinum at a

lower density of 80-85%. In constrained films, the median aspect ratio of the pores also increases for high densities, although to lower values than for grains. In bulk samples the pores show a lower aspect ratio, revealing a shape similar to that in films with low densities. This shows that, as observed for grains, pore shape is different in constrained films and freely sintered bulk samples, being more anisometric in the case of films.

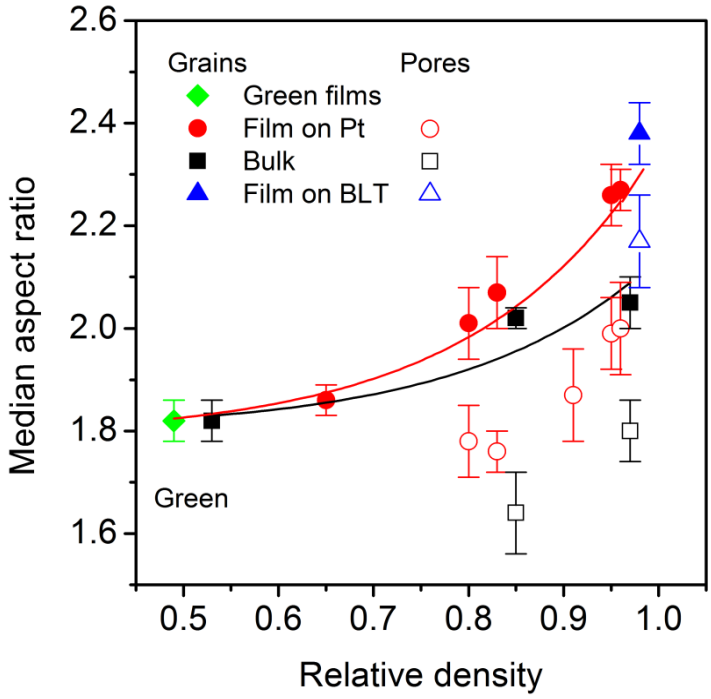

Figure 5.1-16: Median grain and pore aspect ratio as a function of the relative density (trend lines for the median grain aspect ratio in the film on Pt substrate and in bulk are drawn). Grains and pores elongation is higher in films than in bulk and increases with the rigidity of the substrate.

Figure 5.1-17 and Figure 5.1-18 illustrate the evolution of the grain orientation distribution as function of relative density for films and bulk. The represented weighted cumulative length, corresponding to the length multiplied by the aspect ratio of grains or pores is an interesting parameter because it exaggerates the contribution of the more elongated entities, better reflecting any anisotropic orientation. First, it is

important to notice that the green state is not isotropic, neither for films or bulk (Figure 5.1-17 (a)). Particles are indeed initially not isometric but have an aspect ratio of 1.8. By electrophoretic deposition or uniaxial pressing these elongated crystals can be oriented parallel to the substrate or perpendicular to the load. Interestingly, green compacts show a similar microstructure, which facilitates comparison between films and bulk (Figure 5.1-17 (a)). In the films on Pt, this tendency to particle/grain alignment parallel to the substrate, i.e. in-plane, increases with density (Figure 5.1-17 (b) and Figure 5.1-18). For high densities (96%) (Figure 5.1-17 (b)) only a small fraction of grains have orientation close to the vertical direction, i.e. out-of-plane. A high degree of grain orientation is also observed for films on BLT rigid substrates (Figure 5.1-17 (d)), whereas in the bulk sample, even at 97% of relative density (Figure 5.1-17 (c)) grains remain less oriented, with a distribution similar to the one obtained in the green state (Figure 5.1-17 (a)).

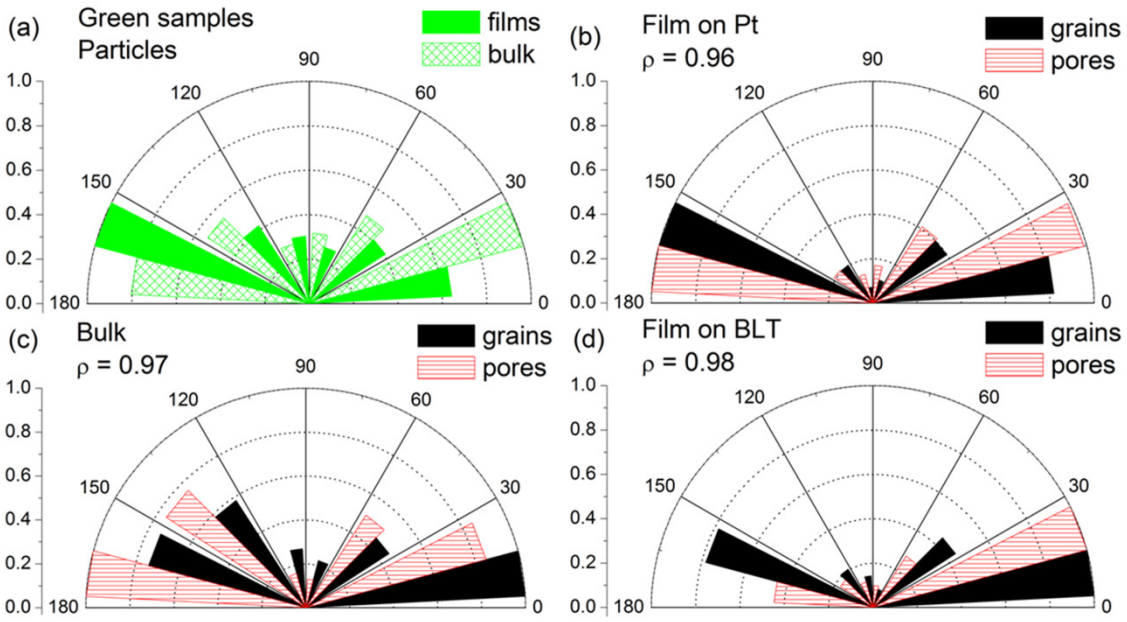

Figure 5.1-17: Grain and pore orientation distributions (cumulative lengths) for BLT (a) films and bulk green samples and sintered samples at 1500 °C for 180 min: (b) film on Pt, (c) bulk and (d) film on BLT. In the films, grains and pores tend to in-plane orientation. In the bulk sample, grains and pores are less oriented.

Similarly, pore orientation distribution is given in Figure 5.1-17 and Figure 5.1-18. The tendency to in-plane orientation is also present in the constrained films and also increases with the density, in close relation with the behaviour of the grains. Once more, dense bulk samples show lower anisotropy in the pore orientation than films, in agreement with the results obtained for grains.

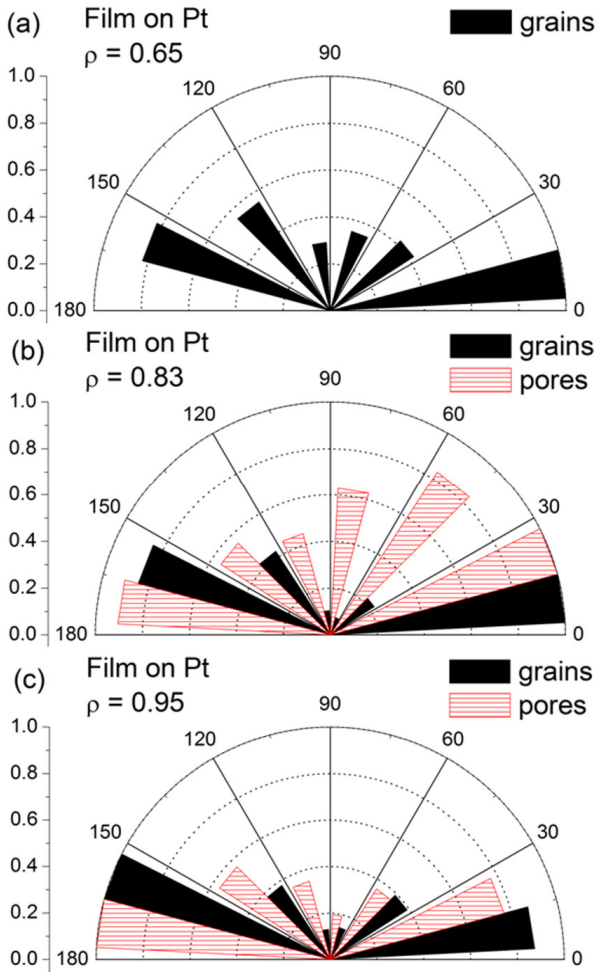

Figure 5.1-18: Grain and pore orientation distributions (cumulative lengths) for BLT films on Pt substrate along densification at 1500 °C for (a) 0 min, (b) 30 min and (c) 120 min. Grains and pores in-plane orientation increases along densification.

A quantification of the degree of orientation extracted from the orientation distributions of grains and pores is presented in Figure 5.1-19. This orientation factor

corresponds to the fraction of weighted cumulative lengths of grains or pores with orientation in the ranges 0° - 30° and 150° - 180°, i.e. oriented almost parallel to the substrate. Within this criterion, a random orientation would correspond to an orientation factor of 0.33.

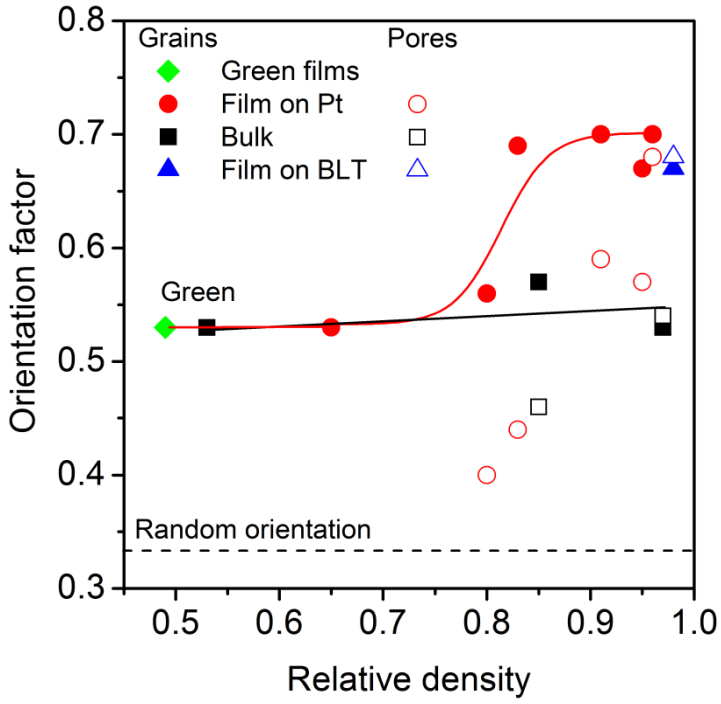

Figure 5.1-19: Grain and pore orientation factor as a function of the relative density for films and bulk. In the films, the orientation factor strongly increases with density, whereas in the bulk sample the orientation factor is nearly constant until the end of densification.

It is very interesting to see that, in spite of a similar degree of particle orientation in the green state, film and bulk samples reveal strongly different evolutions. The grain orientation factor of the constrained films increases with increasing density to around 70% of grains oriented in-plane at high densities. In contrast, the bulk sample shows only a slight increase of the grain orientation factor from the green state until the end of densification. While particles present some degree of orientation at low densities, the corresponding orientation of pores is less marked at low densities. But, like grains,

pores become more horizontally oriented with increasing density, reaching an orientation factor similar to the one of the grains when the microstructure enters the final stage of sintering.

5.1.3.3.1 Discussion

Clear changes in particle and pore shape and orientation have been quantitatively measured for BLT films. While the preferential orientation of grains due to the reduction of neck growth under tension or effect of stress on the grain boundary motion is more expected, the orientation of pores along the substrate needs to be rationalized. This strongly contrasts indeed with the results on STO on the previous chapter and with observations made on zirconia, alumina and LTCC constrained layers [85; 111; 112; 116; 375] for which preferential orientation of pores along the thickness direction was noticed. In those previous results, only limited grain growth took place (final grain size up to 5-6 times the initial particle size). Only for glass-ceramic composites, smaller pores in partially constrained films followed, to a lesser extent, the orientation of alumina filler particles as they remained attached to them [111]. The existence of a strong correlation between grain and pore anisotropy in BLT films and their orientation parallel to the substrate needs to be further understood.

The degree of grain orientation of films on Pt starts to increase sharply as soon as strong grain growth takes place (for relative density values higher than 80%, as shown in Figure 5.1-14). This orientation is thus not related to anisotropy in interparticle contact area (necks) or reorientation of grains, but really to grain growth, i.e. grain boundary motion. And, whereas grain orientation factor stagnates, pore orientation factor increases rapidly in this density range with more elongated pores attached to plane solid/vapour interfaces. Logically, sintered films on BLT rigid substrates and bulk samples show a higher and lower degree of anisotropy, respectively, in spite of similar initial density and microstructure.

Platelet particles are characteristic of BLT powders due to the anisotropy in the lattice parameters, a morphology that is retained in the sintered ceramics [181]. As reported by

Zheng *et al.* [146] most of the grains in the bulk ceramics were aligned normal to the pressing direction applied during sample forming. In agreement with these observations, our results also show some grain orientation in bulk but an even more pronounced one in the constrained sintered films. Initial orientation is favoured by the elongated shape of the particles combined with the shaping process. Nevertheless, this argument does not account for the net increase in anisotropy during constrained sintering.

The correlation between the orientation of grains and pores must be induced by the grains, which are more oriented than pores (from the beginning of densification). So, as densification takes place, grains are increasingly growing in a more oriented way, driving the pore orientation, too. Similar observation was reported by Ollagnier *et al.* [11] for LTCC materials. Alumina filler particles poorly wet by the glass matrix phase were also more oriented than pores and controlled the anisotropy.

The strong interaction between the grains and pore trajectories can be clearly seen in Figure 5.1-20, considering the well known Zener relation [390]:

$$G = \beta \frac{r}{f_{inc}} \qquad (5.1\text{-}3)$$

where G stands for the average limiting grain size, r for the average inclusion or pore size, f_{inc} for the inclusion volume fraction (or porosity in the case of pores) and β for a numerical constant dependent on the inclusion distribution features, assuming spherical shape. This equation is usually valid for pores in the intermediate stage of sintering, which are essentially immobile, and for final stage whenever the condition of pore immobility can be verified [390; 391]. Deviations from the spherical shape and pore orientation lead to the increase of the grain boundary-pore contact and, consequently to the raising of the pinning pressure [392].

The trend line in Figure 5.1-20 was drawn only with points corresponding to films on Pt, although the points from bulk samples and films on BLT rigid substrates fall near the line. From the slope of this line a Zener constant value, β=0.2, could be determined. This value is much lower than what has been already reported for other

systems where no significant anisotropic effects are observed; for instance, values ranging from 1 to 5 were experimentally determined for CoO [393], NaF [394] and Mn doped ZnO [395].

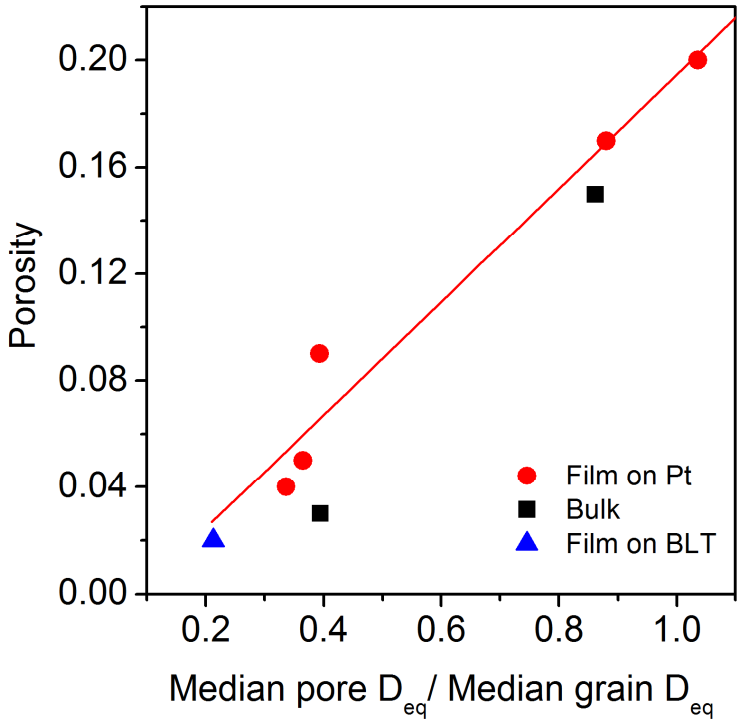

Figure 5.1-20: Porosity as a function of the ratio pore to grain size (a trend line was drawn for points corresponding to the film on Pt substrate).

The low value of the Zener constant means a very effective pore pinning effect during grain growth which will contribute to the increase of anisotropy by the following mechanism: first, BLT films present already some grain orientation in the green state which seeds oriented grain growth and, consequently, pore orientation accompanying the grain growth; second, grain growth enhancement is triggered during constrained sintering by the tensile in-plane stress, which increases grain boundary motion and leads to a significantly larger and wider grain size distribution; and third, the preferential pore orientation parallel to the substrate increases the pinning pressure in the grain boundaries with equivalent orientation, restraining more effectively its

movement and therefore increasing the particle orientation and aspect ratio during grain growth.

Taking this into account, the observed increased grain and pore anisotropy during sintering must be mostly dependent on the grain growth and the final grain size will determine the attained degree of anisotropy. In Figure 5.1-21 the representation of the grain shape factor as function of the median grain area shows very clearly that all the values from BLT films and bulk fall in the same trend line defined by films on Pt. This confirms the previous statements on the development of anisotropy, independently of the possible geometrical constraints present during sintering.

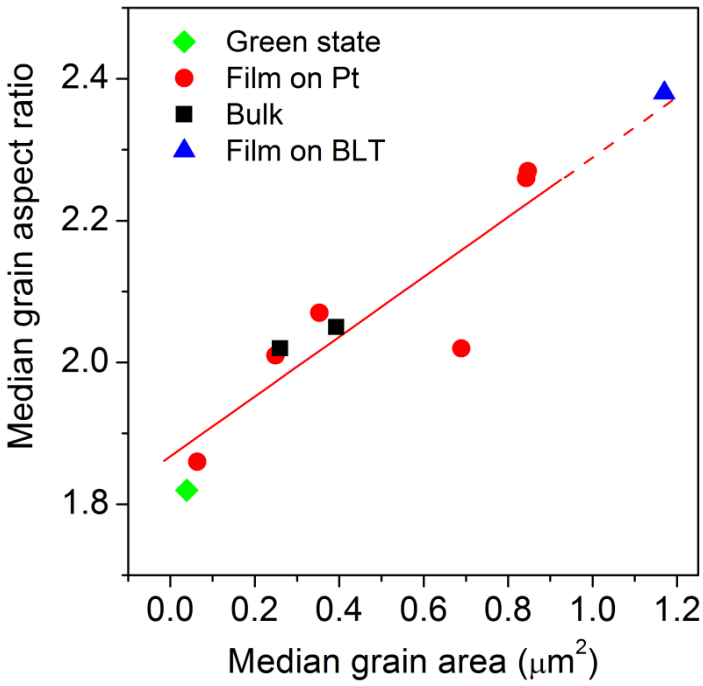

Figure 5.1-21: Dependence of the median grain aspect ratio on the median grain area. All the values from BLT films and bulk fall in the same trend line.

The effect of chemical reaction between films and substrate on the grain growth has been discarded by chemical analysis and by the large grain growth for BLT films on dense BLT. The presence of a wetting liquid phase was also ruled out by TEM

observation of grain boundaries and triple points. As initial microstructures and densities are similar for all samples, the reason for the increased grain growth kinetics must therefore be related to the stress developing during constrained sintering.

5.1.3.4 Texture

The microstructural analysis of grain orientation in constrained sintered films and freely sintered bulk samples revealed a similar particle orientation in the green state in films and bulk and a very different evolution of grain orientation during sintering. Indeed, grain orientation parallel to the substrate significantly increased during the constrained sintering of the films, leading to highly anisotropic microstructures. On the other hand, such increase was not verified in the bulk samples, which revealed much more random microstructures. This difference was attributed to the effect of the stress from the substrate in the constrained sintering of the films.

Such preferred grain orientation particularly marked in the films may be expected to correspond to a non-random preferred crystallographic orientation, called texture. Therefore, the microstructure texture was investigated by XRD in BLT films constrained sintered on Pt and compared to bulk samples.

Figure 5.1-22 illustrates the position of the films and bulk samples in the XRD texture measurements relatively to the X-ray beam. As shown, the top surface of the films and the equivalent bulk surface, which is that perpendicular to the pressing direction, were analyzed. In this way, a crystallographic orientation of 0˚ corresponds to the direction parallel to the substrate in the case of films and to the perpendicular to the pressing direction in the case of bulk samples.

The presence of a strong texture can be described by the width of the orientation distribution function which can be approximately determined by a rocking curve of the sample with the XRD detector fixed at the corresponding diffraction angle 2θ. The smaller the Full Width at Half Maximum (FWHM) of the rocking curve, the better the orientation of the textured sample.

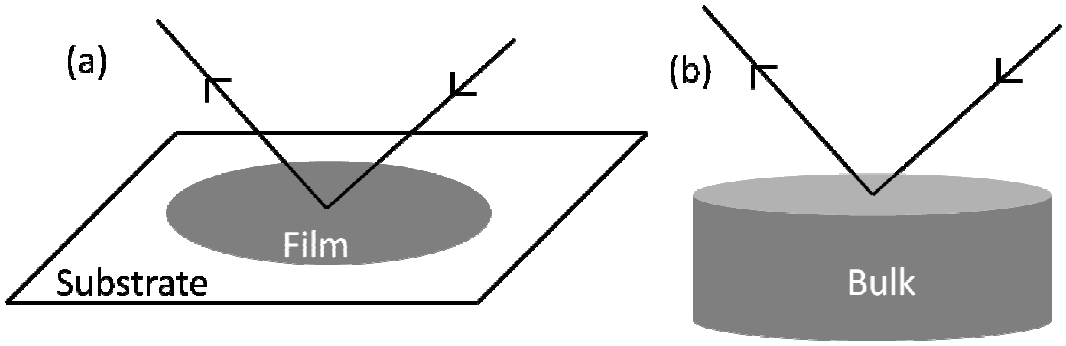

Figure 5.1-22: Schematics of the position of (a) films and (b) bulk samples in the XRD texture measurements.

Figure 5.1-23 presents rocking curves around the Bragg angle corresponding to the (110) plane ($2\theta = 32.13^{\circ}$) for green and sintered (180 min) BLT films and bulk samples.

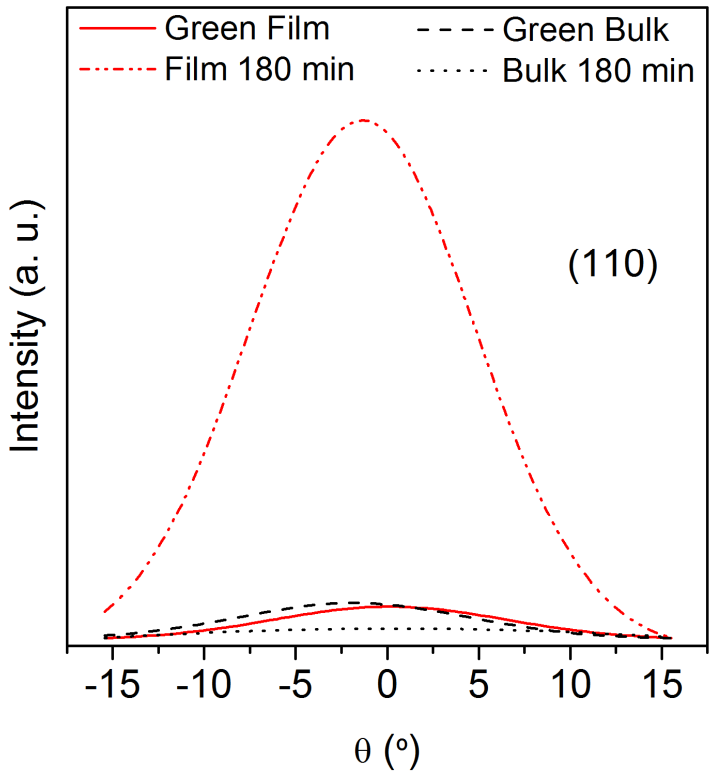

Figure 5.1-23: Rocking curves around the Bragg angle of the (110) plane for films on Pt and bulk samples. Film and bulk green samples are very similar but the texture evolution during sintering is markedly different.

An important observation is that, despite the different processing routes, the rocking curves of the green samples (films on Pt and bulk) are practically equivalent. In fact, the FWHM of the curves is 18˚ and 17˚ for the green film and green bulk, respectively. These results confirm the previous quantification of particle orientation (Figure 5.1-19) that revealed similar bulk and film samples in the green state. Additionally, and again in agreement with the previous SEM microstructure observations, a small broad peak is observed in the curves of the green samples showing some degree of orientation already at the green state.

Furthermore, the sintered films show a severe increase of the peak towards an FWHM of 14˚, which reveals a strong texture increase during constrained sintering. On the other hand, the rocking curve of the sintered bulk sample shows a very broad peak (with a FWHM of 29˚), suggesting a reduction in the degree of texture relatively to the green sample.

A more detailed texture analysis can be made using X-ray pole figures. Pole figures register the variation in the diffracted intensity with respect to direction in the specimen. A pole figure is a two-dimensional projection of the three-dimensional probability of finding a pole to a lattice plan (*hkl*) in a certain sample direction [297]. The principle is simple: in order to determine the orientation of a given lattice plane of a single crystallite, the detector is first set to the proper Bragg angle, 2θ of the diffraction peak of interest, then the sample is rotated in a goniometer until the lattice plane (hkl) is in the reflection condition (i.e. the normal to the lattice plane is the bisectrix between incident and diffracted beam). In the case of a polycrystalline sample, the intensity recorded at a certain sample orientation is proportional to the volume fraction of crystallites with their lattice planes in reflection geometry.

Figure 5.1-24 presents (110) pole figures of green and sintered BLT films and bulk samples. The centre of the pole figures corresponds to 0˚ inclination of the (110) plane with the sample surface and the lines to 30˚, 60˚ and 90˚, respectively, from the centre to the border of the figures.

Regarding the green samples, the previous observations are again confirmed. The projected piercings of the (110) plane are mainly grouped in a central band in both

films (Figure 5.1-24 (a)) and bulk (Figure 5.1-24 (b)) green samples. This observation shows once more that there is already some crystallographic preferred orientation in the green state and, more importantly, confirm that both samples are similar at the starting point.

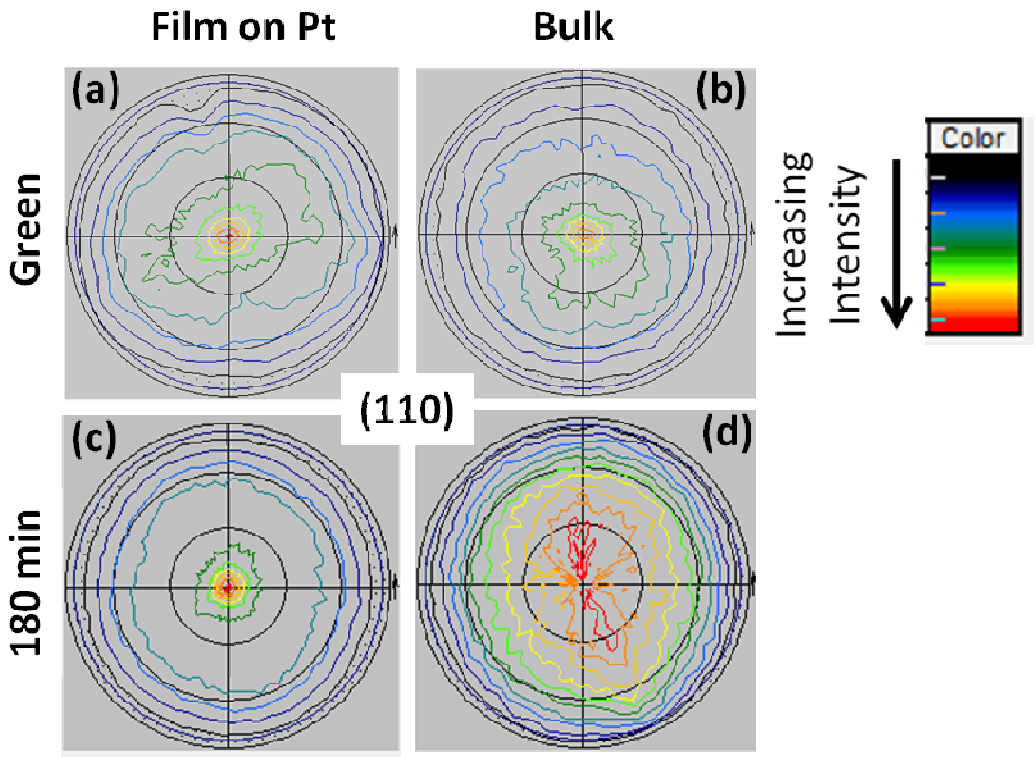

Figure 5.1-24: X-ray (110) pole figures for (a) and (b) green and (c) and d) sintered BLT films and bulk samples. Green films and bulk samples have similar degree of texture but sintered films are much more textured than sintered bulk specimens.

On the other hand, (110) pole figures of the sintered specimens of films and bulk, in Figure 5.1-24 (c) and (d), respectively, are very different. Regarding the films, the high diffracted intensity is even more concentrated in the centre of the pole figure, corresponding to a 0˚ inclination of the (110) plane relatively to the sample surface (which is parallel to the substrate).

These results are in agreement with the previously described SEM observations and with the rocking curves in Figure 5.1-23. Moreover, a similar textured microstructure on $BaNd_2Ti_5O_{14}$ EPD thick films was reported by our group [19]. A (*hk*0) preferred orientation of BNT thick films was observed, which increased with the sintering temperature.

Concerning the bulk sample, the projected piercings of the same plane are much more disperse; there is a high diffraction intensity corresponding to a wide range of crystallographic orientations. These observations strongly suggest a more random microstructure of the bulk samples than that of the films, corroborating the previous observations of SEM microstructures and rocking curves.

In addition, in Figure 5.1-25 (a) the (100) pole figure of the sintered films shows a high diffraction intensity recorded for around 45˚ of the (100) plane with the sample surface. This result is in conformity with the 0˚ inclination of the (110) plane presented above. Furthermore, it fits the illustration of the predominant crystallographic orientation parallel to the substrate in the sintered films displayed in Figure 5.1-26, taking as example one crystallographic hexagonal unit cell. The longest *c-axis* is then parallel to the substrate, consistent with the grain orientation observed by SEM in the cross-section microstructures.

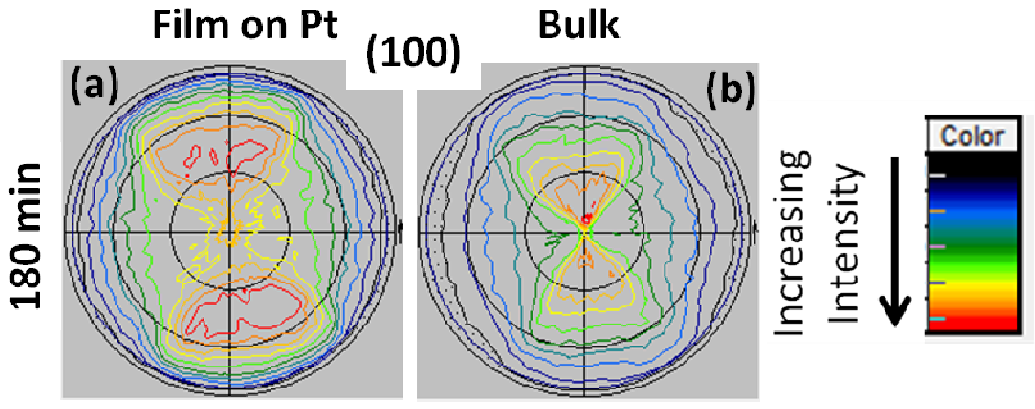

Figure 5.1-25: (100) pole figures for BLT (a) film on Pt and (b) bulk samples sintered for 180 min.

On the other hand, the (100) pole figure of the bulk sample shows lower intensity peak and the relatively higher intensity regions in the pole figure are located closer to 0˚ than in the case of films. These observations indicate a lower degree of texture for the bulk samples and, unlike films, in bulk samples the tendency of (100) planes to orient closer to the perpendicular to the pressing direction is lower.

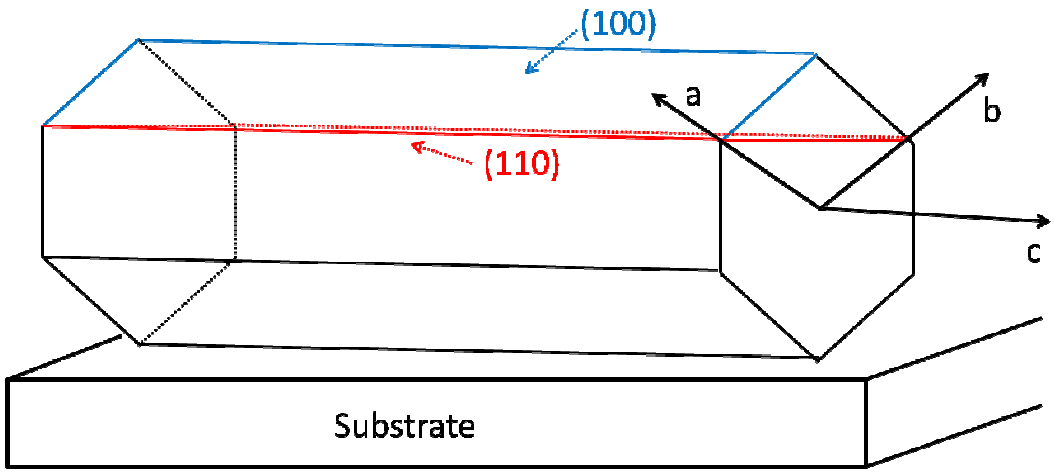

Figure 5.1-26: Schematic illustration of the in-plane crystallographic orientation of BLT films.

The texture analysis undoubtedly demonstrates that, in the green state, films and bulk samples have a similar degree of particle orientation but, during sintering, the texture evolution is very different. Indeed, in the sintered samples most of the crystallographic (110) planes in the films are oriented with 0˚ (parallel) to the substrate, whereas the same planes in the bulk show a nearly random orientation. It is shown that the microstructural anisotropy is accompanied by a crystallographic texture, which is much more striking in the constrained films than in the freely sintered bulk.

5.1.3.5 Dielectric properties

The relation between the anisotropic microstructure resulting from constrained sintered of BLT films and the dielectric properties was also investigated. The dielectric properties of BLT films on Pt sintered at 1500 ˚C for 120, 180 and 720 min were measured from room temperature to 120 ˚C and compared to those of bulk sintered in the same conditions for 180 min. In this way, the temperature stability of the dielectric properties of the material can be assessed and correlated with the microstructure anisotropy above presented.

With increasing sintering time from 120 to 720 min, the median grain area increases from 0.84 to 1.49 μm^2 and median grain aspect ratio from 2.26 to 2.64. Similarly, an increase of the grain orientation factor from 0.64 to 0.76 is verified.

The data presented in the following figures regarding the dielectric properties is the result of fitting averaged values from more than three experimental runs. The experimental deviations are under 5%.

Figure 5.1-27 shows the dependence on the temperature, between 30 and 120 ˚C, of the relative permittivity at 100 kHz (measured in the direction normal to the substrate plane or parallel to the pressing direction) for films on Pt and bulk. The relative permittivity of films is always slightly lower than the permittivity of bulk specimen (ε_r=49). Since the density of all samples is equivalent (maximum difference of 2%) and no porosity layer near the substrate was observed in films, this decrease of the permittivity is probably related to the anisotropic microstructure described above which is maximized in the films.

In fact, as given in Table 5.1-1 for comparison with the present results, Zheng *et al.* [146] reported the dependence of the electrical response on the anisotropy of the microstructure of BLT ceramics. Different values for the relative permittivity were obtained depending on the direction of the measurement, normal or parallel to the pressing direction, corresponding to different grain orientations [146].

Similar behaviour was also observed in $BaNd_2Ti_5O_{14}$ thick films [19]. The authors reported needle shaped grains and a decrease of the permittivity with the increase of the

sintering temperature and consequent increase in grain aspect ratio, which was attributed to the polarization dependence on the crystal growth anisotropy [19], in agreement with the present results for BLT thick films.

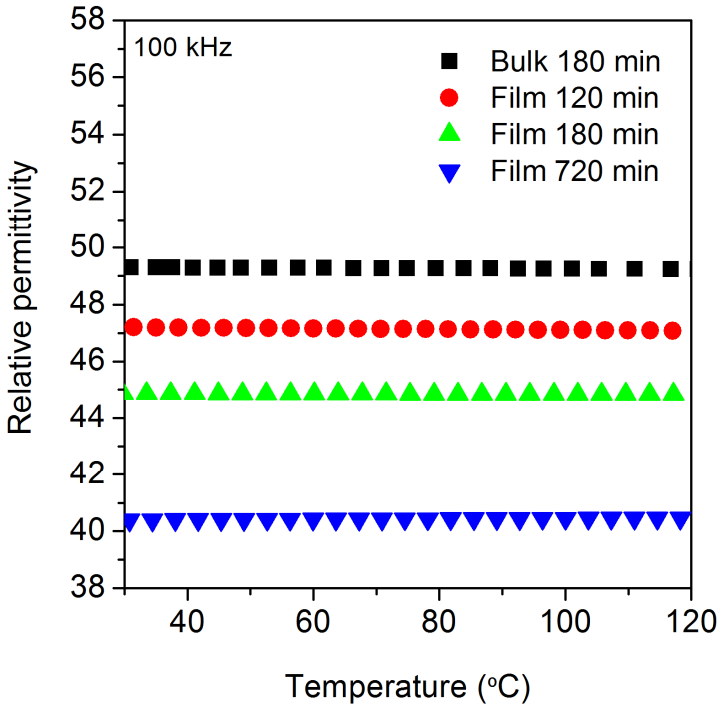

Figure 5.1-27: Relative permittivity dependence on the temperature at 100 kHz for bulk and film samples. The permittivity of BLT is very stable with the temperature and slightly decreases with the isothermal time.

Worthy of note is the fact that, regarding all bulk and films samples, the permittivity shows almost no variation with the temperature, in the entire temperature range of 25 to 120 ˚C. This is reflected in the temperature coefficient of permittivity, $TC\varepsilon_r$, plotted in Figure 5.1-28 (a) as a function of the isothermal sintering time and in Figure 5.1-28 (b) as a function of the orientation factor. $TC\varepsilon_r$ was measured between 30 and 120 ˚C in terms of the parameter defined in equation (2.2-4).

The values of $TC\varepsilon_r$ are very low, between -29 and 18 *ppm*/˚C, indicating remarkable temperature stability and meeting the demands for functional applications. The

coefficients of the bulk and film samples sintered for 180 min are similar, -7 and -8 *ppm*/˚C, respectively. Nevertheless, the evolution of $TC\varepsilon_r$ with the sintering time for the films shows a clear dependence on the microstructural anisotropy. The microstructural changes lead to a variation of the $TC\varepsilon_r$ from negative (-29 *ppm*/˚C, after 120 min) to positive (18 *ppm*/˚C) after 720 min of isothermal sintering time.

These observations show that simply by choosing the appropriate sintering conditions leading to the right degree of microstructure anisotropy is possible to tailor the dielectric response of BLT thick films, namely to obtain temperature-stable zero $TC\varepsilon_r$ BLT films for functional applications.

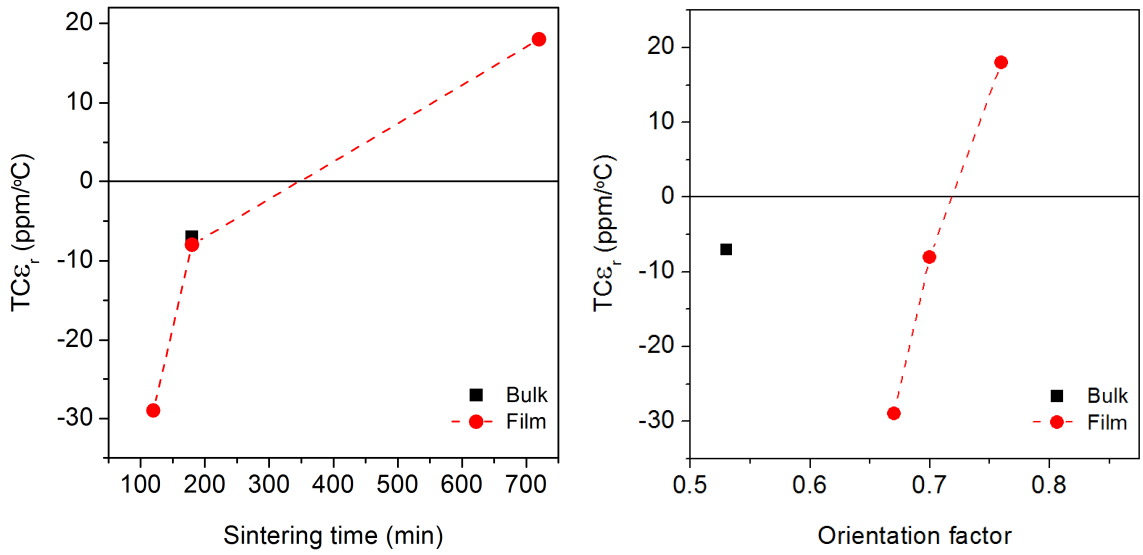

Figure 5.1-28: Temperature coefficient of permittivity, $TC\varepsilon_r$, at 100 kHz as a function of (a) the isothermal sintering time and (b) the grain orientation factor. $TC\varepsilon_r$ reveals a clear dependence on the microstructural anisotropy.

As reported in the literature, $TC\varepsilon_r$ depends on many factors, namely on the tolerance factor [216], ordering of perovskite B-site cations [396] or grain aspect ratio [19]. Additionally, in the case of films, the changes induced by the stresses from the substrate during

constrained sintering, namely the altered evolution of the degree of microstructure anisotropy must be considered. In this sense, the dependence on the degree of anisotropy of the overall dielectric properties, but particularly of the temperature coefficient of permittivity, is expected.

Indeed, the presented results suggest a dependence of the $TC\varepsilon_r$ on increasing degree of microstructure anisotropy developed during constrained sintering in BLT thick films, in agreement with previous observations in $BaNd_2Ti_5O_{14}$ [19], which indicated a change in $TC\varepsilon_r$ as the result of the anisotropy changes in the textured morphology of $BaNd_2Ti_5O_{14}$ films. These previous findings, as well as the present ones, show that the above described effects of the substrate on the sintering films during constrained sintering offer a way of tailoring not only the microstructure of functional materials but also their dielectric response, namely with regard to the fundamental temperature stability quantified by $TC\varepsilon_r$.

Table 5.1-1: Dielectric properties reported for BLT.

	ε_r	$Q.f$ (GHz)	τ_f ($ppm/^{\circ}C$)	Ref.
$Ba(La_{1-y}Al_y)_4Ti_4O_{15}$	44	47000	1.3	[143]
BLT	43	11583	-17	[145]
BLT	49	16222	-13	[144]
BLT	45	43589	-2	[146]
BLT Normal [(a)]	52	--	--	[146]
BLT Parallel [(a)]	42	--	--	[146]
BLT	49	0.004 [(b)]	-7	This work
BLT films	41 to 47	~ 0.001 to ~ 0.006 [(b)]	-29 to 18	This work

[(a)] to the pressing direction. [(b)] $tan\delta$ at 100 kHZ

Regarding the dielectric losses, Figure 5.1-29 presents the loss tangent at 100 kHz as a function of the temperature for bulk and films. Despite some fluctuations, all samples revealed low losses, of the order of 10^{-3}, adequate for low loss applications. There is no obvious relation with the sintering time (or anisotropy development). The measured losses for the samples sintered for 180 min are around 0.006 for films and slightly lower, around 0.004, for bulk. Values of loss tangent around 0.003 were obtained for 720 min of sintering time and below that value for 120 min.

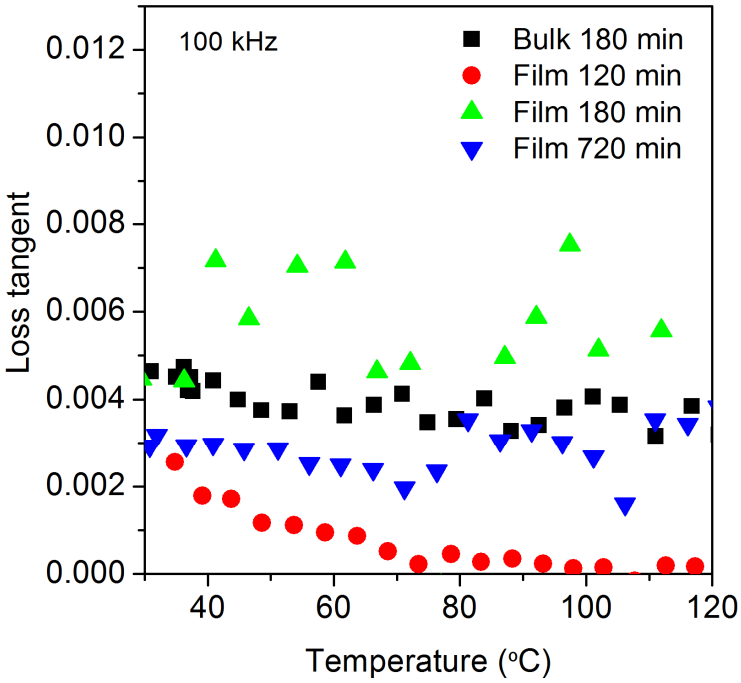

Figure 5.1-29: Loss tangent dependence on the temperature at 100 kHz for bulk and film samples. All samples revealed low losses, adequate for low loss applications.

Other factors that should be considered in the dielectric response of the films is the effect of the interface between film and substrate and the stress exerted by the substrate on the dielectric layer. For example, the effect of stress on the dielectric properties is recognized on STO thin films, which exhibit very different dielectric properties depending on the substrate stress [397; 398]. STO thin films under minimal strain were reported to yield high dielectric constant and low loss tangent while thin

films under either tensile or compressive strain exhibit reduced dielectric constant and high loss [397]. The tunability of epitaxially strained STO thin films was also found to be strongly dependent on the in-plane lattice parameter, showing markedly different behaviour for tensile and compressive strains [398]. Nevertheless, due to the different scale of the film thickness, the case of thick films is of a different nature. Furthermore, the flexibility of the Pt substrate may lead to a reduced stress on the dielectric layer. Therefore, the effect of the stress from the substrate on the present thick films needs further investigation, which may lead to an alternative way of tailoring the dielectric response of functional materials processed in the form of thick films.

5.1.4 Summary

The sintering behaviour of BLT thick films on Pt foils and rigid BLT substrates was addressed in this work. In agreement with previous studies on constrained sintering of ceramic layers, the densification was retarded. However and unexpectedly, constrained films attained a similar final density and showed a significantly larger grain size than their bulk counterparts. These results are even more visible in BLT films sintered on rigid BLT substrates. It is proposed that tensile compatibility stresses induced by the geometrical constraint may increase the mobility of the grain boundaries or the driving force for transport enhancing grain growth.

Anisotropic microstructure with elongated grains and pores oriented parallel to the substrate were developed during the constrained sintering of $BaLa_4Ti_4O_{15}$ thick films, which is not what has been previously observed for other ceramic systems. Although starting from equivalent green microstructures, grain aspect ratio, grain orientation and texture are significantly different in densified films and bulk samples.

There is a strong correlation between grain and pore evolution, which started as soon as grain growth takes place. A stress effect triggering grain growth enhancement as well as a strong Zener pinning effect leads to highly textured microstructures, which is also observed at the crystallographic level.

A dependence of the dielectric response, particularly of $TC\varepsilon_r$, on increasing degree of microstructure anisotropy developed during constrained sintering in BLT thick films was also observed.

Our observations suggest Stress Assisted Grain Growth (SAGG) as a potential technique, alternative to Templated Grain Growth (TGG) [399], to engineer grain boundaries, achieving anisotropic textured microstructures in ceramics with tailored properties.

These results are of relevant importance for technological application of thick dielectric films with a crystallographic texture, because a dependence on the grain anisotropy and size is expected for their dielectric response.

5.2 Constrained sintering and dielectric properties of $Ba_{4.5}Nd_9Ti_{18}O_{54}$ thick films

5.2.1 Introduction

Similarly to the above presented case of BLT, $Ba_{4.5}Nd_9Ti_{18}O_{54}$ (BNT) has an anisometric crystal structure [172; 182]. BNT has a tungsten bronze-type like crystal structure, with an orthorhombic symmetry and unit cell parameters of a = 22.3367(5) Å, b = 7.6738(1) Å and c = 12.1842(3) Å [172]. As previously discussed, the crystallographic anisometry of these materials usually results in elongated plate or needle-like grains [182]. After sintering, the outcome is grain orientation, as well as significant anisotropy of the dielectric properties [19; 164; 182].

Indeed, similar observations were previously reported by Fu *et al.* [19; 164] on a slightly different composition, $BaNd_2Ti_5O_{14}$ (the 1:1:5 composition in the $BaO\text{-}Nd_2O_3\text{-}TiO_2$ system). Increased grain elongation and texture were observed in thick films compared to bulk ceramics. Moreover, the degree of texture and the aspect ratio of the needle-shaped grains in the thick films were strongly increased with the increase of the sintering temperature. Along with the microstructural changes, the dielectric permittivity decreased and its temperature stability was improved, resulting in near-zero $TC\varepsilon_r$ thick films [19]. The increased grain elongation was attributed to a constrained sintering effect.

In the above cited work, Fu *et al.* [19] observed a Ti-rich amorphous phase in the 1:1:5 composition of the $BaO\text{-}Nd_2O_3\text{-}TiO_2$ system, which was attributed to the eutectic $BaTiO_3$ - TiO_2, occurring at 1312 ˚C [400]. The presence of such amorphous phase during constrained sintering was considered to facilitate the anisotropic grain growth under the effect of the substrate [19].

In this work, the constrained sintering of a similar 1:1:4 composition ($Ba_{4.5}Nd_9Ti_{18}O_{54}$) of the $BaO\text{-}Nd_2O_3\text{-}TiO_2$ system is systematically investigated. Despite some controversy, it is accepted that 1:1:4 is the correct proportion of the oxides in the

monophasic BNT composition [19]. By using the BNT 1:1:4 composition, which has a lower fraction of TiO_2, the aim is to reduce the amount of the TiO_2-rich amorphous phase during sintering and therefore to reduce its effect in promoting the anisotropic grain growth. In that way, it is possible to investigate the behaviour of BNT under constraint conditions without such grain growth enhancement factor, or at least, with minimized effects. Similarly to the previously presented case of BLT, the constrained sintering of BNT 1:1:4 EPD thick films on Pt-foil substrates is systematically addressed and compared to equivalent bulk ceramics. The correlation between microstructure anisotropy development and the dielectric properties of BNT 1:1:4 is also attempted.

High density BNT thick films were obtained by EPD and subsequent constrained sintering. The crystallographic anisometry of the material together with a constrained sintering step resulted in elongated needle-like grains and anisotropic microstructures. The effect of the stress from the substrate during the constrained sintering lead to higher degrees of anisotropy in the films than in the bulk samples, despite the equivalent green state of the samples.

Marked effects of the microstructural anisotropy were detected on the dielectric properties of the BNT films. The constraint from the substrate may be used to control the microstructural anisotropy and to tailor the dielectric response of thick films, namely to obtain a temperature stable dielectric response, as previously observed. The present observations on BNT thick films corroborate the results on BLT.

5.2.2 Experimental details

The experimental procedures were previously described in Chapter 3. BNT powders were calcined at 1200 ˚C for 3h. The additive used in EPD suspensions was triethanolamine (TEA), in the concentration of 1 ml of TEA per 100 ml of ethanol. The deposition time was 2 min. The pressed green films and bulk samples were heated at 25 ˚C up to the sintering temperature of 1350 ˚C and several isothermal times were used, from 0 to 720 min. After polishing, the samples were thermally etched at 1250 ˚C for 10 min for SEM observation.

5.2.3 Results and discussion

5.2.3.1 BNT powders

Figure 5.2-1 presents the XRD diffraction pattern of $Ba_{4.5}Nd_9Ti_{18}O_{54}$ powders. After a calcination of 3h at 1200 ˚C, the BNT powders showed a monophasic composition within the XRD technique detection limits.

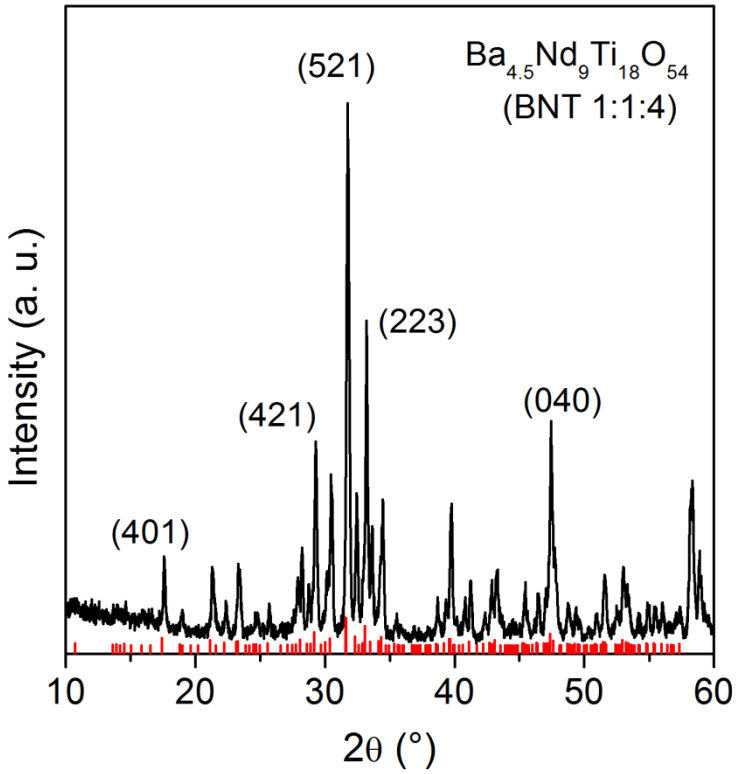

Figure 5.2-1: X-ray diffraction patterns of BNT 1:1:4 powders after calcinations at 1200 ˚C for 3h. PDF card #01-070-9069 used for peak indexation is also presented. Under the detection limits of the XRD technique, the powders are monophasic.

The BNT powders showed a bimodal particle size distribution with maxima around 0.2 and 2 µm. The largest particle diameter is below 3 µm, as shown in Figure 5.2-2. The median of the particle diameter distribution is 0.2 µm. In agreement with these results,

the particle equivalent diameter obtained by image analysis of the green samples cross-sections was 0.3±0.06 µm.

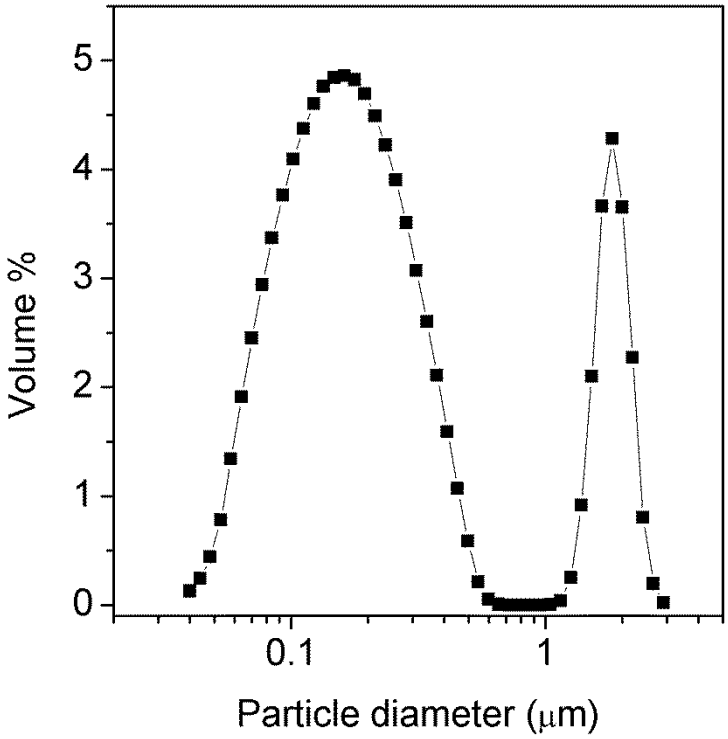

Figure 5.2-2: Particle diameter distribution of BNT powders. BNT powders show a bimodal particle size distribution with maxima around 0.2 and 2 µm.

5.2.3.2 Constrained sintering

Figure 5.2-3 shows SEM microstructures of green BNT samples. Figure 5.2-3 (a) corresponds to a polished cross section of a green film and Figure 5.2-3 (b) to a bulk polished fracture surface parallel to the pressing direction.

The samples showed similar green relative density of 0.50 and 0.53 for films and bulk, respectively. The median particle area measured by image analysis in both samples is 0.07 μm^2, with median aspect ratio of 1.57, revealing some particle elongation already at the green state. Moreover, the green samples showed very similar particle orientation factors: 0.54 was measured for the films and 0.53 for the bulk.

As observed in the BLT study, the BNT green films and bulk samples are also equivalent at that initial state, which is fundamental for appropriate comparison of microstructure development during sintering of thick films and bulk samples.

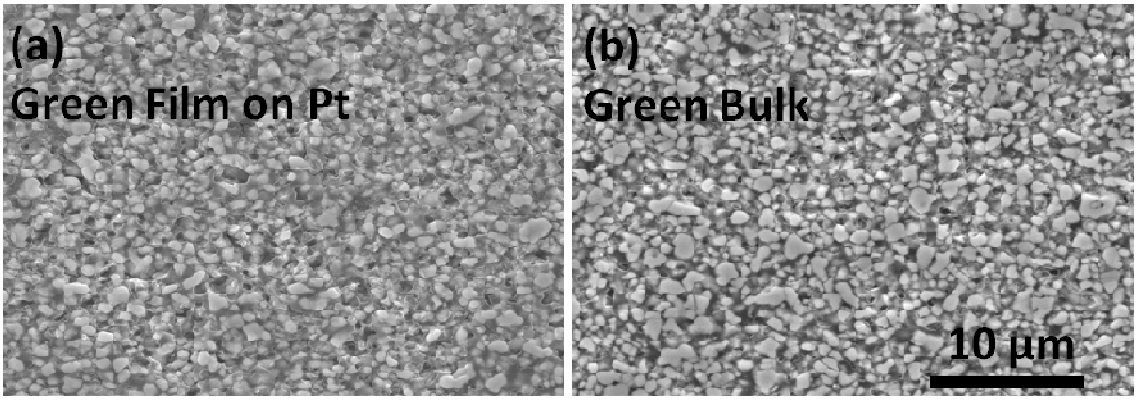

Figure 5.2-3: SEM cross-section microstructures of BNT green samples: (a) film on Pt and (b) bulk. Film and bulk green samples have equivalent microstructures in the green state.

SEM top view microstructures of BNT films sintered at 1350 ˚C on Pt-foil substrates for 0, 60, 180 and 720 min are presented in Figure 5.2-4. The characteristic needle shape of BNT grains [19; 182] is evident from the beginning of the isothermal time and appreciable grain growth is already observed for 0 min.

In fact, elongated grains are clearly visible, with aspect ratio increasing with the isothermal time. This is in agreement with previously observed BNT grain growth along one preferential direction [19; 149; 182], as expected from the anisometric crystal structure [149; 172; 182].

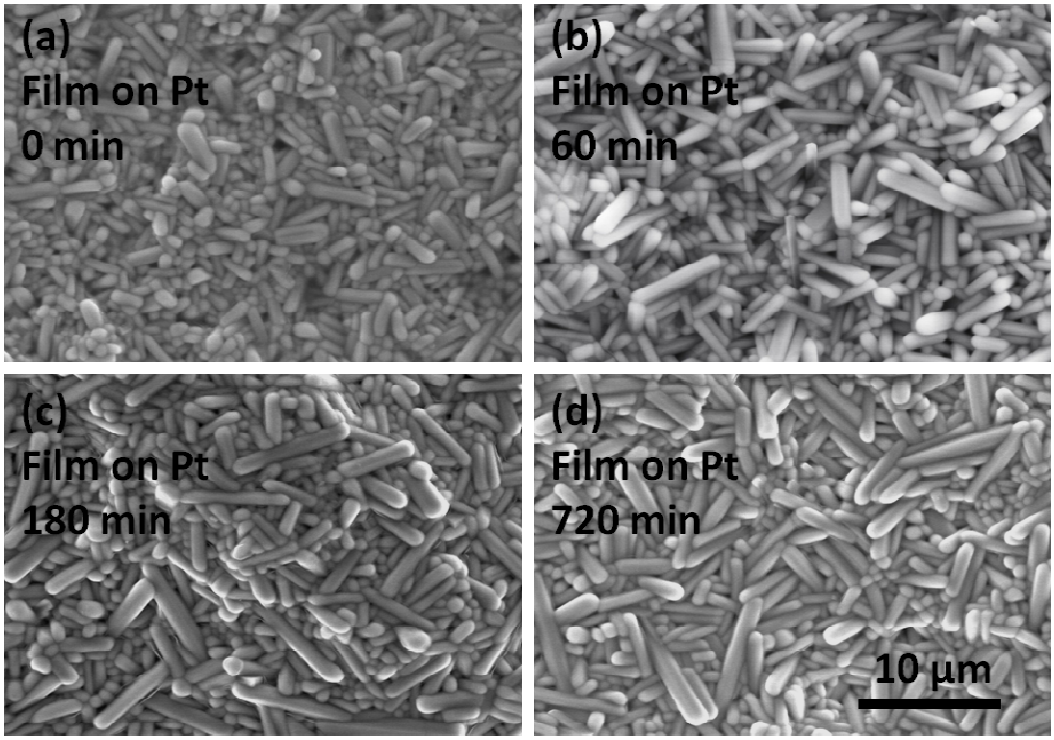

Figure 5.2-4: SEM top-view microstructures of BNT films on Pt after sintering at 1350 ˚C for isothermal times of (a) 0, (b) 60, (c) 180 and (d) 720 min. Grains are needle-shaped and the aspect ratio increases with the isothermal time.

In Figure 5.2-5 the perspective is changed to the cross section, in the case of the films. Regarding the bulk samples, the equivalent is the fracture surface parallel to the pressing direction (or axial direction in the cylindrical-shaped bulk sample). It can be seen that the grains are clearly oriented. This orientation is parallel to the substrate in the films and perpendicular to the pressing direction in the case of the bulk samples. The section of the oriented needle shaped grains results in rounded shapes, giving the appearance of reduced grain growth and small microstructure changes even after 720 min. However, from the top view microstructures in Figure 5.2-4 the evolution is clear and very elongated grains longer than 10 µm are visible after 720 min of sintering time.

Additionally, the cross section microstructures in Figure 5.2-5 show considerably dense films and bulk samples from the beginning of the isothermal time. Nevertheless, the elimination of some residual porosity is still observable. As presented in Table 5.2-1, at

0 min of isothermal time, the films showed a high relative density of 0.94 and the bulk sample a slightly higher value of 0.96.

Table 5.2-1: Relative density of green and sintered BNT films and bulk samples.

	Relative density	
	Film on Pt	**Bulk**
Green	0.50 ± 0.02	0.53 ± 0.02
Isothermal time (min)		
0	0.94 ± 0.02	0.96 ± 0.01
60	0.96 ± 0.01	-
180	0.97 ± 0.01	0.98 ±0.01
720	0.98 ± 0.01	0.98 ± 0.01

The high density of the samples sintered for 0 min shows that, despite the high heating rate of 25 ˚C/min, the densification occurred very fast, mainly during the heating ramp. This may suggest the presence of trace amounts of liquid phase during sintering. However, no evident signs of amorphous phase were detected from the SEM observation of both films and bulk samples.

The films, at the beginning of the isothermal time, seem to have a slightly higher fraction of porosity (0.06) compared to the bulk counterpart (0.04). This is consistent with some densification retardation characteristic of constrained sintering, as observed for BLT. Nevertheless, for the long sintering time of 720 min there is no obvious difference in the attained density between films and bulk samples (0.98), which are both close to full densification. This observation is again in close agreement with the results on the constrained sintering of BLT thick films and in contrast with previous works on constrained sintering on rigid substrates [85; 86; 91; 93; 115; 116], as discussed in the previous section 5.1 of this text.

A very good adhesion of the films to the Pt substrate is clear from the cross-section micrographs in Figure 5.2-5 (a), (b) and (c). Additionally, no porous layer was observed near the substrate, consistent with the homogeneous pore distribution previously verified in the BLT samples.

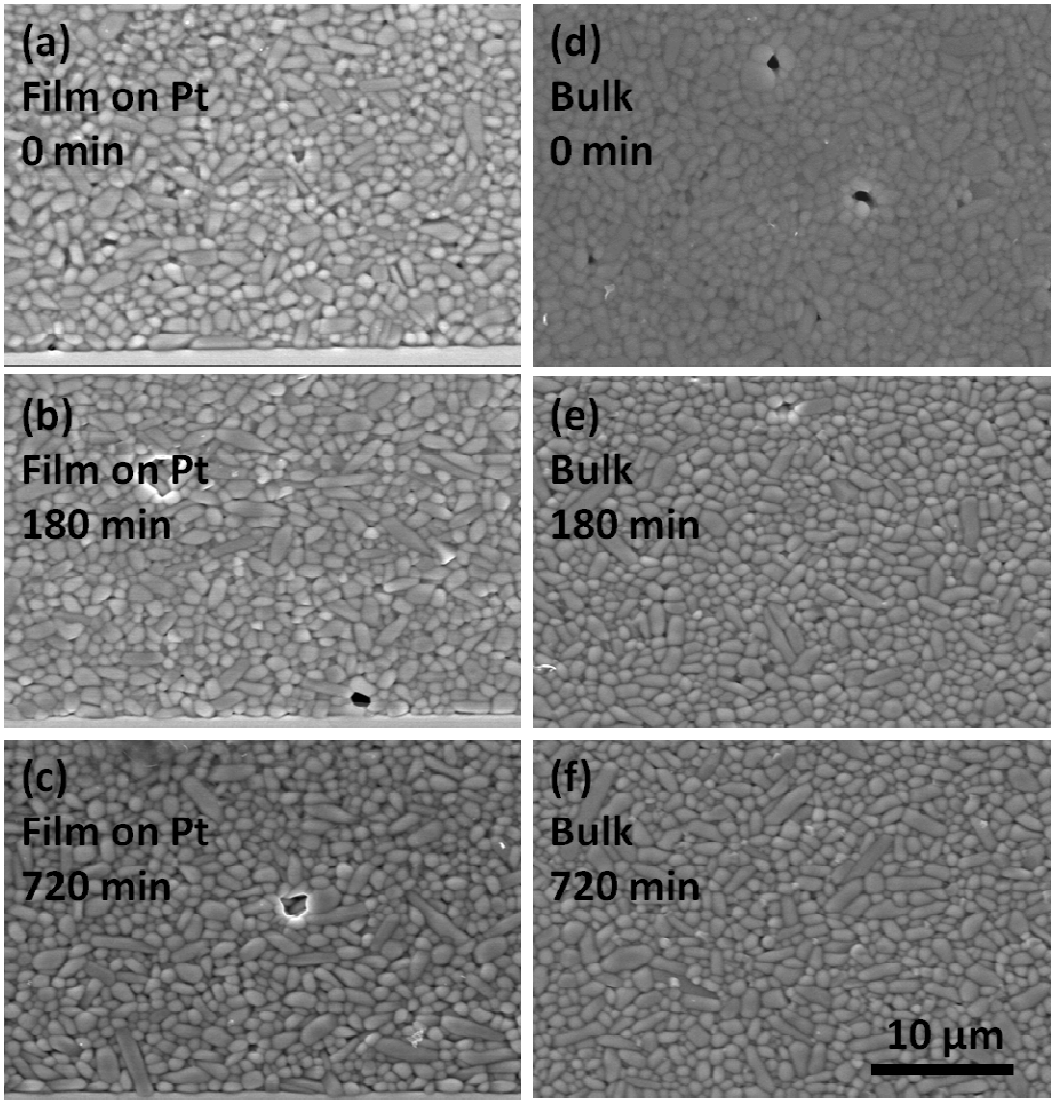

Figure 5.2-5: SEM cross section microstructures of BNT films on Pt (left) and polished fracture surfaces (parallel to the pressing direction) of bulk samples (right) after sintering at 1350 ˚C for (a) and (d) 0, (b) and (e) 180 and (c) and (f) 720 min.

Despite the difficulty originated by the shape and orientation of the grains in the cross section microstructures, the grain size quantification was attempted, as well as regarding other microstructural parameters such as grain aspect ratio and orientation factor. It is important to note that due to the orientation of the needle shaped grains, this quantification refers to the section of the grains resulting in a large underestimation of the real area and aspect ratio of the grains. Nevertheless, the comparison of the microstructures of films and bulk counterparts and the quantification of the respective microstructural parameters may still provide insights on the microstructure development during constrained sintering. The obtained median grain area distribution for films and bulk is presented in Figure 5.2-6.

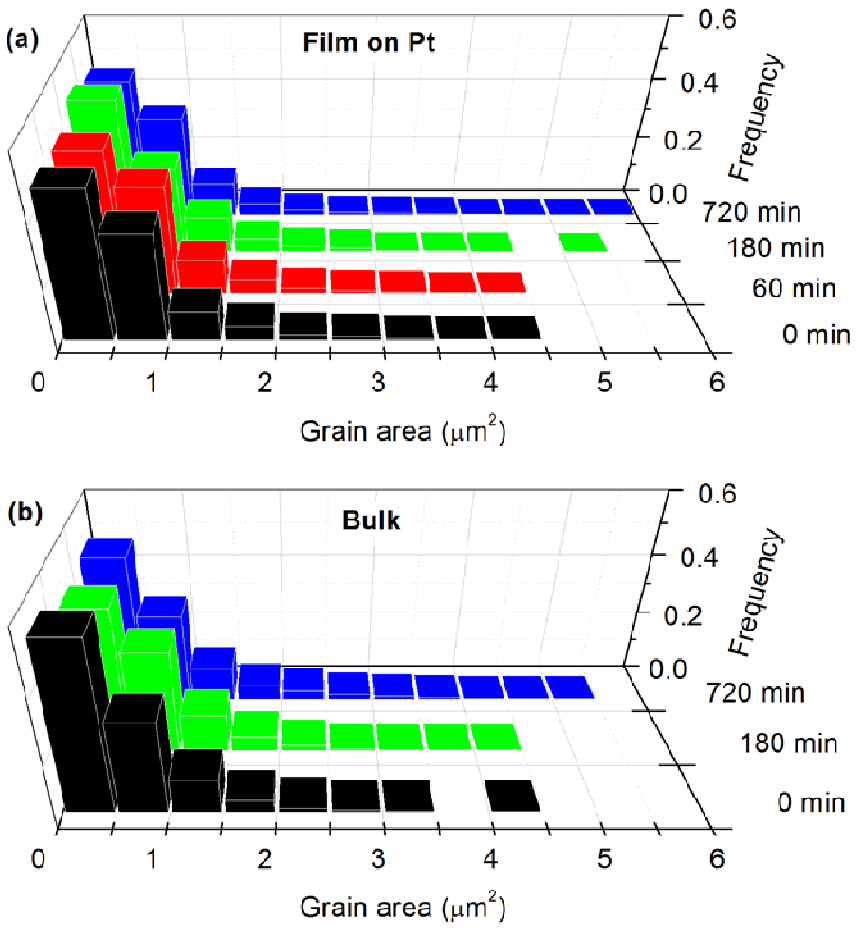

Figure 5.2-6: Grain area distribution for (a) films on Pt and (b) bulk samples for several isothermal times. Films show slightly larger distributions than the bulk samples.

As mentioned, just small changes are measurable. Only for the longer isothermal times the enlargement of the distribution is visible, which is more pronounced in the case of the films than regarding the bulk samples. Similar observations are valid for the samples of 0 min of isothermal time. The bulk sample shows a higher fraction of grains with area smaller than 1 μm^2 and lower fraction of grains with area higher than 3.5 μm^2.

The median grain area of films and bulk is compared along the isothermal time in Figure 5.2-7. Despite the large error bars, the results show larger grains in the films than in the equivalent bulk samples along the entire isothermal time. The difference seems to be larger in the beginning of the isothermal time but is present until the end of the sintering cycle. This may be correlated with the effect of the stress from the substrate leading to enhanced grain growth, as previously observed for BLT.

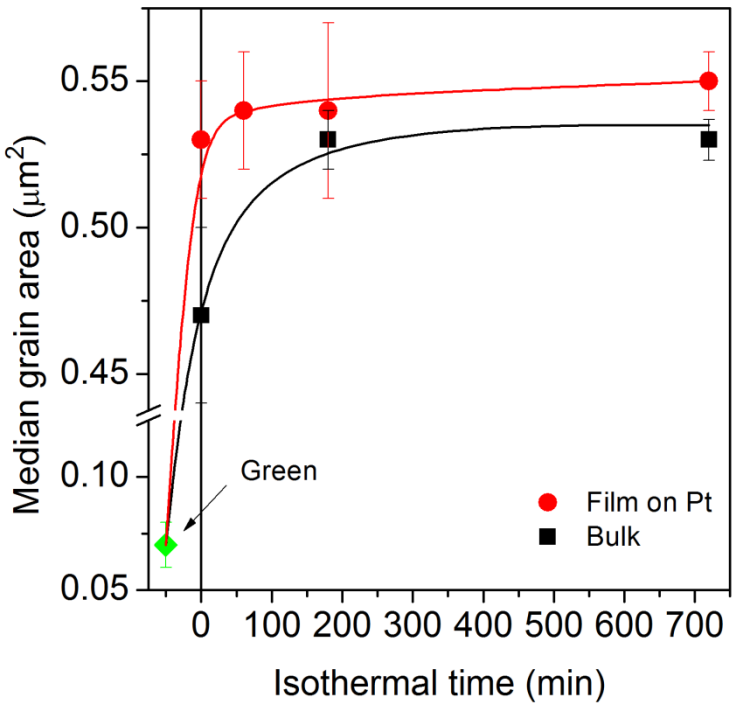

Figure 5.2-7: Median grain area as a function of the isothermal time for films and bulk. Larger grains are observed in the films than in the equivalent bulk samples.

Similar observations regarding the median aspect ratio are depicted in Figure 5.2-8: always larger in the case of the films as compared to the equivalent bulk samples. However, the median grain aspect ratio in the films changed from 1.62 for 60 min of sintering to 1.66 for 180 min and to 1.65 after 720 min. This observation combined with the large error bars suggests a small degree of coarsening and requires a cautious analysis. The decrease of the median grain aspect ratio for the longest sintering time may be related to the experimental error associated with the grain size measurement or may suggest a thickening of the needle-like grains for long sintering times. The second hypothesis is consistent with the increasing of the median grain area plotted in Figure 5.2-7, measured in the cross-sections.

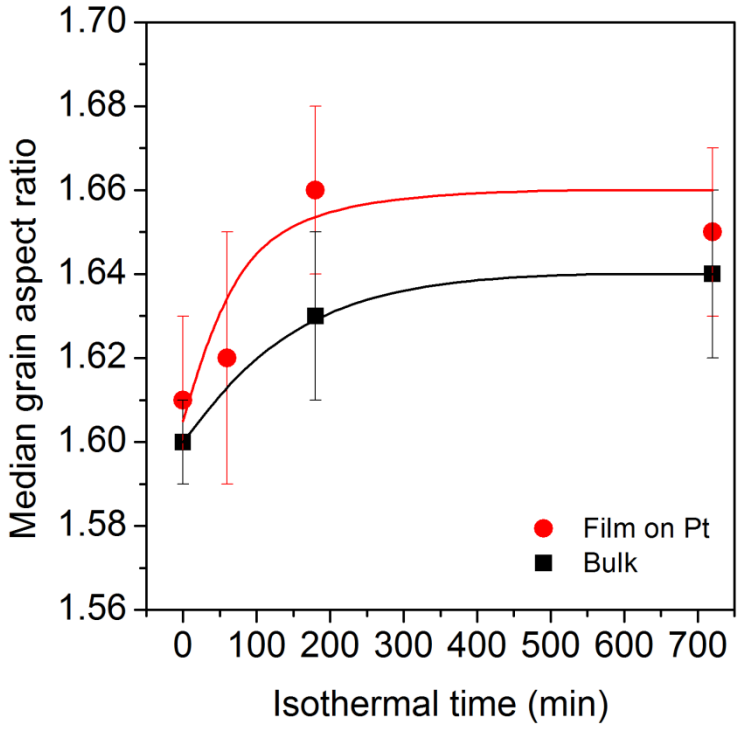

Figure 5.2-8: Median grain aspect ratio as a function of the isothermal time for films and bulk. Grains are more elongated in the films than in bulk specimens.

Another point is that the measured variation of the median grain aspect ratio is much more modest, if compared to the results of Fu *et al.* [19] on BNT 1:1:5 (grain aspect ratio

changed from 5 to 23 with changing sintering temperature from 1300 to 1450 ˚C). Some aspects may be considered. First, the median is much less sensitive to the extremes of a distribution than the average, which may lead to smaller detected variations. Second, as previously discussed, the liquid phase detected in the 1:1:5 composition is expected to be less important in the present 1:1:4 BNT composition, which may lead to slower microstructural development. Third, in the work of Fu *et al*. [19], the sintering temperature was changed from 1350 to 1450 ˚C, whereas in the present work all samples were sintered at 1350 ˚C with changing sintering time. As the mass transport is a thermally activated process, increasing sintering temperature is expected to have a stronger impact on the microstructure development than the sintering time. Finally, the high degree of orientation of the needle shaped grains leads to very small grain aspect ratio (in the cross section) and to small detectable microstructural changes during the isothermal sintering time.

The grains orientation distribution and the grain orientation factor for films and bulk regarding the different isothermal times are presented in Figure 5.2-9 and Figure 5.2-10, respectively. In both cases, from the green state a considerable degree of grain orientation is present. As observed in the green microstructures of Figure 5.2-3, the green samples already show particle orientation. Under the present criterion, a random microstructure would show a grain orientation factor of 0.33 in opposition to 0.54 and 0.53 measured in green films and green bulk.

However, more important is the fact that the orientation of the grains increases much more in the films than in the bulk samples with the increasing of the isothermal time, despite the similar starting point in the green state. The grain orientation is higher in the films already in the beginning of the isothermal time and increases dramatically until 180 min, whereas the increase in the case of the bulk samples is much more modest. After that time, both types of samples seem to have reached a maximum of grain orientation: around 58% in the bulk and nearly 10% more in the films. This observation may be correlated with the evolution of the median grain aspect ratio in Figure 5.2-8, which shows very similar behaviour.

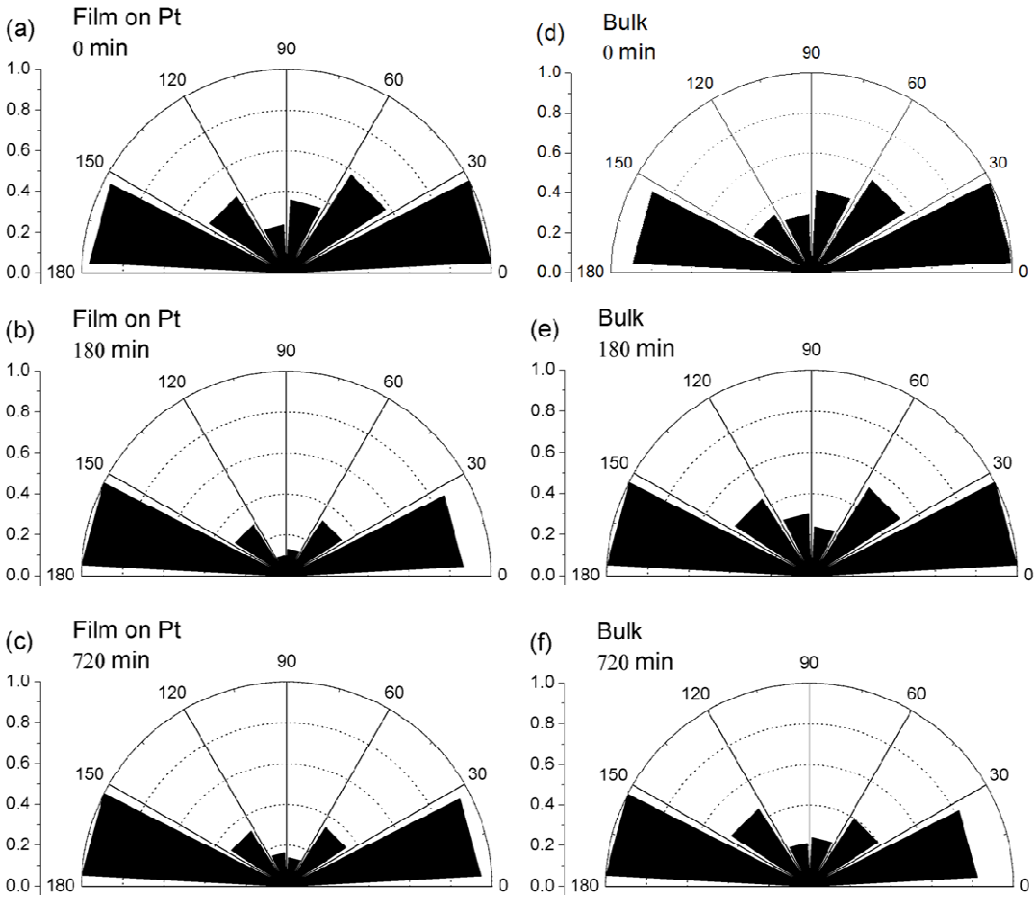

Figure 5.2-9: Grain orientation distribution for films (left) and bulk samples (right) after sintering at 1350 ˚C for isothermal times of (a) and (d) 0, (b) and (e) 180 and (c) and (f) 720 min. In-plane grain orientation is higher in the films than in bulk samples.

These observations are in close agreement with the previously described results on the constrained sintering of BLT and may be discussed based on the same argumentation. Both materials have an anisometric crystal unit cell, which results in grain growth along one preferential direction. This characteristic grain growth behaviour combined with the particularities of the constrained sintering, namely the effect of the stress from the substrate, leads to enhanced grain growth and more pronounced grain orientation.

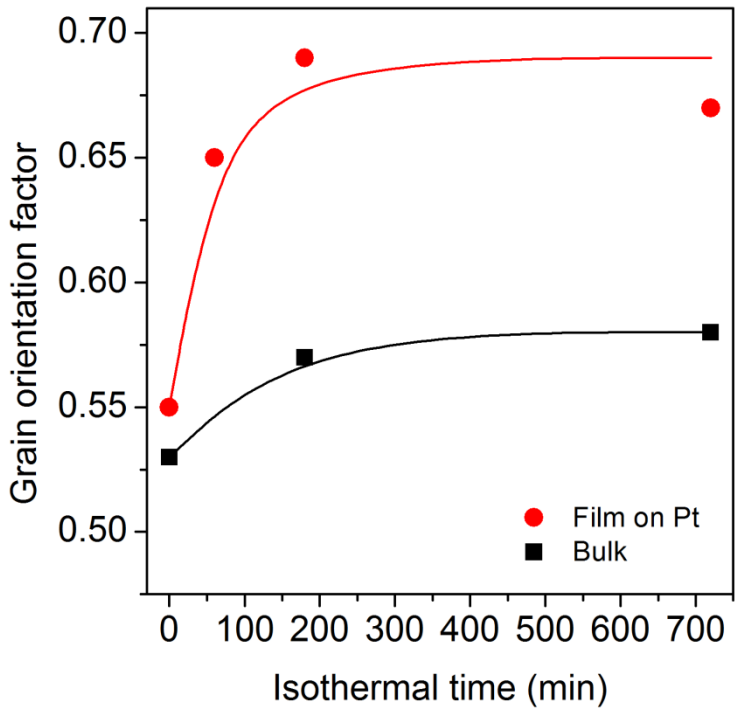

Figure 5.2-10: Dependence of the grains orientation factor on the isothermal time for films and bulk. With increasing isothermal time, grains orientation increases much more in the films than in the bulk samples.

As previously discussed, the microstructural anisotropy is expected to have a strong impact on the dielectric properties. Such correlation is presented in the following section.

5.2.3.3 Dielectric properties

Figure 5.2-11 shows the dependence on the temperature, between 30 and 120 ˚C, of the relative permittivity at 1 MHz for bulk and films on Pt (measured in the direction normal to the substrate plane in the films and in the pressing direction for the bulk). The permittivity obtained in the films for 60 min of isothermal time (ε_r=69) is very close to that measured for bulk sintered for 180 min (ε_r=70). For longer sintering times, the permittivity of the films is always lower than that of the bulk specimen. The decrease is nearly systematic, although not large, from around 69 (for 60 min of sintering time) to

64, after sintering for 720 min. Sintering times of 120 and 180 min yielded similar relative permittivity values around 67. These values are close to those previously reported for BNT 1:1:4, presented in Table 5.2-2 for comparison.

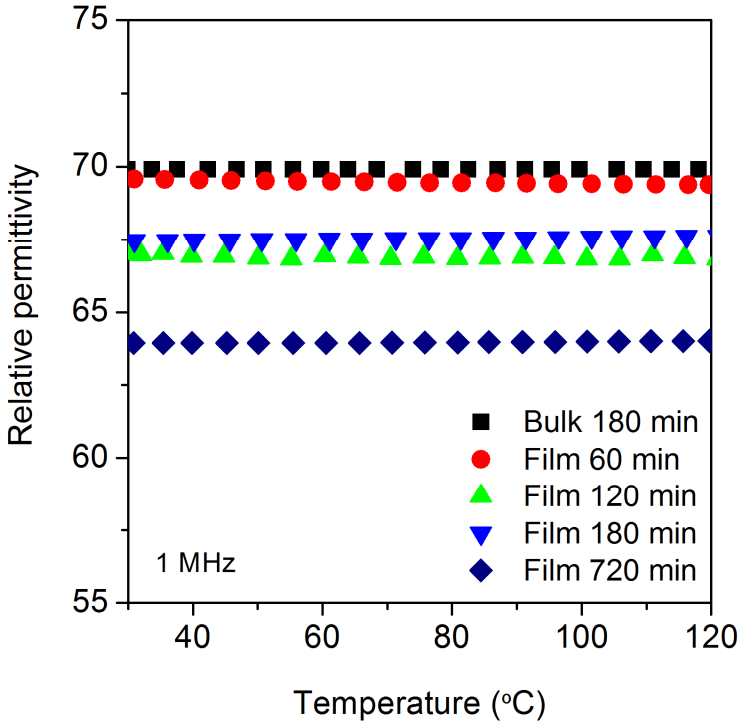

Figure 5.2-11: Relative permittivity as a function of the temperature for films and bulk. In all samples, the permittivity is nearly independent of the temperature.

Moreover, as expected from previous results on the similar 1:1:5 BNT [19] and on BLT, the permittivity of bulk and films of 1:1:4 BNT shows a very weak dependence of the temperature. In fact, as plotted in Figure 5.2-12, the temperature coefficient of permittivity, $TC\varepsilon_r$, equation (2.2-4), of the 180 min sintered bulk sample is almost zero, 0.3 *ppm*/˚C. Regarding the films, a dependence of the $TC\varepsilon_r$ on the sintering time, and consequently on the microstructure anisotropy, is again observed. In fact, the evolution of the $TC\varepsilon_r$ along the isothermal sintering of BNT films in Figure 5.2-12 is intimately correlated with the variation of the median grain aspect ratio (also in Figure 5.2-8) and with the grain orientation factor in Figure 5.2-10. Along with the increase in

grain aspect ratio and orientation factor, the $TC\varepsilon_r$ evolves from negative for 60 and 120 min of sintering time to positive values after sintering for longer times.

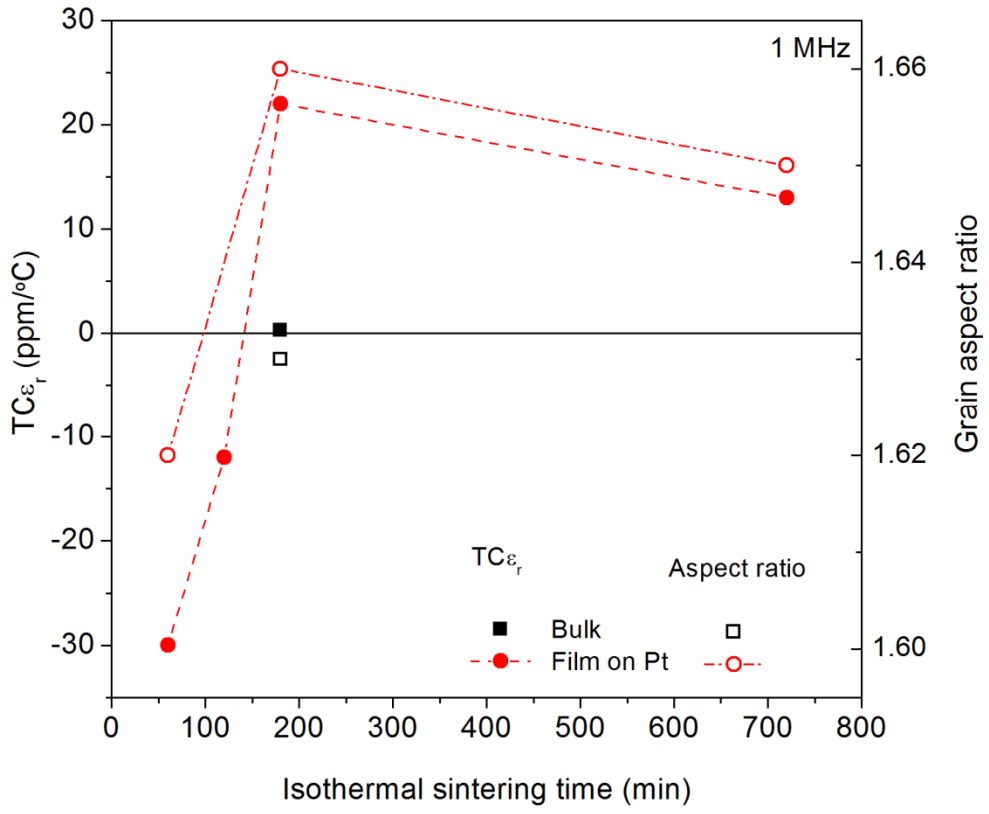

Figure 5.2-12: Temperature coefficient of permittivity, $TC\varepsilon_r$, at 1 MHz and median grain aspect ratio as a function of the isothermal sintering time. $TC\varepsilon_r$ is low and intimately correlated with microstructure anisotropy.

These observations are again in agreement with the results of Fu *et al.* [19] on $BaNd_2Ti_5O_{14}$ (BNT 1:1:5): as the sintering temperature increased from 1300 to 1450 ˚C, $TC\varepsilon_r$ changed from -114 to +12 *ppm*/˚C, associated with the increase of the grains aspect ratio. As argued by the authors [19], the anisotropic grain growth during constrained sintering of BNT films suppresses the out of plane polarization response and, as a consequence, decreases the polarization and increases $TC\varepsilon_r$ which may reach, for the proper sintering conditions, the zero $TC\varepsilon_r$ value. This possibility of tailoring the

$TC\varepsilon_r$ of thick films by manipulating the sintering temperature is indeed very important from the technological point of view.

Table 5.2-2: Dielectric properties reported for BNT (1:1:4 and 1:1:5).

Material	**Frequency**	ε_r	***tanδ* or *Q* or *Q.f***	τ_f (*ppm/*˚C)	**Ref.**
BNT 1:1:5 films	1 MHz	107	0.0006 (Q=1666)	+58.5	[164]
BNT 1:1:5	1 MHz	88	0.0003 (Q=3333)	-36.8	[164]
BNT 1:1:5	3.5 GHz	91	Q=1771	-8 to -46	[a]
BNT 1:1:4	6.5 GHz	84	Q.f=7800 GHz	+88	[152]
BNT 1:1:4	4.7 GHz	45	Q.f=13500 GHz	--	[151]
BNT 1:1:4	3.7 GHz	76	Q.f=5600 GHz	+77	[150]
BNT 1:1:4	1 MHz	70	0.0002	+0.3	This work
BNT 1:1:4 films	1 MHz	64 to 69	0.001 to 0.006	-30 to +22	This work

[a] Fuji Titanium Industry Co, Lda

Figure 5.2-13 presents the loss tangent of 1:1:4 BNT films and bulk samples as function of the temperature. The bulk samples showed very low losses, around $2x10^{-4}$. The films showed slightly higher loss tangent, of the order of 10^{-3}, which seems to decrease for long sintering times, to values closer to those of the bulk sample.

The differences in the dielectric response between films and bulk specimens may be related with the densification retardation on the films as compared to the bulk specimens. However, as presented in Table 5.2-1, the difference in relative density of films and bulk is small (0.94 for films and 0.96 for bulk at the beginning of the isothermal time) and the porosity fraction is reduced. Therefore, a significant effect of the differences in density is not expected.

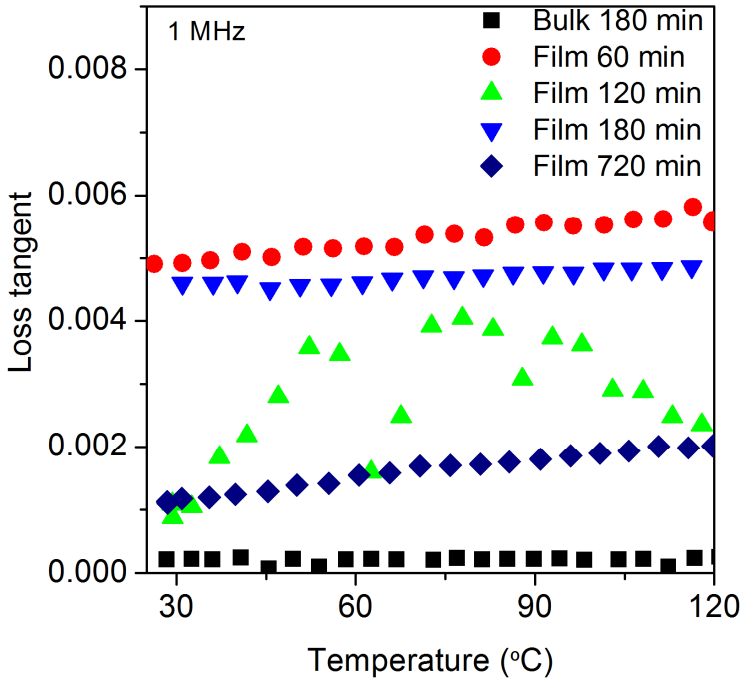

Figure 5.2-13: Loss tangent dependence on the temperature at 1 MHz for bulk and film samples. All samples show low losses, lower for the bulk sample.

As previously discussed regarding the BLT thick films, the effect of the interface and of the stress from the substrate may play a role in the dielectric properties of the films. Such effect has a strong impact on the dielectric response of thin films [397; 398]. However, the flexibility of the Pt substrate and the different relation between substrate and dielectric layer in thick films creates a diverse situation. Nonetheless, the effect of the stress from the substrate constraint should be considered and subjected to a systematic investigation.

5.2.4 Summary

The constrained sintering of 1:1:4 BNT ($Ba_{4.5}Nd_9Ti_{18}O_{54}$) films deposited by EPD on Pt-foil substrates was investigated and compared to freely sintered bulk samples. The present observations on BNT confirmed the previously described results on BLT.

Green films and bulk samples showed equivalent green density and particle orientation. After sintering, high density thick films highly adherent to the Pt foil were obtained, despite the constraint from the substrate. The crystallographic anisometry of the material resulted in elongated needle-like grains and anisotropic microstructures, without any evident sighs of liquid phase either in film or bulk samples. The effect of the stress from the substrate during constrained sintering lead to higher degrees of anisotropy in the films than in the bulk samples, despite the equivalent samples at the green state. Enhanced grain growth and higher degree of grain orientation were observed in the films, which are attributed to the effect of the stress form the substrate during constrained sintering.

Marked effects of the microstructural anisotropy on the dielectric properties were also detected on 1:1:4 BNT films. Along with the increase in grain aspect ratio and orientation factor, the relative permittivity slightly decreased and the $TC\varepsilon_r$ evolved from negative to positive with the increase of the isothermal sintering time. These observations demonstrate that the constraint from the substrate may be used to control the microstructural anisotropy of BNT thick films and tailor the dielectric properties of the material, namely to obtain a temperature stable dielectric response.

6 Conclusions and Future Work

6.1 Conclusions

The accomplishments of this work are the fruit of several collaborations. I have much to thank to several persons, as it is stated in the beginning of this thesis. Countless scientific discussions were at the origin and contributed to the improvement of the ideas developed in this work along the last years.

This study is also the result of intense lab work. It covers a wide range of aspects in advanced ceramic materials science, from powders preparation, to processing, in the form of bulk and thick films, to the final properties. Several materials were investigated and a vast number of characterization techniques employed.

STO is a classic example of the cubic perovskite structure and it is tolerant to some extent to stoichiometry variations, which are determinant for the microstructural evolution and dielectric response. Therefore, the effect of nonstoichiometry on the grain growth and bulk and grain boundary contributions to the dielectric response of STO ceramics was systematically investigated.

Related to an increase of the grain boundary mobility, the increase of the attained grain size and the enlargement of the grain size distribution with the decrease of Sr/Ti ratio are observed.

The resistivity of bulk and grain boundaries is systematically decreased in nonstoichiometric STO samples as compared to stoichiometric material. The effect is much stronger for the grain boundaries than for the bulk. Systematic dependences on the nonstoichiometry were also observed for the temperature dependence of the conductivity (much more affected in the case of the grain boundary contribution), bulk and grain boundary capacitance and grain boundary thickness.

In addition to the effects on grain interiors, these observations are consistent with the formation of different grain boundary complexions dependent on the nonstoichiometry (and nonstoichiometry induced defects), which lead to the observed

different microstructure evolution and diverse dielectric response. It is demonstrated in this work that nonstoichiometry may be used as a tool for microstructure tailoring and grain boundary engineering enabling the design of the dielectric properties of STO ceramics.

A grain growth anomaly and its relation with the dielectric response were also investigated in a Ti-rich STO composition (Sr/Ti = 0.995). Discontinuities on the dependence of grain size on the sintering temperature are observed. Four grain growth regimens are defined, with transitions at temperatures around 1500, 1550 and 1605 ˚C, which correspond to grain size decreases, despite the increasing sintering temperature. This study shows that the anomalous grain growth behaviour is directly related to the presence of an amorphous phase, which amount varies with the temperature and shows trends that may be related with a scenario of retrograde solubility of the excess TiO_2.

The dielectric response of the grain boundaries is much more affected by the sintering temperature than that of the bulk counterpart. Indeed, the grain growth regimens and discontinuous variation of the amount of detected amorphous phase are also correlated with changes in the activation energy for grain boundary conductivity and in the grain boundary thickness. These new results have great scientific and technological relevance in tailoring the microstructure and dielectric response of STO-based materials and using grain boundary complexion behaviour for materials design.

On the other hand, the current need for continuous miniaturization and increased integration in microelectronic and communications industry requires the substitution of components previously fabricated from bulk ceramics by, for example, thick films. Thick films of stoichiometric and nonstoichiometric STO compositions were successfully deposited by EPD on Pt-foil substrates. Acetone and ethanol are suitable suspension media for the EPD of STO powders. The best EPD performance was obtained using acetone with the addition of iodine.

The STO deposit weight is dependent on the concentration of the suspension, on the amount of iodine added and on the deposition time and voltage. These dependences can be used to control the thickness and quality of the films. Cold isostatic pressing of

the green films enhances markedly the final density of the films. The effect of the nonstoichiometry on the microstructure of the constrained sintered thick films revealed to be similar to the case of bulk ceramics: increased densification and grain size and enlargement of the distribution with decreasing Sr/Ti ratio. Grains shape is equiaxied independently of the stoichiometry and substrate constraint.

Regarding $BaO\text{-}Ln_2O_3\text{-}TiO_2$ (Ln = La or Nd) low loss dielectric materials, the anisometry in the lattice parameters usually leads to elongated grains. The constrained sintering of $BaO\text{-}Ln_2O_3\text{-}TiO_2$ (Ln = La or Nd) compositions was addressed and compared to equivalent freely sintered bulk samples. The evolution of pore and grain anisotropy, as well as of the crystallographic texture, along densification under the effect of the substrate were investigated and correlated to the dielectric response of the materials.

Green films and bulk samples of BLnT (Ln = La or Nd) showed equivalent green density, particle orientation and degree of crystallographic texture at the starting point. After sintering, high density thick films highly adherent to the Pt foil were obtained, despite the constraint from the substrate. The crystallographic anisometry of the materials resulted in elongated platelet-like (BLT) and needle-like (BNT) grains and anisotropic microstructures.

In agreement with previous studies on constrained sintering of ceramic layers, the constrained densification of BLnT (Ln = La or Nd) on Pt-foil substrates is retarded. However and unexpectedly, constrained sintered films attained a similar final density and showed a significantly larger grain size than their bulk counterparts. These results are even more visible in BLT films sintered on rigid BLT substrates. It is then proposed that tensile compatibility stresses induced by the geometrical constraint may increase the mobility of the grain boundaries or the driving force for transport enhancing grain growth.

Anisotropic microstructures with elongated grains and pores oriented parallel to the substrate were developed during the constrained sintering of BLT thick films, which is different than previously results for other ceramic systems. Although starting from equivalent green microstructures, grain aspect ratio, grain orientation and texture are

significantly increased in dense films and remain nearly constant in equivalent bulk samples.

The experiments on 1:1:4 BNT confirmed the results on BLT. The effect of the stress from the substrate during constrained sintering of 1:1:4 BNT also lead to higher degrees of anisotropy in the films than in the bulk samples, despite the equivalent samples at the green state. Enhanced grain growth and higher degree of grain orientation were observed in the films, which are attributed to the effect of the stress form the substrate during constrained sintering.

There is a strong correlation between grain and pore evolution in BLT films, which starts as soon as grain growth takes place. A stress effect triggering grain growth enhancement as well as a strong Zener pinning effect leads to highly textured microstructures, which is also observed at the crystallographic level.

Marked effects of the microstructural anisotropy on the dielectric properties were also detected on the BLnT (Ln = La or Nd) thick films. Along with the increase in grain aspect ratio, orientation factor and degree of crystallographic texture, the relative permittivity is slightly decreased and the $TC\varepsilon_r$ evolves from negative to positive with the increase of the isothermal sintering time.

These observations demonstrate that the constraint from the substrate may be used to control the microstructural anisotropy of BLnT (Ln = La or Nd) thick films on Pt-foil substrates and tailor the dielectric properties of the material, namely to obtain a temperature stable dielectric response in miniaturized devices.

Stress Assisted Grain Growth is proposed as a potential technique to engineer grain boundaries, achieving anisotropic textured microstructures in ceramics with tailored properties. These results are relevant for the technological application of thick dielectric films with a crystallographic texture, due to the observed dependence on the microstructure anisotropy of the dielectric response.

6.2 Future work

Several scientific and technologically important answers were found in the course of this study. However, science is never a finished story and new questions were raised. In this context, suggestions for further work are following.

. The role of defects (namely oxygen vacancies) on the matter and charge transport in nonstoichiometric STO should be further and deeply investigated.

. The grain growth anomaly in STO and the hypothesis of retrograde solubility should be further investigated by thermodynamic modelling. The hypothesis should also be tested on compositions with different Sr/Ti ratios.

. A systematic and detailed HRTEM investigation should be performed on the grain boundaries of STO compositions, correlating the different grain boundary mobilities and dielectric responses to grain boundary complexions.

. The influence of the constrained sintering (namely, the vertical pore orientation) and of the nonstoichiometry on STO thick films still need to be systematically addressed on more developed microstructures along long isothermal times. Their combined effects on the dielectric properties should also be addressed in order to achieve STO thick films with tailored and optimized properties.

. An analysis of the effect of stresses developed during the constrained sintering of thick films on the grain boundary characteristics should be performed by detailed HRTEM characterization. The stress from the substrate may lead to “damage” in the grain boundaries. The clear observation of defects induced by the substrate on the grain boundaries would be a great contribution for the understanding of the role of the substrate on the microstructure evolution during constrained sintering. Additionally, the substrate stress effects may somehow have a role on the formation of particular grain boundary complexions, which may affect the electrical response of functional materials, and therefore clearly deserve to be explored.

. The highly oriented and elongated platelet or needle shaped grains of BLnT (Ln = La or Nd) leads to difficulties in the microstructural analysis and parameter quantification. In this context, X-ray based 3D tomography techniques could be useful.

. The evolution of the crystallographic texture of 1:1:4 BNT on constrained sintered thick films and freely sintered bulk samples is yet to be performed.

. The effect of the anisotropic microstructures developed during constrained sintering on the dielectric properties at microwave frequencies of BLnT (Ln = La or Nd) tick films should be assessed.

These aspects suggested for further investigation, as are the results presented in this thesis, may be of great contribution for a better understanding, control and optimization of functional materials properties.

7 References

[1] A. J. Moulson and J. M. Herbert, "Electroceramics", Chapman & Hall: London (1990).

[2] G. H. Haertling, "Ferroelectric ceramics: History and technology", *J Am Ceram Soc,* 82 [4] 797 (1999).

[3] N. Setter, "Electroceramics: looking ahead", *J Eur Ceram Soc,* 21 [10-11] 1279 (2001).

[4] N. Setter and R. Waser, "Electroceramic materials", *Acta Mater,* 48 [1] 151 (2000).

[5] H. S. Bennett, R. Brederlow, J. C. Costa, P. E. Cottrell, W. M. Huang, A. A. Immorlica, J. E. Mueller, M. Racanelli, H. Shichijo, C. E. Weitzel and B. Zhao, "Device and technology evolution for Si-based RF integrated circuits", *IEEE T Electron Dev,* 52 [7] 1235 (2005).

[6] P. K. Panda, "Review: environmental friendly lead-free piezoelectric materials", *J Mater Sci,* 44 [19] 5049 (2009).

[7] M. T. Sebastian, "Dielectric materials for wireless communication" Elsevier Science Publishers: Amsterdam (2008).

[8] R. Ubic, I. M. Reaney and W. E. Lee, "Microwave dielectric solid-solution phase in system BaO-Ln_2O_3-TiO_2 (Ln = lanthanide cation)", *Int Mater Rev,* 43 [5] 205 (1998).

[9] R. A. Dorey and R. W. Whatmore, "Electroceramic thick film fabrication for MEMS", *J Electroceram,* 12 [1-2] 19 (2004).

[10] Y. Tohdo, K. Kakimoto, H. Ohsato, H. Yamada and T. Okawa, "Microwave dielectric properties and crystal structure of homologous compounds $ALa_4Ti_4O_{15}$ (A=Ba, Sr and Ca) for base station applications", *J Eur Ceram Soc,* 26 [10-11] 2039 (2006).

[11] S. B. Narang and S. Bahel, "Low loss dielectric ceramics for microwave applications: a review", *J Ceram Process Res,* 11 [3] 316 (2010).

[12] H. Ohsato, "Research and development of microwave dielectric ceramics for wireless communications", *J Ceram Soc Jpn,* 113 [1323] 703 (2005).

[13] A. K. Tagantsev, V. O. Sherman, K. F. Astafiev, J. Venkatesh and N. Setter, "Ferroelectric materials for microwave tunable applications", *J Electroceram,* 11 [1-2] 5 (2003).

[14] N. Yamaoka, "$SrTiO_3$-based boundary-layer capacitors", *Am Ceram Soc Bull,* 65 [8] 1149-52 (1986).

[15] K. Koumoto, Y. F. Wang, R. Z. Zhang, A. Kosuga and R. Funahashi, "Oxide thermoelectric materials: A nanostructuring approach", *Annu Rev Mater Res,* 40 363 (2010).

[16] S. Witek, D. M. Smyth and H. Pickup, "Variability of the Sr/Ti ratio in $SrTiO_3$", *J Am Ceram Soc,* 67 [5] 372 (1984).

[17] N. Harre, D. Mercurio, G. Trolliard and B. Frit, "Crystal structure of $BaLa_4Ti_4O_{15}$, member n = 5 of the homologous series $(Ba,La)_nTi_{n-1}O_{3n}$ of cation-deficient perovskite-related compounds", *Mater Res Bull,* 33 [10] 1537 (1998).

[18] H. Ohsato and M. Imaeda, "The quality factor of the microwave dielectric materials based on the crystal structure - as an example: the $Ba_{6-3x}R_{8+2x}Ti_{18}O_{54}$ (R = rare earth) solid solutions", *Mater Chem Phys,* 79 [2-3] 208 (2003).

[19] Z. Fu, P. M. Vilarinho, A. Y. Wu and A. I. Kingon, "Textured microstructure and dielectric properties relationship of $BaNd_2Ti_5O_{14}$ thick films prepared by electrophoretic deposition", *Adv Funct Mater,* 19 [7] 1071 (2009).

[20] R. M. German, "Sintering theory and practice", John Wiley & Sons: Oxford (1996).

[21] S. J. L. Kang, "Sintering: densification, grain growth and microstructure", Elsevier: Oxford (2005).

[22] M. N. Rahaman, "Ceramic processing and sintering", 2nd ed. Marcel Dekker: New York (2003).

[23] R. M. German, P. Suri and S. Park, "Review: liquid phase sintering", *J Mater Sci,* 44 [1] 1 (2009).

[24] G. W. Scherer, "Constitutive models for viscous sintering", pp. 1-18. in Mechanics of Granular Materials and Powder Systems, Vol. 37. Edited by M. M. Mehrabadi. ASME, New York (1992).

[25] N. J. Shaw, "Densification and coarsening during solid-state sintering of ceramics: A review of the models. I. Densification", *Powder Metall Int,* 21 [3] 16 (1989).

[26] N. J. Shaw, "Densification and coarsening during solid-state sintering of ceramics: A review of the models. II. Grain-growth", *Powder Metall Int,* 21 [5] 31 (1989).

[27] N. J. Shaw, " Densification and coarsening during solid-state sintering of ceramics: A review of the models. III. Coarsening" *Powder Metall Int,* 21 [6] 25 (1989).

[28] R. L. Coble, "Sintering crystalline solids. I. Intermediate and final state diffusion models", *J Appl Phys,* 32 [5] 787 (1961).

[29] R. M. German, "Liquid-phase sintering", Plenum press: New York (1985).

[30] W. D. Kingery, "Densification during sintering in the presence of a liquid phase. I. Theory", *J Appl Phys,* 30[3] 301 (1959).

[31] K. S. Hwang, R. M. German and F. V. Lenel, "Capillary forces between spheres during agglomeration and liquid phase sintering", *Metall. Trans. A,* 18A 11 (1987).

[32] R. J. Brook, "Controlled grain growth", pp. 331. in Treatise on Materials Science and Technology, Vol. 9. Edited by F. F. Y. Wang. Academic Press, New York (1976).

[33] G. S. Rohrer, "Grain boundary energy anisotropy: a review", *J Mater Sci,* 46 [18] 5881 (2011).

[34] I. W. Chen, "Mobility control of ceramic grain-boundaries and interfaces", *Mat Sci Eng A-Struct,* 166 [1-2] 51 (1993).

[35] S. J. Dillon, M. Tang, W. C. Carter and M. P. Harmer, "Complexion: A new concept for kinetic engineering in materials science", *Acta Mater,* 55 [18] 6208 (2007).

[36] C. B. Carter, "Structure and microstructure of interfaces in ceramics materials", in Surfaces and interfaces of ceramic materials. Edited by L. C. Dufour, C. Monty and G. P. Ervas. Kluwer Academic Publishers, Dordrecht, The Netherlands (1989).

[37] K. R. Kinsman and H. I. Aaronson, "Structure of crystalline interfaces", *Mater Charact,* 39 [2-5] 209 (1997).

[38] W. D. Callister, "Fundamentals of materials science and engineering. An interactive e-text", John Willey & Sons, Inc.: New York (2001).

[39] B. B. Straumal, B. Baretzky, O. A. Kogtenkova, A. S. Gornakova and V. G. Sursaeva, "Faceting-roughening of twin grain boundaries", *J Mater Sci,* 47 [4] 1641 (2012).

[40] D. G. Brandon, "The structure of high-angle grain boundaries", *Acta Metall Mater,* 14 [11] 1479 (1966).

[41] A. P. Sutton and R. W. Balluffi, "Overview no. 61 On geometric criteria for low interfacial energy", *Acta Metall Mater,* 35 [9] 2177 (1987).

[42] S. von Alfthan, N. A. Benedek, L. Chen, A. Chua, D. Cockayne, K. J. Dudeck, C. Elsasser, M. W. Finnis, C. T. Koch, B. Rahmati, M. Ruhle, S. J. Shih and A. P. Sutton, "The structure of grain boundaries in strontium titanate: theory, simulation and electron microscopy", *Annu Rev Mater Res,* 40 557 (2010).

[43] V. G. Sursaeva, B. B. Straumal, A. S. Gornakova, L. S. Shvindlerman and G. Gottstein, "Effect of faceting on grain boundary motion in Zn", *Acta Mater,* 56 [12] 2728 (2008).

[44] S. B. Lee, D. Y. Yoon and M. F. Henry, "Abnormal grain growth and grain boundary faceting in a model Ni-base superalloy", *Acta Mater,* 48 [12] 3071 (2000).

[45] S. Y. Chung, D. Y. Yoon and S. J. L. Kang, "Effects of donor concentration and oxygen partial pressure on interface morphology and grain growth behavior in $SrTiO_3$", *Acta Mater,* 50 [13] 3361 (2002).

[46] S. B. Lee, W. Sigle, W. Kurtz and M. Ruhle, "Temperature dependence of faceting in Σ5(310)[001] grain boundary of $SrTiO_3$", *Acta Mater,* 51 [4] 975 (2003).

[47] S. Y. Choi and S. J. L. Kang, "Sintering kinetics by structural transition at grain boundaries in barium titanate", *Acta Mater,* 52 [10] 2937 (2004).

[48] Y. I. Jung, S. Y. Choi and S. J. L. Kang, "Effect of oxygen partial pressure on grain boundary structure and grain growth behavior in $BaTiO_3$", *Acta Mater,* 54 [10] 2849 (2006).

[49] S. B. Lee, J. H. Lee, P. S. Cho, D. Y. Kim, W. Sigle and F. Phillipp, "High-temperature resistance anomaly at a strontium titanate grain boundary and its correlation with the grain-boundary faceting-defaceting transition", *Adv Mater,* 19 [3] 391 (2007).

[50] S. J. Dillon and M. P. Harmer, "Multiple grain boundary transitions in ceramics: A case study of alumina", *Acta Mater,* 55 [15] 5247 (2007).

[51] S. J. L. Kang, Y. I. Jung and K. S. Moon, "Principles of microstructural design in two-phase systems", *Mater Sci Forum,* 558-559 827 (2007).

[52] W. Jo, D. Y. Kim and N. M. Hwang, "Effect of interface structure on the microstructural evolution of ceramics", *J Am Ceram Soc,* 89 [8] 2369 (2006).

[53] B. K. Lee, S. Y. Chung and S. J. L. Kang, "Grain boundary faceting and abnormal grain growth in $BaTiO_3$", *Acta Mater,* 48 [7] 1575 (2000).

[54] C. W. Park and D. Y. Yoon, "Effects of SiO_2, CaO_2 and MgO additions on the grain growth of alumina", *J Am Ceram Soc,* 83 [10] 2605 (2000).

[55] Y. J. Park, N. M. Hwang and D. Y. Yoon, "Abnormal growth of faceted (WC) grains in a (Co) liquid matrix", *Metall Mater Trans A,* 27 [9] 2809 (1996).

[56] Y. I. Jung, S. Y. Choi and S. J. L. Kang, "Grain-growth behavior during stepwise sintering of barium titanate in hydrogen gas and air", *J Am Ceram Soc,* 86 [12] 2228 (2003).

[57] M. P. Harmer, "The phase behavior of interfaces", *Science,* 332[6026] 182-83 (2011).

[58] S. J. Dillon and M. P. Harmer, "Relating grain boundary complexion to grain boundary kinetics II: Silica-doped alumina", *J Am Ceram Soc,* 91 [7] 2314 (2008).

[59] S. J. Dillon and M. P. Harmer, "Relating grain-boundary complexion to grain-boundary kinetics I: Calcia-doped alumina", *J Am Ceram Soc,* 91 [7] 2304 (2008).

[60] S. J. Dillon and M. P. Harmer, "Demystifying the role of sintering additives with "complexion"", *J Eur Ceram Soc,* 28 [7] 1485 (2008).

[61] M. P. Harmer, "Interfacial kinetic engineering: How far have we come since Kingery's inaugural Sosman address?", *J Am Ceram Soc,* 93 [2] 301 (2010).

[62] J. Luo, "Grain boundary complexions: The interplay of premelting, prewetting and multilayer adsorption", *Appl Phys Lett,* 95 [7] (2009).

[63] S. J. Dillon and G. S. Rohrer, "Mechanism for the development of anisotropic grain boundary character distributions during normal grain growth", *Acta Mater,* 57 [1] 1 (2009).

[64] J. G. Dash, A. W. Rempel and J. S. Wettlaufer, "The physics of premelted ice and its geophysical consequences", *Rev Mod Phys,* 78 [3] 695 (2006).

[65] J. W. Cahn, "Critical-point wetting", *J Chem Phys,* 66 [8] 3667 (1977).

[66] J. Luo and Y. M. Chiang, "Wetting and prewetting on ceramic surfaces", *Annu Rev Mater Res,* 38 227 (2008).

[67] J. G. Dash, "Surface Melting", *Contemp Phys,* 30 [2] 89 (1989).

[68] J. Luo, "Stabilization of nanoscale quasi-liquid interfacial films in inorganic materials: A review and critical assessment", *Crit Rev Solid State,* 32 [1-2] 67 (2007).

[69] J. Luo, "Liquid-like interface complexion: From activated sintering to grain boundary diagrams", *Curr Opin Solid St M,* 12 [5-6] 81 (2008).

[70] K. M. Asl and J. Luo, "Impurity effects on the intergranular liquid bismuth penetration in polycrystalline nickel", *Acta Mater,* 60 [1] 149 (2012).

[71] J. Luo, H. F. Wang and Y. M. Chiang, "Origin of solid-state activated sintering in Bi_2O_3-doped ZnO", *J Am Ceram Soc,* 82 [4] 916 (1999).

[72] J. Luo and X. M. Shi, "Grain boundary disordering in binary alloys", *Appl Phys Lett,* 92 101901 (2008).

[73] X. M. Shi and J. Luo, "Grain boundary wetting and prewetting in Ni-doped Mo", *Appl Phys Lett,* 94 [25] 251908 (2009).

[74] V. K. Gupta, D. H. Yoon, H. M. Meyer and J. Luo, "Thin intergranular films and solid-state activated sintering in nickel-doped tungsten", *Acta Mater,* 55 [9] 3131 (2007).

[75] B. K. Yoon, S. Y. Choi, T. Yamamoto, Y. Ikuhara and S. J. L. Kang, "Grain boundary mobility and grain growth behavior in polycrystals with faceted wet and dry boundaries", *Acta Mater,* 57 [7] 2128 (2009).

[76] M. Bäurer, D. Weygand, P. Gumbsch and M. J. Hoffmann, "Grain growth anomaly in strontium titanate", *Scripta Mater,* 61 [6] 584 (2009).

[77] A. G. Evans, "Perspective on the development of high-toughness ceramics", *J Am Ceram Soc,* 73 [2] 187 (1990).

[78] R. R. Tummala, "Ceramic packaging", in Microelectronics Packaging Handbook. Edited by R. R. Tummala and E. J. Rymaszewski. Van Nostrand Reinhold, New York (1989).

[79] W. J. Borland and S. Ferguson, "Embedded passive components in printed wiring boards: a technology review" in CircuiTree Mag (2001).

[80] G. L. Brennecka, J. F. Ihlefeld, J. P. Maria, B. A. Tuttle and P. G. Clem, "Processing technologies for high-permittivity thin films in capacitor applications", *J Am Ceram Soc,* 93 [12] 3935 (2010).

[81] H. F. Cheng, Y. C. Chen and I. N. Lin, "Frequency response of microwave dielectric $Bi_2(Zn_{1/3}Nb_{2/3})_2O_7$ thin films laser deposited on indium-tin oxide coated glass", *J Appl Phys,* 87 [1] 479 (2000).

[82] J. S. Reed, "Principles of ceramic processing" Wiley & Sons: New York (1995).

[83] L. Besra and M. Liu, "A review on fundamentals and applications of electrophoretic deposition (EPD)", *Prog Mater Sci,* 52 [1] 1 (2007).

[84] D. J. Green, O. Guillon and J. Rödel, "Constrained sintering: A delicate balance of scales", *J Eur Ceram Soc,* 28 [7] 1451 (2008).

[85] J. B. Ollagnier, O. Guillon and J. Rödel, "Constrained sintering of a glass ceramic composite: I. Asymmetric laminate", *J Am Ceram Soc,* 93 [1] 74 (2010).

[86] O. Guillon, E. Aulbach, J. Rödel and R. K. Bordia, "Constrained sintering of alumina thin films: Comparison between experiment and modeling", *J Am Ceram Soc,* 90 [6] 1733 (2007).

[87] A. Mohanram, S. H. Lee, G. L. Messing and D. J. Green, "Constrained sintering of low-temperature co-fired ceramics", *J Am Ceram Soc,* 89 [6] 1923 (2006).

[88] R. K. Bordia and A. Jagota, "Crack-growth and damage in constrained sintering films", *J Am Ceram Soc,* 76 [10] 2475 (1993).

[89] T. Rasp, C. Jamin, A. Wonisch, T. Kraft and O. Guillon, "Shape distortion and delamination during constrained sintering of ceramic stripes: Discrete element simulations and experiments", *J Am Ceram Soc,* 95 [2] 586 (2012).

[90] J. N. Calata, G. Q. Lu and T. J. Chuang, "Constrained sintering of glass, glass-ceramic and ceramic coatings on metal substrates", *Surf Interface Anal,* 31 [7] 673 (2001).

[91] T. J. Garino and H. K. Bowen, "Kinetics of constrained-film sintering", *J Am Ceram Soc,* 73 [2] 251 (1990).

[92] J. Bang and G. Q. Lu, "Densification kinetics of glass-films constrained on rigid substrates", *J Mater Res,* 10 [5] 1321 (1995).

[93] J. W. Choe, J. N. Calata and G. Q. Lu, "Constrained-film sintering of a gold circuit paste", *J Mater Res,* 10 [4] 986 (1995).

[94] G. Q. Lu, R. C. Sutterlin and T. K. Gupta, "Effect of mismatched sintering kinetics on camber in a Low-Temperature Cofired Ceramic Package", *J Am Ceram Soc,* 76 [8] 1907 (1993).

[95] J. B. Ollagnier, "Constraint and anisotropy during sintering of a LTCC material" PhD Thesis. Fachbereich Material und Geowissenschaften, Technischen Universität Darmstadt, Darmstadt (2008).

[96] R. K. Bordia and G. W. Scherer, "On Constrained Sintering. I. Constitutive Model for a Sintering Body", *Acta Metall Mater,* 36 [9] 2393 (1988).

[97] E. A. Olevsky, "Theory of sintering: from discrete to continuum", *Mat Sci Eng R,* 23 [2] 41 (1998).

[98] G. W. Scherer and T. Garino, "Viscous sintering on a rigid substrate", *J Am Ceram Soc,* 68 [4] 216 (1985).

[99] G. W. Scherer and S. M. Rekhson, "Viscoelastic-elastic composites. I. General-theory", *J Am Ceram Soc,* 65 [7] 352 (1982).

[100] O. Guillon, "Partial constrained sintering of ceramic layers on metallic substrates: A comparison between modeling and experiments", *J Am Ceram Soc,* 94 [4] 1040 (2011).

[101] Y. Zhao and L. R. Dharani, "Theoretical-model for the analysis of a ceramic thin-film sintering on a non-sintering substrate", *Thin Solid Films,* 245 [1-2] 109 (1994).

[102] E. A. Olevsky, X. Wang, A. Maximenko and M. A. Meyers, "Fabrication of net-shape functionally graded composites by electrophoretic deposition and sintering: Modeling and experimentation", *J Am Ceram Soc,* 90 [10] 3047 (2007).

[103] C. L. Martin and R. K. Bordia, "The effect of a substrate on the sintering of constrained films", *Acta Mater,* 57 [2] 549 (2009).

[104] R. Raj and R. K. Bordia, "Sintering behavior of bi-modal powder compacts", *Acta Metall Mater,* 32 [7] 1003 (1984).

[105] R. K. Bordia and G. W. Scherer, "On constrained sintering. II. Comparison of constitutive models", *Acta Metall Mater,* 36 [9] 2399 (1988).

[106] R. Z. Zuo, E. Aulbach and J. Rödel, "Experimental determination of sintering stresses and sintering viscosities", *Acta Mater,* 51 [15] 4563 (2003).

[107] R. Z. Zuo, E. Aulbach and J. Rödel, "Viscous Poisson's coefficient determined by discontinuous hot forging", *J Mater Res,* 18 [9] 2170 (2003).

[108] R. K. Bordia, R. Z. Zuo, O. Guillon, S. M. Salamone and J. Rödel, "Anisotropic constitutive laws for sintering bodies", *Acta Mater,* 54 [1] 111 (2006).

[109] D. Bernard, O. Guillon, N. Combaret and E. Plougonven, "Constrained sintering of glass films: Microstructure evolution assessed through synchrotron computed microtomography", *Acta Mater,* 59 [16] 6228 (2011).

[110] K. R. Venkatachari and R. Raj, "Shear deformation and densification of powder compacts", *J Am Ceram Soc,* 69 [6] 499 (1986).

[111] J. B. Ollagnier, D. J. Green, O. Guillon and J. Rödel, "Constrained sintering of a glass ceramic composite: II. Symmetric laminate", *J Am Ceram Soc,* 92 [12] 2900 (2009).

[112] O. Guillon, L. Weiler and J. Rödel, "Anisotropic microstructural development during the constrained sintering of dip-coated alumina thin films", *J Am Ceram Soc,* 90 [5] 1394 (2007).

[113] Y. C. Lin and J. H. Jean, "Constrained sintering of silver circuit paste", *J Am Ceram Soc,* 87 [2] 187 (2004).

[114] O. Guillon and I. Nettleship, "Microstructural characterization of alumina films during constrained sintering", *J Am Ceram Soc,* 93 [3] 627 (2010).

[115] O. Guillon, S. Krauss and J. Rödel, "Influence of thickness on the constrained sintering of alumina films", *J Eur Ceram Soc,* 27 [7] 2623 (2007).

[116] R. Mücke, N. H. Menzler, H. P. Buchkremer and D. Stover, "Cofiring of thin zirconia films during SOFC manufacturing", *J Am Ceram Soc,* 92 [1] S95 (2009).

[117] F. Li, J. Z. Pan, O. Guillon and A. Cocks, "Predicting sintering deformation of ceramic film constrained by rigid substrate using anisotropic constitutive law", *Acta Mater,* 58 [18] 5980 (2010).

[118] H. Ohsato, T. Tsunooka, T. Sugiyama, K. Kakimoto and H. Ogawa, "Forsterite ceramics for millimeterwave dielectrics", *J Electroceram,* 17 [2-4] 445 (2006).

[119] W. Wersing, "Microwave ceramics for resonators and filters", *Curr Opin Solid St M,* 1 [5] 715 (1996).

[120] H. Ohsato, "Origins of high Q on microwave tungstenbronze-type like $Ba_{6-3x}R_{8+2x}Ti_{18}O_{54}$ (R: rare earth) dielectrics based on the atomic arrangements", *J Eur Ceram Soc,* 27 [8-9] 2911 (2007).

[121] I. M. Reaney and D. Iddles, "Microwave dielectric ceramics for resonators and filters in mobile phone networks", *J Am Ceram Soc,* 89 [7] 2063 (2006).

[122] A. Hessel, "General characteristics of traveling-wave antennas", pp. 151. in Antenna Theory. Edited by R. E. C. a. F. J. Zucker. McGraw-Hill, New York (1969).

[123] S. J. Fiedziuszko, I. C. Hunter, T. Itoh, Y. Kobayashi, T. Nishikawa, S. N. Stitzer and K. Wakino, "Dielectric materials, devices and circuits", *IEEE T Microw Theory,* 50 [3] 706 (2002).

[124] W. G. Spitzer, R. C. Miller, L. E. Howarth and D. A. Kleinman, "Far infrared dielectric dispersion in $BaTiO_3$, $SrTiO_3$ and TiO_2", *Phy Rev,* 126 [5] 1710 (1962).

[125] S. B. Cohn, "Microwave bandpass filters containing high-Q dielectric resonators", *IEEE T Microw Theory,* 16 [4] 218 (1968).

[126] R. L. Bolton, "Temperature compensating ceramic capacitors in the system barium-rare earth oxide titania" Ph.D Thesis. The University of Illinois (1968).

[127] D. J. Masse, R. A. Pucel, D. W. Readey, E. A. Maguire and C. P. Hartwig, "New low-loss high K temperature-compensated dielectric for microwave applications", *Pr Inst Electr Elect,* 59 [11] 1628 (1971).

[128] T. Negas, G. Yeager, S. Bell, N. Coats and I. Minis, "$BaTi_4O_9$/$Ba_2Ti_9O_{20}$-based ceramics resurrected for modern microwave applications", *Am Ceram Soc Bull,* 72 [1] 80 (1993).

[129] H. M. Obryan, J. Thomson and J. K. Plourde, "New BaO-TiO_2 compound with temperature-stable high permittivity and low microwave loss", *Am Ceram Soc Bull,* 53 [4] 338 (1974).

[130] N. Ichinose and H. Yamamoto, "Effect of additives on microwave dielectric properties in low-temperature firing (Mg,Ca)TiO_3 based ceramics", *Ferroelectrics,* 201 [1-4] 255 (1997).

[131] H. Jantunen, R. Rautioaho, A. Uusimaki and S. Leppavuori, "Compositions of $MgTiO_3$-$CaTiO_3$ ceramic with two borosilicate glasses for LTCC technology", *J Eur Ceram Soc,* 20 [14-15] 2331 (2000).

[132] K. Wakino, K. Minai and H. Tamura, "Microwave characteristics of (Zr,Sn)TiO_4 and BaO-PbO-Nd_2O_3-TiO_2 dielectric resonators", *J Am Ceram Soc,* 67 [4] 278 (1984).

[133] S. Hirano, T. Hayashi and A. Hattori, "Chemical-processing and microwave characteristics of (Zr,Sn)TiO_4 microwave dielectrics", *J Am Ceram Soc,* 74 [6] 1320 (1991).

[134] T. Tsunooka, M. Androu, Y. Higashida, H. Sugiura and H. Ohsato, "Effects of TiO_2 on sinterability and dielectric properties of high-Q forsterite ceramics", *J Eur Ceram Soc,* 23 [14] 2573 (2003).

[135] Y. P. Guo, H. Ohsato and K. I. Kakimoto, "Characterization and dielectric behavior of willemite and TiO_2-doped willemite ceramics at millimeter-wave frequency", *J Eur Ceram Soc,* 26 [10-11] 1827 (2006).

[136] N. M. Alford and S. J. Penn, "Sintered alumina with low dielectric loss", *J Appl Phys,* 80 [10] 5895 (1996).

[137] H. Ohsato, T. Tsunooka, M. Ando, Y. Ohishi, Y. Miyauchi and K. Kakimoto, "Millimeter-wave dielectric ceramics of Alumina and Forsterite with high quality factor and low dielectric constant", *J Korean Ceram Soc,* 40 350 (2003).

[138] Y. Ohishi, Y. Miyauchi, H. Ohsato and K. Kakimoto, "Controlled temperature coefficient of resonant frequency of Al_2O_3-TiO_2 ceramics by annealing treatment", *Jpn J Appl Phys 2,* 43 [6A] L749 (2004).

[139] S. H. Wu, G. Q. Wang, Y. S. Zhao and H. Su, "BaO-TiO_2 microwave ceramics", *J Eur Ceram Soc,* 23 [14] 2565 (2003).

[140] D. W. Kim, K. H. Ko, D. K. Kwon and K. S. Hong, "Origin of microwave dielectric loss in $ZnNb_2O_6$-TiO_2", *J Am Ceram Soc,* 85 [5] 1169 (2002).

[141] H. J. Lee, K. S. Hong, S. J. Kim and I. T. Kim, "Dielectric properties of MNb_2O_6 compounds (where M=Ca, Mn, Co, Ni, or Zn)", *Mater Res Bull,* 32 [7] 847 (1997).

[142] M. Udovic, M. Valant and D. Suvorov, "Dielectric characterisation of ceramics from the TiO_2-TeO_2 system", *J Eur Ceram Soc,* 21 [10-11] 1735 (2001).

[143] T. Okawa, K. Kiuchi, H. Okabe and H. Ohsato, "Microwave dielectric properties of $Ba_nLa_4Ti_{3+n}O_{12+3n}$ homologous compounds and substitution of trivalent cations for La", *Ferroelectrics,* 272 [1] 345 (2002).

[144] I. N. Jawahar, N. I. Santha and M. T. Sebastian, "Microwave dielectric properties of MO-La_2O_3-TiO_2 (M = Ca, Sr, Ba) ceramics", *J Mater Res,* 17 [12] 3084 (2002).

[145] C. Vineis, P. K. Davies, T. Negas and S. Bell, "Microwave dielectric properties of hexagonal perovskites", *Mater Res Bull,* 31 [5] 431 (1996).

[146] H. Zheng, D. I. Woodward, L. Gillie and I. M. Reaney, "Structure and microwave dielectric properties of $BaLa_4Ti_4O_{15}$", *J Phys-Condens Mat,* 18 [31] 7051 (2006).

[147] S. Nishigaki, S. Yano, H. Kato, T. Hirai and T. Nonomura, "BaO-TiO_2-WO_3 microwave ceramics and crystalline $BaWO_4$", *J Am Ceram Soc,* 71 [1] C11 (1988).

[148] M. H. Weng, T. J. Liang and C. L. Huang, "Lowering of sintering temperature and microwave dielectric properties of $BaTi_4O_9$ ceramics prepared by the polymeric precursor method", *J Eur Ceram Soc,* 22 [9-10] 1693 (2002).

[149] H. Ohsato, "Science of tungstenbronze-type like $Ba_{6-3x}R_{8+2x}Ti_{18}O_{54}$ (R = rare earth) microwave dielectric solid solutions", *J Eur Ceram Soc,* 21 [15] 2703 (2001).

[150] S. Solomon, N. Santha, I. N. Jawahar, H. Sreemoolanadhan, M. T. Sebastian and P. Mohanan, "Tailoring the microwave dielectric properties of $BaRE_2Ti_4O_{12}$ and $BaRE_2Ti_5O_{14}$ ceramics by compositional variations", *J Mater Sci-Mater El,* 11 [8] 595 (2000).

[151] M. C. Wu, M. K. Hsieh, C. W. Yen, Y. C. Huang, W. T. Huang and W. F. Su, "Low sintering $BaNd_2Ti_4O_{12}$ microwave ceramics prepared by CuO thin layer coated powder", *J Eur Ceram Soc,* 27 [8-9] 2835 (2007).

[152] R. Ubic*.,* PhD thesis. University of Sheffield, UK (1998).

[153] D. W. Kim, B. Park, J. H. Chung and K. S. Hong, "Mixture behavior and microwave dielectric properties in the low-fired TiO_2-CuO system", *Jpn J Appl Phys,* 39 [5A] 2696 (2000).

[154] D. Zhou, H. Wang, X. Yao and L. X. Pang, "Sintering behavior and microwave dielectric properties of Bi_2O_3-ZnO-Nb_2O_5-based ceramics sintered under air and N_2 atmosphere", *Ceram Int,* 34 [4] 901 (2008).

[155] H. B. Hong, D. W. Kim and K. S. Hong, "Microwave dielectric properties of $Bi_2(Zn_{1/3}Ta_{2/3})_2O_7$ polymorphs", *Jpn J Appl Phys,* 42 [8] 5172 (2003).

[156] A. Borisevich and P. K. Davies, "Microwave dielectric properties of $Li_{1+x-y}M_{1-x-3y}Ti_{x+4y}O_3$ ($M=Nb^{5+}$, Ta^{5+}) solid solutions", *J Eur Ceram Soc,* 21 [10-11] 1719 (2001).

[157] M. Valant, A. K. Axelsson and N. Alford, "Review of $Ag(Nb,Ta)O_3$ as a functional material", *J Eur Ceram Soc,* 27 [7] 2549 (2007).

[158] M. Valant, D. Suvorov, C. Hoffmann and H. Sommariva, "$Ag(Nb,Ta)O_3$-based ceramics with suppressed temperature dependence of permittivity", *J Eur Ceram Soc,* 21 [15] 2647 (2001).

[159] T. Okawa, K. Kiuchi, H. Okabe and H. Ohsato, "Microwave dielectric properties of $Ba_nLa_4Ti_{3+n}O_{12+3n}$ homologous series", *Jpn J Appl Phys 1,* 40 [9B] 5779 (2001).

[160] V. A. Saltykova, O. V. Melnikova, N. V. Leonova and N. F. Fedorov, "$La_4Ti_3O_{12}$-$BaTiO_3$ System", *Russ J Inorg Chem,* 30 [1] 190 (1985).

[161] D. Kolar, S. Gaberscek, B. Volavsek, H. S. Parker and R. S. Roth, "Synthesis and crystal-chemistry of $BaNd_2Ti_3O_{10}$, $BaNd_2Ti_5O_{14}$ and $Nd_4Ti_9O_{24}$", *J Solid State Chem,* 38 [2] 158 (1981).

[162] R. Ratheesh, H. Sreemoolanadhan, M. T. Sebastian and P. Mohanan, "Preparation, characterization and dielectric properties of ceramics in the BaO-Nd_2O_3-TiO_2 system", *Ferroelectrics,* 211 [1-4] 1 (1998).

[163] C. J. Rawn, D. P. Birnie, M. A. Bruck, J. H. Enemark and R. S. Roth, "Structural investigation of $Ba_{6-3x}Ln_{8+2x}Ti_{18}O_{54}$ (x = 0.27, Ln = Sm) by single crystal X-ray diffraction in space group Pnma (No. 62)", *J Mater Res,* 13 [1] 187 (1998).

[164] Z. Fu, A. Wu, P. M. Vilarinho, A. I. Kingon and R. Wordenweber, "Low dielectric loss $BaNd_2Ti_5O_{14}$ thick films prepared by an electrophoretic deposition technique", *Appl Phys Lett,* 90 [5] 052912 (2007).

[165] C. T. Dervos, E. Thirios, J. Novacovich, P. Vassiliou and P. Skafidas, "Permittivity properties of thermally treated TiO_2", *Mater Lett,* 58 [9] 1502 (2004).

[166] M. Valant and P. K. Davies, "Crystal chemistry and dielectric properties of chemically substituted $(Bi_{1.5}Zn_{1.0}Nb_{1.5})O_7$ and $Bi_2(Zn_{2/3}Nb_{4/3})O_7$ pyrochlores", *J Am Ceram Soc,* 83 [1] 147 (2000).

[167] S. George, M. T. Sebastian, S. Raman and P. Mohanan, "Novel low loss, low permittivity glass-ceramic composites for LTCC applications", *Int J Appl Ceram Tec,* 8 [1] 172 (2011).

[168] M. Valant and D. Suvorov, "New high-permittivity $AgNb_{1-x}Ta_xO_3$ microwave ceramics: Part II, Dielectric characteristics", *J Am Ceram Soc,* 82 [1] 88 (1999).

[169] N. Teneze, D. Mercurio, G. Trolliard and B. Frit, "Cation-deficient perovskite-related compounds $(Ba,La)_nTi_{n-1}O_{3n}$ (n=4, 5 and 6): a Rietveld refinement from neutron powder diffraction data", *Mater Res Bull,* 35 [10] 1603 (2000).

[170] G. Trolliard, N. Harre, D. Mercurio and B. Frit, "Cation-deficient perovskite-related $(Ba,La)_nTi_{n-\delta}O_{3n}$ ($n \geq 4\delta$) microphases in the $La_4Ti_3O_{12}$-$BaTiO_3$ system: An HRTEM approach", *J Solid State Chem,* 145 [2] 678 (1999).

[171] G. Trolliard, N. Teneze, P. Boullay and D. Mercurio, "TEM study of cation-deficient-perovskite related $A_nB_{n-1}O_{3n}$ compounds: the twin-shift option", *J Solid State Chem,* 177 [4-5] 1188 (2004).

[172] C. C. Tang, M. A. Roberts, F. Azough, C. Leach and R. Freer, "Synchrotron X-ray diffraction study of $Ba_{4.5}Nd_9Ti_{18}O_{54}$ microwave dielectric ceramics at 10-295 K", *J Mater Res,* 17 [3] 675 (2002).

[173] W. Wersing, "High frequency ceramic dielectrics and their application for microwave components" in Electronic Ceramics. Edited by B. C. H. Steele. Elsevier Applied Science, London (1991).

[174] P. Laffez, G. Desgardin and B. Raveau, "Influence of calcination, sintering and composition upon microwave properties of the $Ba_{6-x}Sm_{8+2x/3}Ti_{18}O_{54}$-type oxide", *J Mater Sci,* 27 [19] 5229 (1992).

[175] H. Zheng, I. M. Reaney, D. Muir, T. Price and D. M. Iddles, "Composite dielectric ceramics based on BaO-Ln_2O_3-TiO_2 (Ln = Nd, La)", *Jpn J Appl Phys 1,* 44 [5A] 3087 (2005).

[176] P. M. Vilarinho, A. Mahajan, I. Sterianou and I. M. Reaney, "Layered composite thick films for dielectric applications", *J Eur Ceram Soc* (*In Press*).

[177] Q. L. Zhang, H. Yang and H. P. Sun, "A new microwave ceramic with low-permittivity for LTCC applications", *J Eur Ceram Soc,* 28 [3] 605 (2008).

[178] H. Zheng, I. M. Reaney, D. Muir, T. Price and D. M. Iddles, "Effect of glass additions on the sintering and microwave properties of composite dielectric ceramics based on $BaO-Ln_2O_3-TiO_2$ (Ln = Nd, La)", *J Eur Ceram Soc,* 27 [16] 4479 (2007).

[179] M. Mirsaneh, I. M. Reaney, Y. Han, I. Sterianou and O. P. Leisten, "Low sintering temperature high permittivity glass ceramic composites for dielectric loaded microwave antennas", *Adv Appl Ceram,* 110 [7] 387 (2011).

[180] M. T. Sebastian and H. Jantunen, "Low loss dielectric materials for LTCC applications: a review", *Int Mater Rev,* 53 [2] 57 (2008).

[181] Y. Fukami, K. Wada, K. Kakimoto and H. Ohsato, "Microstructure and microwave dielectric properties of $BaLa_4Ti_4O_{15}$ ceramics with template particles", *J Eur Ceram Soc,* 26 [10-11] 2055 (2006).

[182] C. Hoffmann and R. Waser, "Hot-forging of $Ba_{6-3x}RE_{8+2x}Ti_{18}O_{54}$ ceramics (RE=La, Ce, Nd, Sm)", *Ferroelectrics,* 201 [1-4] 127 (1997).

[183] A. S. Bhalla, R. Y. Guo and R. Roy, "The perovskite structure - a review of its role in ceramic science and technology", *Mater Res Innov,* 4 [1] 3 (2000).

[184] K. A. Muller and H. Burkard, "$SrTiO_3$ - An intrinsic quantum paraelectric below 4K", *Phys Rev B,* 19 [7] 3593-602 (1979).

[185] P. A. Fleury and J. M. Worlock, "Electric-field-induced Raman scattering in $SrTiO_3$ and $KTaO_3$", *Phys Rev,* 174 [2] 613 (1968).

[186] H. Uwe and T. Sakudo, "Stress-induced ferroelectricity and soft phonon modes in $SrTiO_3$", *Phys Rev B,* 13[1] 271 (1976).

[187] M. Itoh, R. Wang, Y. Inaguma, T. Yamaguchi, Y. J. Shan and T. Nakamura, "Ferroelectricity induced by oxygen isotope exchange in strontium titanate perovskite", *Phys Rev Lett,* 82 [17] 3540 (1999).

[188] J. G. Bednorz and K. A. Muller, "$Sr_{1-X}ca_xTiO_3$ - An XY quantum ferroelectric with transition to randomness", *Phys Rev Lett,* 52 [25] 2289 (1984).

[189] V. V. Lemanov, E. P. Smirnova, P. P. Syrnikov and E. A. Tarakanov, "Phase transitions and glasslike behavior in $Sr_{1-x}Ba_xTiO_3$", *Phys Rev B,* 54 [5] 3151 (1996).

[190] F. W. Lytle, "X-ray diffractometry of low-temperature phase transformations in strontium titanate", *J Appl Phys,* 35 [7] 2212 (1964).

[191] H. P. R. Frederikse, W. R. Thurber and W. R. Hosler, "Electronic transport in strontium titanate", *Phys Rev,* 134 [2A] A442 (1964).

[192] J. F. Schooley, W. R. Hosler and M. L. Cohen, "Superconductivity in semiconducting $SrTiO_3$", *Phys Rev Lett,* 12 [17] 474 (1964).

[193] S. Ohta, T. Nomura, H. Ohta and K. Koumoto, "High-temperature carrier transport and thermoelectric properties of heavily La- or Nb-doped $SrTiO_3$ single crystals", *J Appl Phys,* 97 [3] (2005).

[194] A. Tkach, "Strontium titanate based ceramics for tunable device applications" PhD thesis. University of Aveiro, Aveiro (2005).

[195] A. Tkach, P. M. Vilarinho and A. L. Kholkin, "Structure-microstructure-dielectric tunability relationship in Mn-doped strontium titanate ceramics", *Acta Mater,* 53 [19] 5061 (2005).

[196] O. G. Vendik, E. K. Hollmann, A. B. Kozyrev and A. M. Prudan, "Ferroelectric tuning of planar and bulk microwave devices", *J Supercond,* 12 [2] 325 (1999).

[197] M. E. Lines and A. M. Glass, "Principles and applications of ferroelectric and related materials", Clarendon Press: Oxford (1977).

[198] H. Shen, Y. W. Song, H. Gu, P. C. Wang and Y. M. Xi, "A high-permittivity $SrTiO_3$-based grain boundary barrier layer capacitor material single-fired under low temperature", *Mater Lett,* 56 [5] 802 (2002).

[199] J. Y. Li, S. T. Li and M. A. Alim, "The effect of reducing atmosphere on the $SrTiO_3$ based varistor-capacitor materials", *J Mater Sci-Mater El,* 17 [7] 503 (2006).

[200] J. Y. Li, S. H. Luo and M. A. Alim, "The role of TiO_2 powder on the $SrTiO_3$-based synthesized varistor materials", *Mater Lett,* 60 [6] 720 (2006).

[201] K. D. Johnson and V. P. Dravid, "Grain boundary barrier breakdown in niobium donor doped strontium titanate using in situ electron holography", *Appl Phys Lett,* 74 [4] 621 (1999).

[202] A. Kingon, "Perovskites: Is the ultimate memory in sight?", *Nat Mater,* 5 [4] 251 (2006).

[203] D. E. Kotecki, J. D. Baniecki, H. Shen, R. B. Laibowitz, K. L. Saenger, J. J. Lian, T. M. Shaw, S. D. Athavale, C. Cabral, P. R. Duncombe, M. Gutsche, G. Kunkel, Y. J.

Park, Y. Y. Wang and R. Wise, "(Ba,Sr)TiO_3 dielectrics for future stacked-capacitor DRAM", *IBM J ResDev,* 43 [3] 367 (1999).

[204] K. Eisenbeiser, J. M. Finder, Z. Yu, J. Ramdani, J. A. Curless, J. A. Hallmark, R. Droopad, W. J. Ooms, L. Salem, S. Bradshaw and C. D. Overgaard, "Field effect transistors with $SrTiO_3$ gate dielectric on Si", *Appl Phys Lett,* 76 [10] 1324 (2000).

[205] R. Meyer and R. Waser, "Resistive donor-doped $SrTiO_3$ sensors: I. Basic model for a fast sensor response", *Sensor Actuat B-Chem,* 101 [3] 335 (2004).

[206] T. Kolodiazhnyi and A. Petric, "The applicability of Sr-deficient n-type $SrTiO_3$ for SOFC anodes", *J Electroceram,* 15 [1] 5 (2005).

[207] K. Bouzehouane, P. Woodall, B. Marcilhac, A. N. Khodan, D. Crete, E. Jacquet, J. C. Mage and J. P. Contour, "Enhanced dielectric properties of $SrTiO_3$ epitaxial thin film for tunable microwave devices", *Appl Phys Lett,* 80 [1] 109 (2002).

[208] M. A. Saifi and L. E. Cross, "Dielectric properties of strontium titanate at low temperature", *Phys Rev B,* 2 [3] 677 (1970).

[209] K. H. Lee, S. W. Kim, H. Ohta and K. Koumoto, "Ruddlesden-Popper phases as thermoelectric oxides: Nb-doped $SrO(SrTiO_3)_n$ (n=1,2)", *J Appl Phys,* 100 [6] (2006).

[210] K. H. Lee, Y. F. Wang, S. W. Kim, H. Ohta and K. Koumoto, "Thermoelectric properties of Ruddlesden-Popper phase n-type semiconducting oxides: La-, Nd- and Nb-doped $Sr_3Ti_2O_7$", *Int J Appl Ceram Tec,* 4 [4] 326 (2007).

[211] J. W. Fergus, "Oxide materials for high temperature thermoelectric energy conversion", *J Eur Ceram Soc,* 32 [3] 525 (2012).

[212] T. M. Tritt and M. A. Subramanian, "Thermoelectric materials, phenomena and applications: A bird's eye view", *MRS Bull,* 31 [3] 188 (2006).

[213] J. T. Last, "Infrared-absorption studies on barium titanate and related materials", *Phys Rev,* 105 [6] 1740 (1957).

[214] G. M. Choi, H. L. Tuller and D. Goldschmidt, "Electronic-transport behavior in single-crystalline $Ba_{0.03}Sr_{0.97}TiO_3$", *Phys Rev B,* 34 [10] 6972 (1986).

[215] V. M. Goldschmidt, "*Geochemisce verterlungsgesetze der elemente*" Norske Videnskap: Oslo (1927).

[216] I. M. Reaney, E. L. Colla and N. Setter, "Dielectric and structural sharacteristics of Ba-based and Sr-based complex perovskites as a function of tolerance factor", *Jpn J Appl Phys 1,* 33 [7A] 3984 (1994).

[217] S. K. Mishra, R. Ranjan, D. Pandey and B. J. Kennedy, "Powder neutron diffraction study of the antiferroelectric phase transition in $Sr_{0.75}Ca_{0.25}TiO_3$", *J Appl Phys,* 91 [7] 4447 (2002).

[218] T. Mitsui and W. B. Westphal, "Dielectric and X-ray studies of $Ca_xBa_{1-x}TiO_3$ and $Ca_xSr_{1-x}TiO_3$", *Phys Rev,* 1 [5] 1354 (1961).

[219] L. Rimai and G. A. Demars, "Electron paramagnetic resonance of trivalent gadolinium ions in strontium and barium titanates", *Phys Rev,* 127 [3] 702 (1962).

[220] H. Unoki and T. Sakudo, "Electron spin resonance of Fe^{3+} in $SrTiO_3$ with special reference to 110K phase transition", *J Phys Soc Jpn,* 23 [3] 546 (1967).

[221] E. M. Levin, C. R. Robbins and H. F. McMurdie, "Phase diagrams for ceramists" The American Ceramic Society: Columbus (1964).

[222] A. M. J. Seuter, "Defect chemistry and clectrical transport properties of barium-titanate", *Philips Res Repts,* 1 (1974).

[223] S. Aggarwal and R. Ramesh, "Point defect chemistry of metal oxide heterostructures", *Annu Rev Mater Sci,* 28 463 (1998).

[224] D. M. Smyth, "The defect chemistry of metal oxides" Oxford University Press, Inc.: New York (2000).

[225] Y. H. Han, M. P. Harmer, Y. H. Hu and D. M. Smyth, "A^{2+}/Ti nonstoichiometry in alkaline earth titanates, $ATiO_3$", pp. 73-75. in Transport in Nonstoichiometric Compounds. Edited by G. Simkovich and V. S. Stubican. Plenun Press, New York (1985).

[226] F. A. Kroger and H. J. Vink, "Relations between the concentrations of imperfections in crystalline solids", *Solid State Phys,* 3 307 (1956).

[227] S. A. Long and R. N. Blumenthal, "Ti-rich nonstoichiometric $BaTiO_3$: II. Analysis of defect structure", *J Am Ceram Soc,* 54 [11] 577 (1971).

[228] N. H. Chan, R. K. Sharma and D. M. Smyth, "Non-stoichiometry in undoped $BaTiO_3$", *J Am Ceram Soc,* 64 [9] 556 (1981).

[229] D. M. Smyth, "Defect structure in perovskite titanates", *Curr Opin Solid St M,* 1 [5] 692 (1996).

[230] N. H. Chan, R. K. Sharma and D. M. Smyth, "Non-stoichiometry in $SrTiO_3$", *J Electrochem Soc,* 128 [8] 1762 (1981).

[231] R. Meyer, R. Waser, J. Helmbold and G. Borchardt, "Cationic surface segregation in donor-doped $SrTiO_3$ under oxidizing conditions", *J Electroceram,* 9 [2] 103 (2002).

[232] M. J. Akhtar, Z. U. N. Akhtar, R. A. Jackson and C. R. A. Catlow, "Computer-simulation studies of strontium titanate", *J Am Ceram Soc,* 78 [2] 421 (1995).

[233] R. Moos and K. H. Hardtl, "Defect chemistry of donor-doped and undoped strontium titanate ceramics between 1000 and 1400 ˚C", *J Am Ceram Soc,* 80 [10] 2549 (1997).

[234] R. Waser, "Bulk conductivity and defect chemistry of acceptor-doped strontium-titanate in the quenched state", *J Am Ceram Soc,* 74 [8] 1934 (1991).

[235] N. H. Chan and D. M. Smyth, "Defect chemistry of donor-doped $BaTiO_3$", *J Am Ceram Soc,* 67 [4] 285 (1984).

[236] H. M. Chan, M. P. Harmer and D. M. Smyth, "Compensating defects in highly donor-doped $BaTiO_3$", *J Am Ceram Soc,* 69 [6] 507 (1986).

[237] A. Yamada and Y. M. Chiang, "Nature of cation vacancies formed to compensate donors during oxidation of barium titanate", *J Am Ceram Soc,* 78 [4] 909 (1995).

[238] Y. M. Chiang and T. Takagi, "Grain-boundary chemistry of barium-titanate and strontium-titanate: II. Origin of electrical barriers in positive-temperature-coefficient thermistors", *J Am Ceram Soc,* 73 [11] 3286 (1990).

[239] K. Gomann, G. Borchardt, A. Gunhold, W. Maus-Friedrichs and H. Baumann, "Ti diffusion in La-doped $SrTiO_3$ single crystals", *Phys Chem Chem Phys,* 6 [13] 3639 (2004).

[240] K. Gomann, G. Bochardt, M. Schulz, A. Gomann, W. Maus-Friedrichs, B. Lesage, O. Kaitasov, S. Hoffman-Eifert and T. Schneller, "Sr diffusion in undoped and La-doped $SrTiO_3$ single crystals under oxidizing conditions", *Phys Chem Chem Phys,* 7 [9] 2053 (2005).

[241] U. Balachandran and N. G. Eror, "Oxygen nonstoichiometry of tantalum-doped $SrTiO_3$", *J Less-Common Met,* 85 [1] 11 (1982).

[242] D. Y. Wang and K. Umeya, "Depletion layer dielectric properties of positive temperature coefficient of resistance barium titanate", *J Am Ceram Soc,* 73 [6] 1574 (1990).

[243] N. Wilcox, V. Ravikumar, R. P. Rodrigues, V. P. Dravid, M. Vollman, R. Waser, K. K. Soni and A. G. Adriaens, "Investigation of grain-boundary segregation in acceptor and donor-doped strontium titanate", *Solid State Ionics,* 75 127 (1995).

[244] Y. M. Chiang and T. Takagi, "Grain boundary chemistry of barium titanate and strontium titanate: I. High-temperature equilibrium space-charge", *J Am Ceram Soc,* 73 [11] 3278 (1990).

[245] R. Waser and R. Hagenbeck, "Grain boundaries in dielectric and mixed conducting ceramics", *Acta Mater,* 48 [4] 797 (2000).

[246] R. Waser, "Electronic-properties of grain-boundaries in $SrTiO_3$ and $BaTiO_3$ ceramics", *Solid State Ionics,* 75 89-99 (1995).

[247] M. Bäurer, S. J. Shih, C. Bishop, M. P. Harmer, D. Cockayne and M. J. Hoffmann, "Abnormal grain growth in undoped strontium and barium titanate", *Acta Mater,* 58 [1] 290 (2010).

[248] N. D. Browning, J. P. Buban, H. O. Moltaji, S. J. Pennycook, G. Duscher, K. D. Johnson, R. P. Rodrigues and V. P. Dravid, "The influence of atomic structure on the formation of electrical barriers at grain boundaries in $SrTiO_3$", *Appl Phys Lett,* 74 [18] 2638 (1999).

[249] R. F. Klie and N. D. Browning, "Atomic scale characterization of oxygen vacancy segregation at $SrTiO_3$ grain boundaries", *Appl Phys Lett,* 77 [23] 3737-39 (2000).

[250] M. Kim, G. Duscher, N. D. Browning, K. Sohlberg, S. T. Pantelides and S. J. Pennycook, "Nonstoichiometry and the electrical activity of grain boundaries in $SrTiO_3$", *Phys Rev Lett,* 86 [18] 4056 (2001).

[251] M. Bäurer, H. Stormer, D. Gerthsen and M. J. Hoffmann, "Linking grain boundaries and grain growth in ceramics", *Adv Eng Mater,* 12 [12] 1230 (2010).

[252] K. Szot, M. Pawelczyk, J. Herion, C. Freiburg, J. Albers, R. Waser, J. Hulliger, J. Kwapulinski and J. Dec, "Nature of the surface layer in ABO_3-type perovskites at elevated temperatures", *Appl Phys A-Mater,* 62 [4] 335 (1996).

[253] K. Szot and W. Speier, "Surfaces of reduced and oxidized $SrTiO_3$ from atomic force microscopy", *Phys Rev B,* 60 [8] 5909 (1999).

[254] A. Kazimirov, D. M. Goodner, M. J. Bedzyk, J. Bai and C. R. Hubbard, "X-ray surface diffraction analysis of structural transformations on the (001) surface of oxidized $SrTiO_3$", *Surf Sci,* 492 [1-2] L711 (2001).

[255] K. Szot, W. Speier, U. Breuer, R. Meyer, J. Szade and R. Waser, "Formation of micro-crystals on the (100) surface of $SrTiO_3$ at elevated temperatures", *Surf Sci,* 460 [1-3] 112 (2000).

[256] K. Szot, W. Speier, J. Herion and C. Freiburg, "Restructuring of the surface region in $SrTiO_3$", *Appl Phys A-Mater,* 64 [1] 55 (1997).

[257] U. Balachandran and N. G. Eror, "On the defect structure of strontium-titanate with excess SrO", *J Mater Sci,* 17 [7] 2133 (1982).

[258] N. G. Eror and U. Balachandran, "Electrical-conductivity in strontium titanate with nonideal cationic ratio", *J Solid State Chem,* 42 [3] 227 (1982).

[259] L. Amaral, A. M. R. Senos and P. M. Vilarinho, "Sintering kinetic studies in nonstoichiometric strontium titanate ceramics", *Mater Res Bull,* 44 [2] 263 (2009).

[260] A. Ianculescu, A. Brăileanu and G. Voicu, "Synthesis, microstructure and dielectric properties of antimony-doped strontium titanate ceramics" *J Eur Ceram Soc,* 27 [2-3] 1123 (2007).

[261] I. K. You, J. D. Byun and Y. H. Kim, "The microstructure and electrical conductivity of WO_3-doped $SrTiO_3$ ceramics", *Solid State Ionics,* 83 [1-2] 159 (1996).

[262] T. Suzuki, Y. Nishi and M. Fujimoto, "Defect structure in homoepitaxial non-stoichiometric strontium titanate thin films", *Philos Mag A,* 80 [3] 621 (2000).

[263] M. Bäurer, H. Kungl and M. J. Hoffmann, "Influence of Sr/Ti stoichiometry on the densification behavior of strontium titanate", *J Am Ceram Soc,* 92 [3] 601 (2009).

[264] G. S. Rohrer, "Influence of interface anysotropy on grain growth and coarsening", *Annu Rev Mater Res,* 35 [1] 99 (2005).

[265] T. Sano and G. S. Rohrer, "Experimental evidence for the development of bimodal grain size distributions by the nucleation-limited coarsening mechanism", *J Am Ceram Soc,* 90 [1] 211 (2007).

[266] S. Y. Chung and S. J. L. Kang, "Effect of dislocations on grain growth in strontium titanate", *J Am Ceram Soc,* 83 [11] 2828 (2000).

[267] S. Y. Chung and S. J. L. Kang, "Intergranular amorphous films and dislocations-promoted grain growth in $SrTiO_3$", *Acta Mater,* 51 [8] 2345 (2003).

[268] S. B. Lee, W. Sigle and M. Ruhle, "Faceting behavior of an asymmetric $SrTiO_3$ Σ5[001] tilt grain boundary close to its defaceting transition", *Acta Mater,* 51 [15] 4583 (2003).

[269] S. Y. Chung, S. J. L. Kang and V. P. Dravid, "Effect of sintering atmosphere on grain boundary segregation and grain growth in niobium-doped $SrTiO_3$", *J Am Ceram Soc,* 85 [11] 2805 (2002).

[270] C. J. Peng and Y. M. Chiang, "Grain-growth in donor-doped $SrTiO_3$", *J Mater Res,* 5 [6] 1237 (1990).

[271] M. H. Lin and H. Y. Lu, "Site-occupancy of yttrium as a dopant in BaO-excess $BaTiO_3$", *Mat Sci Eng A-Struct,* 335 [1-2] 101 (2002).

[272] C. J. Peng and H. Y. Lu, "Compensation effect in semiconducting barium-titanate", *J Am Ceram Soc,* 71 [1] C44 (1988).

[273] J. J. Xing, H. Gu, Y. U. Heo and M. Takeguchi, "Initial transient structure and chemistry of intergranular glassy films in ferric-oxide doped strontium titanate ceramics", *J Mater Sci,* 46 [12] 4361 (2011).

[274] A. Fossdal, M. A. Einarsrud and T. Grande, "Phase equilibria in the pseudo-binary system SrO-Fe_2O_3", *J Solid State Chem,* 177 [8] 2933 (2004).

[275] J. S. Chen, R. J. Young and T. B. Wu, "Densification and microstructural development of $SrTiO_3$ sintered with V_2O_5", *J Am Ceram Soc,* 70 [10] C260 (1987).

[276] L. Amaral, A. M. R. Senos and P. M. Vilarinho, "Nonstoichiometry effects in $SrTiO_3$ ceramics assessed by Transmission Electron Microscopy", *Microsc Microanal,* 14 [Suppl. 3] 5 (2008).

[277] A. Tkach, P. M. Vilarinho, A. M. R. Senos and A. L. Kholkin, "Effect of nonstoichiometry on the microstructure and dielectric properties of strontium titanate ceramics", *J Eur Ceram Soc,* 25 [12] 2769 (2005).

[278] C. Bae, J. G. Park, Y. H. Kim and H. Jeon, "Abnormal grain growth of niobium-doped strontium titanate ceramics", *J Am Ceram Soc,* 81 [11] 3005 (1998).

[279] S. J. Shih, S. Lozano-Perez and D. J. H. Cockayne, "Investigation of grain boundaries for abnormal grain growth in polycrystalline $SrTiO_3$", *J Mater Res,* 25 [2] 260 (2010).

[280] C. Bae, J. G. Park and Y. H. Kim, "Effect of powder characteristics on the microstructure and electrical property of Nb-doped $SrTiO_3$", *J Korean Phys Soc,* 32 S296 (1998).

[281] I. Corni, M. P. Ryan and A. R. Boccaccini, "Electrophoretic deposition: From traditional ceramics to nanotechnology", *J Eur Ceram Soc,* 28 [7] 1353 (2008).

[282] Y. Fukada, N. Nagarajan, W. Mekky, Y. Bao, H. S. Kim and P. S. Nicholson, "Electrophoretic deposition - mechanisms, myths and materials", *J Mater Sci,* 39 [3] 787 (2004).

[283] P. Sarkar and P. S. Nicholson, "Electrophoretic deposition (EPD): Mechanisms, kinetics and application to ceramics", *J Am Ceram Soc,* 79 [8] 1987 (1996).

[284] O. O. Van der Biest and L. J. Vandeperre, "Electrophoretic deposition of materials", *Annu Rev Mater Sci,* 29 327 (1999).

[285] I. Zhitomirsky, "Cathodic electrodeposition of ceramic and organoceramic materials. Fundamental aspects", *Adv Colloid Interfac,* 97 [1-3] 279-317 (2002).

[286] B. Ferrari and R. Moreno, "EPD kinetics: A review", *J Eur Ceram Soc,* 30 [5] 1069 (2010).

[287] M. E. Orazem and B. Tribollet, "Electrochemical impedance spectroscopy", John Wiley & Sons, Inc: New Jersey (2008).

[288] J. T. S. Irvine, D. C. Sinclair and A. R. West, "Electroceramics: Characterization by impedance spectroscopy", *Adv Mater,* 2 [3] 132 (1990).

[289] E. Barsoukov and J. R. Macdonald, "Impedance spectroscopy theory, experiment and applications", 2nd ed. John Wiley & Sons, Inc.: New Jersey (2005).

[290] P. S. Nicholson, P. Sarkar and X. Huang, "Electrophoretic deposition and its use to synthesize ZrO_2/Al_2O_3 micro-laminate ceramic-ceramic composites", *J Mater Sci,* 28 [23] 6274 (1993).

[291] I. Zhitomirsky, "Electrophoretic deposition of chemically bonded ceramics in the system $CaO\text{-}SiO_2\text{-}P_2O_5$", *J Mater Sci Lett,* 17 [24] 2101 (1998).

[292] G. Anne, K. Vanmeensel, J. Vleugels and O. Van der Biest, "Influence of the suspension composition on the electric field and deposition rate during electrophoretic deposition", *Colloid Surface A,* 245 [1-3] 35 (2004).

[293] T. G. Sweeney and R. W. Whatmore, "Electrophoretic deposition of ferroelectric thin films", *Ferroelectrics,* 187 57 (1996).

[294] Z. Fu, "$BaNd_2Ti_5O_{14}$ thick films for microelectronics fabricated by electrophoretic deposition", PhD Thesis. University of Aveiro, Aveiro (2008).

[295] R. Jenkins and R. L. Snyder, "Introduction to X-ray powder diffractometry", John Wiley and Sons: New York (1996).

[296] W. L. Bragg, "The diffraction of short electromagnetic waves by a crystal", *Proceedings of the Cambridge Philosophical Society,* 17 43 (1913).

[297] U. F. Kocks, C. Tomé and H. R.Wenk, "Texture and anisotropy", Cambridge University Press: Cambridge, UK (1998).

[298] J. Goldstein, D. E. Newbury, D. C. Joy, C. E. Lyman, P. Echlin, E. Lifshin, L. Sawyer and J. R. Michael, "Scanning electron microscopy and X-ray microanalysis", 3rd ed. Kluwer Academic New York (2003).

[299] D. B. Williams and C. B. Carter, "Transmission electron microscopy: a textbook for materials science", Vol. 1. Plenum Press: New York (1996).

[300] A. Benninghoven, F. G. Rüdenauer and H. W. Werner, "Secondary ion mass spectrometry: Basic concepts, instrumental aspects, applications and trends", Wiley: New York (1987).

[301] R. C. Buchanan, "Ceramic materials for electronics - processing, properties and applications", Marcel Dekker: New York (1991).

[302] R. W. Whatmore, "Ferroelectrics, microsystems and nanotechnology", *Ferroelectrics,* 225 [1-4] 985 (1999).

[303] J. Van Tassel and C. A. Randall, "Electrophoretic deposition and sintering of thin/thick PZT films", *J Eur Ceram Soc,* 19 [6-7] 955 (1999).

[304] P. M. Vilarinho, " Functional materials: Properties, processing and applications", pp. 3 .in Scanning Probe Microscopy: Characterization, Nanofabrication and Device Application of Functional Materials, NATO Science Series, II. Mathematics, Physics and Chemistry – Vol. 186. Edited by P. M. Vilarinho, Y. Rosenwaks and A. Kingon. Kluwer Academic Publishers, Dordrecht, The Netherlands (2005).

[305] J. Ma and W. Cheng, "Electrophoretic deposition of lead zirconate titanate ceramics", *J Am Ceram Soc,* 85 [7] 1735 (2002).

[306] A. Y. Wu, P. M. Vilarinho and A. I. Kingon, "Ceramic processing strategies for thick films on copper foils", *Acta Mater,* 58 [6] 2282 (2010).

[307] J. G. P. Binner, "Advanced ceramic processing and technology", William Andrew Publishing (1990).

[308] H. C. Hamaker, "Formation of a deposit by electrophoresis", *Transactions of the Faraday Society,* 35 279 (1940).

[309] M. E. Labib and R. Williams, "An experimental comparison between the aqueous pH scale and the electron donicity scale", *Colloid Polym Sci,* 264 [6] 533 (1986).

[310] O. Stern, "The theory of the electrolytic double shift", *Elektrochem,* 30 508 (1924).

[311] J. Lyklema, "Water at interfaces: A colloid-chemical approach", *J Colloid Interf Sci,* 58 [2] 242-50 (1977).

[312] N. L. Weise, editor, "SME mineral processing handbook", Society of Mining Engineers: New York (1985).

[313] M. Zarbov, I. Schuster and L. Gal-Or, "Methodology for selection of charging agents for electrophoretic deposition of ceramic particles", *J Mater Sci,* 39 [3] 813-17 (2004).

[314] B. V. Deryaguin and L. D. Landau, "A theory of the stability of strongly charged lyophobic sols and of the adhesion of strongly charged particles in the solution of electrolytes", *Acta Physicochim USSR,* 14 633 (1941).

[315] E. J. W. Verwey and J. T. G. Overbeek, "Theory of the stability of lyophobic colloids", Elsevier: Amsterdam (1948).

[316] H. C. Hamaker and E. J. W. Verwey, "Colloid stability. The role of the forces between the particles in electrodeposition and other phenomena.", *Transactions of the Faraday Society,* 35 [3] 0180-85 (1940).

[317] F. Grillon, D. Fayeulle and M. Jeandin, "Quantitative image-analysis of electrophoretic coatings", *J Mater Sci Lett,* 11 [5] 272 (1992).

[318] H. Koelmans, "Suspensions in non-aqueous media", *Phillips Res Repts,* 10 161 (1995).

[319] A. R. Boccaccini, D. C. Meng and J. Ioannou, "Bioglass-based scaffolds with carbon nanotube coating for bone tissue engineering", *J Mater Sci-Mater M,* 20 [10] 2139 (2009).

[320] H. Negishi, K. Yamaji, N. Sakai, T. Horita, H. Yanagishita and H. Yokokawa, "Electrophoretic deposition of YSZ powders for solid oxide fuel cells", *J Mater Sci,* 39 [3] 833 (2004).

[321] S. Novak, K. Rade, K. Konig and A. R. Boccaccini, "Electrophoretic deposition in the production of SiC/SiC composites for fusion reactor applications", *J Eur Ceram Soc,* 28 [14] 2801 (2008).

[322] O. Van der Biest, S. Put, G. Anne and J. Vleugels, "Electrophoretic deposition for coatings and free standing objects", *J Mater Sci,* 39 [3] 779 (2004).

[323] I. Zhitomirsky and L. Gal-Or, "Electrophoretic deposition of hydroxyapatite", *J Mater Sci-Mater M,* 8 [4] 213 (1997).

[324] R. Moreno and B. Ferrari, "Effect of the slurry properties on the homogeneity of alumina deposits obtained by aqueous electrophoretic deposition", *Mater Res Bull,* 35 [6] 887 (2000).

[325] R. W. Powers, "Electrophoretic forming of β-alumina ceramic", *J Electrochem Soc,* 122 [4] 490-500 (1975).

[326] B. Ferrari and R. Moreno, "The conductivity of aqueous Al_2O_3 slips for electrophoretic deposition", *Mater Lett,* 28 [4-6] 353 (1996).

[327] R. N. Basu, C. A. Randall and M. J. Mayo, "Fabrication of dense zirconia electrolyte films for tubular solid oxide fuel cells by electrophoretic deposition", *J Am Ceram Soc,* 84 [1] 33 (2001).

[328] Z. Y. Peng and M. L. Liu, "Preparation of dense platinum-yttria stabilized zirconia and yttria stabilized zirconia films on porous $La_{0.9}Sr_{0.1}MnO_3$ (LSM) substrates", *J Am Ceram Soc,* 84 [2] 283-88 (2001).

[329] J. R. Macdonald, "Impedance spectroscopy", *Ann Biomed Eng,* 20 [3] 289- (1992).

[330] E. M. Purcell, "Electricity and Magnetism", McGraw-Hill New York (1985).

[331] R. Schmidt, W. Eerenstein, T. Winiecki, F. D. Morrison and P. A. Midgley, "Impedance spectroscopy of epitaxial multiferroic thin films", *Phys Rev B,* 75 [24] (2007).

[332] J. C. C. Abrantes, J. A. Labrincha and J. R. Frade, "Applicability of the brick layer model to describe the grain boundary properties of strontium titanate ceramics", *J Eur Ceram Soc,* 20 [10] 1603 (2000).

[333] J. Fleig and J. Maier, "The impedance of ceramics with highly resistive grain boundaries: Validity and limits of the brick layer model", *J Eur Ceram Soc,* 19 [6-7] 693 (1999).

[334] J. Fleig, "The grain boundary impedance of random microstructures: numerical simulations and implications for the analysis of experimental data", *Solid State Ionics,* 150 [1-2] 181 (2002).

[335] C. H. Hsu and F. Mansfeld, "Technical note: Concerning the conversion of the constant phase element parameter Y_0 into a capacitance", *Corrosion,* 57 [9] 747 (2001).

[336] R. Schmidt, J. Wu, C. Leighton and I. Terry, "Dielectric response to the low-temperature magnetic defect structure and spin state transition in polycrystalline $LaCoO_3$", *Phys Rev B,* 79 [12] 125105 (2009).

[337] M. Demartin, C. Herard, C. Carry and J. Lemaitre, "Dedensification and anomalous grain growth during sintering of undoped barium titanate", *J Am Ceram Soc,* 80 [5] 1079 (1997).

[338] P. R. Rios, "Abnormal grain-growth in materials containing particles", *Acta Metall Mater,* 42 [3] 839 (1994).

[339] J. E. Burke and D. Turnbull, "Recrystallization and grain growth", *Progr Metal Phys,* 3 [0] 220 (1952).

[340] S. J. Dillon, S. K. Behera and M. P. Harmer, "An experimentally quantifiable solute drag factor", *Acta Mater,* 56 [6] 1374 (2008).

[341] J. R. Jurado, M. T. Colomer and J. R. Frade, "Impedance spectroscopy of $Sr_{0.97}Ti_{1-x}Fe_xO_{3-\delta}$ materials with moderate Fe-contents", *Solid State Ionics,* 143 [2] 251 (2001).

[342] L. C. Walters and R. E. Grace, "Formation of point defects in strontium titanate", *J Phys Chem Solids,* 28 [2] 239 (1967).

[343] M. Vollman and R. Waser, "Grain boundary defect chemistry of acceptor-doped titanates: Space charge layer width", *J Am Ceram Soc,* 77 [1] 235 (1994).

[344] M. Vollman, R. Hagenbeck and R. Waser, "Grain-boundary defect chemistry of acceptor-doped titanates: Inversion layer and low-field conduction", *J Am Ceram Soc,* 80 [9] 2301 (1997).

[345] W. L. Warren, K. Vanheusden, D. Dimos, G. E. Pike and B. A. Tuttle, "Oxygen vacancy motion in perovskite oxides", *J Am Ceram Soc,* 79 [2] 536 (1996).

[346] I. Denk, J. Claus and J. Maier, "Electrochemical investigations of $SrTiO_3$ boundaries", *J Electrochem Soc,* 144 [10] 3526 (1997).

[347] J. R. Jurado, M. T. Colomer and J. R. Frade, "Electrical characterization of $Sr_{0.97}Ti_{1-x}Fe_xO_3$-delta by complex impedance spectroscopy: I. materials with low iron contents", *J Am Ceram Soc,* 83 [11] 2715 (2000).

[348] J. Fleig and J. Maier, "A finite element study on the grain boundary impedance of different microstructures", *J Electrochem Soc,* 145 [6] 2081 (1998).

[349] C. Tande, D. Perez-Coll and G. C. Mather, "Surface proton conductivity of dense nanocrystalline YSZ", *J Mater Chem,* 22 11208 (2012).

[350] O. J. Dura, M. A. L. de la Torre, L. Vazquez, J. Chaboy, R. Boada, A. Rivera-Calzada, J. Santamaria and C. Leon, "Ionic conductivity of nanocrystalline yttria-stabilized zirconia: Grain boundary and size effects", *Phys Rev B,* 81 [18] (2010).

[351] J. Öijerholm, "Ionic transport in metal oxides studied in situ by impedance spectroscopy and cyclic voltammetry", PhD thesis. Royal Institute of Technology, Stockholm (2007).

[352] M. Bäurer, L. F. Zagonel, N. Barrett and M. J. Hoffmann, "Changes in macroscopic behaviour through segregation in niobium doped strontium titanate", *Journal of Physics: Conference Series,* 94 012015 (2008).

[353] J. H. Hwang, K. D. Johnson, T. O. Mason and V. P. Dravid, "Single grain boundary characterization of Nb-doped $SrTiO_3$ bicrystals using ac four-point impedance spectroscopy", *Appl Phys Lett,* 76 [18] 2621 (2000).

[354] S. B. Lee, J. H. Lee, Y. H. Cho, D. Y. Kim, W. Sigle, F. Phillipp and P. A. van Aken, "Grain-boundary plane orientation dependence of electrical barriers at Σ5 boundaries in $SrTiO_3$", *Acta Mater,* 56 [18] 4993 (2008).

[355] J. P. Han, P. Q. Mantas and A. M. R. Senos, "Densification and grain growth of Al-doped ZnO", *J Mater Res,* 16 [2] 459 (2001).

[356] C. F. Yang and S. H. Lo, "Grain growth for CuO-BaO mixtures added $BaTi_{1-x}O_{3+2x}$ ceramics", *Mater Res Bull,* 32 [12] 1713 (1997).

[357] J. Chung, J. Kim, B. Jang, Y. Ahn, H. Lee and W. Yoon, "Effect of retrograde solubility on the purification of MG Si during fractional melting", *Sol Energ Mat Sol C,* 95 [1] 45 (2011).

[358] E. R. Weber, "Transition-metals in silicon", *Appl Phys A-Mater,* 30 [1] 1 (1983).

[359] A. L. McKelvey, "Retrograde solubility in semiconductors", *Metall Mater Trans A,* 27 [9] 2704 (1996).

[360] F. A. Trumbore, "Solid solubilities of impurity elements in germanium and silicon", *At&T Tech J,* 39 [1] 205 (1960).

[361] S. V. Varamban and K. T. Jacob, "Discussion of "Retrograde solubility in semiconductors"", *Metall Mater Trans A,* 29 [5] 1525 (1998).

[362] D. Navon and V. Chernyshov, "Retrograde solubility of aluminum in silicon", *J Appl Phys,* 28 [7] 823 (1957).

[363] G. S. Pomrehn, E. S. Toberer, G. J. Snyder and A. van de Walle, "Entropic stabilization and retrograde solubility in Zn_4Sb_3", *Phys Rev B,* 83 [9] (2011).

[364] L. S. Chang, B. B. Straumal, E. Rabkin, W. Gust and F. Sommer, "The solidus line of the Cu-Bi phase diagram", *J Phase Equilib,* 18 [2] 128 (1997).

[365] C. Y. Chen and R. M. Cohen, "Zn solubility limit in GaAs: Growth versus equilibrium", *J Cryst Growth,* 167 [1-2] 17 (1996).

[366] S. K. Kim and J. K. Park, "In-situ measurement of continuous cooling β->α transformation behavior of CP-Ti", *Metall Mater Trans A,* 33 [4] 1051 (2002).

[367] X. M. Shi and J. Luo, "Decreasing the grain boundary diffusivity in binary alloys with increasing temperature", *Phys Rev Lett,* 105 [23] (2010).

[368] S. P. S. Badwal, "Grain-boundary resistivity in zirconia-based materials - Effect of sintering temperatures and impurities", *Solid State Ionics,* 76 [1-2] 67 (1995).

[369] J. E. Bauerle, "Study of solid electrolyte polarization by a complex admittance method", *J Phys Chem Solids,* 30 [12] 2657 (1969).

[370] N. M. Beekmans and L. Heyne, "Correlation between impedance, microstructure and composition of calcia-stabilized zirconia", *Electrochim Acta,* 21 [4] 303 (1976).

[371] T. Mathews, N. Rabu, J. R. Sellar and B. C. Muddle, "Fabrication of $La_{1-x}Sr_xGa_{1-y}Mg_yO_{3-(x+y)/2}$ thin films by electrophoretic deposition and its conductivity measurement", *Solid State Ionics,* 128 [1-4] 111 (2000).

[372] P. M. Vilarinho, Z. Fu, A. Wu and A. I. Kingon, "Critical role of suspension media in electrophoretic deposition: The example of low loss dielectric $BaNd_2Ti_5O_{14}$ thick films", *J Phys Chem B* (*In press*).

[373] I. Zhitomirsky and A. Petric, "Electrophoretic deposition of electrolyte materials for solid oxide fuel cells", *J Mater Sci,* 39 [3] 825-31 (2004).

[374] E. Aulbach, R. Zuo and J. Rödel, "Laser-assisted high-resolution loading dilatometer and applications", *Exp Mech,* 44 [1] 71 (2004).

[375]X. Wang and A. Atkinson, "Microstructure evolution in thin zirconia films: Experimental observation and modelling", *Acta Mater,* 59 [6] 2514 (2011).

[376] R. K. Kirby, "Platinum - a thermal expansion reference material", *Int J Thermophys,* 12 [4] 679 (1991).

[377] J. R. Tesmer and M. A. Nastasi, "Handbook of modern ion beam materials analysis", Materials Research Society: Pittsburgh, Pennsylvania (1995).

[378] K. B. Shim, N. T. Cho and S. W. Lee, "Silver diffusion and microstructure in LTCC multilayer couplers for high frequency applications", *J Mater Sci,* 35 [4] 813 (2000).

[379] W. C. Hu, C. R. Yang, W. L. Zhang, G. J. Liu and D. Dong, "The diffusion of Pt in BST films on Pt/Ti/SiO_2/Si substrate by sol-gel method", *J Sol-Gel Sci Techn,* 39 [3] 293 (2006).

[380] M. Winning, G. Gottstein and L. S. Shvindlerman, "Stress induced grain boundary motion", *Acta Mater,* 49 [2] 211 (2001).

[381] M. Winning, G. Gottstein and L. S. Shvindlerman, "On the mechanisms of grain boundary migration", *Acta Mater,* 50 [2] 353 (2002).

[382] D. S. Gianola, S. Van Petegem, M. Legros, S. Brandstetter, H. Van Swygenhoven and K. J. Hemker, "Stress-assisted discontinuous grain growth and its effect on the deformation behavior of nanocrystalline aluminum thin films", *Acta Mater,* 54 [8] 2253 (2006).

[383] D. U. Kim, S. G. Kim, W. T. Kim, J. Cho, H. N. Han and P. R. Cha, "Effect of microelasticity on grain growth: Texture evolution and abnormal grain growth", *Scripta Mater,* 64 [12] 1079 (2011).

[384] B. J. Kellett and F. F. Lange, "Hot forging characteristics of transformation-toughened Al_2O_3/ZrO_2 composites", *J Mater Res,* 3 [3] 545 (1988).

[385] D. S. Wilkinson and C. H. Cáceres, "On the mechanism of strain-enhanced grain growth during superplastic deformation", *Acta Metall Mater,* 32 [9] 1335 (1984).

[386] J. Besson and M. Abouaf, "Microstructural changes in alumina during hot isostatic pressing", *Mater Sci Eng A,* 109 37 (1989).

[387] J. Besson and M. Abouaf, "Grain growth enhancement in alumina during hot isostatic pressing", *Acta Metall Mater,* 39 [10] 2225 (1991).

[388] J. Langer, M. J. Hoffmann and O. Guillon, "Direct comparison between hot pressing and electric field-assisted sintering of submicron alumina", *Acta Mater,* 57 [18] 5454 (2009).

[389] A. Atkinson, J.-S. Kim, R. Rudkin, S. Taub and X. Wang, "Stress induced by constrained sintering of 3YSZ films measured by substrate creep", *J Am Ceram Soc,* 94 [3] 717 (2011).

[390] C. Zener, "Grains, phases and interfaces: an interpretation of microstructure", *Trans. Am. Inst. Miner. Metall. Soc.,* 175 pp. 15 (as communicated by C.S. Smith) (1948).

[391] Y. X. Liu and B. R. Patterson, "Stereological analysis of Zener pinning", *Acta Mater,* 44 [11] 4327 (1996).

[392] W. B. Li and K. E. Easterling, "The influence of particle-shape on Zener drag", *Acta Metall Mater,* 38 [6] 1045 (1990).

[393] A. Miro and M. R. Notis, "Materials science research", pp. 457. Vol. 13. Edited by G. C. Kuczynski. Plenum Press, New York (1980).

[394] D. Uskokovic, V. Petrovic and M. M. Ristic, "Materials science research", pp. 471. Vol. 13. Edited by G. C. Kuczynski. Plenum Press, New York (1980).

[395] H. P. Han, P. Q. Mantas and A. M. R. Senos, "Sintering kinetics of undoped and Mn-doped zinc oxide in the intermediate stage", *J Am Ceram Soc,* 88 [7] 1773 (2005).

[396] L. A. Bendersky, J. J. Krajewski and R. J. Cava, "Dielectric properties and microstructure of $Ca_5Nb_2TiO_{12}$ and $Ca_5Ta_2TiO_{12}$", *J Eur Ceram Soc,* 21 [15] 2653 (2001).

[397] J. H. Hao, L. Zhi and J. Gao, "Effects of substrate on the dielectric and tunable properties of epitaxial $SrTiO_3$ thin films", *J Appl Phys,* 100 [11] 114107 (2006).

[398] A. Antons, J. B. Neaton, K. M. Rabe and D. Vanderbilt, "Tunability of the dielectric response of epitaxially strained $SrTiO_3$ from first principles", *Phys Rev B,* 71 [2] 024102 (2005).

[399] G. L. Messing, S. Trolier-McKinstry, E. M. Sabolsky, C. Duran, S. Kwon, B. Brahmaroutu, P. Park, H. Yilmaz, P. W. Rehrig, K. B. Eitel, E. Suvaci, M. Seabaugh and K. S. Oh, "Templated grain growth of textured piezoelectric ceramics", *Crit Rev Solid State,* 29 [2] 45 (2004).

[400] H. M. Obryan and J. Thomson, "Phase-equilibria in TiO_2-rich region of system Bao-TiO_2", *J Am Ceram Soc,* 57 [12] 522 (1974).